Metallurgical Analysis of Rim Cracking in an LP Steam Turbine Disc

NP-1532
Research Project 1398-1

Final Report, September 1980
Work Completed, February 1980

Prepared by

SOUTHWEST RESEARCH INSTITUTE
P.O. Drawer 28510
6220 Culebra Road
San Antonio, Texas 78284

Principal Investigator
H. C. Burghard, Jr.

Prepared for

Electric Power Research Institute
3412 Hillview Avenue
Palo Alto, California 94304

DISTRIBUTION OF THIS DOCUMENT IS UNLIMITED

EPRI Project Manager
M. Kolar

Reliability, Availability, and Economics Program
Nuclear Power Division

DISCLAIMER

This report was prepared as an account of work sponsored by an agency of the United States Government. Neither the United States Government nor any agency thereof, nor any of their employees, makes any warranty, express or implied, or assumes any legal liability or responsibility for the accuracy, completeness, or usefulness of any information, apparatus, product, or process disclosed, or represents that its use would not infringe privately owned rights. Reference herein to any specific commercial product, process, or service by trade name, trademark, manufacturer, or otherwise does not necessarily constitute or imply its endorsement, recommendation, or favoring by the United States Government or any agency thereof. The views and opinions of authors expressed herein do not necessarily state or reflect those of the United States Government or any agency thereof.

DISCLAIMER

Portions of this document may be illegible in electronic image products. Images are produced from the best available original document.

ORDERING INFORMATION

Requests for copies of this report should be directed to Research Reports Center (RRC), Box 50490, Palo Alto, CA 94303, (415) 965-4081. There is no charge for reports requested by EPRI member utilities and affiliates, contributing nonmembers, U.S. utility associations, U.S. government agencies (federal, state, and local), media, and foreign organizations with which EPRI has an information exchange agreement. On request, RRC will send a catalog of EPRI reports.

Copyright © 1986 Electric Power Research Institute, Inc.

EPRI authorizes the reproduction and distribution of all or any portion of this report and the preparation of any derivative work based on this report, in each case on the condition that any such reproduction, distribution, and preparation shall acknowledge this report and EPRI as the source.

NOTICE

This report was prepared by the organization(s) named below as an account of work sponsored by the Electric Power Research Institute, Inc. (EPRI). Neither EPRI, members of EPRI, the organization(s) named below, nor any person acting on their behalf: (a) makes any warranty or representation, express or implied, with respect to the accuracy, completeness, or usefulness of the information contained in this report, or that the use of any information, apparatus, method, or process disclosed in this report may not infringe privately owned rights; or (b) assumes any liabilities with respect to the use of, or for damages resulting from the use of, any information, apparatus, method, or process disclosed in this report.

Prepared by
Southwest Research Institute
San Antonio, Texas

EPRI PERSPECTIVE

PROJECT DESCRIPTION

Cracking of low-pressure steam turbine discs has significantly reduced the availability of nuclear power plants over the last few years; it has also caused concern regarding plant safety. EPRI has a program to determine the reason(s) why discs crack.

Turbine manufacturers and the Nuclear Regulatory Commission have similar programs. The EPRI program provides an independent perspective which supplements the other industry programs. RP1398-1, the first project in the EPRI program, examines the metallurgy of cracked discs. This is the final report for RP1398-1.

PROJECT OBJECTIVES

The work was divided into two tasks; the objectives for each task were:

Task I--Failure Analysis of a Cracked Disc

1. Magnetic particle inspection
2. Metallographic examinations
3. Fractographic examinations
4. Chemical analyses

Task II--Comparative Analysis of Several Discs

1. Mechanical properties
2. Chemical analyses
3. Polarization curves

PROJECT RESULTS

Task I concludes that stress corrosion was the primary cause of cracking, but does not find direct evidence of corrosives. An independent analysis, conducted by the turbine manufacturer, found chlorides and hydroxides on the crack surfaces. The turbine owner reported finding a small number of deposits on the turbine when the

cracks were discovered. Task II shows that the disc material meets the current specifications. Operating-stress calculations and measurement of residual stresses would help clarify whether stress or corrosion dominates the cracking.

Task I finds disc cracks which were not observed during field inspections. Nondestructive examination methods and procedures should be evaluated to determine why this occurred.

Metallurgists and others responsible for failure analyses of turbine discs should find this report useful.

Michael J. Kolar, Project Manager
Nuclear Power Division

FINAL REPORT

For

TASK I

ABSTRACT

An investigation of the nature of in-service cracking in LP turbine rotors encountered in a PWR nuclear power plant was performed. The investigation was based on a metallurgical evaluation of disc rim samples from one of the two rotors involved. The program included a detailed magnetic particle inspection of the rim samples, in-depth metallographic and fractographic examinations of cracked blade attachment steeples and chemical analyses of the disc material.

The metallurgical examination identified two characteristics of the cracking: 1) the mode of cracking was predominantly intergranular, and 2) all cracking developed as the result of multiple crack initiation. On the basis of the observations made, it is concluded that the primary mechanism involved was a form of stress corrosion cracking. No direct evidence of the presence of any crack-inducing contaminant species was obtained. Therefore, the specific type of SCC involved and the root cause of the cracking could not be positively identified.

The results of this investigation, and the present understanding of similar incidents in other plants, do not provide a basis for specific measures for prevention of in-service SCC in turbine components. The only courses of action that can be proposed at the present time are: 1) utilization of lower strength disc materials, and 2) reduction of the level of impurities in the steam.

CONTENTS

ILLUSTRATIONS

ILLUSTRATIONS (Continued)

SUMMARY

A metallurgical investigation of in-service cracking of LP turbine rotors in a nuclear steam electric generating station was carried out. The particular unit involved is a 739 MW PWR system incorporating one high-pressure and two-low pressure turbines. Rim cracking occurred at the blade attachment area in the L-3 and L-4 (5R and 6R) rows in both LP turbines approximately 6-1/2 years after initial start-up. The objective of the investigation was to identify the cracking mechanism and provide information related to possible causes. The program included a detailed magnetic particle inspection of rim samples from one of the rotor discs, metallographic and fractographic examinations of related cracked blade attachment steeples and chemical analyses of the disc material.

The principal observations made in this investigation are summarized as follows:

1. The chemical composition of the disc material conforms to that usually specified for NiCrMoV low-alloy steels employed for LP turbine discs. The particular disc in question was manufactured to a proprietary materials specification similar to ASTM A 471.

2. The disc material exhibited a microstructure of tempered bainite typical of quenched and tempered NiCrMoV alloy steel. A duplex microstructure, characterized by grain sizes of ASTM 4-5 and ASTM 6-7, was observed. No microstructural defects or abnormalities of any significance were observed in any of the specimens examined.

3. Extensive cracking was observed in the blade attachment steeples of all three disc rim samples. Conventional magnetic particle inspection of the intact samples revealed cracking in 30 of the 5R steeples and in 36 of the 6R steeples (42 steeples total in each row). Cracking was observed on both the inlet and outlet faces of the steeples.

4. The cracks observed in the rim segment samples can be classified into three types according to location and orientation.

   Type I - Cracks located along the steeple serrations and oriented in a generally tangential direction through the steeple cross section.

Type II - Cracks located at the bottom of the blade groove and oriented in a generally radial directon.

Type III - Independent, face-initiated cracks oriented in a generally radial plane and located below the bottom of the blade grooves.

5. The Type I cracks were comprised of numerous connected or overlapping segments extending along the steeple serrations. This feature serves as evidence that the cracking developed by initiation of multiple independent cracks along the steeple serration and propagation of the several segments to the point of junction to form a single crack front.

6. The extent of cracking in particular steeple serrations varied from short cracks near one face to cracking over the full length of the steeple. The most severe Type I crack examined measured approximately 0.10 inch (2.5 mm) deep and extended for the full length of the steeple.

7. The majority of the Type II cracks were located at the outlet face of the rim segments. The largest of these measured approximately 0.1 inch (2.5 mm) along the steeple serration with a maximum depth of approximately 0.06 inch (1.5 mm) in the radial direction.

8. All of the Type III cracks noted were located on the outlet face. The largest of these measured approximately 0.2 inch long by 0.07 deep (5.1 mm x 1.8 mm).

9. All cracks examined, regardless of type, were predominantly intergranular, generally branched, and partially filled with a corrosion product. Two particular Type I cracks exhibited a significant degree of transgranular cracking. In both cases, the transgranular cracking was confined to the later stages of crack propagation.

10. Significant corrosive attack of the steeple serration surfaces, in the form of small, uniformly distributed pits, was evident. Evidence of post-cracking corrosion of the crack surfaces was also noted, particularly at locations near the outer edge.

11. Qualitative analyses of the deposits within cracks and pits indicated that the deposits consist of base metal oxides. No extraneous contaminant species were detected by in situ EDS analysis.

The metallurgical evaluation of the disc rim samples established two chracteristic features of the cracking; namely, the mode of cracking was predominantly intergranular and all cracking developed as a result of multiple crack initiation. It was also established that the cracking was not related to any material defect or abnormality.

The two possible mechanisms by which in-service cracking could have occurred are fatigue and stress corrosion cracking (SCC). The metallographic and fractographic features preclude fatigue as a principal factor in the cracking incident and lead to the conclusion that the primary mechanism involved was a form of stress corrosion cracking.

The metallurgical characteristics of the cracking are consistent with caustic cracking in low-alloy steels. Also, this case is very similar to two other incidents of LP rotor disc cracking in which caustic cracking was identified as either the definite or probably cause. In this case, however, neither the plant operating history nor the metallurgical examinations provided any definite evidence of caustic contamination. In addition, no evidence of other contaminant species was obtained in the laboratory evaluation of the disc samples. Therefore, the specific type of SCC and the root cause of the cracking could not be positively identified. Data from laboratory tests, published in the literature, have provided evidence that CrMo and NiCrMoV steels are susceptible to cracking in pure steam or pure water. Therefore, the possibility exists that the presence of a contaminant species may not be a necessary condition for disc rim cracking.

The results of this investigation and the present understanding of the LP turbine disc cracking encountered in other plants do not provide a basis for establishing specific preventative measures. Further information and data concerning the actual operating environments and the cracking susceptibility of disc materials is necessary. At the present time, only two courses of action can be proposed; namely, the utilization of disc materials with lower yield strengths and implementation of any appropriate steps to reduce contaminant levels in the steam. The data available to date does not assure that such action would definitely prevent cracking, but the indications are that these measures would decrease the likelihood of SCC in LP turbine rotors.

Section 1

INTRODUCTION

Rim cracking occurred in the rotors of two low-pressure turbines during the first 6-1/2 years of operation of a nuclear steam electric generating station. The particular unit involved is rated at 739 MW and incorporates a pressurized water reactor steam generating system, one high-pressure turbine, and two low-pressure turbines. The three turbines are connected in tandem to drive a single generator. The steam generating system employs moisture separator reheaters between the HP turbine exhaust and the LP turbine inlets. The nominal system operating parameters are as follows:

HP Inlet:	745 psig, 510°F (5.14 MPa, 266°C)
Reheat:	175 psig, 476°F (1.21 MPa, 247°C)
	113°F (63°C) superheat
Exhaust:	2 in. Hg abs. (6.75 kPa)

During the first 2-1/2 months of commercial operation the unit experienced two forced outages. The first of these was associated with bearing damage due to loss of lubrication during coast-down after a reactor trip. This outage extended over a period of approximately 8 weeks. The second forced outage occurred due to blading failures in the 6R row. Some rotor damage was also incurred in this incident. Bridge blocks were installed as a temporary repair and plans were made to replace the LP rotors at a later date. New rotors were installed in both LP turbines during the two-year scheduled refueling outage.

The next 41 months of operation of the unit included three scheduled refueling outages and one forced outage for rebalancing. At each outage some blading damage was detected and repaired. The unit was then operated for a period of 15 months, until the next scheduled refueling outage, without any indication of major turbine related problems.

During the scheduled refueling outage, a thorough inspection of both LP turbine rotors was performed by an independent commercial inspection firm. Severe cracking was detected in the blade attachment area in the 5R and 6R rows at both ends of both LP turbines. These two blade rows are contained in the third disc from the center of the rotor, see Figure 1-1. There are 230 blades in each row. At the time the rim cracking was detected, each of the two LP rotors had accumulated approximately 50 months of operating time (excluding outage time).

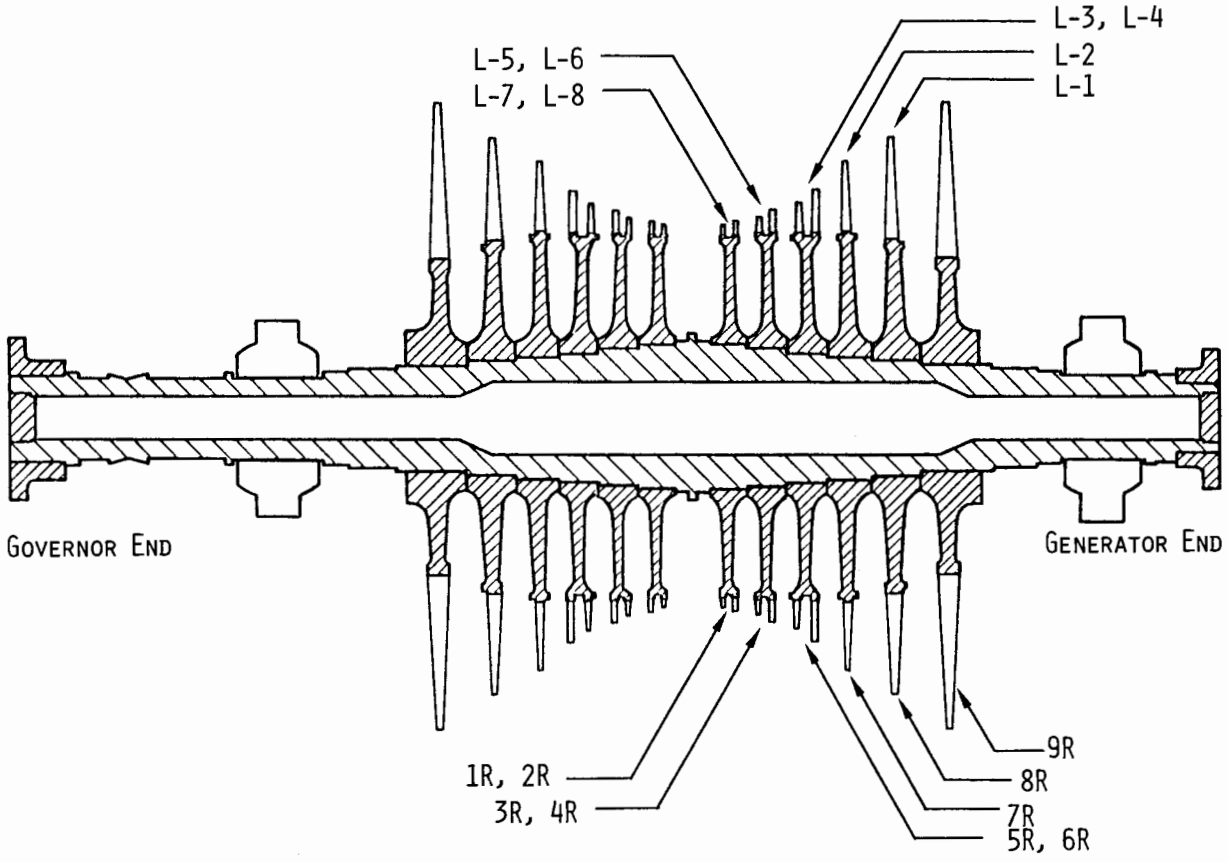

FIGURE 1-1. LP TURBINE ROTOR.

The on-site inspection identified cracks at the serrations of the blade attachment steeples and radial cracks at the base of the steeples. The extent of cracking is summarized as follows:

		No. of Cracked Steeples	
		Gen. End	Gov. End
LP-1	5R	28	38
	6R	51	37
LP-2	5R	43	124
	6R	84	74

A compilation of the on-site inspection data, indicating the extent of cracking, is contained in Appendix A, Figures A-1 through A-8. In view of the extent of cracking observed in the on-site inspection, both LP rotors were removed from service for repair. The original rotors were installed on a temporary basis and the unit was returned to service.

Samples from one of the cracked discs were made available to EPRI and a program was initiated to establish the nature of the cracking and provide information related to possible causes. The program was organized into two separate tasks. Task I consisted of metallurgical evaluation of the particular disc cracking problem described above. This task included visual and magnetic particle inspection of all of the samples, chemical analysis of the disc material, and metallographic and fractographic examination of selected cracked specimens. Task II of the program consists of mechanical properties tests and chemical analysis of disc material from three different turbines in which similar cracking problems have been encountered. The results of the Task I metallurgical evaluation are presented in this report.

The three specimens furnished for the Task I investigation are shown in Figure 1-2. These rim segments, arbitrarily designated as A, B and C, were cut from the third disc of the generator end of the LP-2 rotor. Each sample contained 12-14 blade grooves from the 5R and 6R rows.

To facilitate organization, review and reporting of the data obtained in this investigation, a numbering system was devised to identify any particular crack. The numbering system labeled individual steeples by the adjacent blade numbers and designated particular cracks by crack type (steeple crack or radial crack) and the location on the particular steeple. The crack identification system utilized in this investigation is illustrated in Appendix B.

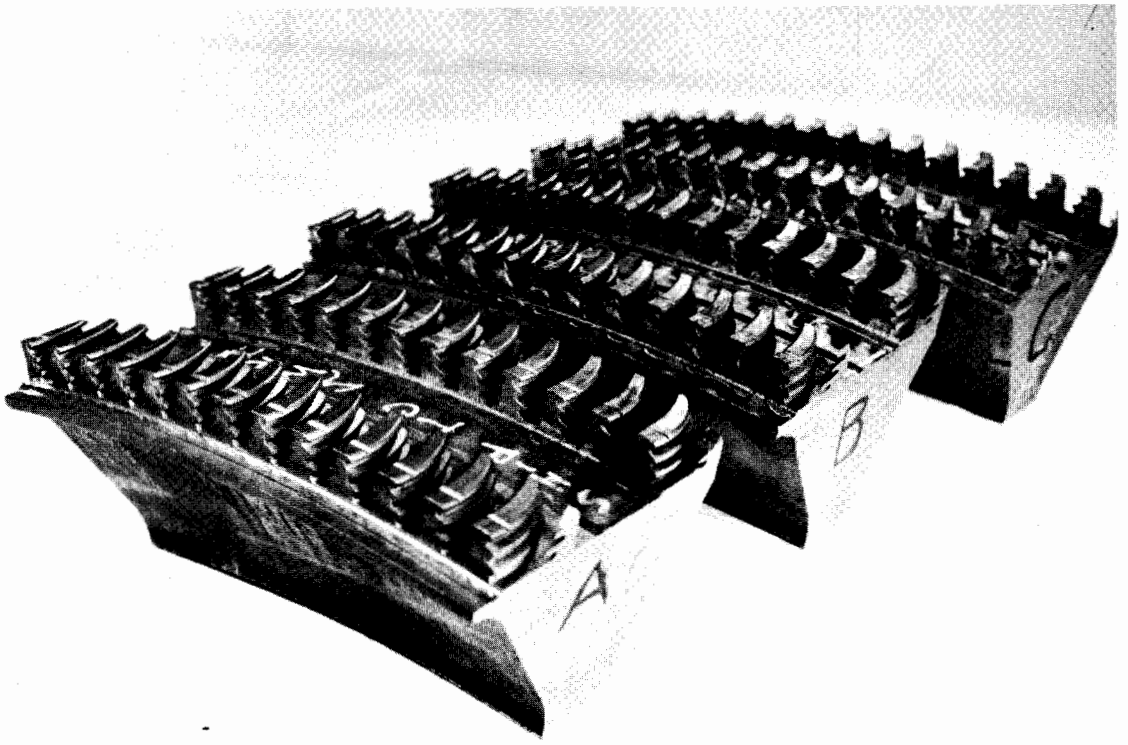

(a) Overall view. Inlet face is at left.

FIGURE 1-2. DISC RIM SAMPLES. Rows 5R and 6R, Disc No. 3, Generator end. See Appx. A for sample locations.

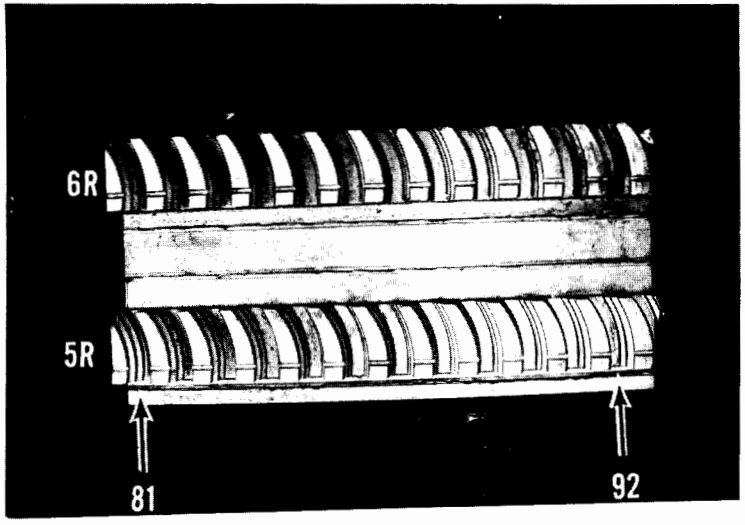

(b) Sample A

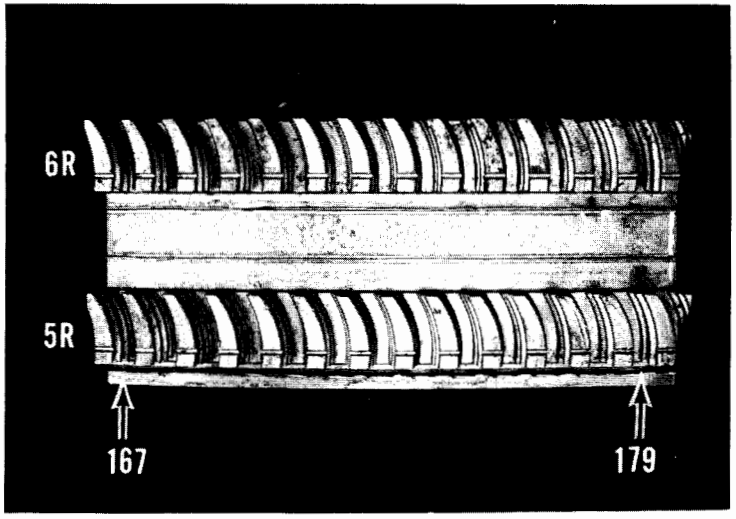

(c) Sample B

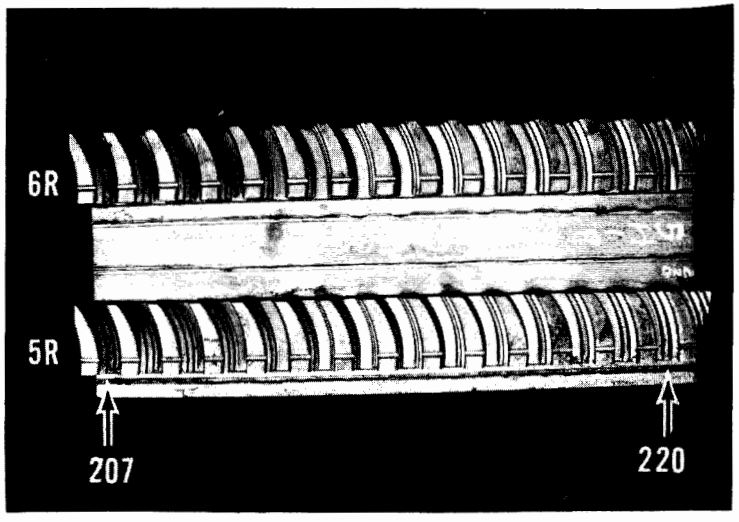

(d) Sample C

FIGURE 1-2 (Cont.). DISC RIM SAMPLES. Rows 5R and 6R, Disc No. 3, Generator end. Inlet face is at bottom. Arrows indicate numbered blade positions. See Appx. A for sample locations.

Section 2

VISUAL AND MAGNETIC PARTICLE INSPECTION

The disc rim samples had been abrasive blast cleaned prior to shipment to SwRI. Upon receipt, all three of the samples presented a clean metallic appearance all over and there was no evidence of any significant rusting or other damage which might have occurred after the abrasive blast cleaning. On the initial visual inspection of the disc rim samples, significant erosion damage was noted on the inlet face of all steeples in both the 5R and 6R rows. Examples of this in-service damage are shown in Figure 2-1.

All three samples were subjected to a magnetic particle (MP) inspection in the laboratory. This inspection was performed utilizing a dc magnetizing yoke and a liquid fluorescent indicator. The magnetizing yoke was positioned at successive points around the circumference in a manner to provide a magnetic field suitable for detection of cracks oriented in either a radial or tangential direction. Successive positions of the yoke were selected to provide overlap so that 100% of the circumference of each disc sample was covered by the inspection.

Numerous crack indications were noted in the steeples of all three samples. A detailed listing of the particular indications noted in the laboratory MP inspection is included in Appendix A, pages A-10, A-11 and A-12. Photographs of typical crack indications are shown in Figure 2-2. In general, the observed crack indications can be categorized in two distinct types; namely, cracks located in the radius on the load-carrying side of the steeple serrations and oriented in a generally tangential direction, and cracks located in the radius at the base of the steeple with a generally radial orientation. For purposes of description and discussion these cracks have been designated as Type I and Type II, respectively, as shown in the schematic diagram of Figure 2-3. A few MP crack indications were noted on the outlet face of each row in a position indicating that the cracks had initiated on the free surface and were not connected to either the Type I or Type II cracks. An example of such a crack indication is evident in Figure 2-2(b).

Distinct crack indications were noted in 30 out of the 42 5R row steeples included in the three samples. The majority of defect indications noted in the 5R row were located at or near the inlet face of the steeples. Most of these indications were evident along the groove surface and were not necessarily apparent

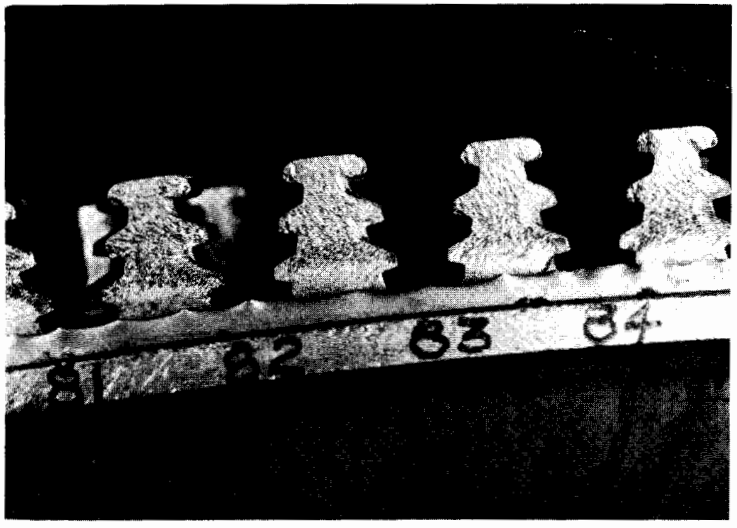

(a) Row 5R, at Blades No. 81 through No. 85.

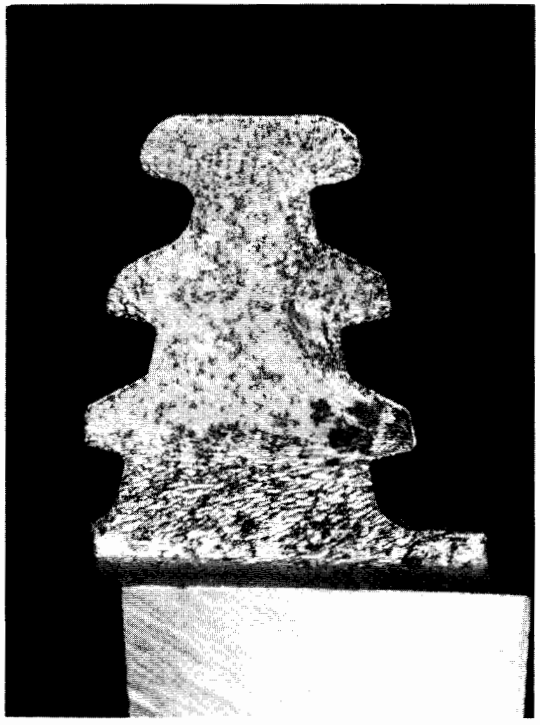

2X

(b) Steeple 210/211, Row 6R.

FIGURE 2-1. EROSION DAMAGE ON INLET FACE OF STEEPLES.

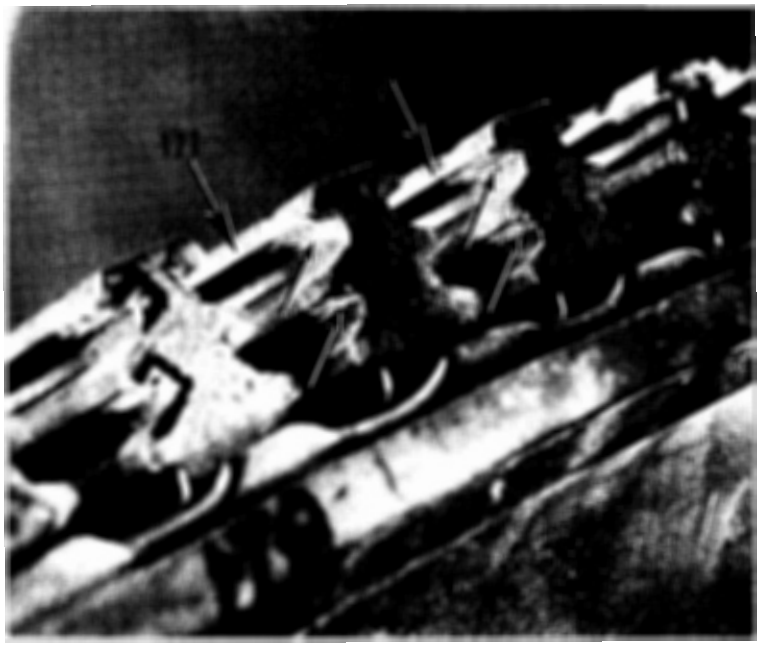

(a) Inlet face, Row 5R at Blades 171-173.

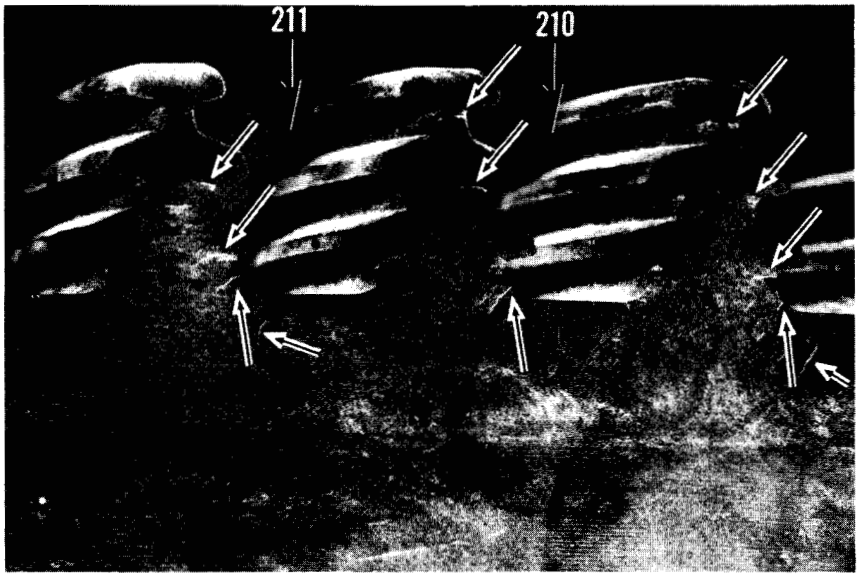

(b) Outlet face, Row 6R at Blades 209-211.

FIGURE 2-2. TYPICAL MAGNETIC PARTICLE CRACK INDICATIONS.

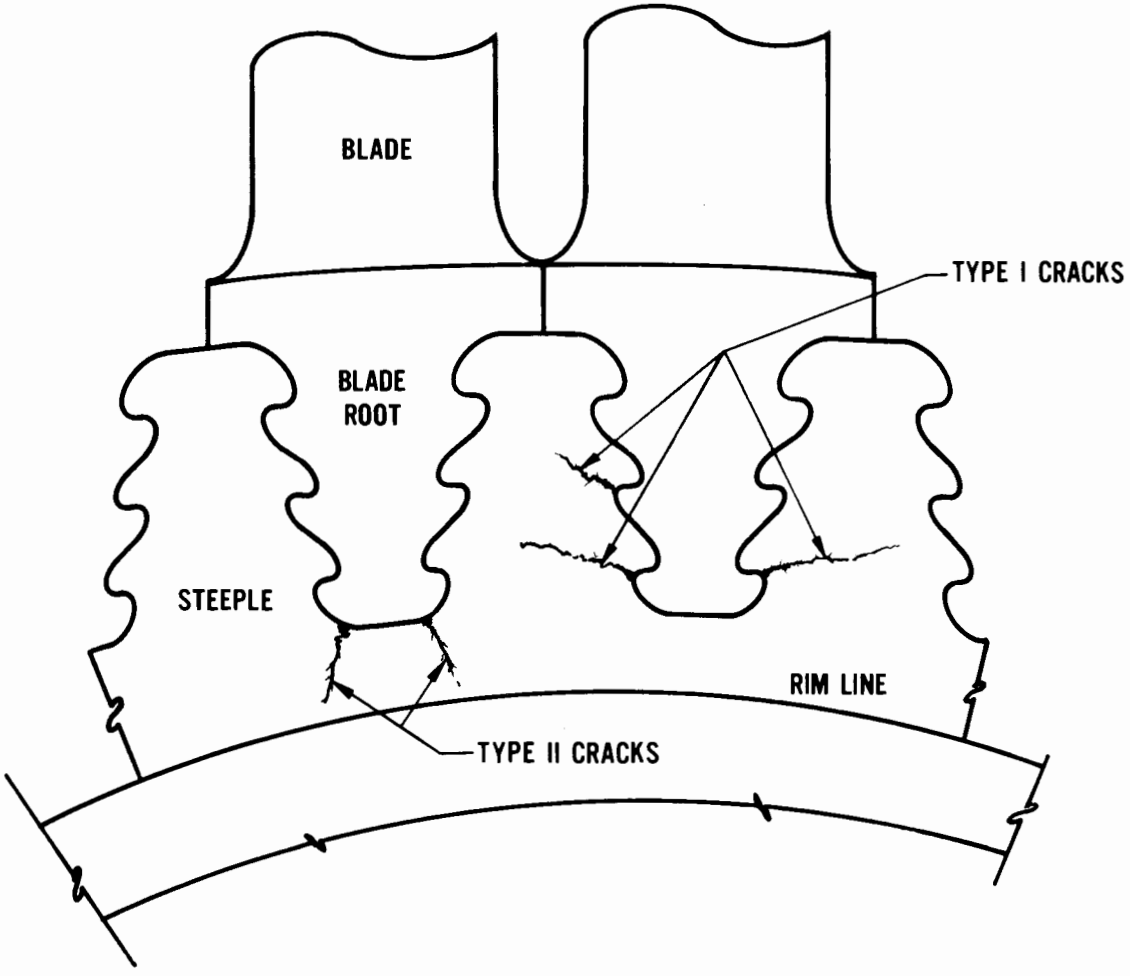

FIGURE 2-3. SCHEMATIC DIAGRAM OF RIM CRACKING.

on the inlet face. It should be noted that the extent of erosion damage on the inlet face hampers detection of small cracks by MP inspection.

In the 6R row, MP crack indications were observed in 36 of the 42 steeples included in the three samples. Of these crack indications, the larger number were located at or near the outlet face. There were several cases in which Type I cracks were identified at all three serrations of one steeple together with Type II radial cracks in the same steeple. Twenty-nine individual steeples in the 6R row exhibited cracks at both the inlet and outlet faces. Twenty-two steeples in the 6R row exhibited crack indications on both the convex and concave sides.

The results of the original on-site magnetic particle inspection of the 5R and 6R blade rows are also presented in Appendix A, Figures A-5 and A-6. Comparison of the laboratory inspection results with the reported field inspection results illustrates that a considerably larger number of crack indications were noted in the laboratory inspection. In particular, no defects were reported in the on-site inspection of that portion of the disc represented by segment A, whereas, in the laboratory inspection, eight of the thirteen 5R steeples in this sample exhibited distinct crack indications and eleven of the thirteen steeples in the 6R row showed evidence of cracking. In this regard, it should be noted that the laboratory inspection of the disc rim samples was performed with the blades removed and that, in general, a more critical inspection can be performed under laboratory conditions. Secondly, many of the crack indications noted in the laboratory inspection did not extend all the way to the inlet or outlet face and could not have been detected with the blades in place. Also, the condition of the inlet faces of both the 5R and 6R rows, due to the in-service erosion, could easily obscure many small inlet face crack indications. These factors serve as an explanation of the differences between the laboratory and on-site MP inspection results.

The laboratory magnetic particle inspection identified distinct crack indications at every location where crack indications were reported in the on-site inspection with one exception. Crack indications were reported at blades 167 and 168 in the 6R row from the on-site inspection while the laboratory MP inspection did not reveal indications at these particular locations.

Section 3

CHEMICAL ANALYSIS

Chemical analyses were performed on two specimens to determine the composition of the disc material. Both specimens were taken from sample B at a location within the rim immediately below Steeple 178/179.

The analyses were performed (at two independent laboratories) utilizing standard spectrographic and wet chemical procedures to establish conformance to specification. The results of both analyses are presented in Table 3-1. The disk was manufactured to a proprietary materials specification similar to ASTM A 471, but the particular specification was not available for review. The composition determined for both specimens meets the requirements of ASTM A 471 in all respects.

Table 3-1

CHEMICAL COMPOSITION OF DISC MATERIAL
All Values in Weight %

Element	Analysis A	Analysis B	ASTM A 471
Ni	3.43	3.35	2.00 - 4.00
Cr	1.72	1.76	0.75 - 2.00
Mo	0.37	0.37	0.20 - 0.70
V	0.14	0.13	0.05 min
C	0.27	0.26	0.35 max$^{\Delta}$
Mn	0.25	0.25	0.70 max
Si	0.03	< 0.02	0.10 max*
P	0.007	0.009*	0.015 max
S	0.008	<0.002*	0.015 max
Cu	0.11	0.099*	--

---

* When vacuum deoxidation is specified. Otherwise Si content is 0.15-0.35.

Δ For Classes 4 and 5.

Section 4

METALLOGRAPHIC EXAMINATIONS

Metallographic specimens were cut from representative steeples in samples B and C for examination to establish the general microstructure of the disc material. Two steeples, one from each row, were sectioned on the centerline in a radial plane. Sections were also taken from both 5R and 6R steeples in planes parallel to the inlet face. These latter specimens were cut to be representative of locations near each face of the steeples and at the mid-thickness. All specimens exhibited similar microstructural features and were characterized by a bainitic structure typical of quenched and tempered NiCrMoV steels. The typical microstructure observed in the examination of these specimens is shown in Figure 4-1.

Selected specimens were also examined after etching with a grain boundary etching reagent*. In each case, the grain boundaries were clearly delineated as shown in Figure 4-1(c). A distinct variation in grain size was noted among the various specimens. In each case, zones of a relatively large grain size were noted at random locations throughout a matrix of generally smaller grains. Grain size measurements were made at representative locations in each specimen in accordance with ASTM E 112 (intercept procedure). These measurements established that the duplex microstructure of the disc material is characterized by grain sizes in two categories: ASTM 6-7 and ASTM 4-5.

Steeples 176/177 from row 5R and 210/211 from row 6R were selected for detailed metallographic examination to establish the microstructural features of the cracking. These two steeples contained cracks representative of all of the types and locations observed in the magnetic particle inspection. Photographs showing the details of the MP crack indications selected for metallographic examination are shown in Figures 4-2 and 4-3. Schematic diagrams showing all of the crack

---

* Etchant: Saturated aqueous solution of picric acid plus 1% sodium tridecylbenzene sulfonate. The etching sensitivity of a particular alloy steel in this reagent is a function of grain boundary phosphorous content (1). In general, the delineation of grain boundaries increases with increasing phosphorous content. The results of this examination provide evidence of phosphorous segregation at grain boundaries, but this etching effect is not necessarily indicative of abnormally high phosphorous content or of an abnormal degree of grain boundary segregation.

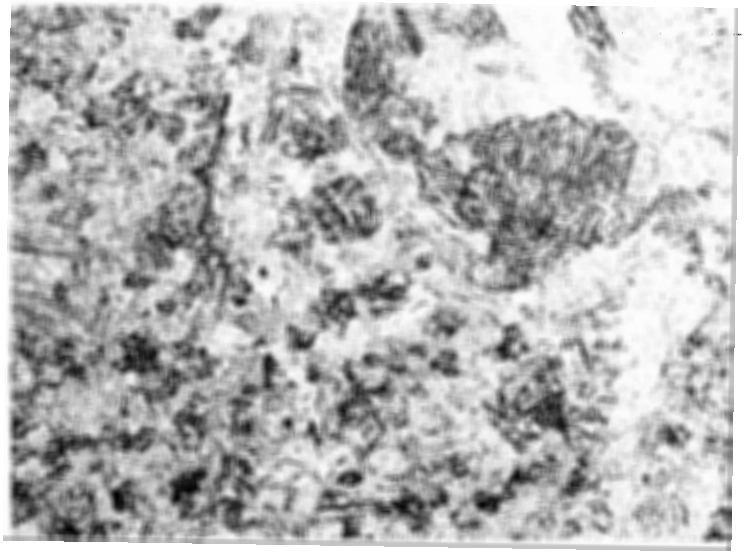

100X

(a) Etchant: Nital

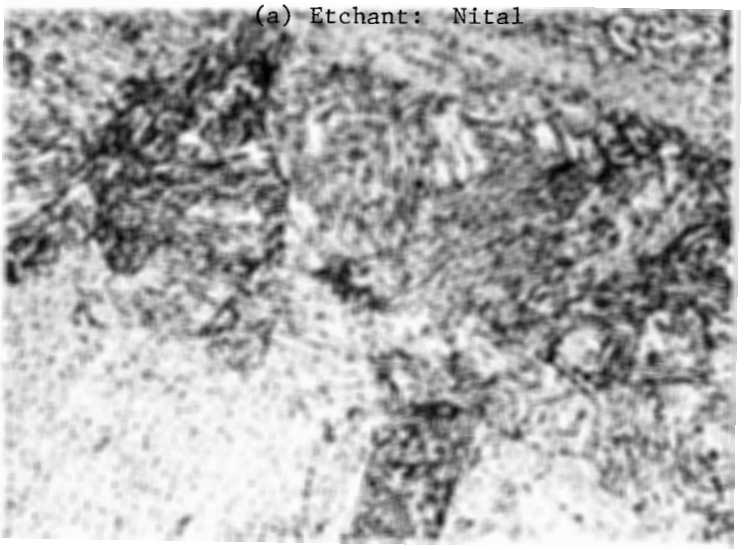

500X

(b) Etchant: Nital

FIGURE 4-1. TYPICAL MICROSTRUCTURE OF DISC MATERIAL.

(These photographs reduced to 90% of their original size)

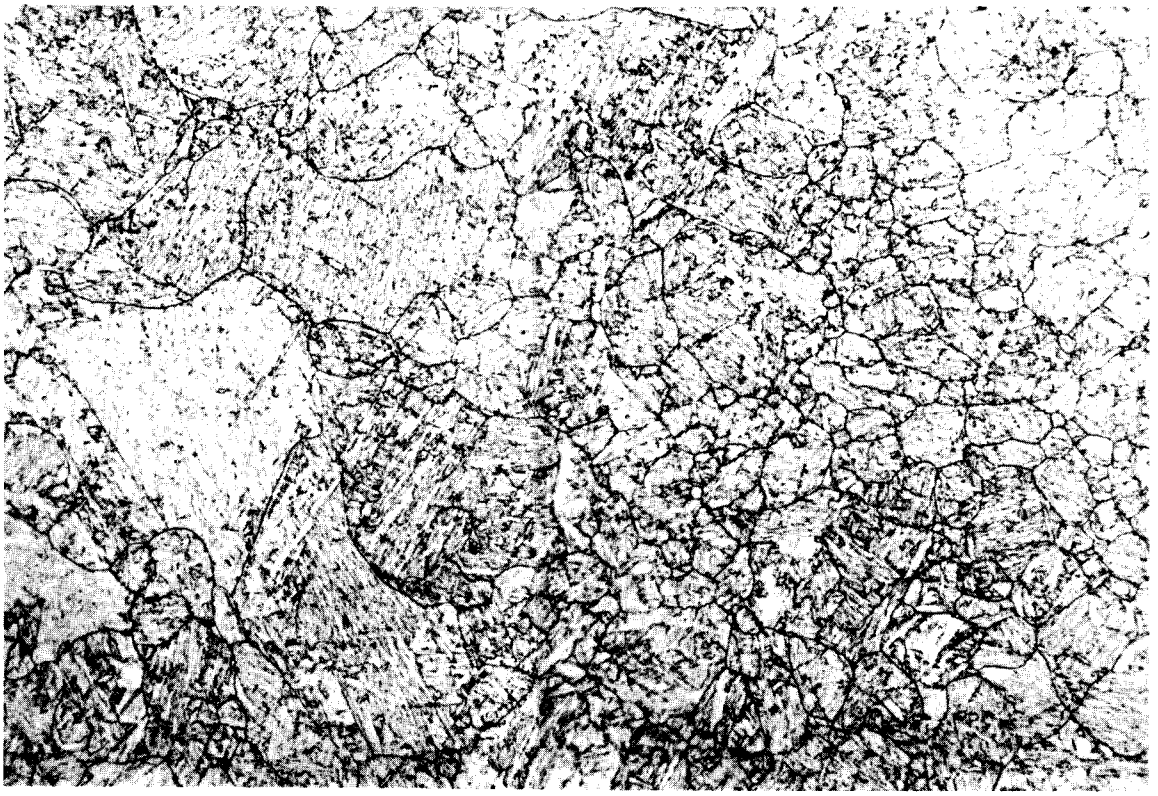

(c) Etchant: Picric acid & wetting agent.
Note duplex structure. Grain size
ASTM 6-7 and ASTM 4-5. 300X

FIGURE 4-1 (Cont.). TYPICAL MICROSTRUCTURE OF DISC MATERIAL.

(This photograph reduced to 90% of its original size)

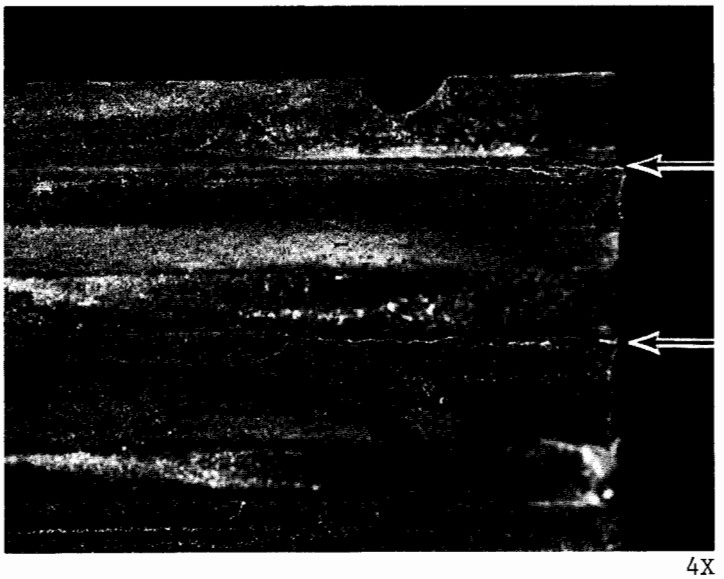

4X

(a) Magnetic particle crack indications, concave side.

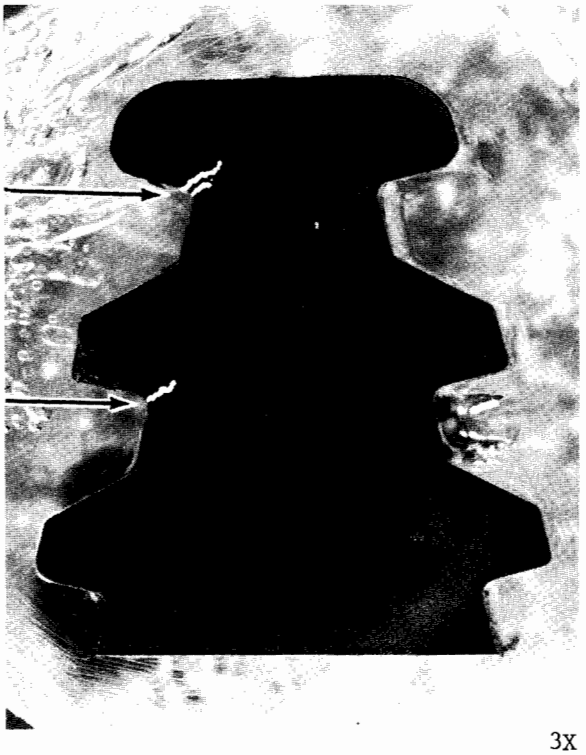

3X

(b) Polished surface. Dark field illumination. Photograph retouched to enhance crack indications.

FIGURE 4-2. CRACK INDICATIONS AT INLET FACE OF STEEPLE 176/177, ROW 5R.

(These photographs reduced to 90% of their original size)

2X

(a) Magnetic particle crack indications. Liquid fluorescent indicator.

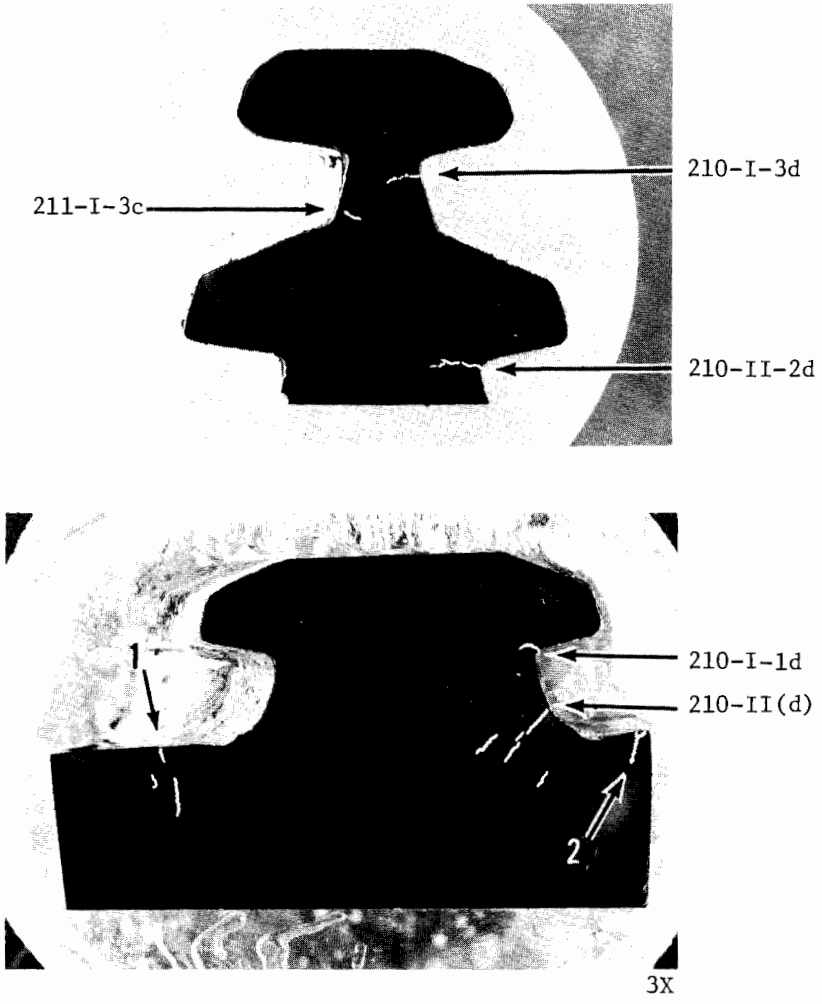

3X

(b) Polished face. Dark field illumination. Photograph retouched to enhance crack indications.

FIGURE 4-3. OUTLET FACE OF STEEPLE 210/211, ROW 6R.

(These photographs reduced to 90% of their original size)

indications noted in the inspection of these particular steeples are shown in Appendix C.

The general configuration of the Type I cracks is illustrated in Figures 4-4 and 4-5. In each case, the cracks are located within the radius on the load bearing side of the serrations and exhibit an irregular path with substantial branching. The microstructural features of each of the Type I cracks examined were similar. The cracks were completely intergranular and exhibited regions with extensive branching or network cracking. The typical microstructural features of the Type I cracks are illustrated by the micrographs of crack 176-I-2b shown in Figures 4-6 and 4-7. In each of the metallographic sections examined the cracks contained a deposit material, particularly within the narrow tight portions near the ends of the cracks. Also, all cracks were nearly filled with this deposit material at the point of intersection with the surface. Other examples of Type I cracks from both the inlet and outlet faces of the 5R and 6R rows are shown in Appendix D, Figures D-1 through D-3.

It should also be noted that two distinct, independent crack segments were evident at some locations, see Figure 4-4(a). This feature indicates that separate independent cracks were present along the groove surface and overlapped at the inlet face. This particular feature was noted in several cases on both the inlet and outlet faces of both rows.

The Type I crack at the outermost serration in steeple 210/211 (Crack 211-I-3c) was isolated from the groove surfaces at the outlet face as shown in Figure 4-8. This defect consisted of a very tight, completely intergranular crack at the outlet face and was completely filled with oxide. In subsequent, sequential metallographic sections the crack decreased in size and was finally completely ground away without exhibiting any connection to the groove surface. These observations indicate that this particular crack initiated on the outlet face of the steeple independent of the blade groove surface.

The overall configuration of the Type II crack in steeple 210/211, [crack 210-II(d)], is shown in Figure 4-9. At the outlet face, this particular crack is comprised of several disconnected segments. The microstructural features at this crack location are shown in Figure 4-10. The initial segment, originating from the groove surface, is relatively straight with some branching evident at the very end of the segment. The material in the immediate vicinity of this straight segment of the crack exhibits an ill-defined, atypical microstructure, see Figure 4-10(a). The nature of the microstructure at this particular location precludes classification of this portion of the cracking as either transgranular or intergranular. The other crack

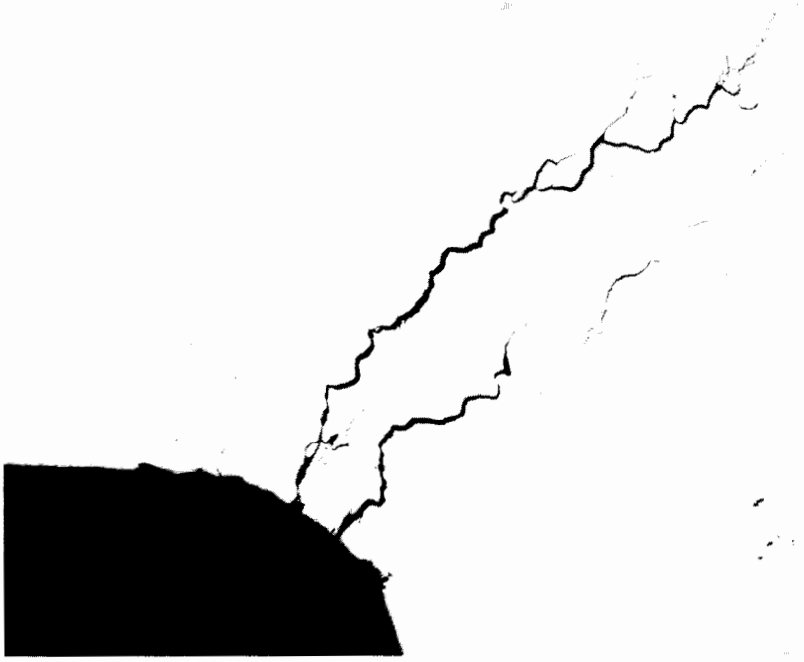

(a) 176-I-3b

(b) 176-I-2b

FIGURE 4-4. CRACKS AT INLET FACE OF STEEPLE 176/177.
Unetched. 50X

(These photographs reduced to 90% of their original size)

FIGURE 4-5. CRACK 210-I-2d, Row 6R. Section at outlet face of Steeple 210/211. See Figure 4-3. Unetched. 50X

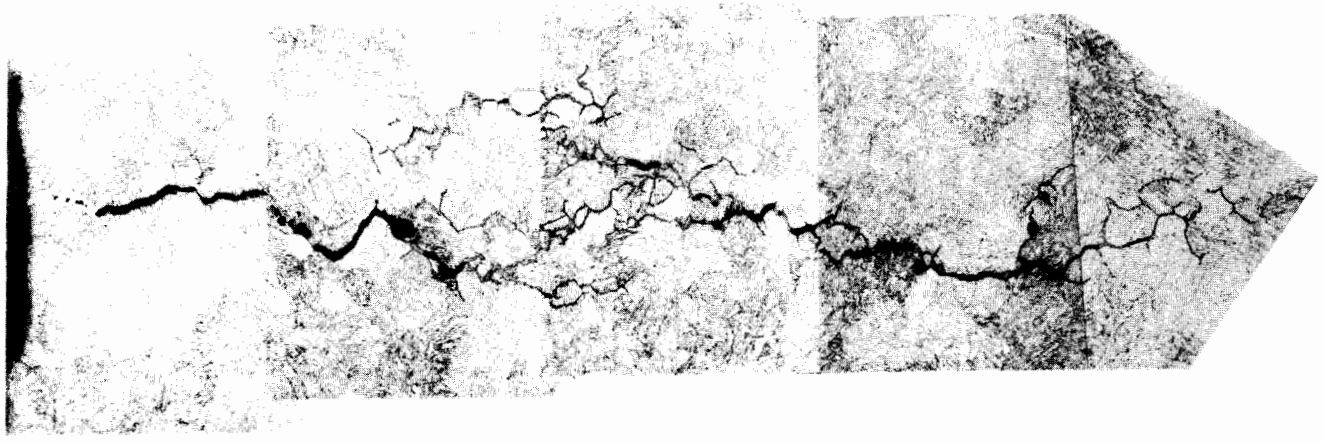

FIGURE 4-6. MICROSTRUCTURE AT CRACK 176-I-2b, ROW 5R.
Section at inlet face. Etchant: Nital.
150X

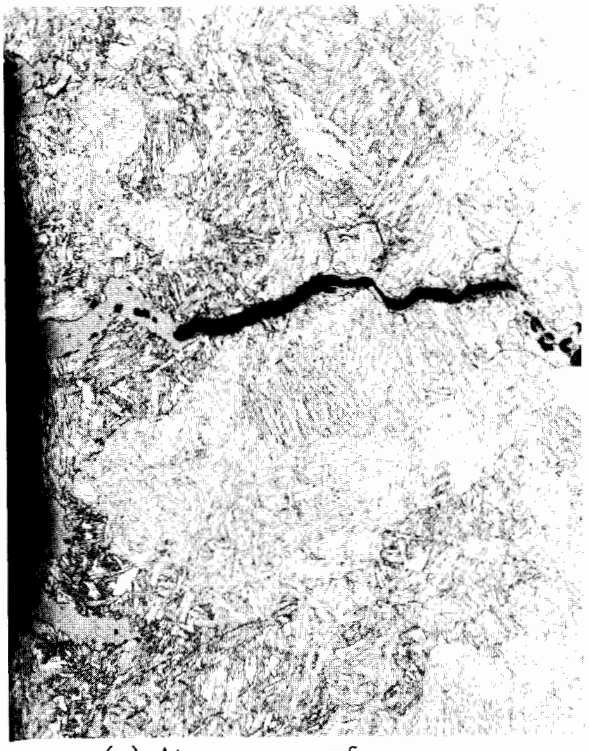

(a) At groove surface

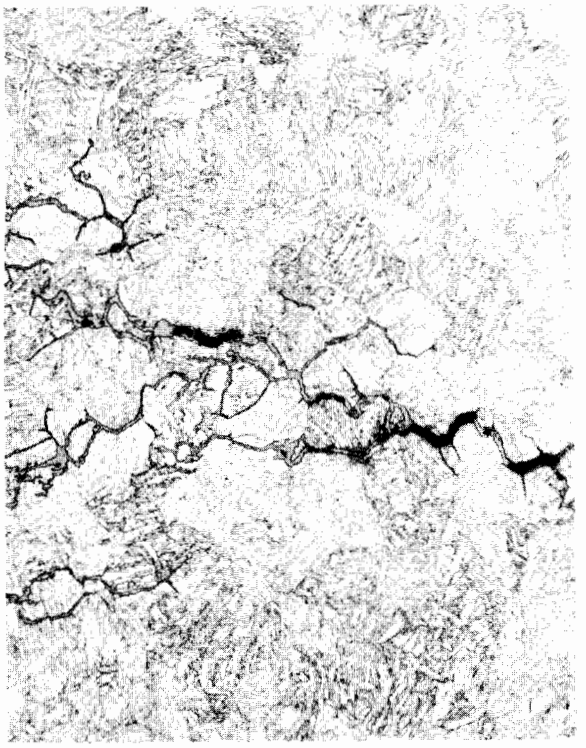

(b) Central portion

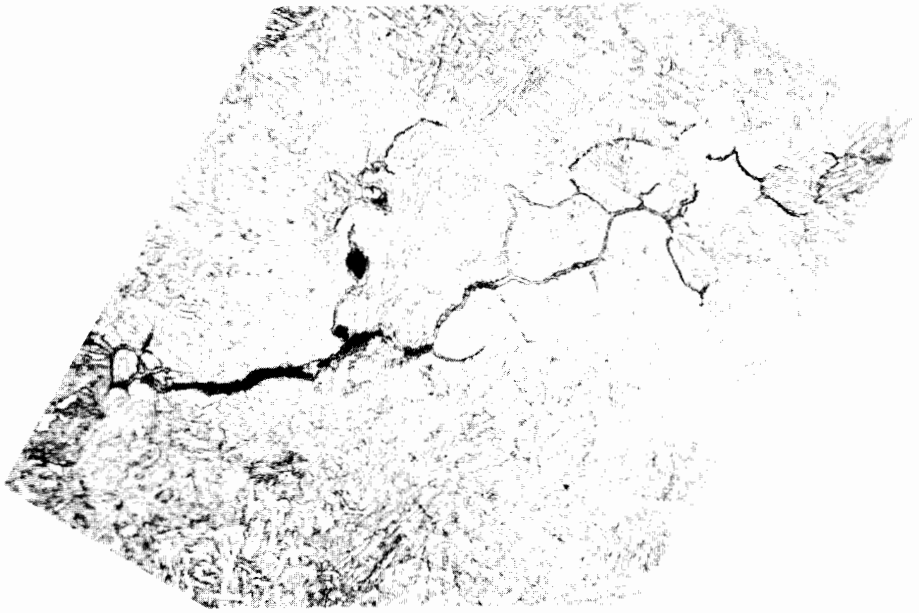

(c) Crack tip

FIGURE 4-7. SEGMENTS OF CRACK 176-I-2b. See Figures 4-4(b) and 4-6. Etchant: Nital. 300X

(These photographs reduced to 90% of their original size)

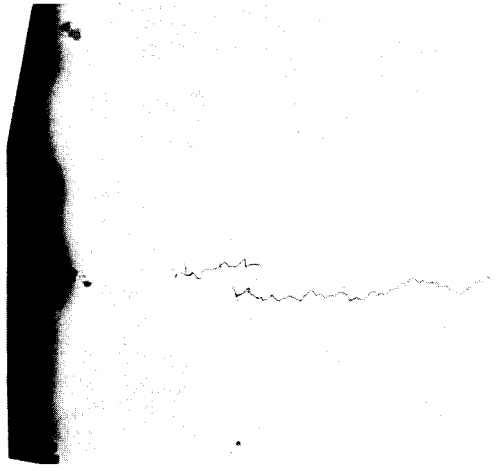

50X

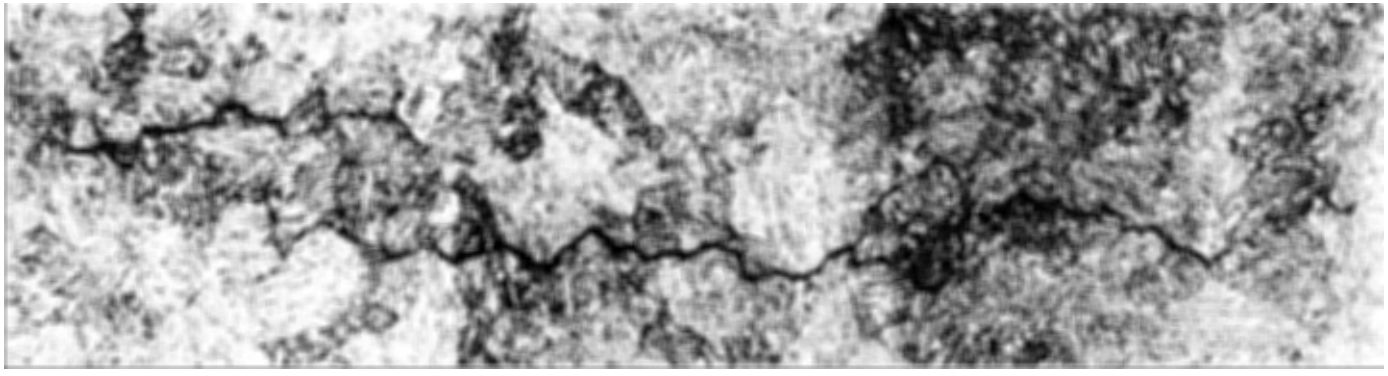

200X

FIGURE 4-8. CRACK 211-I-3c, ROW 6R. Section at outlet face.
See Figure 4-3. Etchant: Nital.

FIGURE 4-9. MICROGRAPH OF CRACK 210-II(d).
At outlet face, Row 6R.
See Figure 4-3. Unetched.
50X

(This photograph reduced to 90% of its original size)

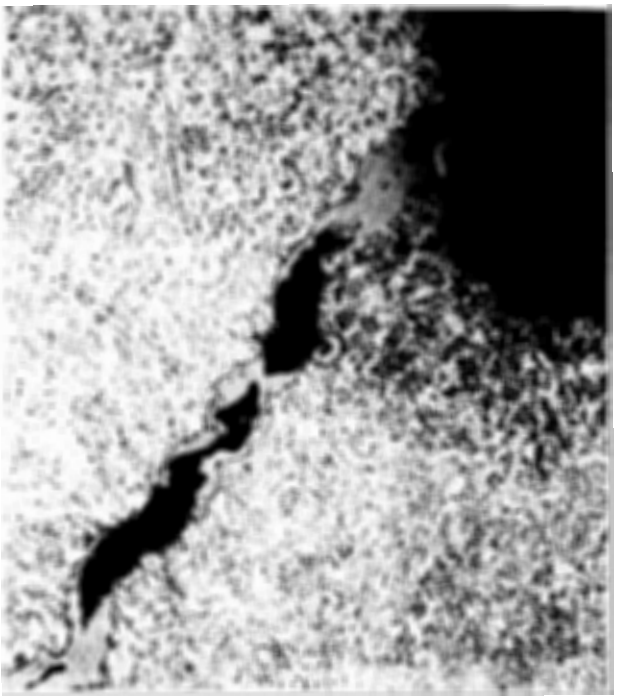

(a) At groove surface.
Position A in Figure 4-9.

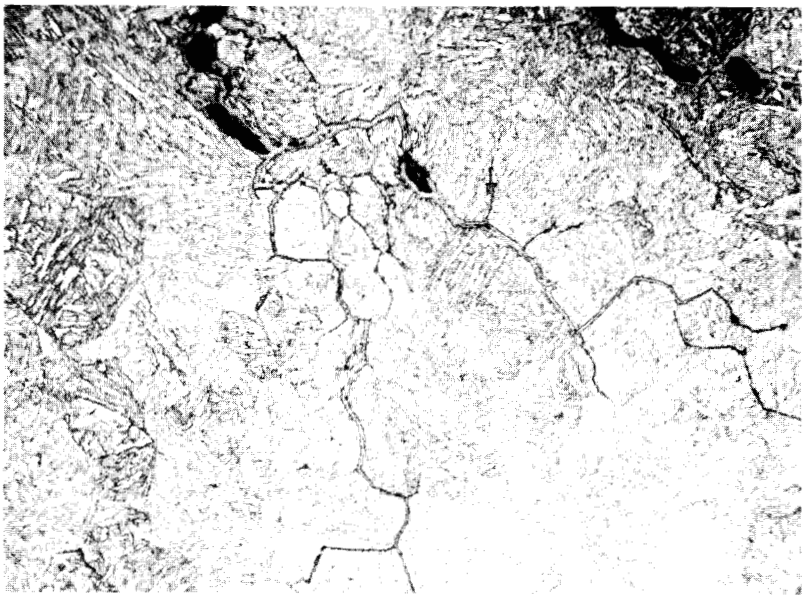

(b) Crack tip. Position B in Figure 4-9.

FIGURE 4-10. SEGMENTS OF CRACK 210-II(d).
Etchant: Nital. 300X

(These photographs reduced to 90% of their original size)

segments observed at the outlet face each exhibit irregular crack paths with significant branching and are clearly intergranular, see Figure 4-10(b). Examination of sequential metallographic sections through crack 210-II(d) established that the separate segments observed at the outlet face were actually connected to the groove surface a short distance beyond the outlet face. At a short distance from the outlet face two overlapping cracks existed in the groove. In each of the sequential sections, all segments of the crack were observed to be completely intergranular including that portion in the immediate vicinity of the groove surface. It was also noted that, at positions beyond the outlet face, the microstructure is comparable to the typical microstructure of the disc material indicating that the zone of atypical microstructure observed at the outlet face represents a highly localized condition. Photomicrographs from the sequential sections are shown in Appendix D, Figure D-4.

Examination of the outlet face of steeple 210/211 after minimal polishing to establish a metallographic surface revealed additional Type II cracks at the bottom of the blade grooves. These cracks are designated as Type II(r) and two such cracks are evident on either side of steeple 210/211 at locations 1 and 2 in Figure 4-3(c). The overall configuration of crack 211-II(r) is shown in Figure 4-11. At the outlet face this crack is comprised of two distinct segments, one at the surface and one isolated segment on the outlet face. Both segments exhibit an irregular path and distinctly intergranular features.

The nature of crack 211-II(r) was explored by sequential metallographic sections. The original specimen taken at the outlet face was progressively ground and reexamined at increments of approximately 0.01 inch (0.25 mm). At progressive locations from the outlet face, the surface connected portion of the crack exhibited clearly intergranular features and evidence of significant corrosive attack along the crack path was evident. The isolated segment, noted at the outlet face, decreased in length in each successive section to a point where only a very small segment [less than 0.006 inch (0.152 mm) long] remained at a section 0.06 inch (1.52 mm) from the outlet face. The results of the sequential sectioning established that the cracking observed at the outlet face consisted of a small Type II crack originating at the blade groove surface and a separate crack which initiated independently at a point on the outlet face*. The microstructural features observed in the sequential sections through crack 211-II(r) are shown in Appendix D,

*Several other cases of crack initiation on the outlet face (remote from the blade groove surface) were noted in this investigation and are described in Section 5.

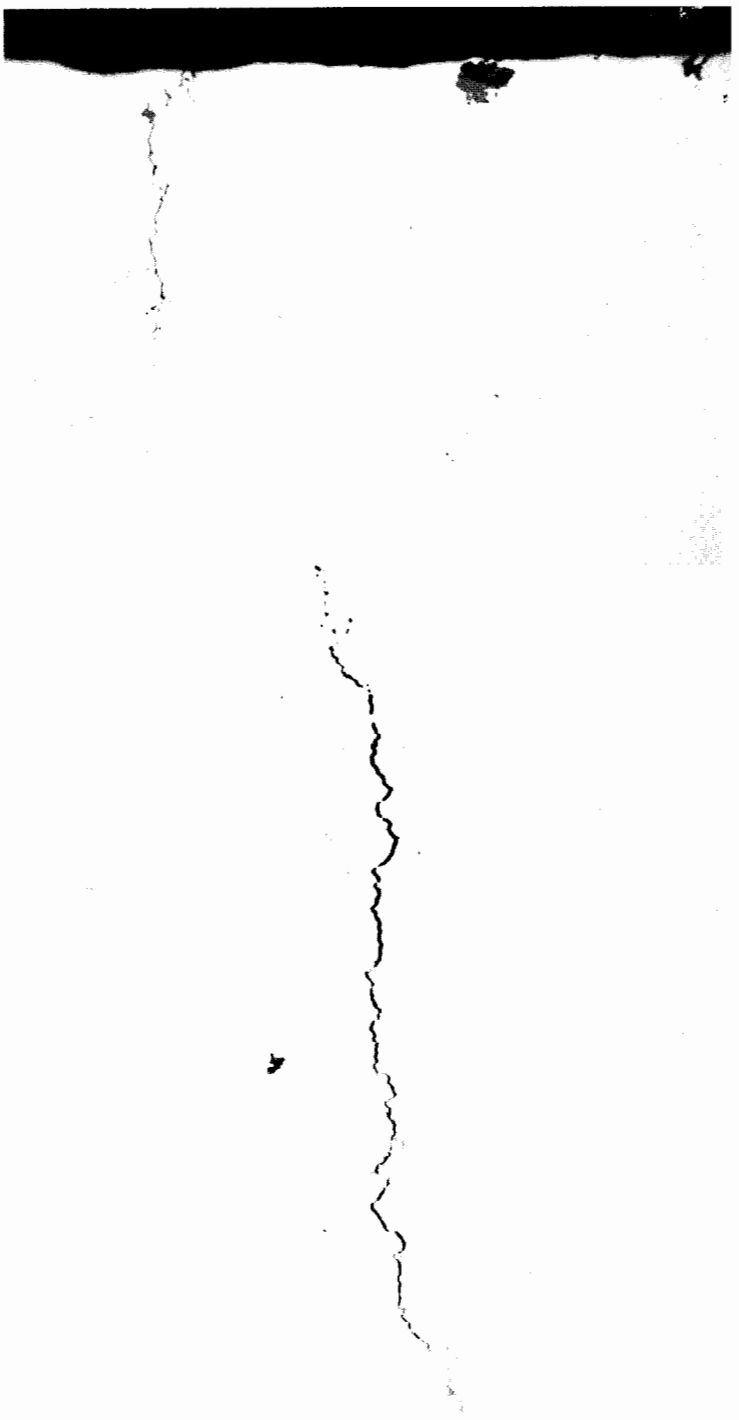

FIGURE 4-11. CRACK 211-II(r), ROW 6R. Location 1, Figure 4-3. Section at outlet face. Unetched. 50X

(These photographs reduced to 90% of their original size)

Figures D-5 and D-6. A second Type II(r) crack [210-II(r)] is shown in Figure D-7.

Energy dispersive X-ray spectroscopy was employed to provide qualitative analyses of deposits within pits and cracks in selected metallographic sections. In every case the principal constituents of the deposits were found to be Fe, Cr and Ni, the predominant element being Fe. Indications of trace amounts of P, Ca and Cu were noted in some cases. The results of these analyses indicate that the deposits within cracks and pits are simply oxides of the base metal. No evidence of any abnormal, extraneous contaminant species was noted. A typical EDS spectrum for the deposit material is shown in Figure D-8.

Section 5

FRACTOGRAPHIC EVALUATIONS

Six individual cracks were selected for detailed fractographic examination. These cracks were chosen on the basis of the character of the crack indications observed in the magnetic particle inspections and were selected to be representative of both Type I and Type II cracks observed in the 5R and 6R rows. The particular cracks examined were as follows:

213-I-2bd, Row 6R	177-I-2b, Row 5R
208-I-2bd, Row 6R	209-II(c), Row 6R
207-I-3b, Row 6R	212-II(d), Row 6R

Steeples, or portion of steeples, containing these particular cracks were cut from the rim disc samples and individual cracks were broken open to expose the crack surfaces. The exposed crack surfaces were examined visually and at low magnification to establish the overall crack shape and size, and in the scanning electron microscope (SEM) to establish the fine-scale topographic features. The various crack surfaces were examined both in the original, as-exposed condition, and after cathodic cleaning to remove surface deposits.

One of the most pronounced Type I MP indications was noted at the second serration on the concave side of Steeple 213/214, Row 6R. This particular crack is designated as 213-I-2bd. A portion of the MP crack indication is shown in Figure 5-1. The crack indication extended for the full length of the steeple and appeared to be comprised of multiple, connected segments. The exposed surface of crack 213-I-2bd is shown in Figure 5-2. A diagram showing the extent of the crack surface relative to the full cross-section area of the steeple at that location is shown in Figure 5-3.

From the macroscopic features of the crack surface, it is evident that the crack is composed of at least eight discrete segments joined by the distinct steps. It was noted in the examination of this specimen that individual crack segments overlapped at many of the macroscopic steps. This factor is evidence that the crack developed by multiple initiation of numerous independent cracks along the groove surface and subsequent growth of these cracks to the point where they joined to form a single crack front. The typical crack depth was measured as approximately 0.10 inch (2.5 mm). As may be noted, the segment at the outlet face corner grew

FIGURE 5-1. MAGNETIC PARTICLE CRACK INDICATIONS. Steeple 213/214. Row 6R. Concave side; outlet face is at left. 2-1/2X

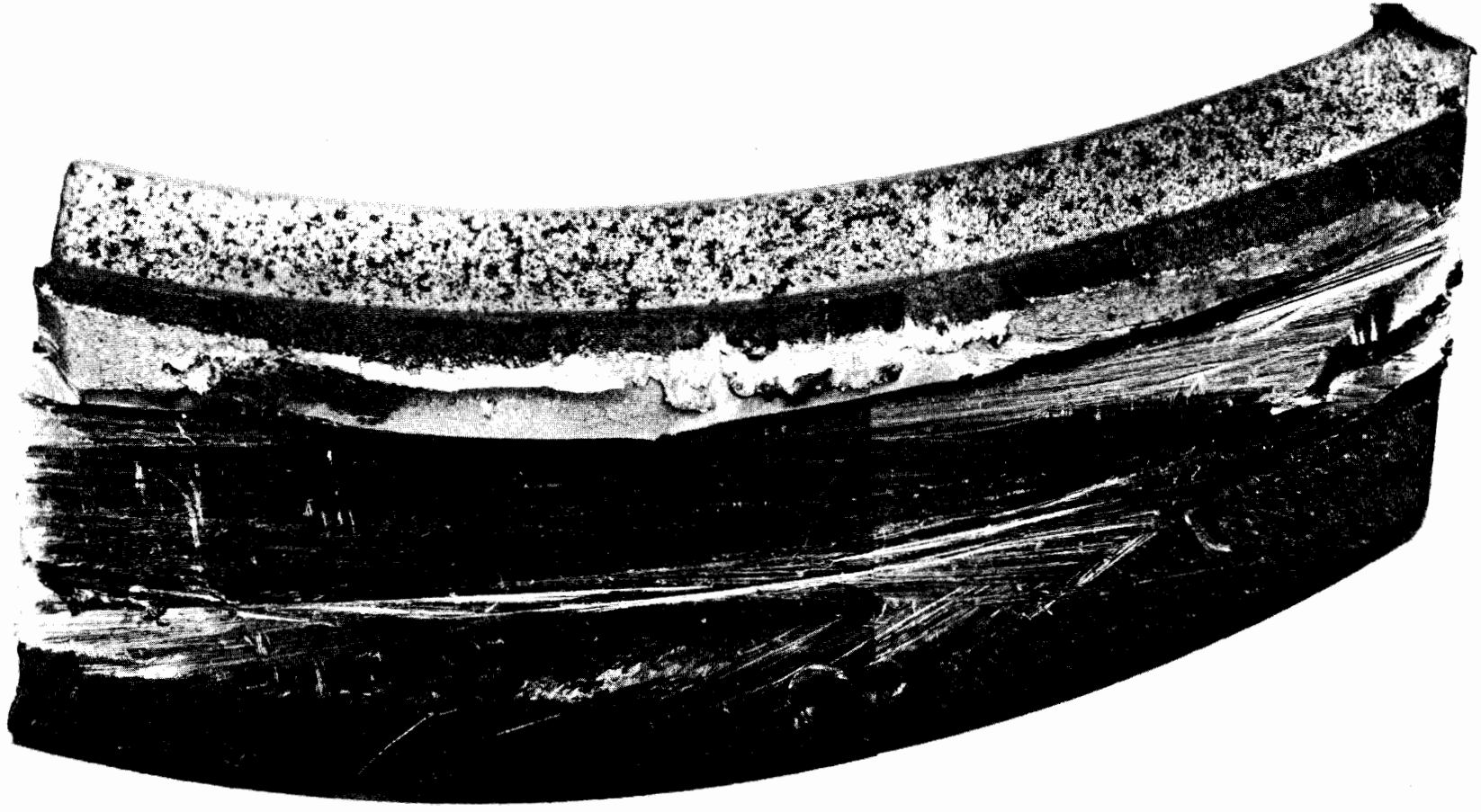

FIGURE 5-2. SURFACE OF CRACK 213-I-2bd, ROW 6R. View inward, inlet face is at right. See Figures 5-1 and 5-3. 4X

(This photograph reduced to 83% of its original size)

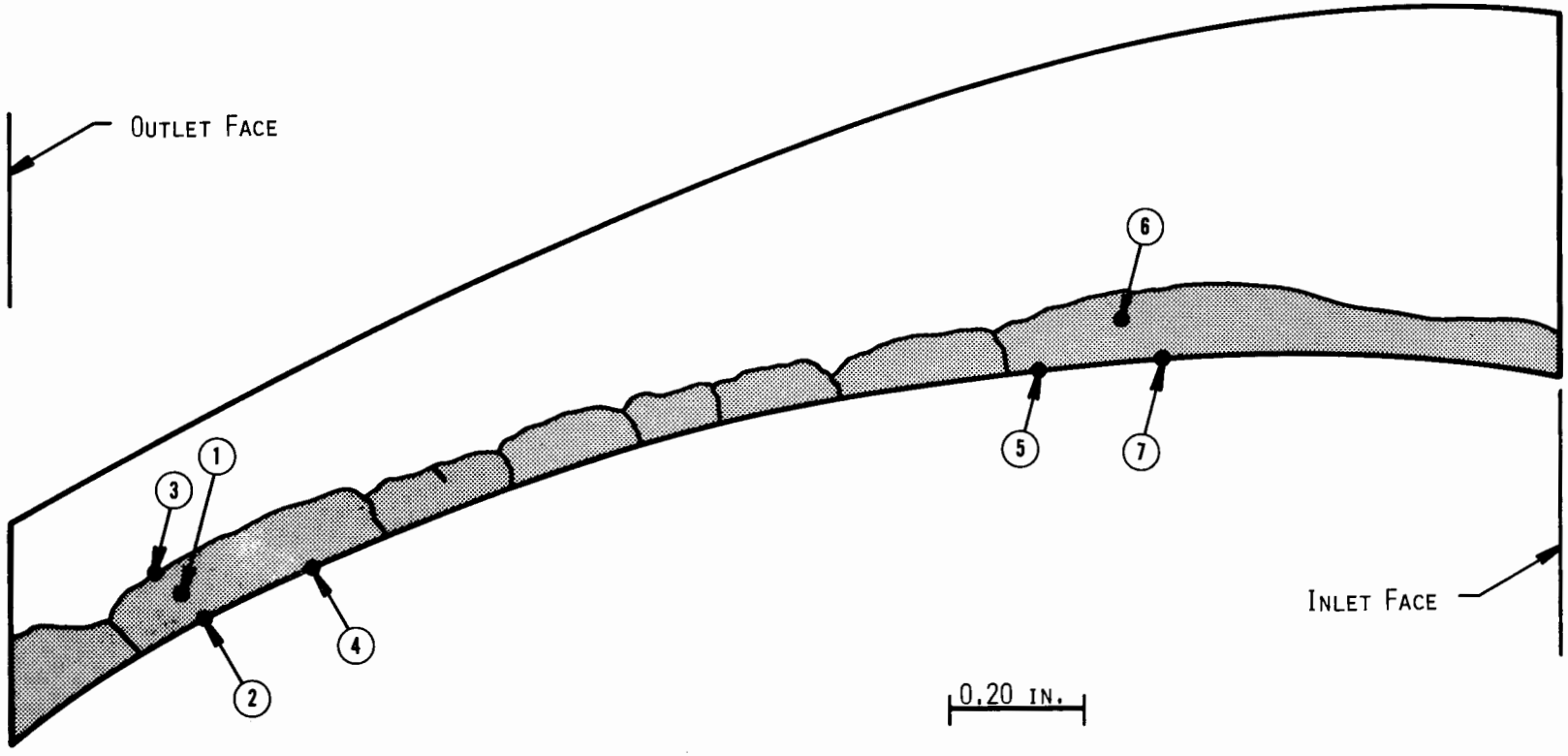

FIGURE 5-3. DIAGRAM OF SURFACE OF CRACK 213-I-2bd, ROW 6R. Outline represents full cross section of steeple at crack location. See Figure 5-2. 4X

(This diagram reduced to 90% of its original size)

to a somewhat larger size than the other crack segments resulting in a crack length of 0.15 inch (3.8 mm) along the outlet face. The total surface area of crack 213-I-2bd comprised approximately 21% of the cross-sectional area of the steeple at that location.

The typical fine-scale topographic features of this crack are shown in Figure 5-4. At all locations examined, the crack surface was characterized by distinct intergranular facets. In particular, clearly defined intergranular features were noted at the extremities of crack propagation as shown in Figure 5-4(d). The initial stages of cracking (at the groove surface) are also completely intergranular but, at most locations along the edge of the crack, evidence of significant corrosive attack of the crack surface was apparent as shown in Figure 5-4(c). Distinct surface deposits were evident at these locations, and it is apparent that many of the original intergranular facets have been altered by corrosive attack. It should be noted that, although the macroscopic features clearly indicate multiple crack initiation, no discrete features identifying particular initiation sites were noted in the SEM examinations. Additional SEM fractographs from crack 213-I-2bd are presented in Appendix E, Figures E-1 and E-2.

Significant pitting of the steeple surface was also observed at locations adjacent to the crack. Examples of this corrosive attack are shown in Figure 5-5.

A second Type I crack of extended length, crack 208-I-2bd, Row 6R, is shown in Figures 5-6 and 5-7. This crack is generally similar to 213-I-2bd, but is not as extensive. As may be noted in Figure 5-7, the total crack surface is comprised of at least sixteen separate segments indicating initiation of at least sixteen independent cracks, each of which grew fairly uniformly to the point of joining to form a single crack front. Typical crack depth over the length of crack 208-I-2d was measured as 0.04 to 0.06 inch (1.0-1.5 mm). The crack surface comprises approximately 15% of the total cross sectional area of the steeple at the second serration. The crack is predominantly intergranular but a significant degree of transgranular fracture was noted in areas representing the later stages of crack propagation. Isolated transgranular facets within an otherwise intergranular zone were also noted. The zone at the edge of the crack surface, representing cracking initiation and early stages of propagation, is completely intergranular. Evidence of post-cracking corrosive attack of the crack surfaces is also apparent. A diagram of crack 208-I-2bd and SEM fractographs illustrating these features are shown in Appendix E, Figures E-3, E-4 and E-5.

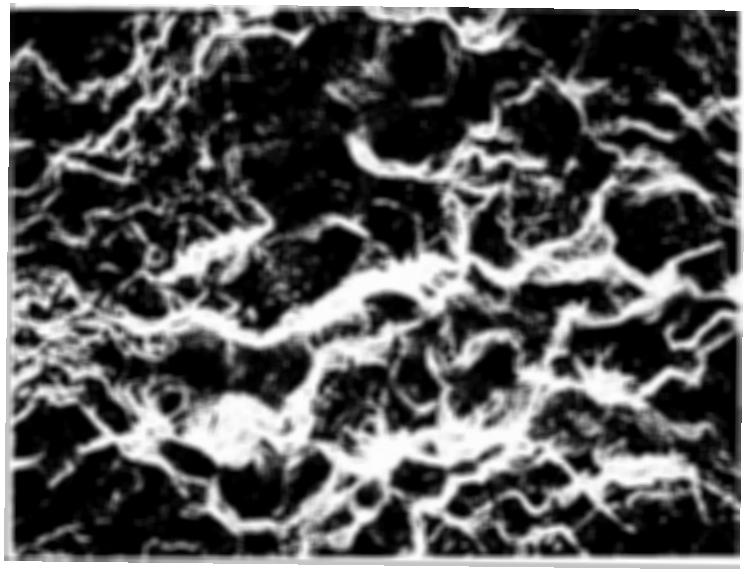

(a) Location 1. No cleaning.

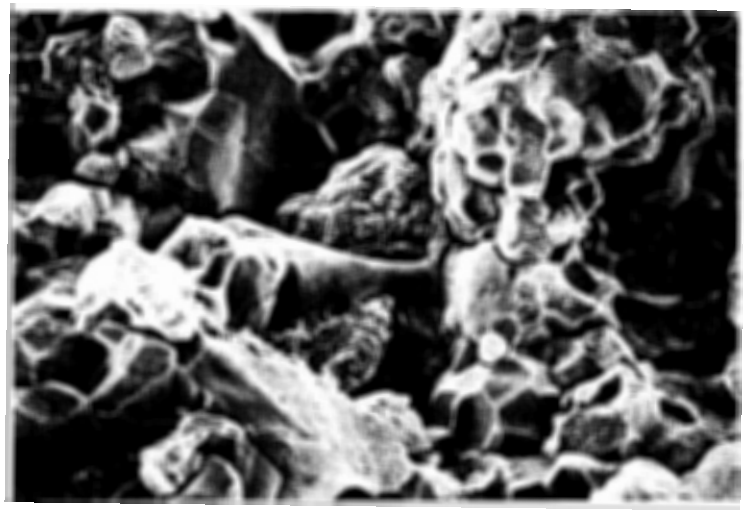

(b) Location 6.

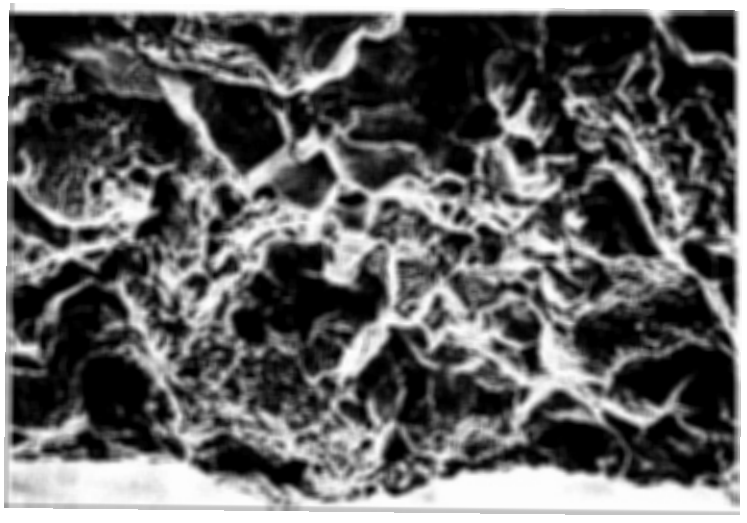

(c) Location 7.

FIGURE 5-4. SEM FRACTOGRAPHS FROM CRACK 213-I-2bd, ROW 6R. See Figure 5-3 for locations. Cathodically cleaned unless otherwise noted. 200X

(These photographs reduced to 90% of their original size)

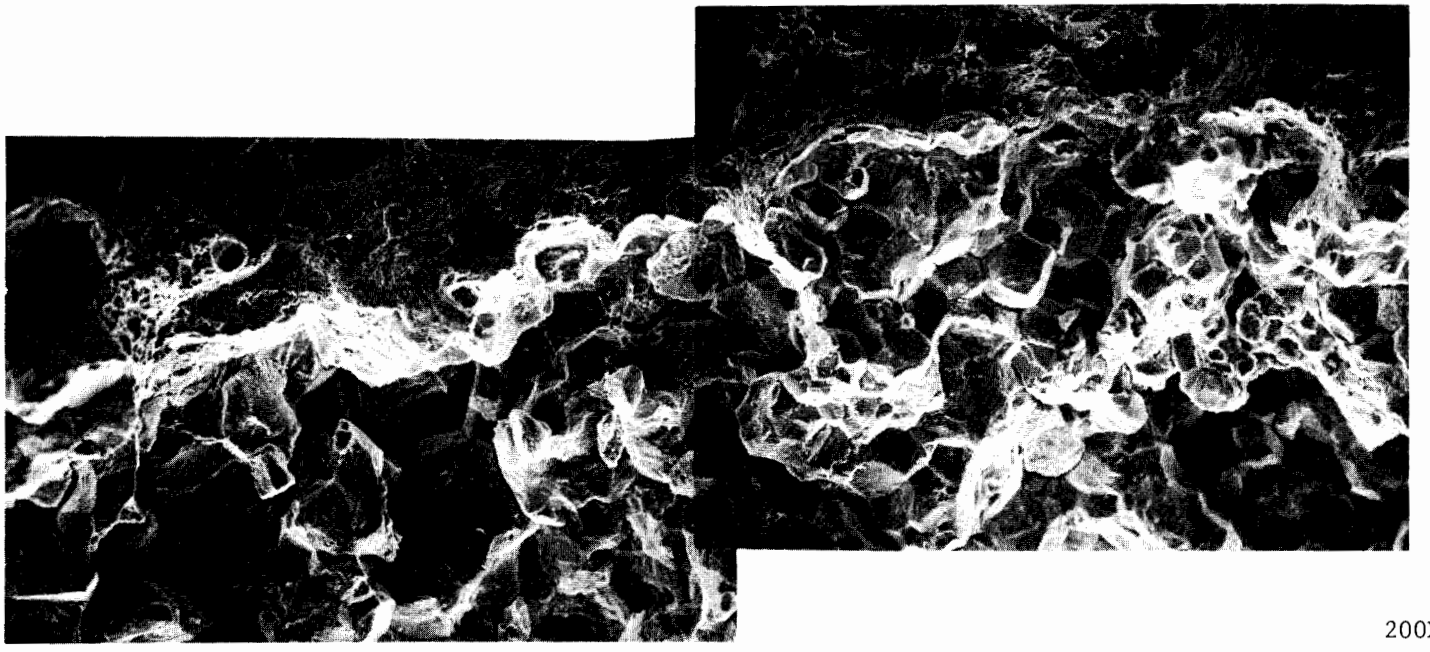

200X

(d) Location 3. At transition to laboratory fracture. No cleaning.

FIGURE 5-4 (Continued). SEM FRACTOGRAPHS FROM CRACK 213-I-2bd, ROW 6R. See Figure 5-3 for locations. Cathodically cleaned unless otherwise noted.

(These photographs reduced to 90% of their original size)

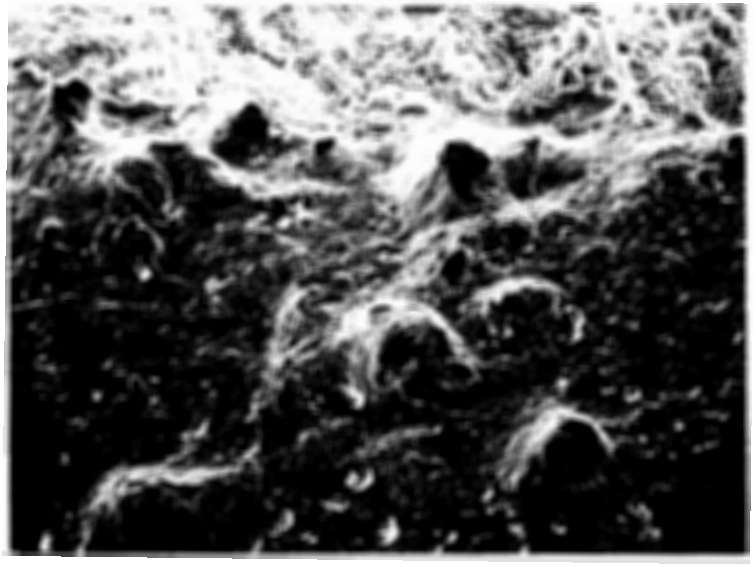

(a) Original condition, no cleaning. 100X

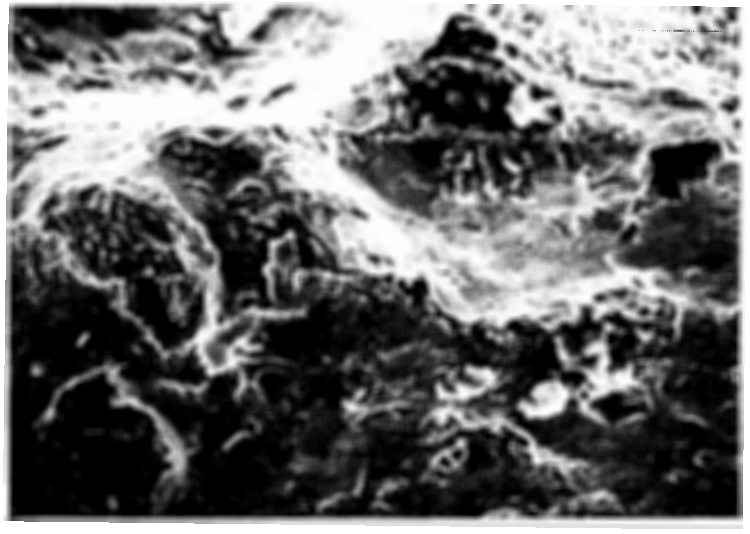

(b) Original condition. 300X

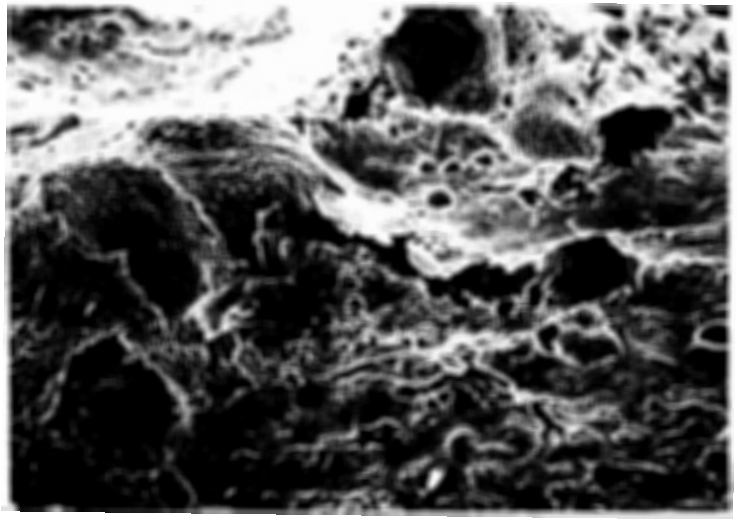

(c) Same as (b) after cathodic cleaning. 300X

FIGURE 5-5 GROOVE SURFACE ADJACENT TO CRACK 213-I-2bd.

(These photographs reduced to 90% of their original size)

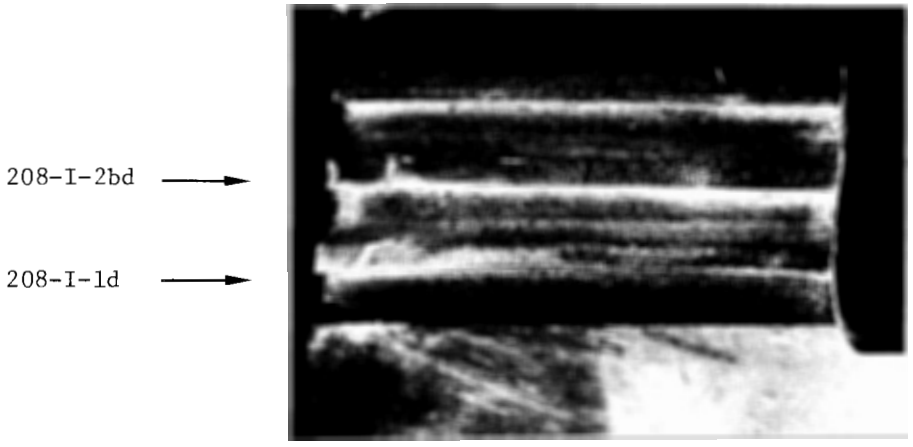

(a) Concave side. 1-1/2X

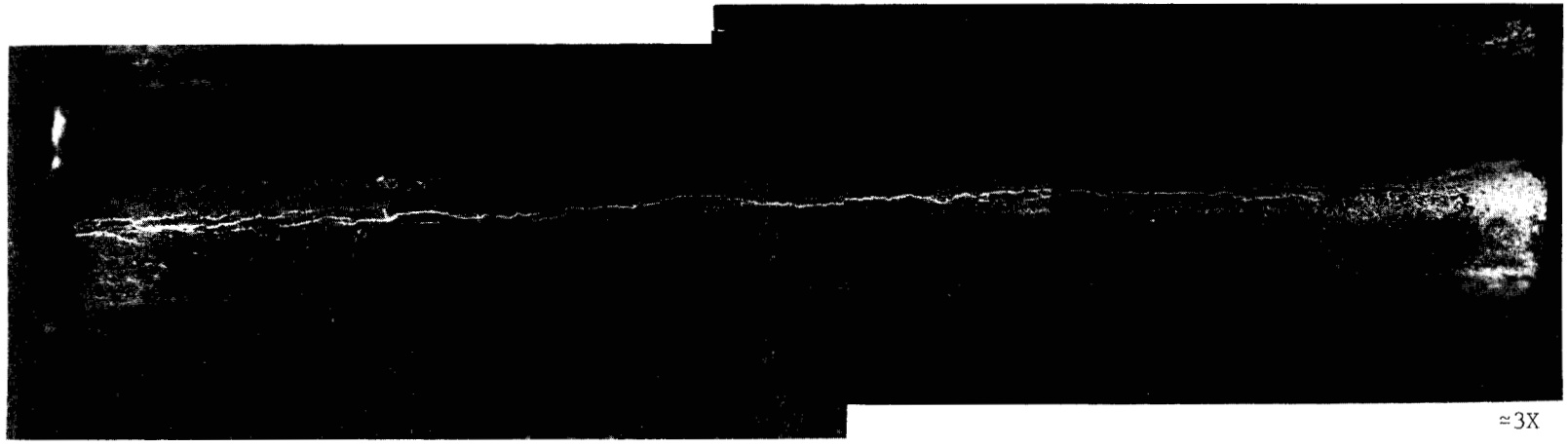

≃3X

(b) Crack 208-I-2bd. Outlet face is at left.

FIGURE 5-6. MAGNETIC PARTICLE CRACK INDICATIONS, STEEPLE 208/209, ROW 6R.

(These photographs reduced to 79% of their original size)

FIGURE 5-7. SURFACE OF CRACK 208-I-2bd, ROW 6R. View inward; outlet face is at left. See Figure 5-6. Fractographic features shown in Appendix E, Figures E-3, E-4 and E-5. 4X

(This photograph reduced to 90% of its original size)

At the extreme end of crack 208-I-2d, near the inlet face, the cracking was very shallow. The extent of cracking in this region was not sufficient to produce a distinct magnetic particle crack indication. SEM examination of this region of the cracking identified several small, discrete, thumbnail shape cracks [approximately 0.013 inch long x 0.005 inch deep (0.330 mm x 0.127 mm)], see Figure 5-8. It is evident that this zone represents the early stages of cracking in which discrete cracks have developed, but have not yet connected with adjacent cracks. Each of the discrete small thumbnail cracks in this zone exhibited completely intergranular features.

Crack 207-I-3bd, Row 6R, represents a case where a short, distinct MP indication was observed on the outlet face, but the extent of cracking along the groove was not evident from conventional magnetic particle examination. The particular MP indications observed at this location are shown in Figure 5-9. Examination of the groove surface along the length of the steeple at low magnification with the aid of a stereo microscope showed that the MP indication consisted of a surface network of numerous, interconnected segments forming a diffuse, indefinite indication under normal visual inspection, see Figure 5-10.

The exposed surface of 207-I-3bd is shown in Figure 5-11. The crack surface at this location is made up of several disconnected segments and the extent of crack propagation is very limited. The maximum crack depth at any point along the groove surface is approximately 0.02 inch (0.51 mm) and the crack surface comprises less than 5% of the cross-sectional area. The separate crack segment located at the outlet face is somewhat larger than any other portion of the crack, and it is this segment that contributed to the MP indication on the outlet face. It should be noted, however, that in the absence of this one larger segment, the remainder of the cracking would probably not be detected by conventional MP inspection. Mixed mode cracking, similar to that of crack 208-I-2d, was also evident in this case. The crack is predominantly intergranular, particularly at the outer edge, but significant proportions of transgranular fracture were noted in the later stages of propagation. A diagram of this crack surface and SEM fractographs from the crack are shown in Appendix E, Figures E-6 and E-7.

The magnetic particle crack indication and the exposed surfaces of crack 177-I-2b are shown in Figure 5-12. This particular crack was located at the inlet face of Steeple 176/177 in Row 5R. The crack was observed to be comprised of two distinct major segments. The principal segment of the crack (located at the inlet face) measures approximately 0.28 inch (7.1 mm) along the groove surface and approximately 0.08 inch (2.0 mm) on the inlet face. This segment is bounded by curved

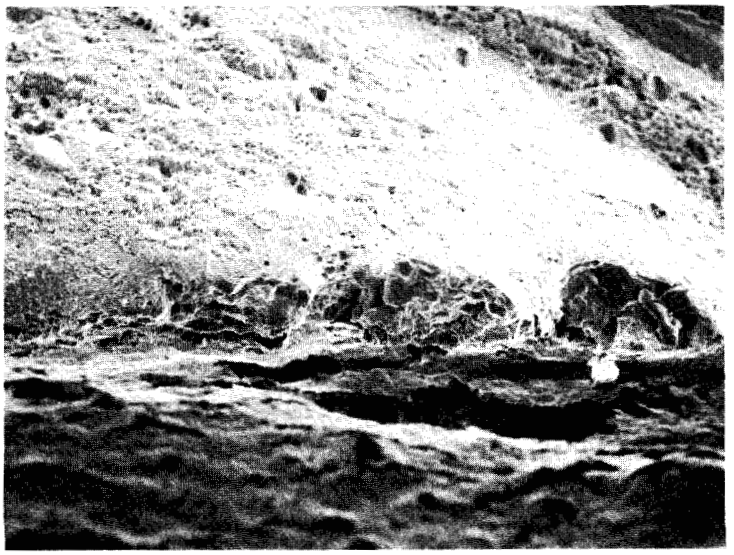

100X

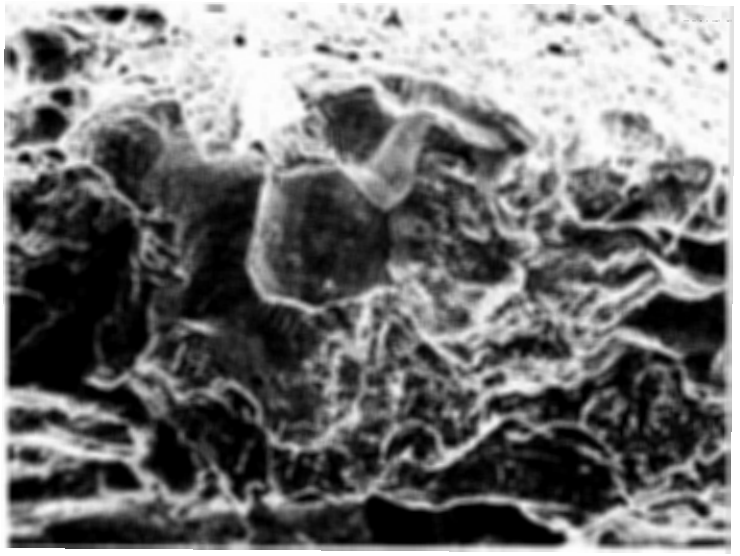

500X

FIGURE 5-8. SEM FRACTOGRAPHS FROM CRACK 208-I-2bd. Location near inlet face. Note separate thumbnail segments in surface and additional partially opened cracks.

(These photographs reduced to 90% of their original size)

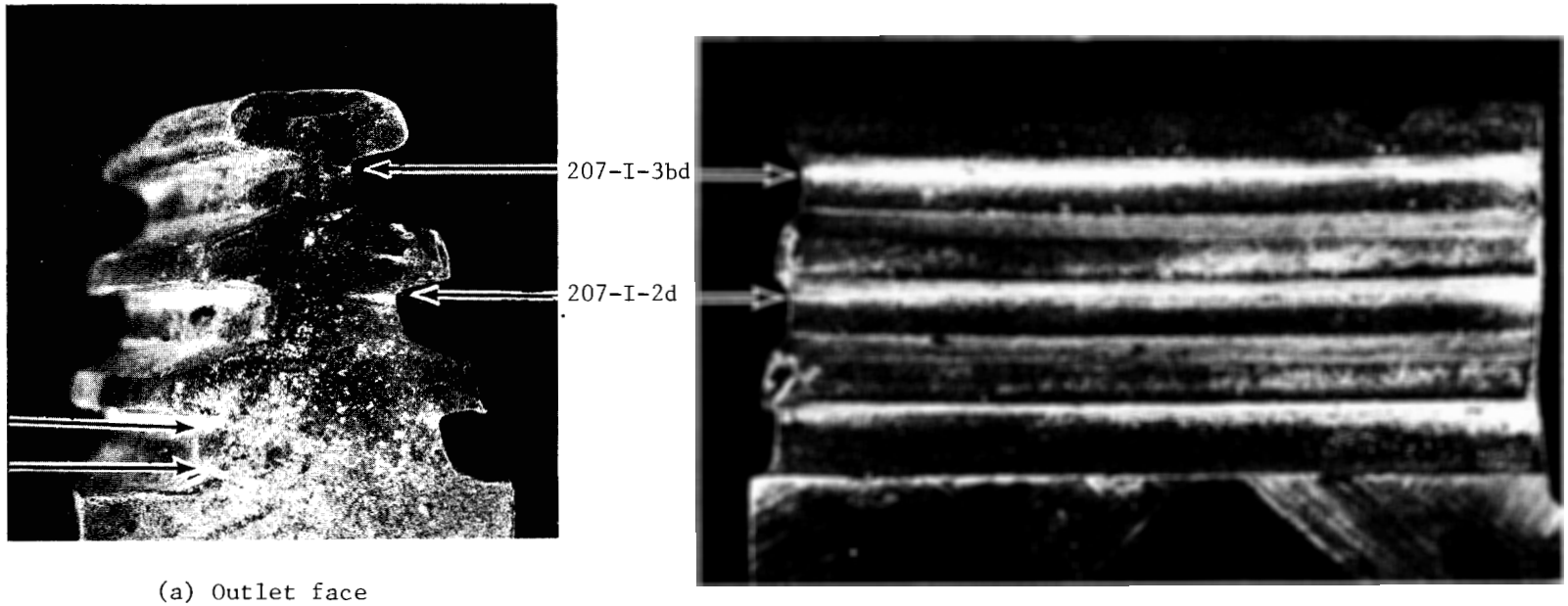

(a) Outlet face

(b) Concave side

FIGURE 5-9. MAGNETIC PARTICLE INDICATIONS, STEEPLE 207/208, ROW 6R. ≈2X

(These photographs reduced to 90% of their original size)

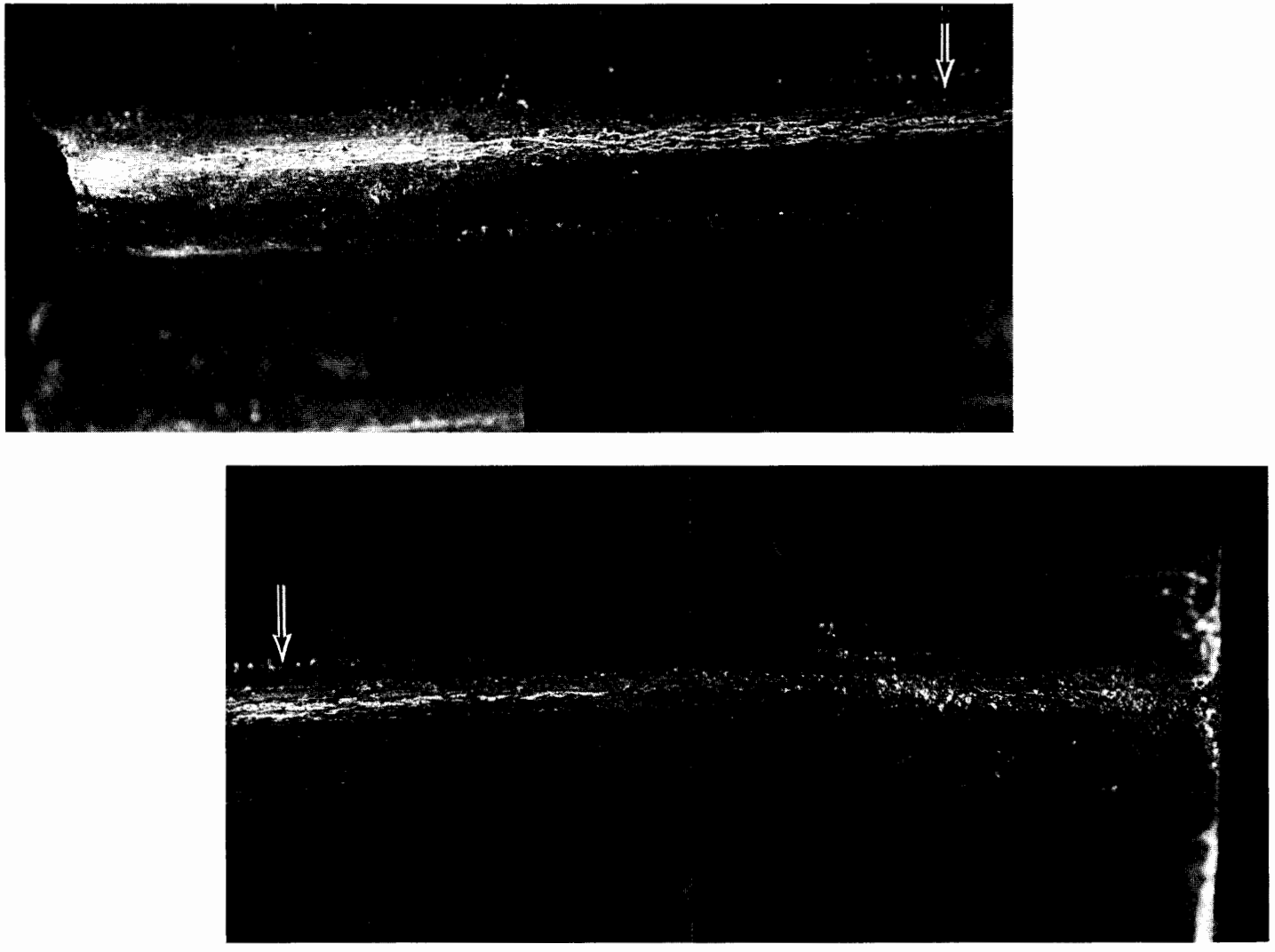

FIGURE 5-10. MAGNETIC PARTICLE CRACK INDICATION FOR CRACK 207-I-3bd, ROW 6R. Outlet face is at left. Arrows indicate match point. 4-1/2X
(These photographs reduced to 80% of their original size)

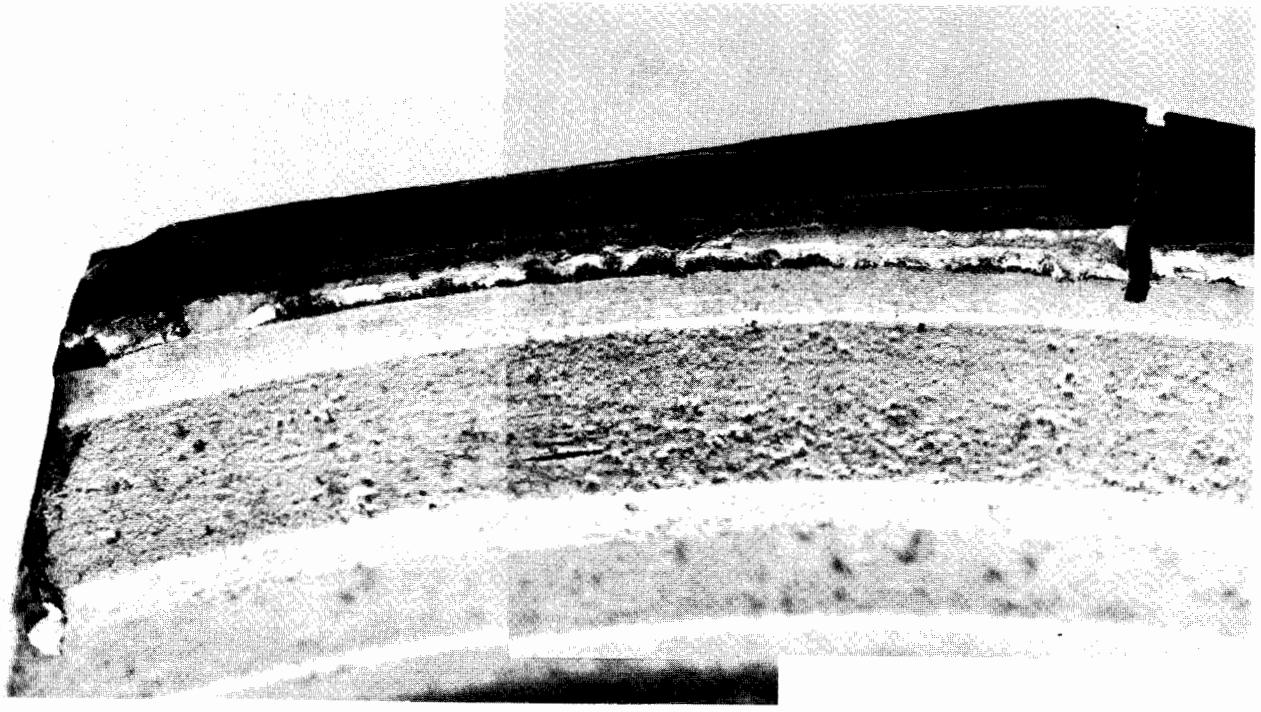

FIGURE 5-11. SURFACE OF CRACK 207-1-3bd. View inward; outlet face is at left. 5X

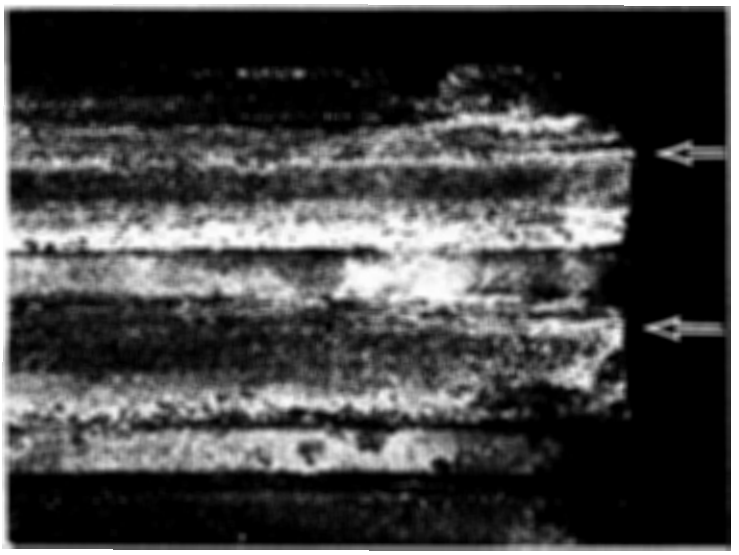

4X

(a) Magnetic particle indications. Concave side of steeple 176/177. Inlet side is at right.

8X

(b) Exposed crack surface. View inward. Inlet side is at right.

FIGURE 5-12. CRACK 177-I-2b, ROW 5R.

(These photographs reduced to 90% of their original size)

crack front and it may be noted that at one particular point, one branch of the crack extended considerably beyond the general crack front. The overall shape of the crack and configuration of the crack front indicate that this segment of the crack initiated at a point along the groove surface [approximately 0.1 inch (2.5 mm) from the inlet face]; not at the blade groove/inlet face corner. The second, thumbnail shaped segment of the crack was located approximately 0.4 inch (10.2 mm) from the inlet face and measured 0.12 inch long x 0.08 inch deep (3.0 mm x 2.0 mm). It is evident in the macrographs of the exposed crack surface [Figure 5-12(b)] that some corrosive attack or very limited cracking occurred along the groove surface between the two main segments of this particular crack.

A diagram of crack 177-I-2b illustrating the size of the crack relative to the cross-section of the steeple is shown in Figure 5-13 and the typical fine-scale topographic features of this crack are shown in Figure 5-14. As may be noted, this particular crack was relatively limited in extent and confined to an area near the inlet face of the steeple. The larger segment measures 0.28 inch (7.1 mm) along the groove with a maximum depth of 0.08 inch (2.0 mm). The crack surface represents only approximately 1% of the cross-sectional area. All areas of the two major segments of the crack surface were characterized by a predominance of distinct intergranular facets as illustrated in Figure 5-14. In particular, it should be noted that distinct intergranular facets were evident at the extremities of crack propagation, see Figure 5-14(c). A few isolated transgranular facets were noted at random locations, Figure 5-14(a). Locations within the two principal segments of this crack exhibited evidence of significant corrosive attack of the crack surface. This attack is particularly evident at locations near the groove surfaces representing the earlier stages of crack propagation, see Figures 5-14(d) and 5-14(f). Significant pitting attack of the blade groove surface was also evident in the general vicinity of crack 177-I-2b. Locations between the two major segments of this particular crack exhibit significant corrosive attack at the groove surface and a very limited degree of intergranular cracking. Additional examples of the fine-scale topographic features of crack 177-I-2b are shown in Figure E-8.

The characteristics of two typical Type II cracks are described in Figures 5-15 through 5-19. The magnetic particle indication of one such crack, 209-II(c) is shown in Figure 5-15. In this case, a distinct Type II crack indication was observed at the radius of the bottom of Steeple 208/209 at the outlet face. In the MP examination a separate independent crack segment, disconnected from the Type II crack indication, was observed on the outlet face. When this particular specimen was broken open, crack 209-II(c) was revealed to consist of a single crack

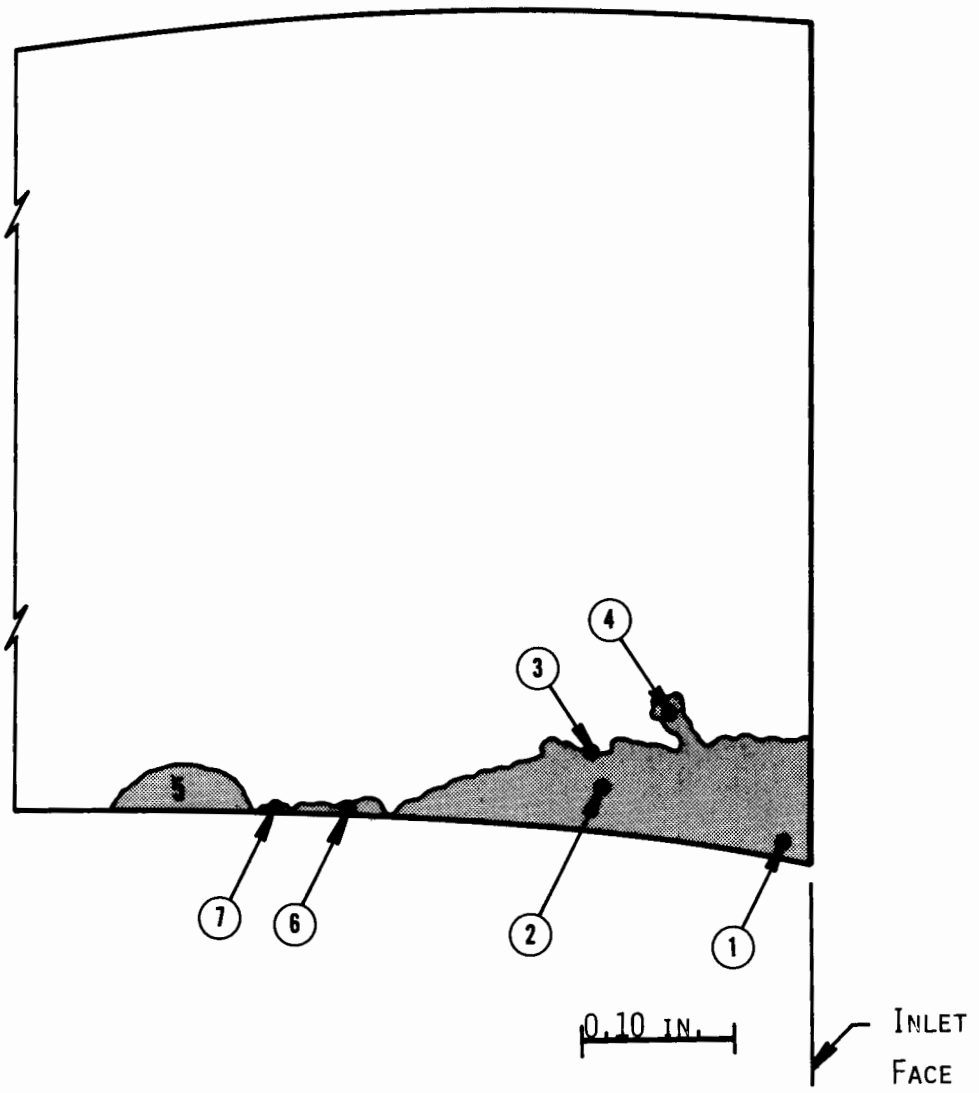

FIGURE 5-13. DIAGRAM OF SURFACE OF CRACK 177-I-2b, ROW 5R. Outline represents cross section of steeple at crack location. 8X

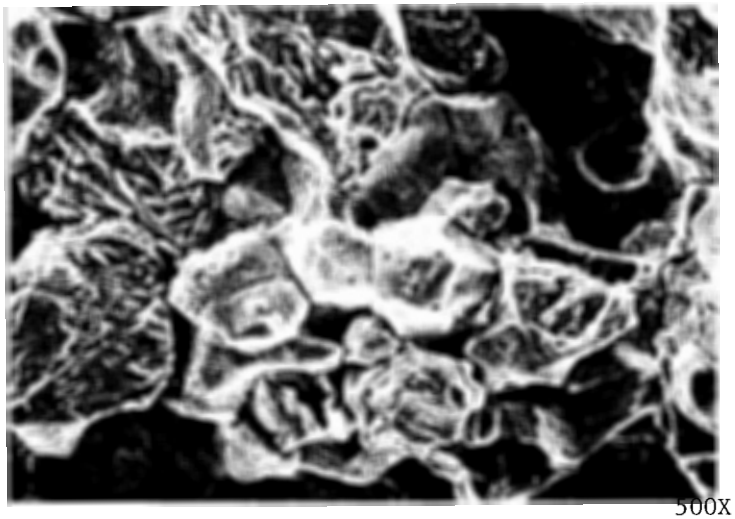

500X

(a) Location 1

700X

(b) Location 2

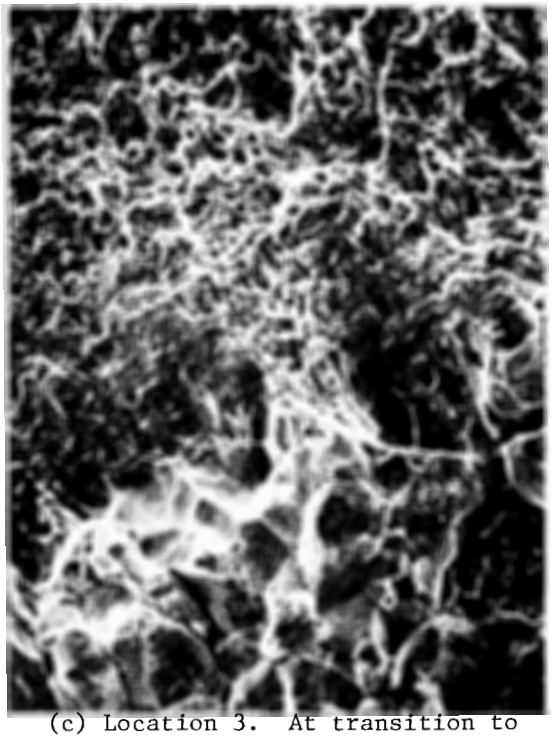

(c) Location 3. At transition to laboratory fracture.

FIGURE 5-14. SEM FRACTOGRAPHS FROM CRACK 177-I-2b. See Figure 5-13 for locations.

(These photographs reduced to 90% of their original size)

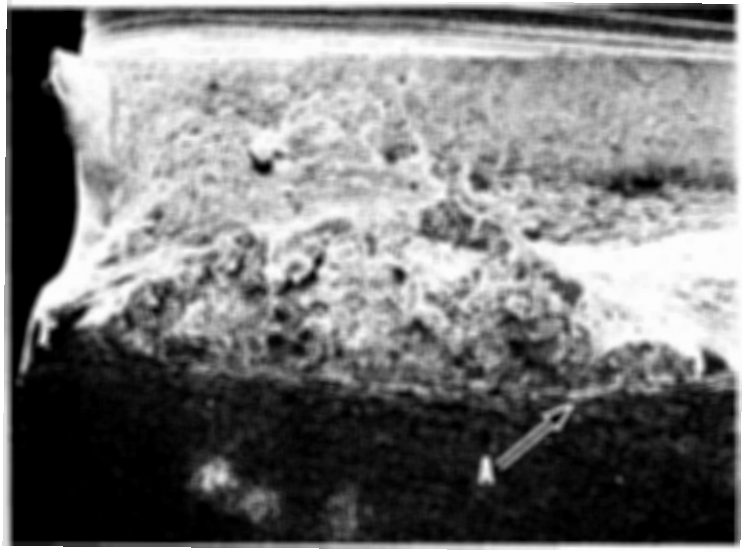

25X

(d) Area 5. Note smaller thumbnail segment at lower right.

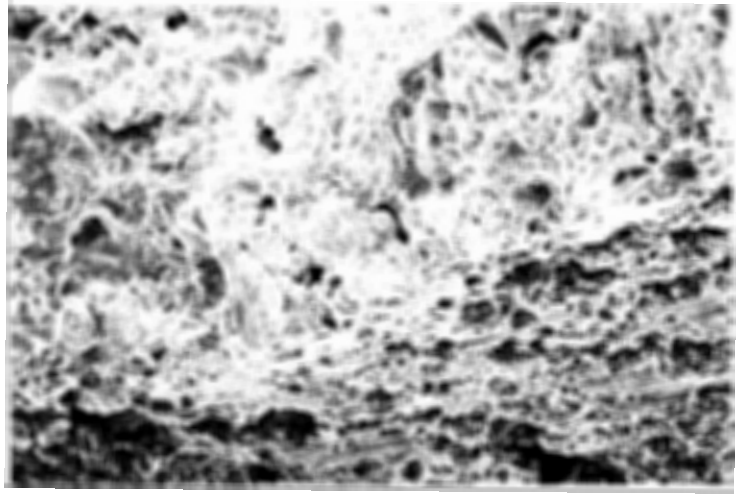

100X

(e) Location 5-A in (d).

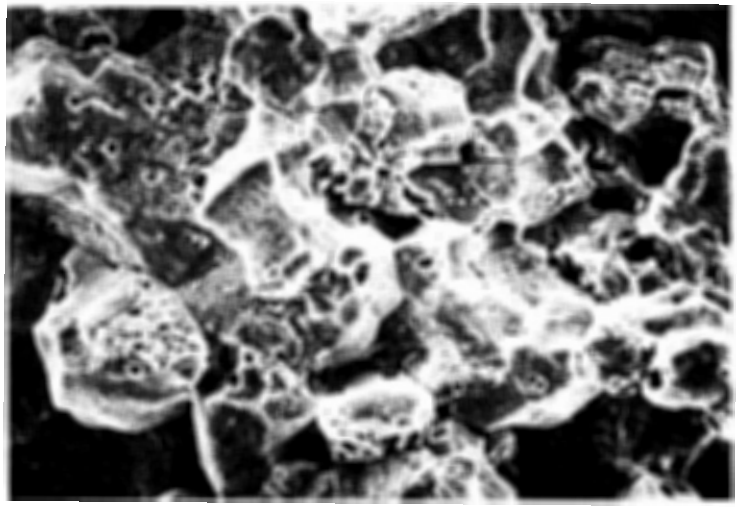

500X

(f) Typical topography in Area 5.

FIGURE 5-14 (Continued). SEM FRACTOGRAPHS FROM CRACK 177-I-2b. See Figure 5-13 for locations.

(These photographs reduced to 90% of their original size)

1.5X

(a) Outlet face. Arrow indicates crack 209-II(c).

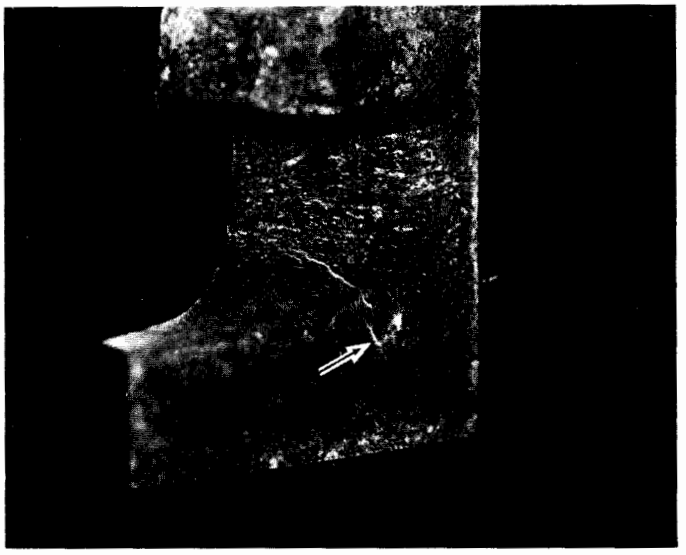

5X

(b) Crack 209-II(c). Note separate crack indication on outlet face (small arrow).

FIGURE 5-15. MAGNETIC PARTICLE CRACK INDICATIONS IN STEEPLE 208/209, ROW 6R.

(These photographs reduced to 90% of their original size)

10X

(a) Optical macrograph.
No cleaning.

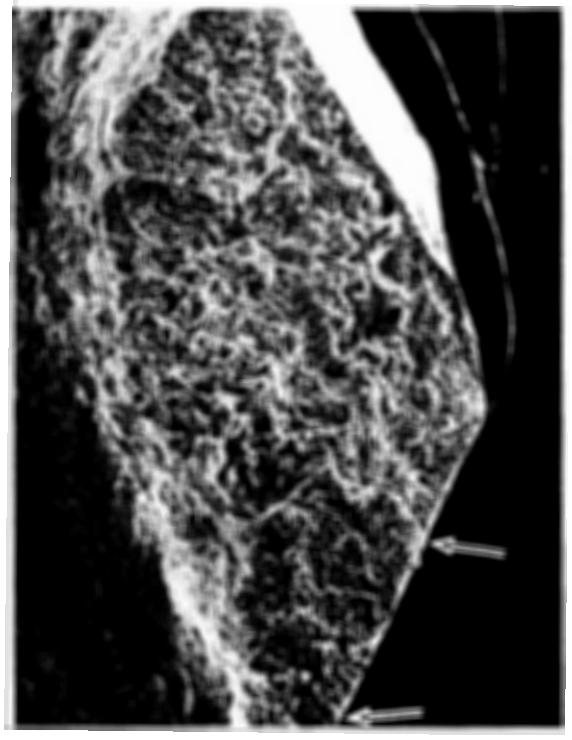

25X

(b) SEM macrograph.
Cathodically cleaned.

FIGURE 5-16. SURFACE OF CRACK 209-II(c), ROW 6R. Note separate, Type III crack designated by arrows [209-III(c)].

(These photographs reduced to 90% of their original size)

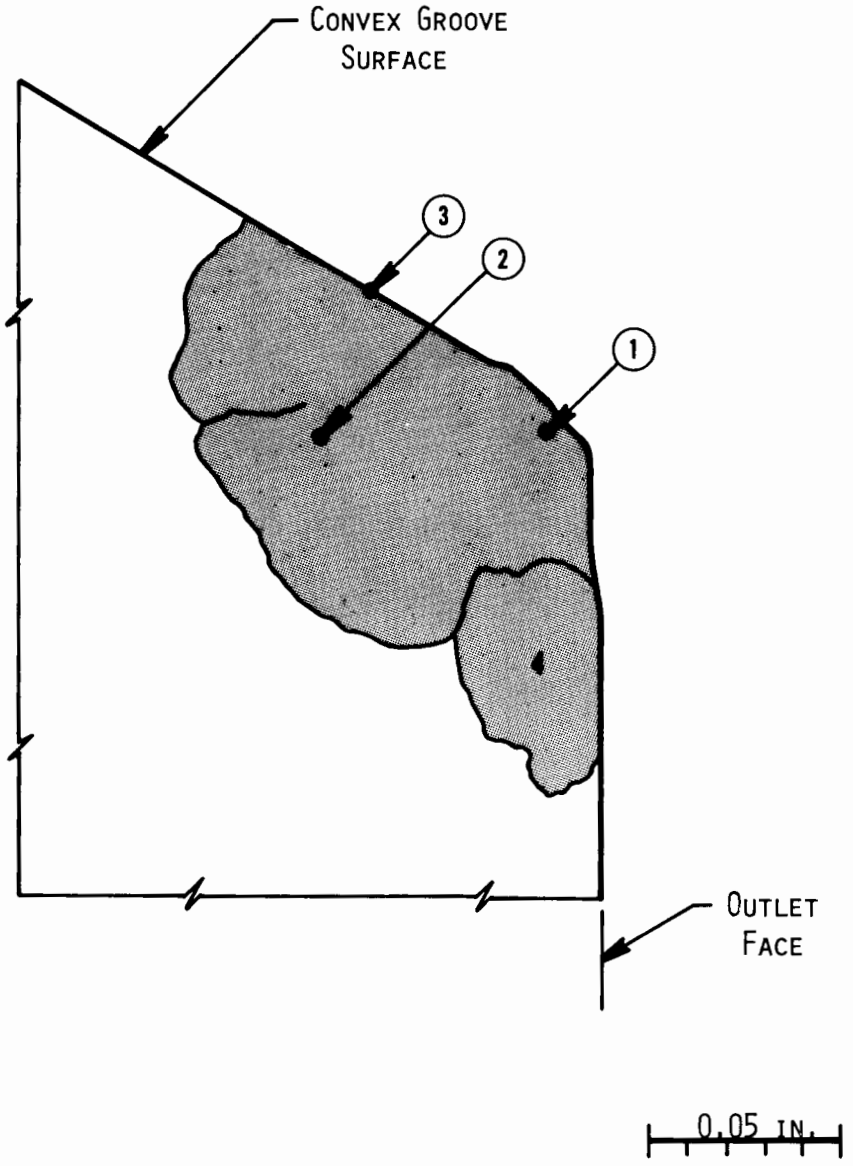

FIGURE 5-17. DIAGRAM OF SURFACE OF CRACK 209-II(c) ROW 6R. 20X

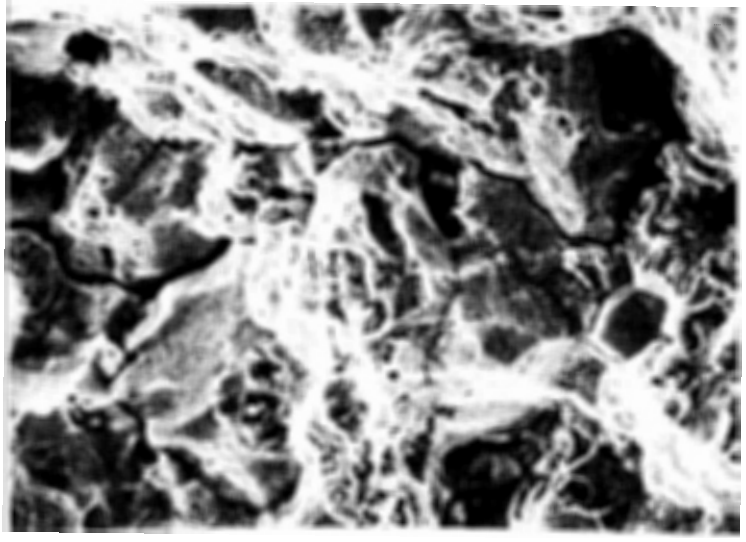

500X

(a) Location 1

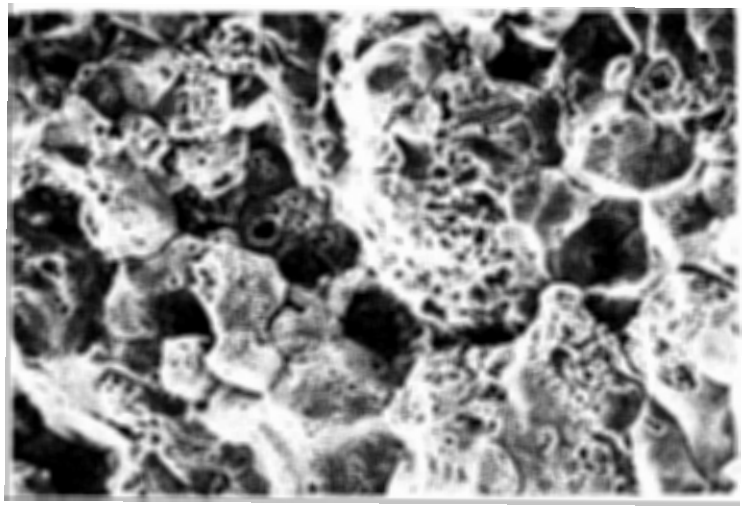

300X

(b) Location 2

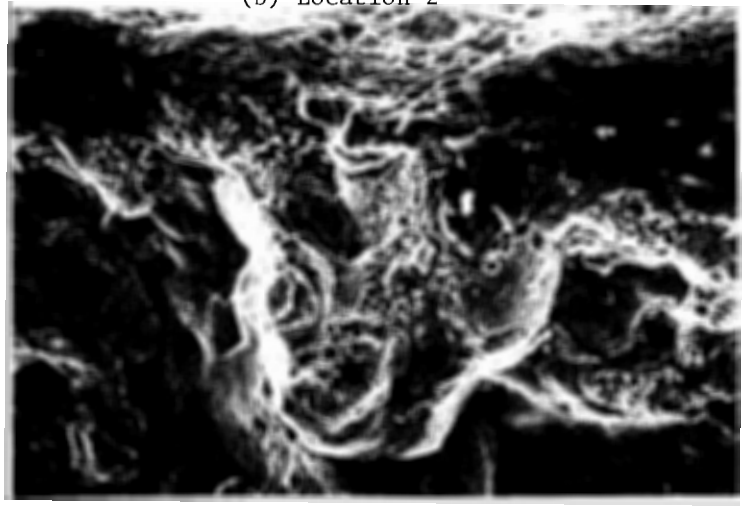

200X

(c) Location 3

FIGURE 5-18. SEM FRACTOGRAPHS FROM CRACK 209-II(c), ROW 6R. See Figure 5-17 for locations.

(These photographs reduced to 90% of their original size)

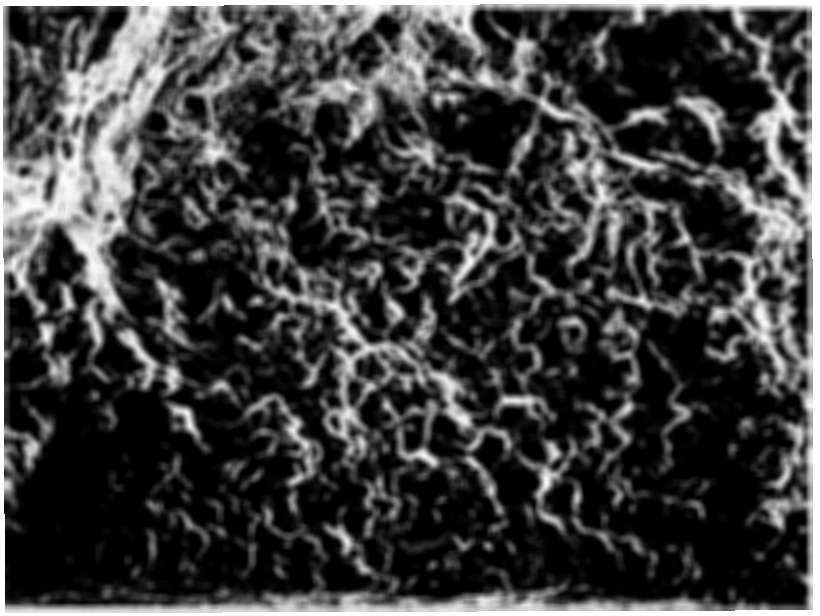

70X

(a) Area 4, Figure 5-17.

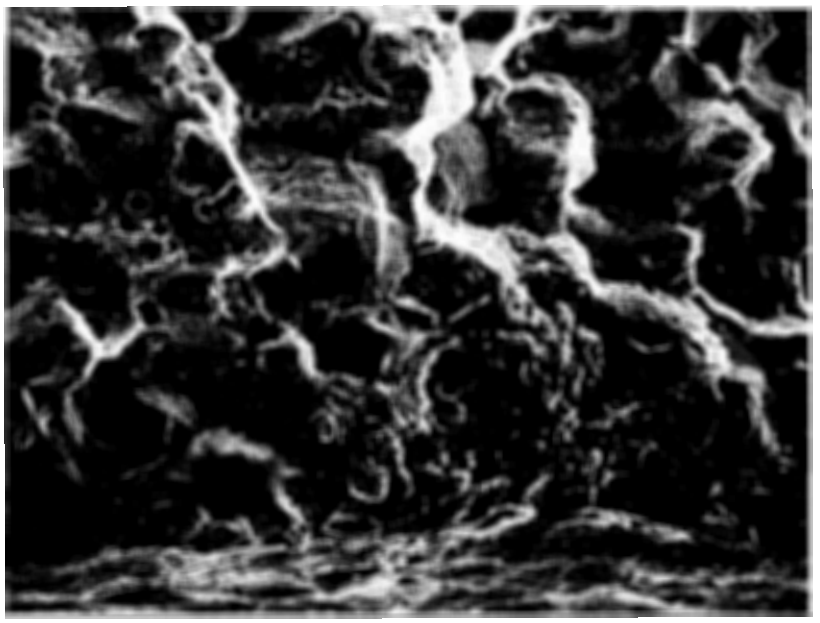

300X

(b) Location at outlet face.
Area 4.

FIGURE 5-19. SEM FRACTOGRAPHS FROM CRACK 209-III(c), ROW 6R.

segment measuring approximately 0.1 inch (2.5 mm) along the groove surface and approximately 0.06 inch (1.5 mm) deep, see Figure 5-16. A second, independent crack segment, separated from 209-II(c) by distinct step, was also evident as shown in Figure 5-16(b). The shape and location of this second segment indicate that this crack corresponds to the separate MP indication noted on the outlet face of the steeple and that it represents a face-initiated crack independent from 209-II(c). The presence of such a face-initiated crack correlates with observations in the metallographic examinations (see Figure D-6).

The diagram of the surface of crack 209-II(c) and representative SEM fractographs from that crack are shown in Figures 5-17, 5-18 and 5-19. Crack 209-II(c) is completely intergranular (Figure 5-18), but no features were observed to indicate a specific initiation site. Based on the shape and dimensions of the crack, it appears that this Type II crack initiated within the blade groove a short distance from the outlet face.

Examination of the topography of this exposed crack surface clearly establishes that the area designated as "4" in Figure 5-17 constitutes a separate independent crack. This type of face-initiated crack is designated as Type III to distinguish it from the more common Type I and Type II cracks which are associated with the blade grooves. This particular Type III crack [209-III(c)], is completely intergranular with some evidence of corrosive attack at the outer edge (Figure 5-19).

Examination of a second Type II crack 212-II(b), revealed features similar to those described for crack 209-II(c); namely, completely intergranular features with indications of initiation within the groove. Opening of the specimen containing crack 212-II(b) also revealed a separate face-initiated crack, 212-III(b), measuring approximately 0.12 inch long by 0.07 inch deep (3.0 mm x 1.8 mm). This Type III crack is also completely intergranular in nature. MP crack indications and fractographs from these Type II and Type III cracks are shown in Appendix E, Figures E-9, E-10 and E-11.

One specimen was cut to contain a Type III MP crack indication isolated from any other cracks. The characteristics of this particular crack, [211-III(d)], are illustrated in Figures 5-20 and 5-21. This crack measured approximately 0.20 inch long x 0.07 inch deep (5.1 mm x 1.8 mm) and is completely intergranular. It is clearly independent of the blade groove and any other cracking. Observations made in the examination of cracks 209-III(c), 212-III(d) and 211-III(d), together with the metallographic observations and overall MP inspection results definitely establish that the numerous small face-initiated cracks developed in these rim segment samples.

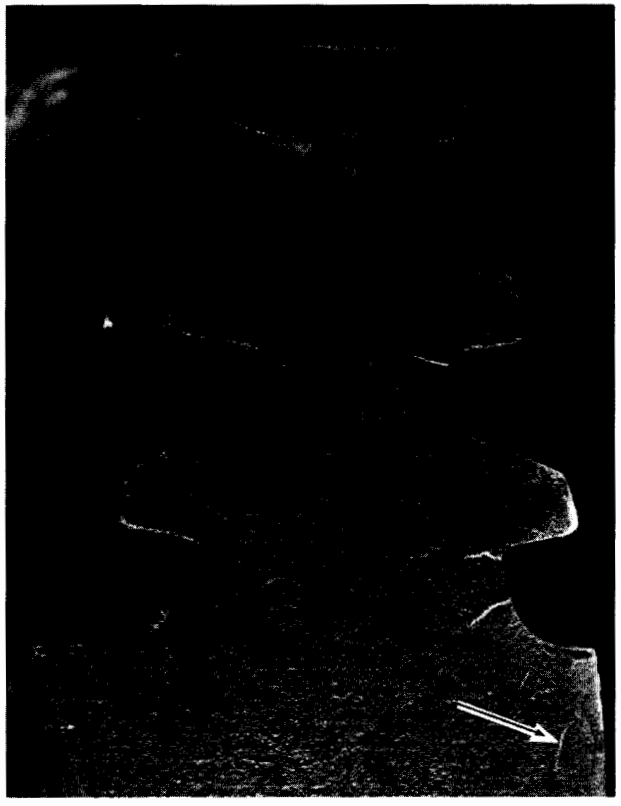

2-1/2X

(a) Magnetic particle indications at outlet face. Arrow marks face initiated crack (211-IIId).

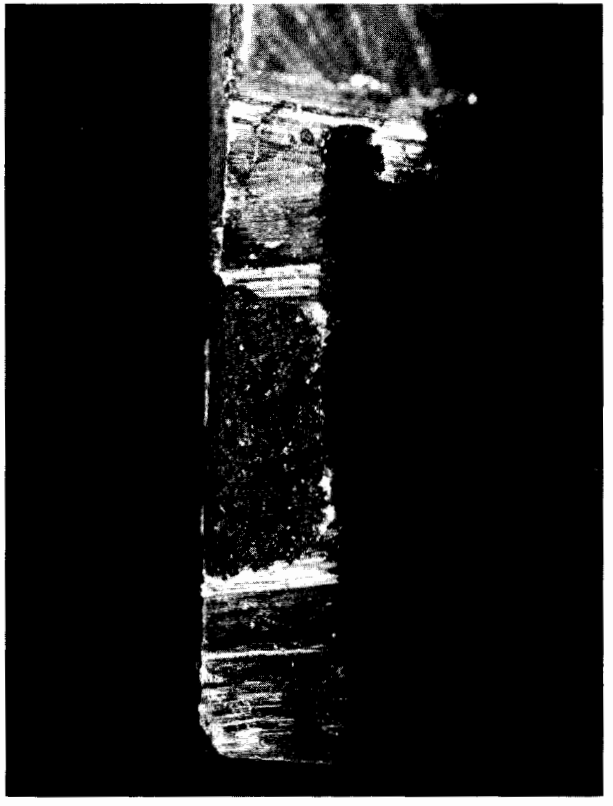

8X

(b) Crack surface. Outlet face is at left.

FIGURE 5-20. FACE INITIATED CRACK AT STEEPLE 211/212, ROW 6R, CRACK 211-III(d).

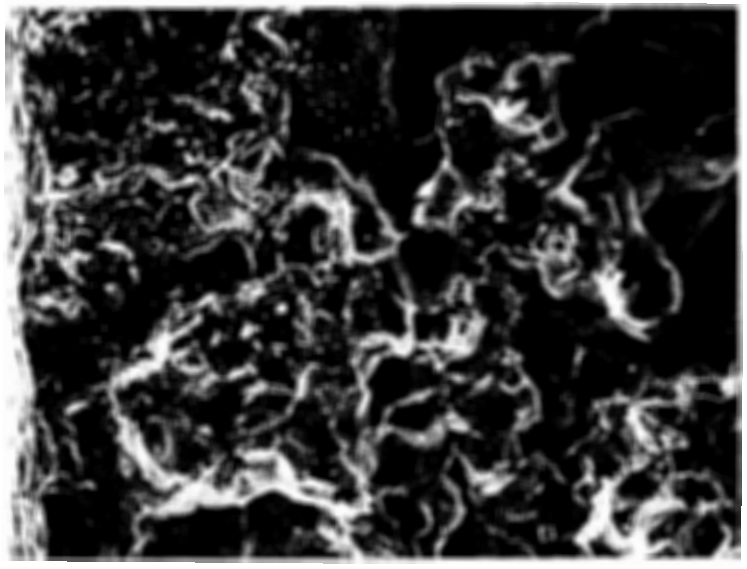

200X

(a) At outlet face edge, no cleaning.
Note surface deposit at edge.

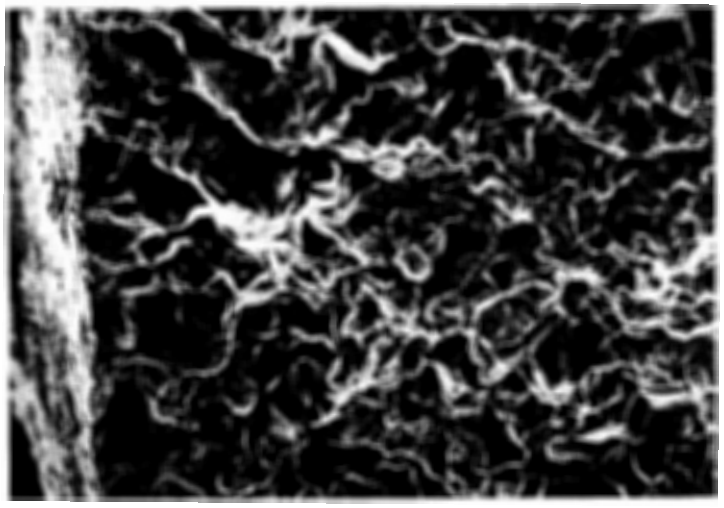

100X

(b) At edge. Cathodically cleaned.

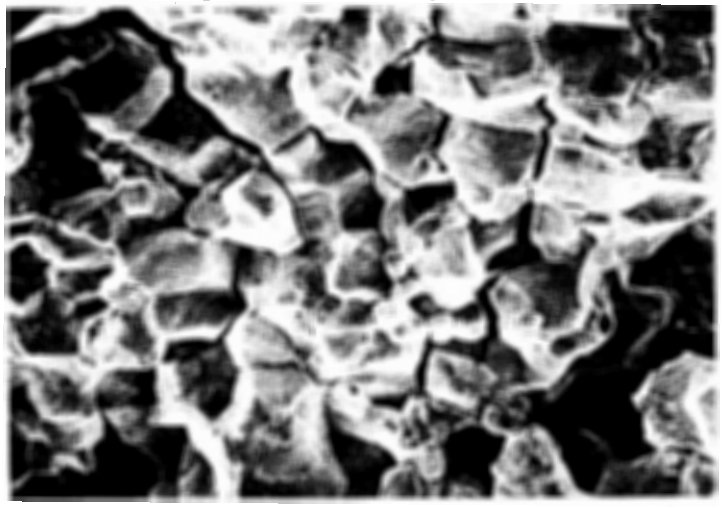

300X

(c) Typical topography. Cathodically cleaned.

FIGURE 5-21. SEM FRACTOGRAPHS FROM CRACK 211-III(d).

(These photographs reduced to 90% of their original size)

In the course of the fractographic examinations, energy dispersive X-ray spectroscopy was employed to provide a qualitative analysis of crack surface deposits. A number of individual spots on each of several crack specimens, representative of the surface deposits observed, were analyzed. Results similar to those of the EDS analysis of crack deposits in metallographic sections were obtained. In every case the principal constituents were found to be Fe, Cr and No. Fe was the predominant element and traces of P were noted at most locations. An example of a typical crack surface EDS spectrum is shown in Appendix E, Figure E-12. No evidence of any extraneous contaminant species was noted.

Section 6

DISCUSSION AND CONCLUSIONS

The principal observations made in this investigation may be summarized as follows:

1. The chemical composition of the disc material conforms to that usually specified for NiCrMoV low-alloy steels employed for LP turbine discs. The particular disc in question was manufactured to a proprietary materials specification similar to ASTM A 471.

2. The disc material exhibited a microstructure of tempered bainite typical of quenched and tempered NiCrMoV alloy steel. A duplex microstructure, characterized by grain sizes of ASTM 4-5 and ASTM 6-7, was observed. No microstructural defects or abnormalities of any significance were observed in any of the specimens examined.

3. Extensive cracking was observed in the blade attachment steeples of all three disc rim samples. Conventional magnetic particle inspection of the intact samples revealed cracking in 30 of the 5R steeples and in 36 of the 6R steeples (42 steeples total in each row). Cracking was observed on both the inlet and outlet faces of the steeples.

4. The cracks observed in the rim segment samples can be classified into three types according to location and orientation.

   Type I - Cracks located along the steeple serrations and oriented in a generally tangential direction through the steeple cross section.

   Type II - Cracks located at the bottom of the blade groove and oriented in a generally radial direction.

   Type III - Independent, face-initiated cracks oriented in a generally radial plane and located below the bottom of the blade grooves.

5. The Type I cracks were comprised of numerous connected or overlapping segments extending along the steeple serrations. This feature serves as evidence that the cracking developed by initiation of multiple independent cracks along the steeple serration and propagation of the several segments to the point of junction to form a single crack front.

6. The extent of cracking in particular steeple serrations varied from short cracks near one face to cracking over the full length of the steeple. The most severe Type I crack examined measured approximately 0.10 inch (2.5 mm) deep and extended for the full length of the steeple. This particular crack penetrated approximately 21% of the cross sectional area of the steeple.

7. The majority of the Type II cracks were located at the outlet face of the rim segments*. The largest of these measured approximately 0.1 inch (2.5 mm) along the steeple serration with a maximum depth of approximately 0.06 in (1.5 mm) in the radial direction.

8. All of the Type III cracks noted were located on the outlet face*. The largest of these measured approximately 0.2 inch long by 0.07 deep (5.1 mm x 1.8 mm).

9. All cracks examined, regardless of type, were predominantly intergranular, generally branched, and partially filled with a corrosion product. Two particular Type I cracks exhibited a significant degree of transgranular cracking. In both cases, the transgranular cracking was confined to the later stages of crack propagation.

10. Significant corrosive attack of the steeple serration surfaces, in the form of small, uniformly distributed pits, was evident. Evidence of post-cracking corrosion of the crack surfaces was also noted, particularly at locations near the outer edge.

11. Qualitative analyses of the deposits within cracks and pits indicated that the deposits consist of base metal oxides. No extraneous contaminant species were detected by in situ EDS analysis.

The metallurgical evaluation of the three rim segment samples identified two characteristic features of the cracking; namely, the mode of cracking was predominantly intergranular and all cracking developed as a result of multiple crack initiation. It was also established that the microstructure of the disc material was normal and that the cracking was not associated with any microstructural defect or abnormality. Consideration of the observations made in this investigation, together with information from other similar cases and data from the literature, provides a rationale for identification of the most probable cracking mechanism. The data obtained also serve to emphasize areas in which further investigation is needed to provide a complete understanding of this type of turbine disc failure.

In view of the fact that the cracking developed in service, two cracking mechanisms are to be considered; namely, fatigue and stress corrosion cracking (SCC).

*Erosion damage on the inlet faces of both rows may have prevented detection of Type II and Type III cracks in the magnetic particle inspections.

Generally, either high-cycle or low-cycle fatigue in quenched and tempered low-alloy steels is generally transgranular as opposed to the predominantly intergranular mode characteristic of the cracking observed in this case. Specifically, laboratory tests have demonstrated that fatigue crack propagation is transgranular in NiCrMoV low-alloy steels subjected to caustic environments (2). The only case of intergranular fatigue crack propagation reported occurred where the potential was controlled at levels well below the free corrosion potential. Even then mixed mode cracking was observed. Thus, the metallographic and fractographic features preclude fatigue as a primary factor in the cracking incident and lead to the conclusion that the cracking developed by one or another form of stress corrosion cracking. The three characteristic features of the cracking identified in this case: namely, intergranular mode, multiple initiation, and significant localized corrosive attack, are all completely consistent with that type of cracking mechanism. Also numerous cases of SCC in fossil fuel and nuclear steam turbine components have been reported (3,4,5).

All cracks exhibited intergranular features completely along the intersection with the free surface indicating that crack initiation was intergranular in all cases. In most cases, cracking was completely intergranular as evidenced by distinct intergranular features at the extremities of the crack. Certain cracks exhibited a transition to the transgranular (or mixed intergranular/transgranular) mode in the later stages of crack propagation. Such a transition could be associated with either a change in the stress intensity factor or a change in environment. It is also possible that fatigue (or corrosion fatigue) could have been involved in the later stage of cracking. Specific identification of the factors which contributed to the transition in cracking mode cannot be made from the available data. The fact that the transgranular mode was not characteristic of all cracking and that it occurred only in the later stages of crack propagation is evidence that this feature is not directly related to the primary mechanism(s) or the root cause of cracking.

One significant factor related to analysis of this incident is the extent and distribution of cracks. Cracking occurred in a high proportion of the steeples and at all of the several susceptible locations on any individual steeple. The nominal operating stresses are different at each of the three steeple serrations (locations of minimum cross-section). If the centrifugal force loading is uniformly distributed over the three serrations, the nominal stress at the lower serration would be higher than that at the outer serration. The bending reactions associated with steam loading would contribute to further variations in stress level among the three serrations and to a stress gradient along any particular

steeple. Also, the Type II and Type III crack locations are subject to the disc hoop stress which may be significantly different from nominal steeple stresses. Thus, cracking occurred at a large number of locations representative of a range of operating stresses.

There are two possible explanations for this phenomenon. First, cracking at a specific location will result in a change in compliance and redistribution of loading among the serrations. This factor could promote cracking at locations other than that of the highest nominal stress and would influence crack propagation. The occurrence of cracking at various locations could also be related to the threshold stress for SCC in the disc material. If the threshold stress is relatively low, crack initiation would be likely at several different locations. In that event, redistribution of load due to propagation of individual cracks would result in a tendency toward uniform crack propagation at the various locations.

The cracking observed in this case is very similar to that encountered in the LP turbines of at least two other PWR, nuclear steam electric generating stations (6,7). In all three cases, cracking was intergranular in nature and the location and orientation of the cracks was similar.

The earlier of the other two cases (Plant D-1) involved severe caustic carry-over resulting from difficulties encountered in the condensate polisher operation and feedwater chemistry control and is directly attributable to caustic cracking. In the second case (Plant E-1) the water and steam chemistry were maintained well within normal operating limits for the two-year service period. On-site tests, prior to removal of the blades, indicated the presence of caustic within the crevices between the blade roots and the mating steeples. Subsequent analyses also identified significant amounts of sodium in turbine and steam piping deposits. That incident is also attributed to caustic cracking, probably due to progressive accumulation of caustic within the blade groove crevices. The disc material composition was essentially identical for all three plants. All discs exhibited similar microstructures except that the grain size for the Plant A discs was larger than for those in the other two cases. In each case, the discs were heat treated to similar strength specifications [U.T.S. = 135 ksi min. (931 MPa), YS = 120-130 ksi (827-896 MPa)].

In comparison of the three incidents of disc rim cracking, certain differences in circumstances are also apparent. One point is that, in the present case, the incidence of crack initiation is significantly higher than in Plant E-1. In the Plant E-1 incident cracking was confined to the 3R row and occurred in only one

of the two LP turbines. The proportion of steeples affected in that row was also lower than that for either row in the particular disc samples examined in the present case. Another difference is that the extent of crack propagation was noticeably less for the present case than for the two earlier cases. In the Plant D-1 and Plant E-1 incidents, certain Type I cracks propagated through as much as 50-80% of the steeple cross section. These differences may be associated with the particular blade root geometry employed in each case and with variations in operating parameters.

It is of interest to note that the three documented in-service disc cracking incidents occurred in plants employing different water chemistry control methods and represent progressively longer times to failure as follows.

Plant D-1:	Severe caustic contamination. Disc cracking and steeple failure after 6 months' operation.
Plant E-1:	All volatile feedwater treatment, closely controlled feedwater and steam chemistry. Disc cracking after two years' service.
Present Incident: (Plant C-1)	Congruent phosphate feedwater treatment, closely controlled feedwater and steam chemistry. Disc cracking after 4 years' service.

Another variable to consider, however, is that the particular steeple geometry was different in each case. Therefore, the different service histories may also be related to differences in nominal operating stresses.

One contaminant species contributing to intergranular stress corrosion cracking in turbine components is NaOH. Caustic carry-over can result from inadequate condensate polisher capacity, improper operation of the polishers, malfunction of moisture separating reheaters, and from feedwater treatment procedures. Forward flow heater condensate drains can also result in a progressive increase in steam contaminant levels. NiCrMoV low-alloy steels, of a similar strength level to that of the present case, have been shown to be susceptible to caustic cracking (3,8). Such cracking is generally observed to be intergranular. Laboratory test data reported in the literature indicate that caustic cracking of low-alloy rotor steels can occur at stress levels comparable to those encountered in service (3,4,8). Sustained load tests in 28% NaOH have also been performed on specimens from a NiCrMoV LP rotor disc in another program at SwRI. In these tests, cracking occurred within 1000 hrs. at stress levels as low as 30.0 ksi (207 MPa).

No direct evidence of the presence of caustic within the blade grooves was obtained in this metallurgical investigation. The EDS analysis of the corrosion products within the pits and cracks indicated that these deposits were base metal oxides and did not provide evidence of any extraneous contaminant species. In this regard, two particular factors should be noted. First, the corrosion deposit formed during SCC does not necessarily identify the specific chemical species responsible for cracking. Corrosion and cracking in caustic environments usually result in the formation of oxides of the base metal and Na is not likely to be present in the corrosion product. In many cases, the role of specific contaminant species in SGG is that of controlling the surface reactions or shifting the electrochemical potential into a range of cracking susceptibility, and the contaminant itself is not directly involved in the formation of the corrosion product. A second point is that the particular rim segments provided for this investigation had been thoroughly cleaned so that no surface deposits were available for analysis. In the consideration of any cracking incident, the absence of direct evidence of a contaminant species within cracks or pits does not preclude the possibility of contaminant-induced stress corrosion cracking.

The unit in which the present disc cracking incident occurred employs U-tube steam generators with blow-down capability. Congruent phosphate water treatment was employed over the entire service period for the particular LP rotors involved. In this type of system, the possible sources of steam contamination are vaporous carryover and mechanical carryover from the steam generators. Vaporous carryover can be significant in drum type fossil-fuel boilers operating at 2600 psi (17.9 MPa) or higher, but diminishes to very low levels at typical PWR system operating pressures (9,10). Mechanical carryover is dependent on the efficiency of the moisture separators and dryers incorporated within the steam generators. In this particular case, it was reported that typical mechanical carryover during steady-load operation was approximately 0.5%. Thus, limited amounts of impurities have been introduced into the steam piping and turbine system, but, since the congruent phosphate is specifically designed to prevent caustic formation, it is unlikely that direct caustic contamination of the steam system occurred. The unit does not employ condensate polishers and the cooling water is very low in dissolved solids. Therefore, the potential for contamination of the condensate is very low. Over the service period in question, the water and steam chemistry was maintained well within accepted limits.

It was reported that the turbine was very clean when opened at the outage during which the cracking was discovered, and that it was difficult to obtain any deposit samples for analysis. Analysis of one small deposit from the LP crossover piping by the turbine manufacturer indicated that carbonates were possibly present, (11), but this result is not definite evidence of caustic contamination.

In view of the particular observations made in this investigation and considering the factors discussed above, it is evident that the cracking developed by in-service intergranular stress corrosion cracking. The metallurgical character of the cracking is consistent with caustic cracking in low-alloy steels and comparable to that involved in two other similar incidents where caustic cracking was identified. No direct evidence of caustic contamination of the blade attachment region was obtained; similarly, there is no evidence to indicate the presence of any other crack inducing contaminant species. Thus, the specific type of stress corrosion cracking and the root cause of the cracking could not be positively identified.

In this regard, it should be noted that this is the second documented case of severe disc rim cracking in LP turbines where the water and steam chemistry were maintained well within accepted operating limits. This factor indicates the possibility of progressive accumulation of caustic (or other contaminant species) within crevices in LP turbines over extended periods of operation in steam with only minimal contaminant levels. It should also be noted that there is evidence in the literature that CrMo and NiCrMoV steels are subject to stress corrosion cracking in pure steam or pure water environments (12,13). Therefore, it must be recognized that the possibility exists that concentration of a contaminant species may not be a necessary condition for disc rim cracking, i.e., that NiCrMoV steels may be susceptible to intergranular SCC in high purity water.

It is generally recognized that the SCC susceptibility of low-alloy steels decreases with decreasing yield strength. An extensive inspection of dismantled LP rotors in Great Britain followed the Hinkley Point A disc failure (5). The distribution of keyway and bore cracking detected in 473 discs representing three alloy compositions is summarized as follows.

Alloy	0.2% YS ksi (MPa)	UTS ksi (MPa)	No. Examined	% Cracked
3-1/2 NiCrMo	88-104 (605-716)	107-130 (736-899)	144	48
3 CrMo	95-101 (653-694)	117-131 (804-905)	261	33
3-1/2 Ni	75-76 (519-524)	90-105 (685-722)	68	0

In this group cracking occurred in a high percentage of the higher strength discs but no cracking had developed in the discs with a yield strength below 80 ksi (551 MPa). Results of bent beam tests on 3 CrMo material in pure steam also

indicate a dependence of cracking susceptibility on strength level (13). In one series of tests, involving specimens heat treated to six different ultimate strengths in the range of 98 to 188 ksi (676-1296 MPa), cracking occurred within 7000 hours for all specimens with ultimate strengths greater than 130 ksi (896 MPa). No cracking developed in specimens with ultimate strengths of 130 ksi (896 MPa) and below. These data from service cases and laboratory tests suggest that there may be a critical yield strength level for SCC susceptibility of rotor disc materials.

The present understanding of the LP turbine disc cracking encountered in various plants does not provide a basis for establishing specific preventative measures. Further information and data concerning actual operating environments and the cracking susceptibility of disc materials is necessary. Several current EPRI programs are directed toward these objectives. At the present time, only two courses of action for minimizing the chances of disc rim cracking can be proposed; namely, the utilization of disc materials with lower yield strengths and initiation of any appropriate action to reduce contaminant levels in the steam to lower levels.

In view of data from case histories and limited laboratory tests, there is some basis for the employment of lower strength materials in new or replacement rotor discs. The available data is not sufficient to conclude that such action would definitely prevent cracking, but the indications are that utilization of lower strength material would decrease the likelihood of in-service SCC in LP turbine rotors. The employment of lower strength rotor discs is, of course, subject to the design limitations of particular machines.

The particular steps that can be taken to improve steam chemistry are dependent on individual plant design features and operating practice. A thorough review of these factors by plant personnel is the only means of identifying possible modification. Some plant designs employ forward flow heater condensate drains with the result that this condensate bypasses the condensate polishers. In such cases, modification of the piping system to direct these drains upstream of the polishers can eliminate one possible source of contaminant concentration.

In considering systems and procedure modifications directed toward improved steam chemistry, it is important to recognize that turbine component cracking problems may not be resolved solely by reductions in water/steam impurity levels. The results of surveys of fossil-fueled and nuclear unit operating experience do not support the assumption that consistent operation with higher purity steam would eliminate in-service cracking (10). Significant stress corrosion failures have been reported for turbines with high purity water systems (once through boilers or steam generators with full-flow condensate polishers). Also, among

the plants surveyed, a higher percentage of turbine component failures occurred in once-through boilers with condensate polishing than in drum type systems with low phosphate water treatment. Data from these surveys suggest that infrequent upsets in steam/water chemistry, rather than the absolute steam purity during steady-load operation, may be a major factor in SCC of turbine components.

REFERENCES

1. A. H. Ucisik, C. J. McMahon, and H. C. Feng, "The Influence of Intercritical Heat Treatment on the Temper Embrittlement Susceptibility of P-Doped Ni-Cr Steel," Met. Trans. Vol. 9A, March 1978, p. 321.

2. Corrosion and Corrosion Cracking of Materials for Water Cooled Reactors. Electric Power Research Institute, FCC7703. EPRI Project RP 311-1, Progress Report, July-Dec. 1977.

3. R. M. Curran and B. R. Seguin, et al, "Stress Corrosion Cracking of Steam Turbine Materials," Southeastern Electric Exchange, Clearwater, Florida, April 1969.

4. J. E. Truman, "Problems of Stress Corrosion Cracking of Steel in Customer Usage," Stress Corrosion Cracking and Hydrogen Embrittlement of Iron-Base Alloys. (Proceedings of the International Conference on Stress Corrosion Cracking and Hydrogen Embrittlement, 1973) p. 111, NACE, Houston, Texas, 1977.

5. J. M. Hodge and I. L. Mogford, "UK Experience of Stress Corrosion Cracking in Steam Turbine Discs." Proc. Instn. Mech. Engrs., Vol. 193, 1979, p. 93.

6. A Metallurgical Investigation of In-service Cracking in a LP Turbine Disk, Final Report, Project No. 02-4453-004, Southwest Research Institute, Sept. 1978.

7. Metallurgical Evaluation of LP Turbine Disc Cracking," Final Report, Project No. 02-4448-003, Southwest Research Institute, June 1978.

8. T. G. McCord, B. W. Bussert, R. M. Curran and G. C. Gould, "Stress Corrosion Cracking of Steam Turbine Materials," Materials Performance, Vol. 15, Feb. 1976.

9. B. W. Bussert, R. M. Curran and G. C. Gould, "The Effect of Water Chemistry on the Reliability of Modern Large Steam Turbines." ASME Paper No. 78-JPGC-Pwr-9. (Presented at the Joint Power Generation Conference, Dallas, Texas, Sept. 1978.)

10. F. Gabrielli and H. A. Grabowski, "Steam Purity at High Pressure-System Considerations." Paper presented at the ASME-IEEE-ASCE Joint Power Generation Conference, Charlotte, N.C., Oct. 1979.

11. Minutes of the EPRI Corrosion Advisory Committee Workshop on Steam Purity for Turbine Protection, May, 1979. P. Goldstein and T. Passell, co-chairmen.

12. F. P. Ford: Private Communication (1978) (Unpublished CERL and CEGB data).

13. B. W. Roberts and P. Greenfield, "Stress Corrosion of Steam Turbine Disc and Rotor Steels." Corrosion, Vol. 35, Sept. 1979, p. 402.

APPENDIX A

MAGNETIC PARTICLE INSPECTION DATA

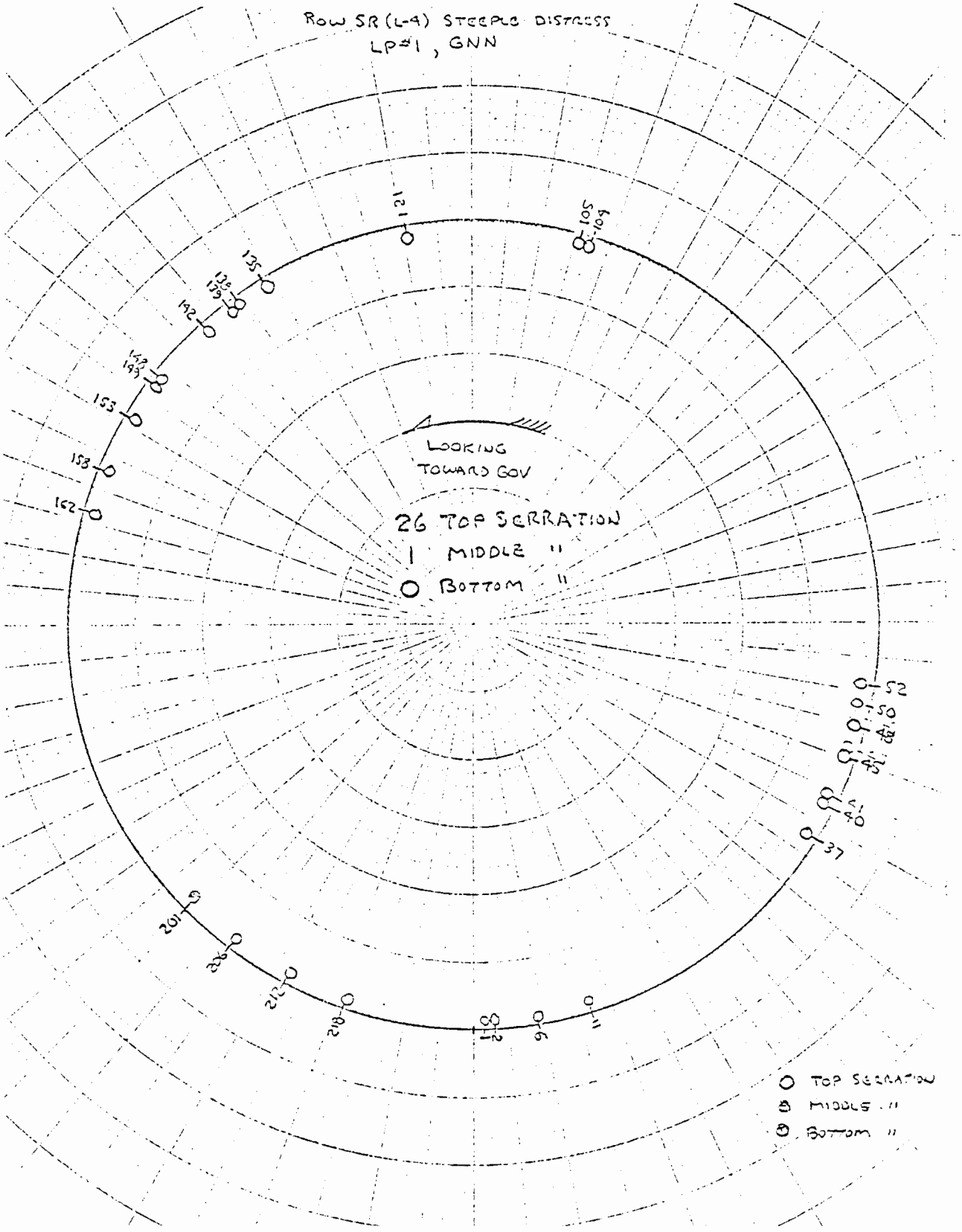

FIGURE A-1, LP-1, ROW 5R (L-4), GEN. END.

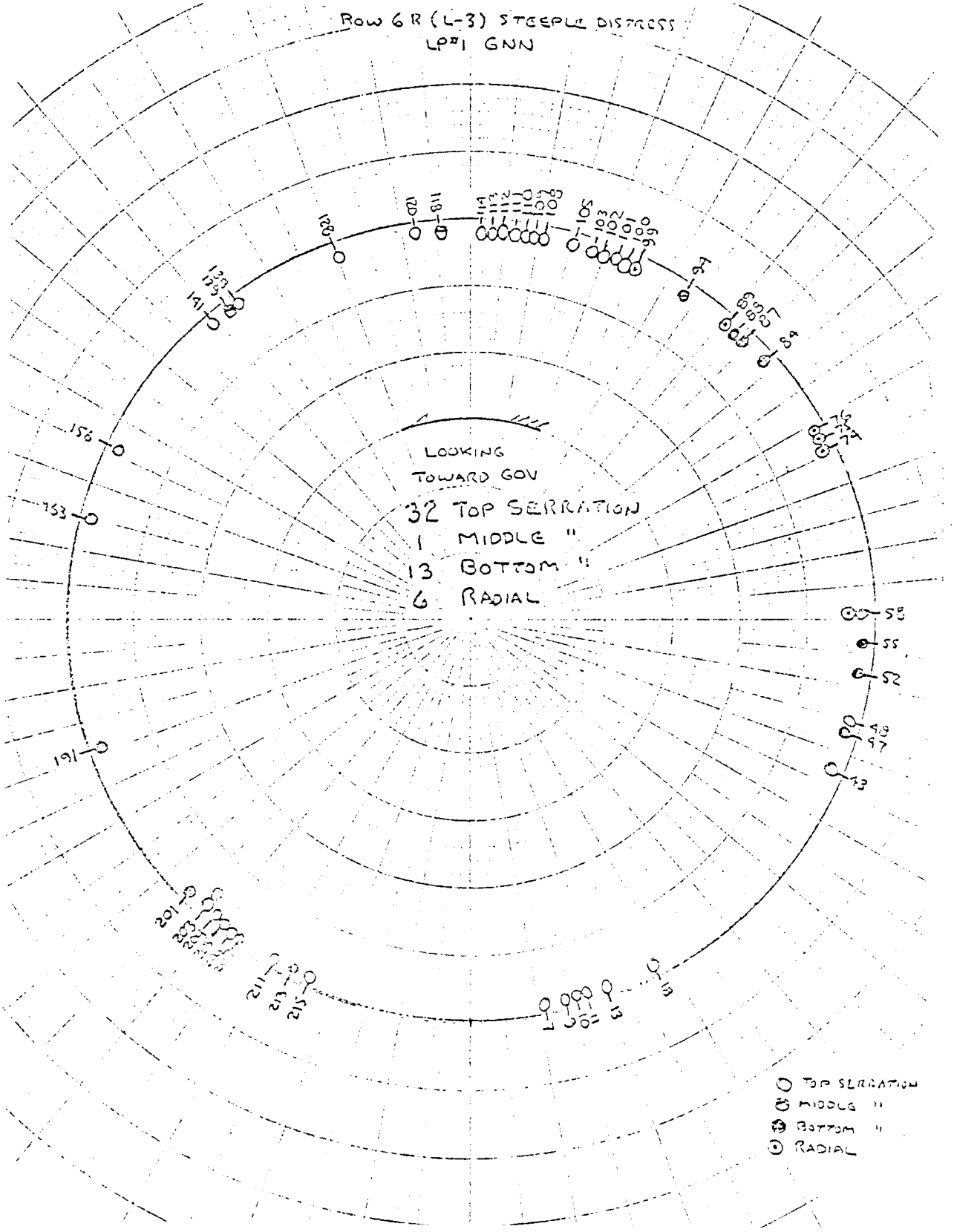

FIGURE A-2, LP-1, ROW 6R (L-3), GEN. END.

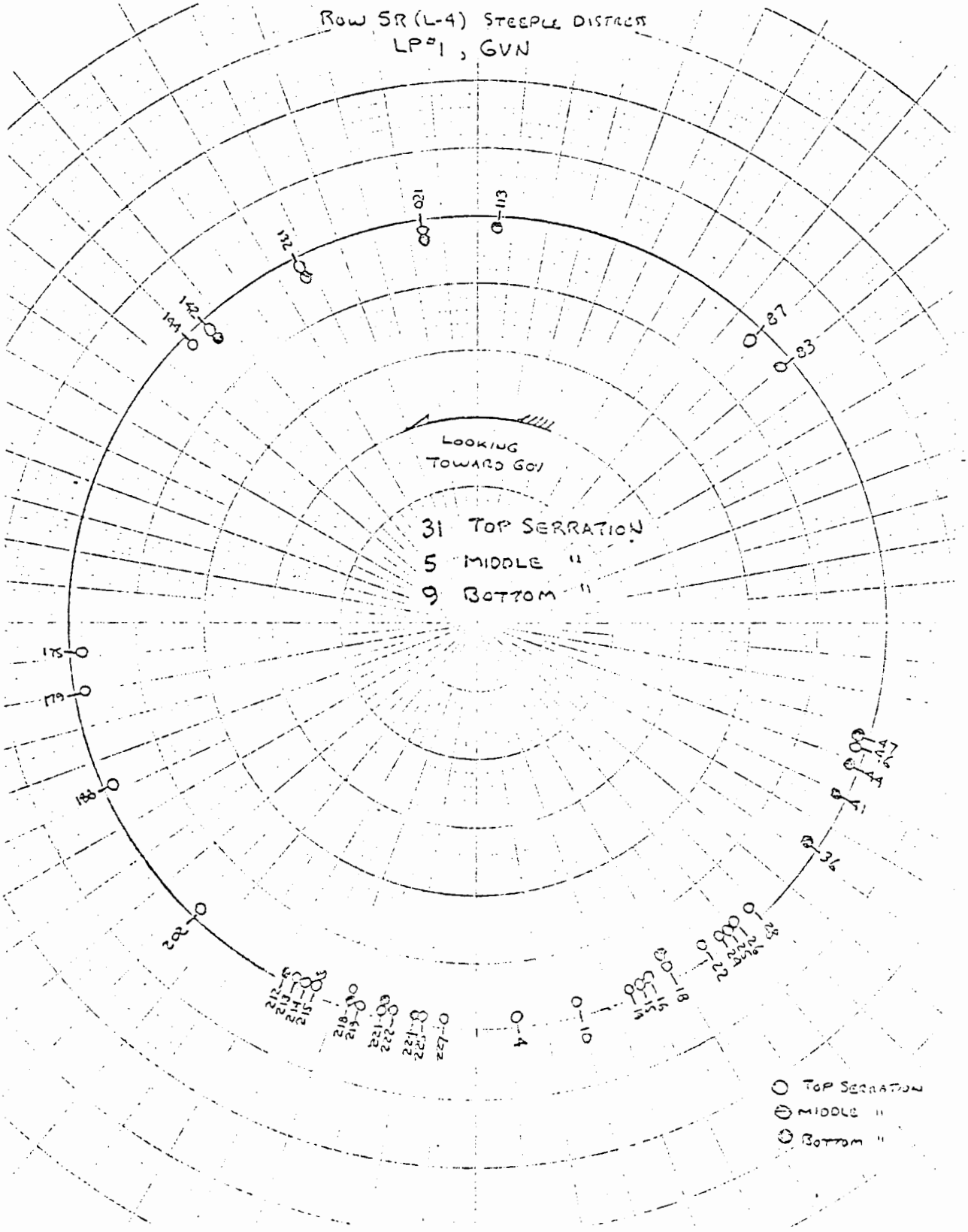

FIGURE A-3, LP-1, ROW 5R (L-4), GOV. END.

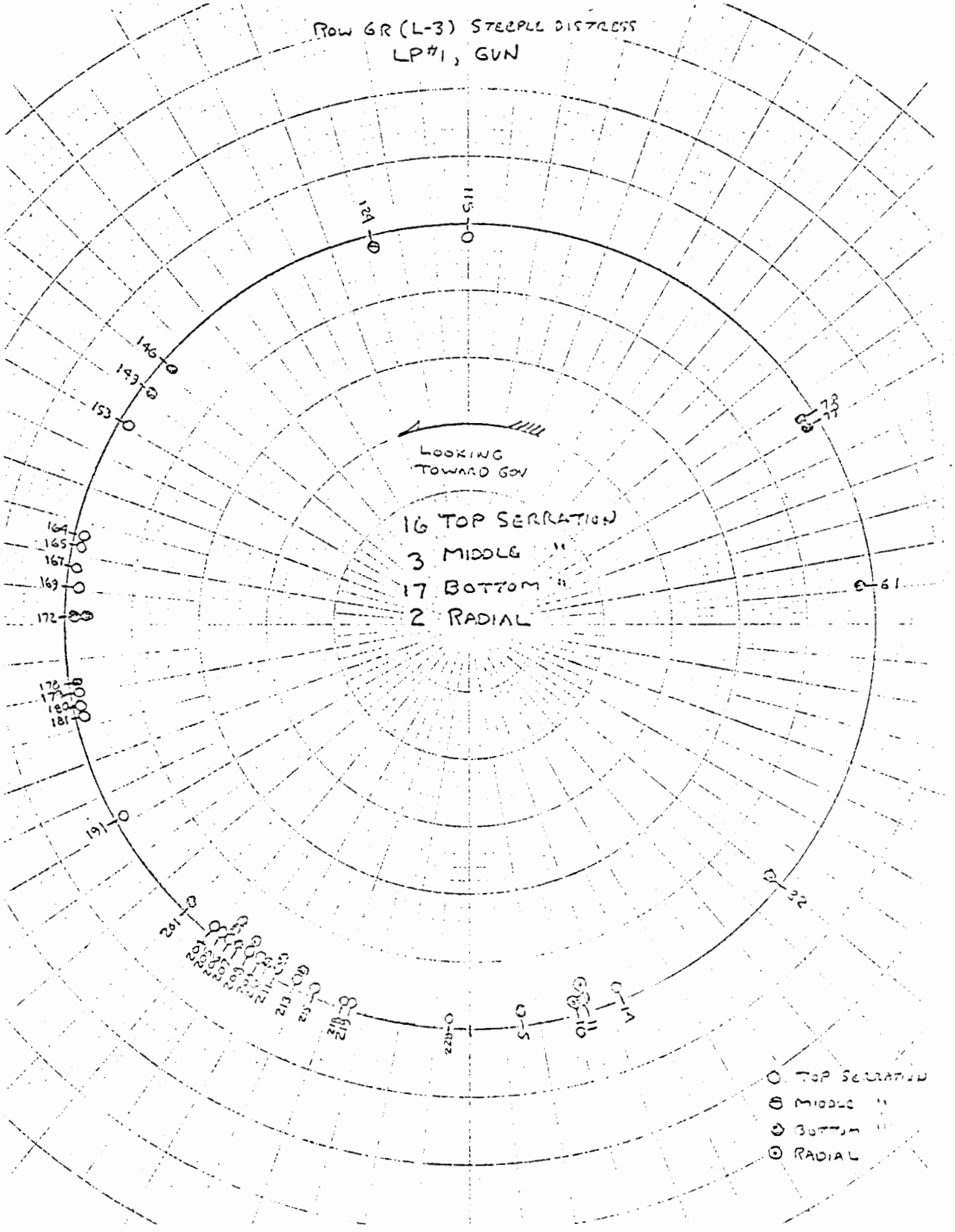

FIGURE A-4, LP-1, ROW 6R (L-3), GOV. END.

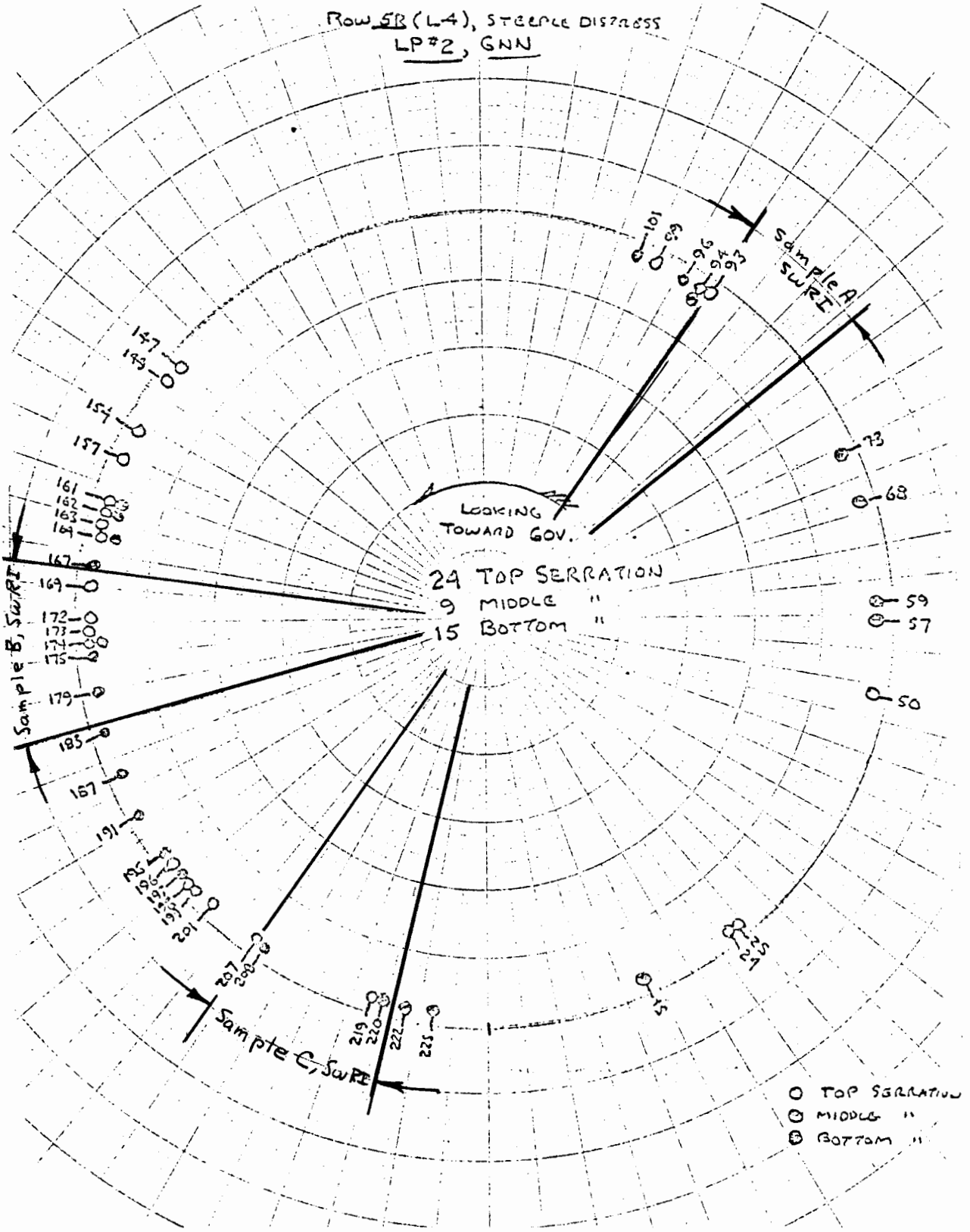

FIGURE A-5, LP-2, ROW 5R (L-4), GEN. END.

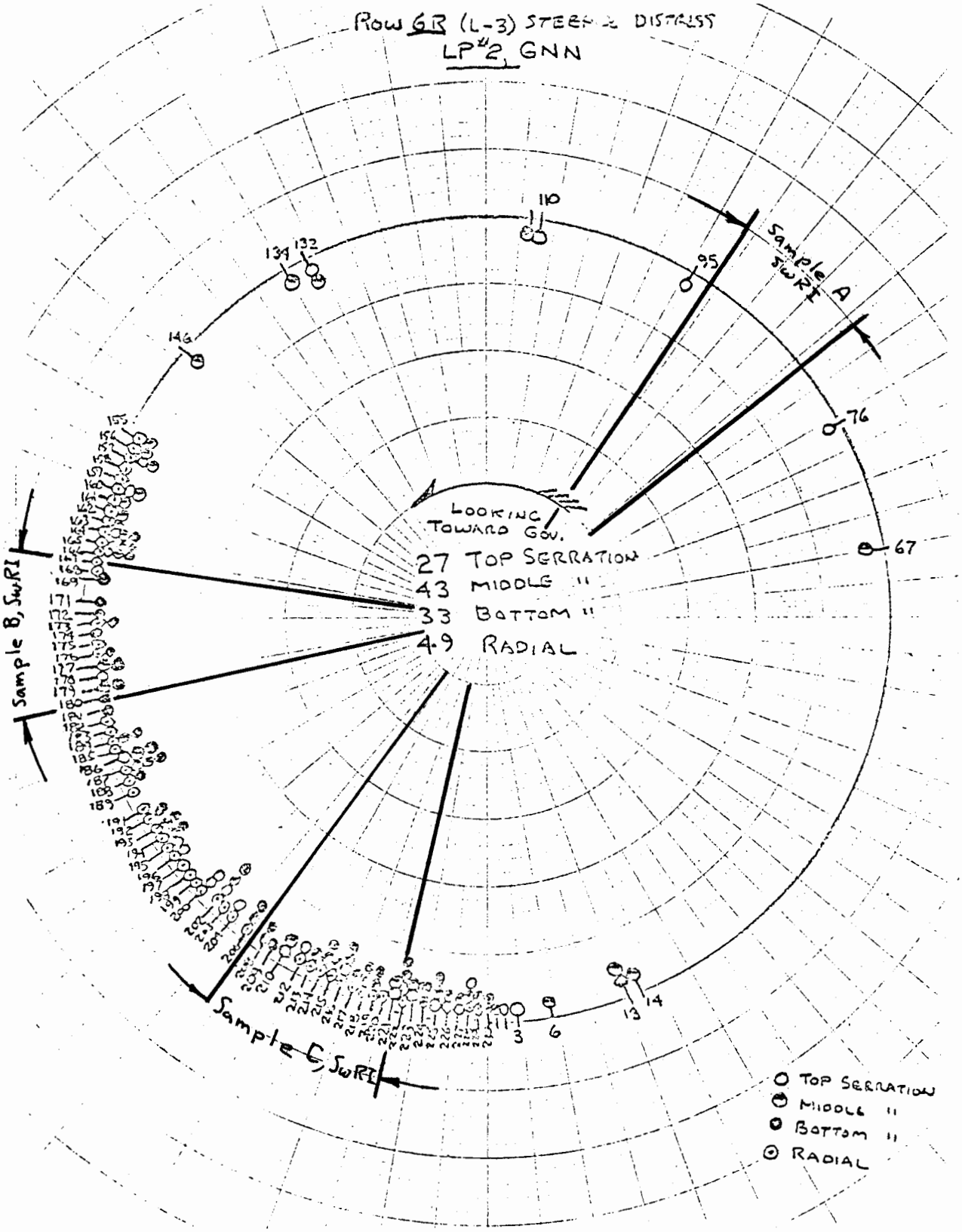

FIGURE A-6, LP-2, ROW 6R (L-3), GEN. END.

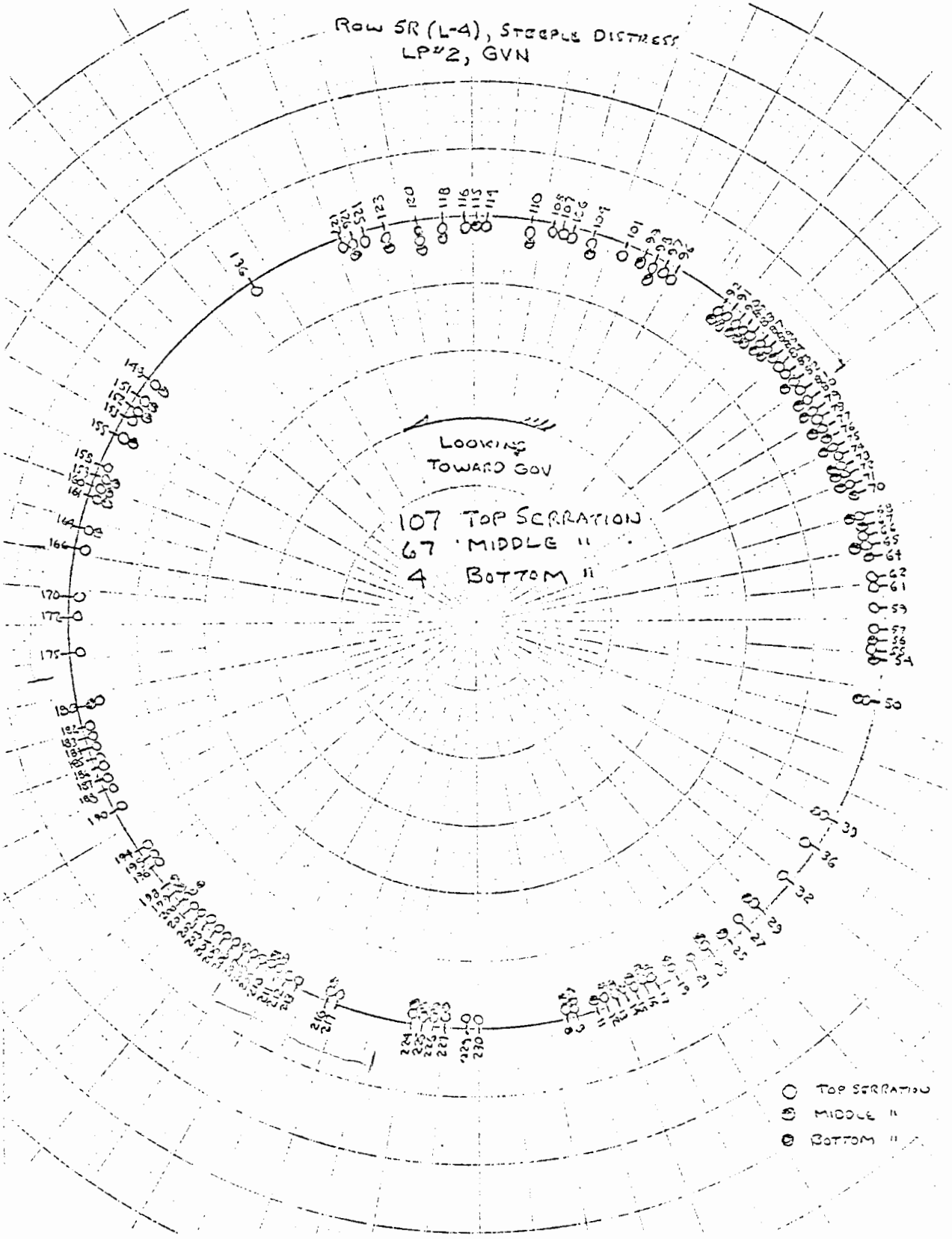

FIGURE A-7, LP-2, ROW 5R (L-4), GOV. END.

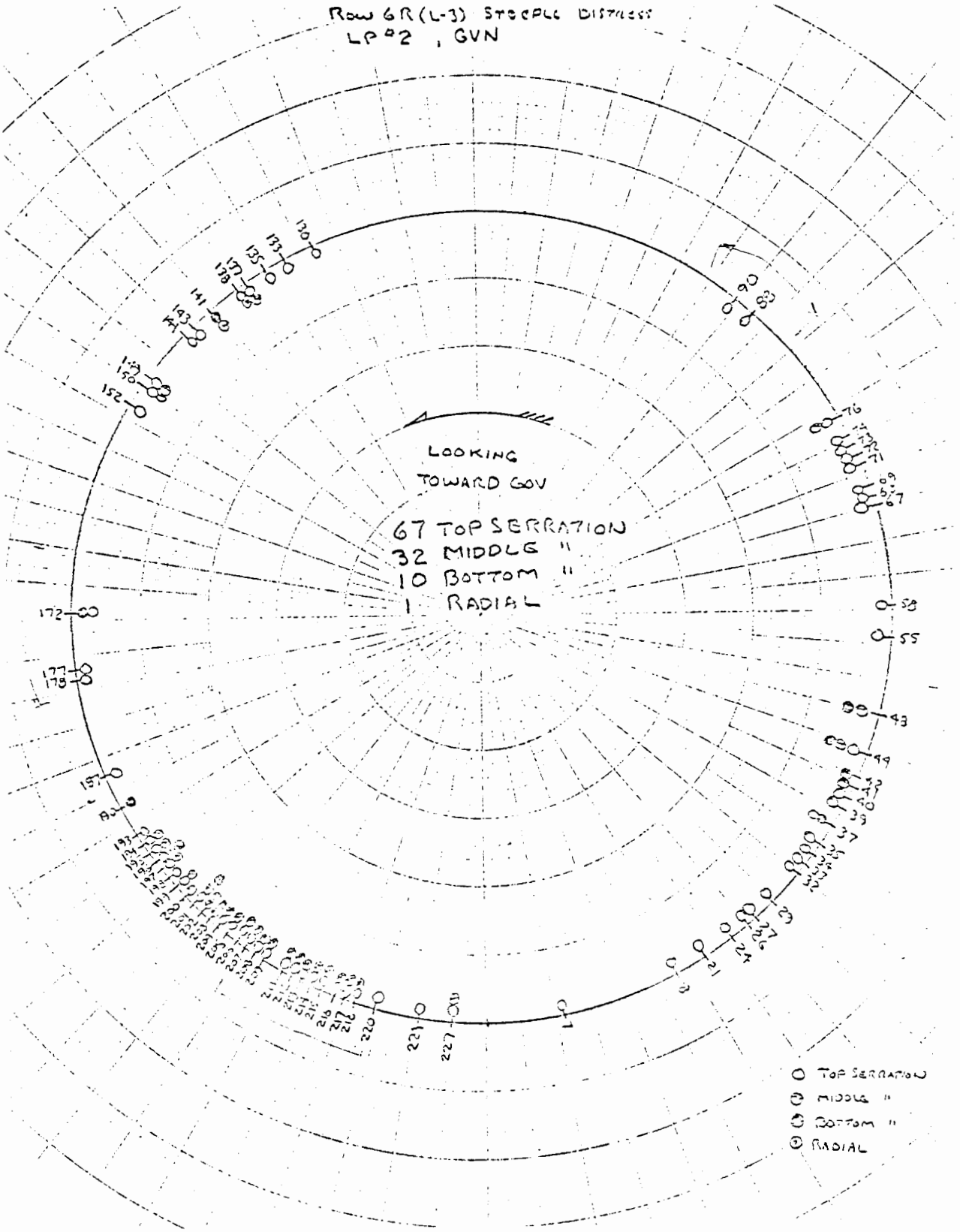

FIGURE A-8, LP-2, ROW 6R (L-3), GOV. END.

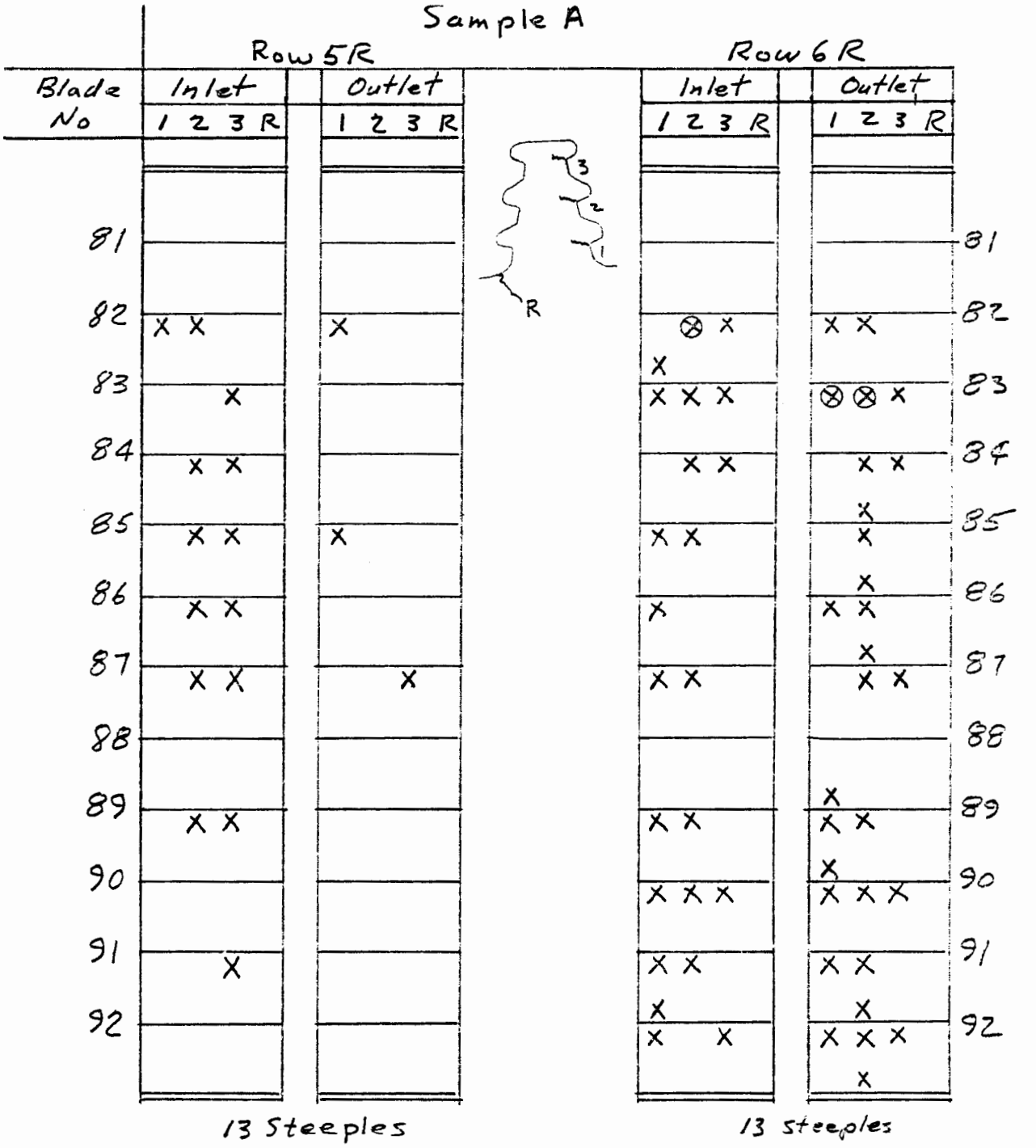
Sample A
Row 5R
Row 6R
Blade No
Inlet
Outlet
1 2 3 R
81
82
83
84
85
86
87
88
89
90
91
92
3
2
1
R
13 Steeples
13 steeples
X - crack in serration
⊗ - crack on face of steeple

Sample B

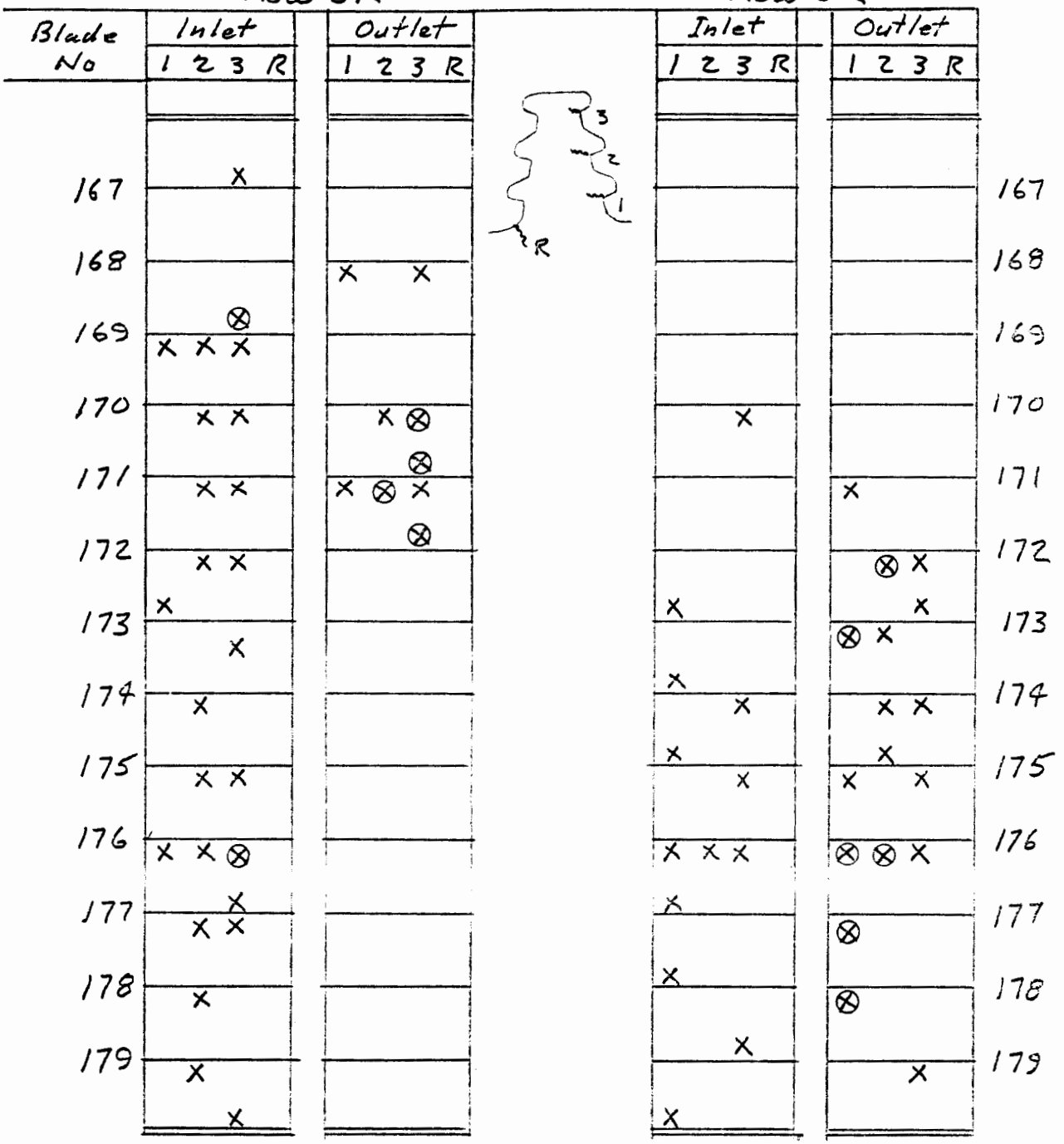

19 steeples

× - crack in serration

⊗ - crack on face of steeple

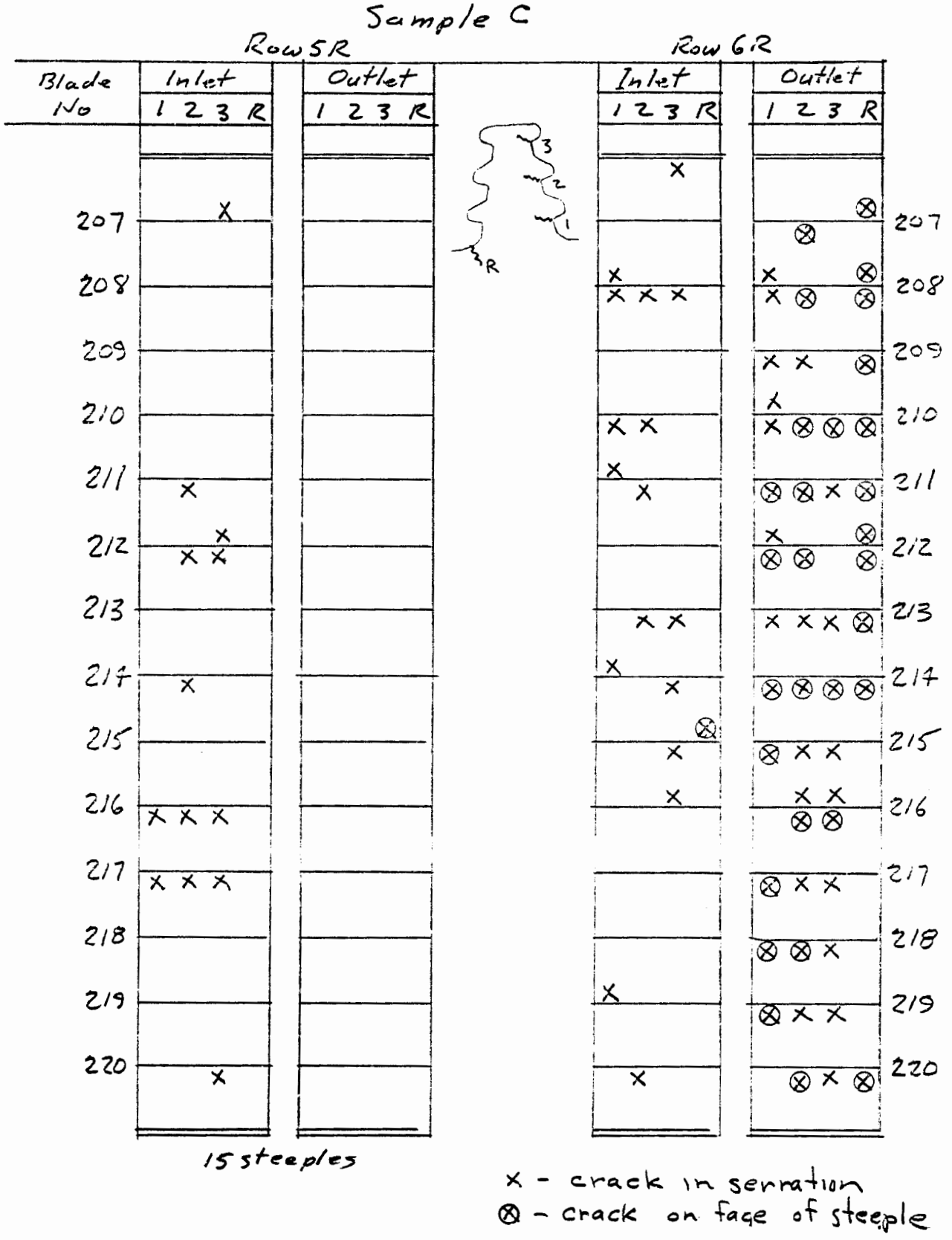
Sample C
Row 5R
Row 6R
Blade No
Inlet
Outlet
1 2 3 R
207
208
209
210
211
212
213
214
215
216
217
218
219
220
3
2
1
R
15 steeples
× - crack in serration
⊗ - crack on face of steeple

APPENDIX B

CRACK DESIGNATION AND NOMENCLATURE

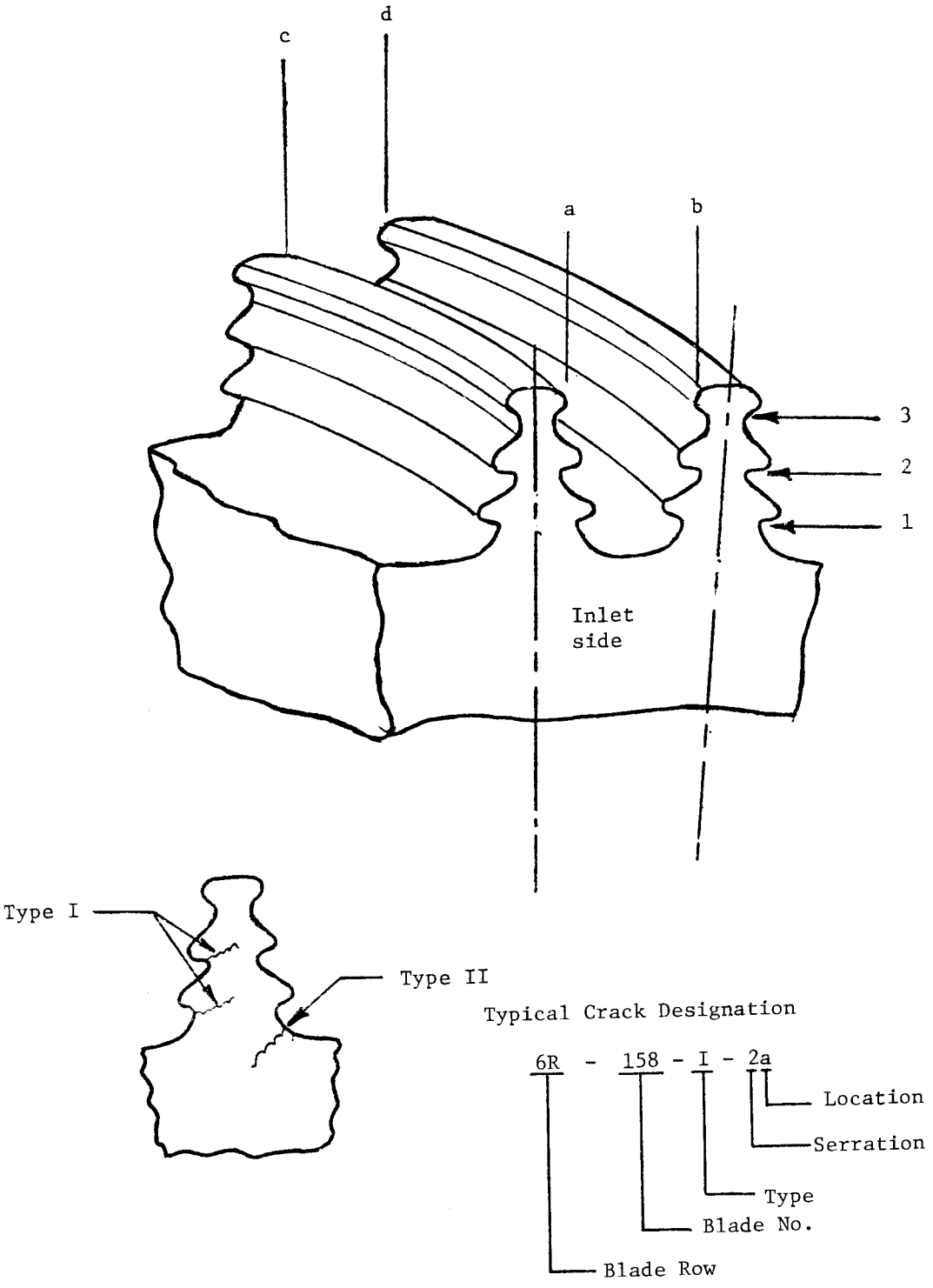

FIGURE B-1. CRACK IDENTIFICATION SYSTEM.

APPENDIX C

CRACK LOCATIONS

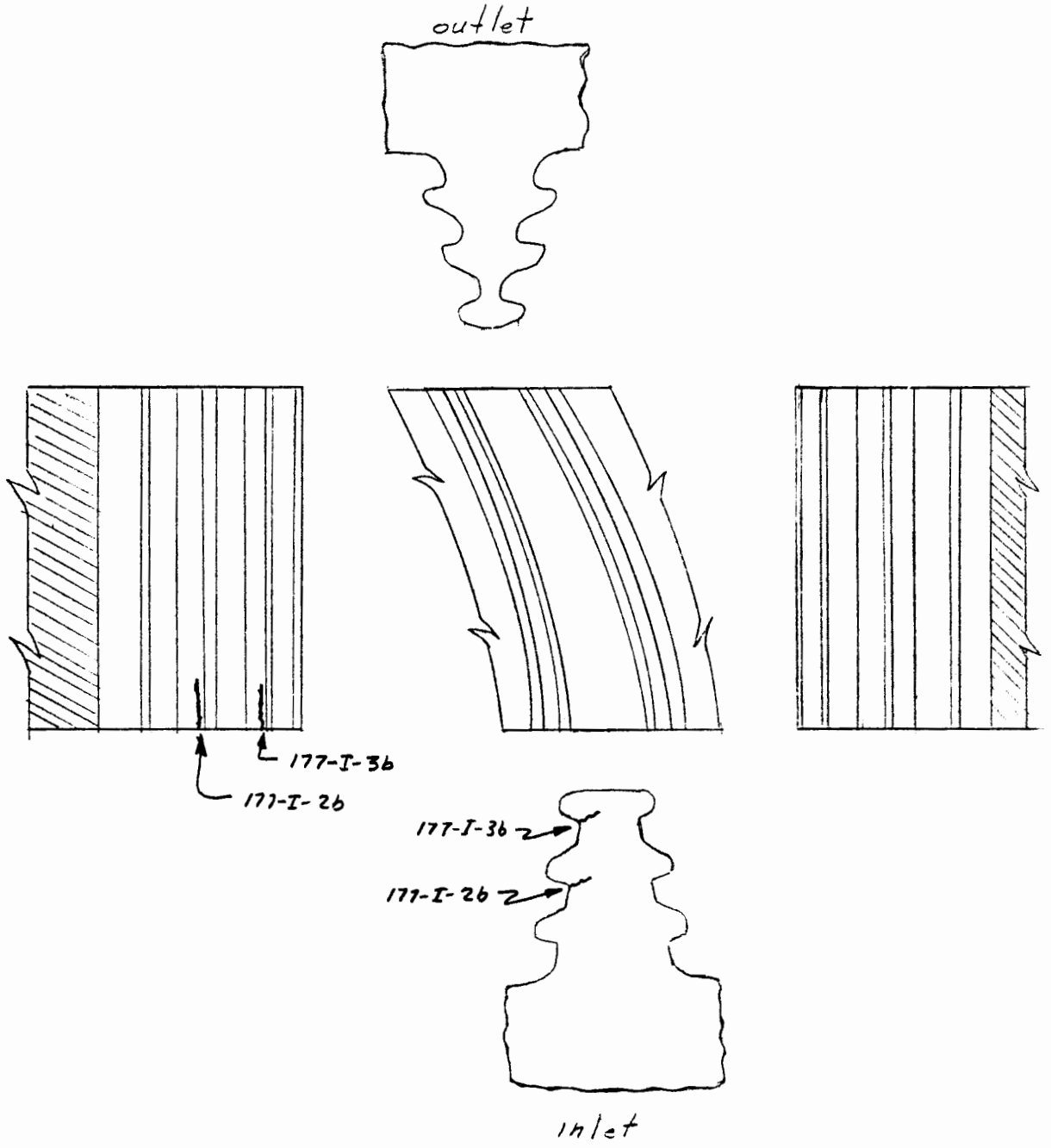

Steeple No. 5R-177/178

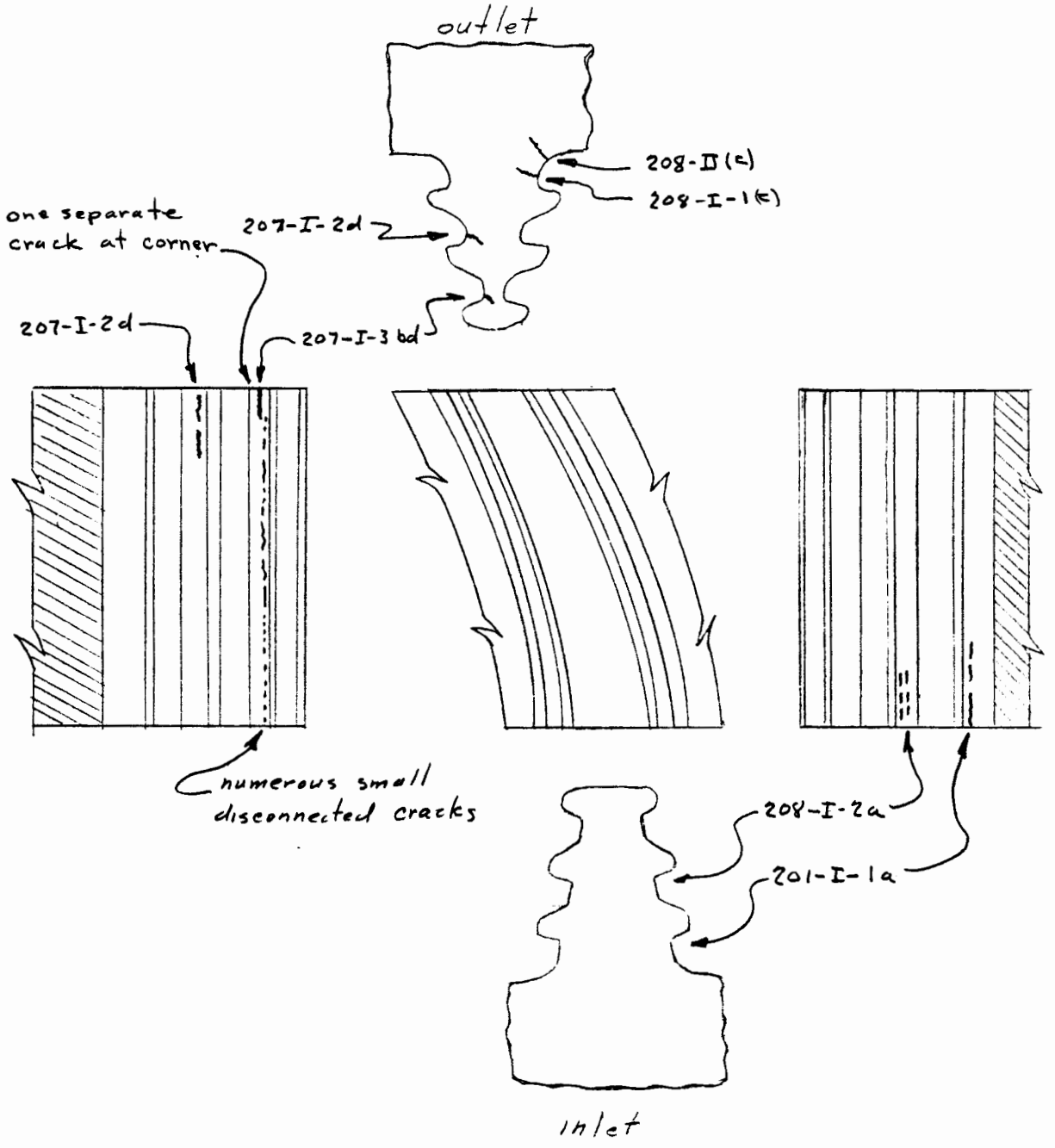

Steeple No 6R-207/208

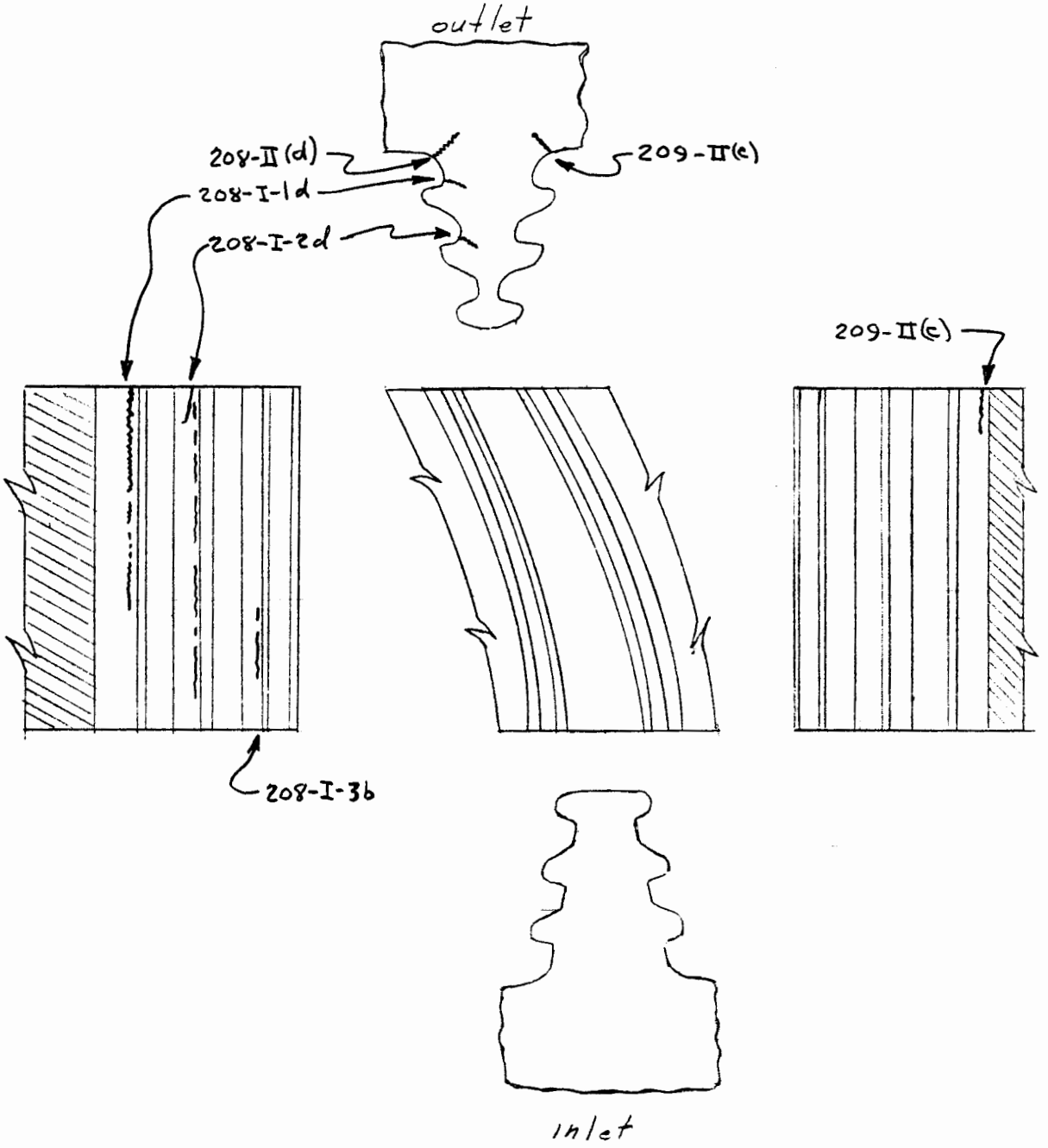

Steeple No. 6R- 208/209

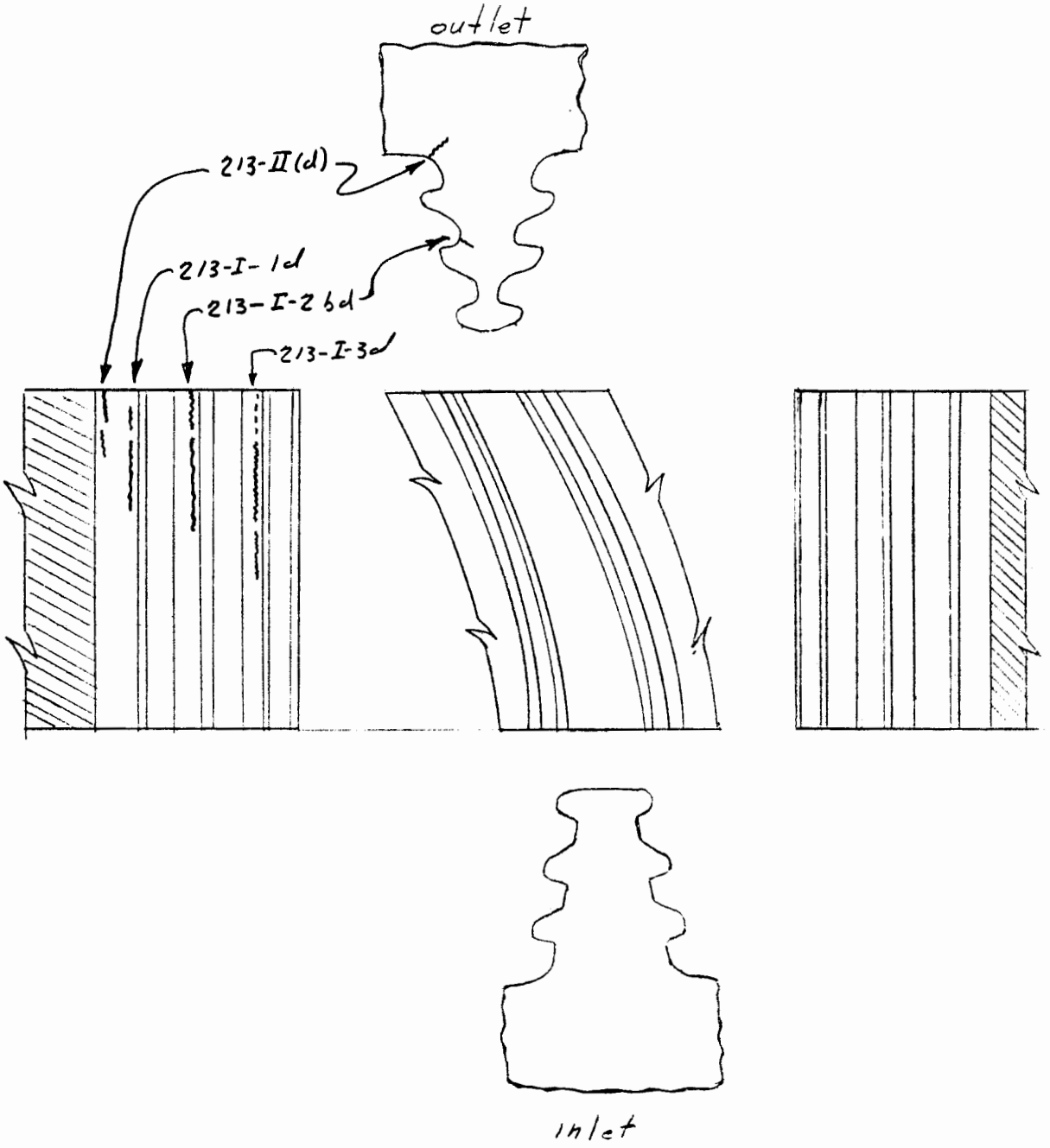

Steeple No 6R-213/214

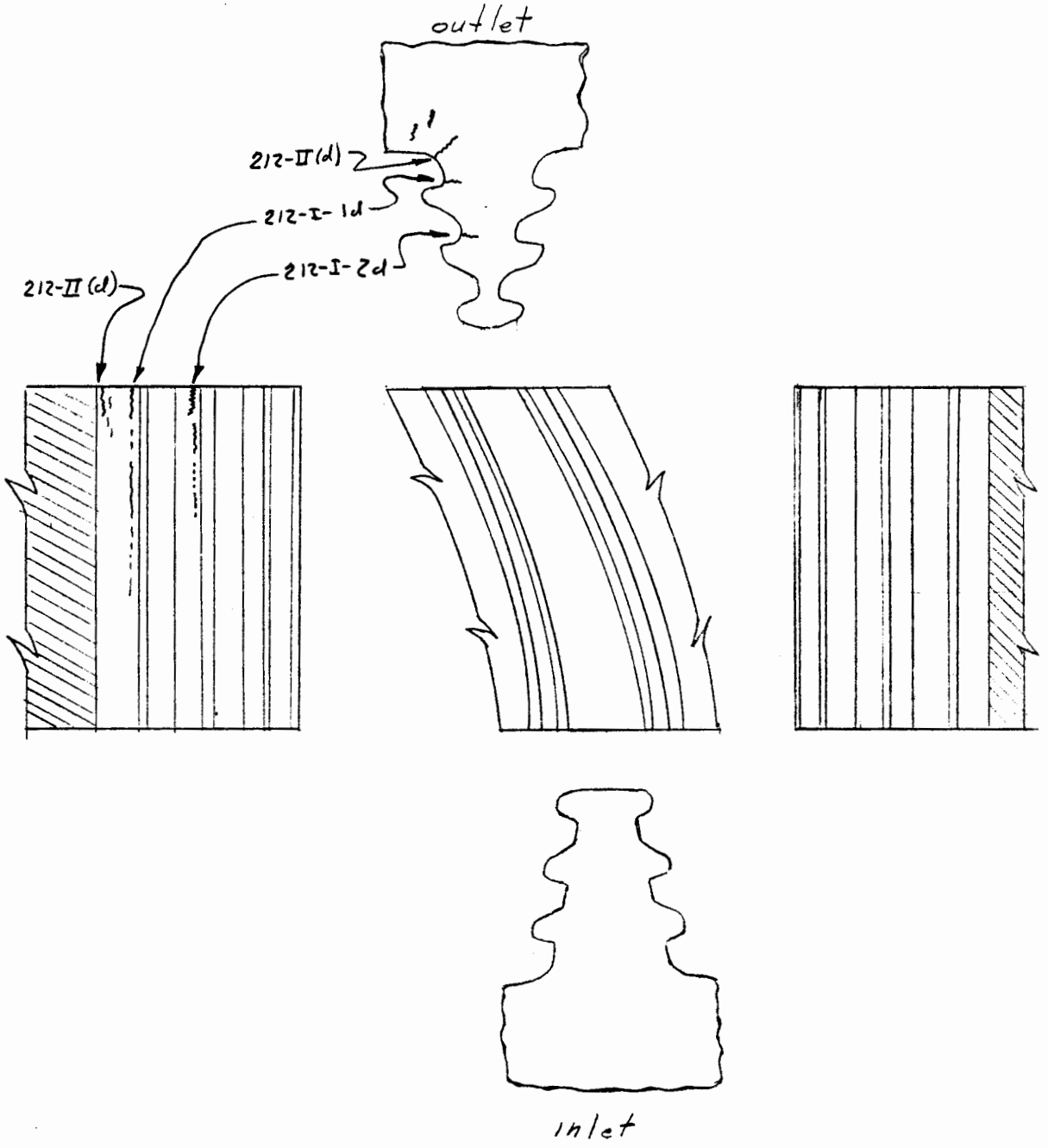

Steeple No. GR-212/213

APPENDIX D

SELECTED MICROGRAPHS

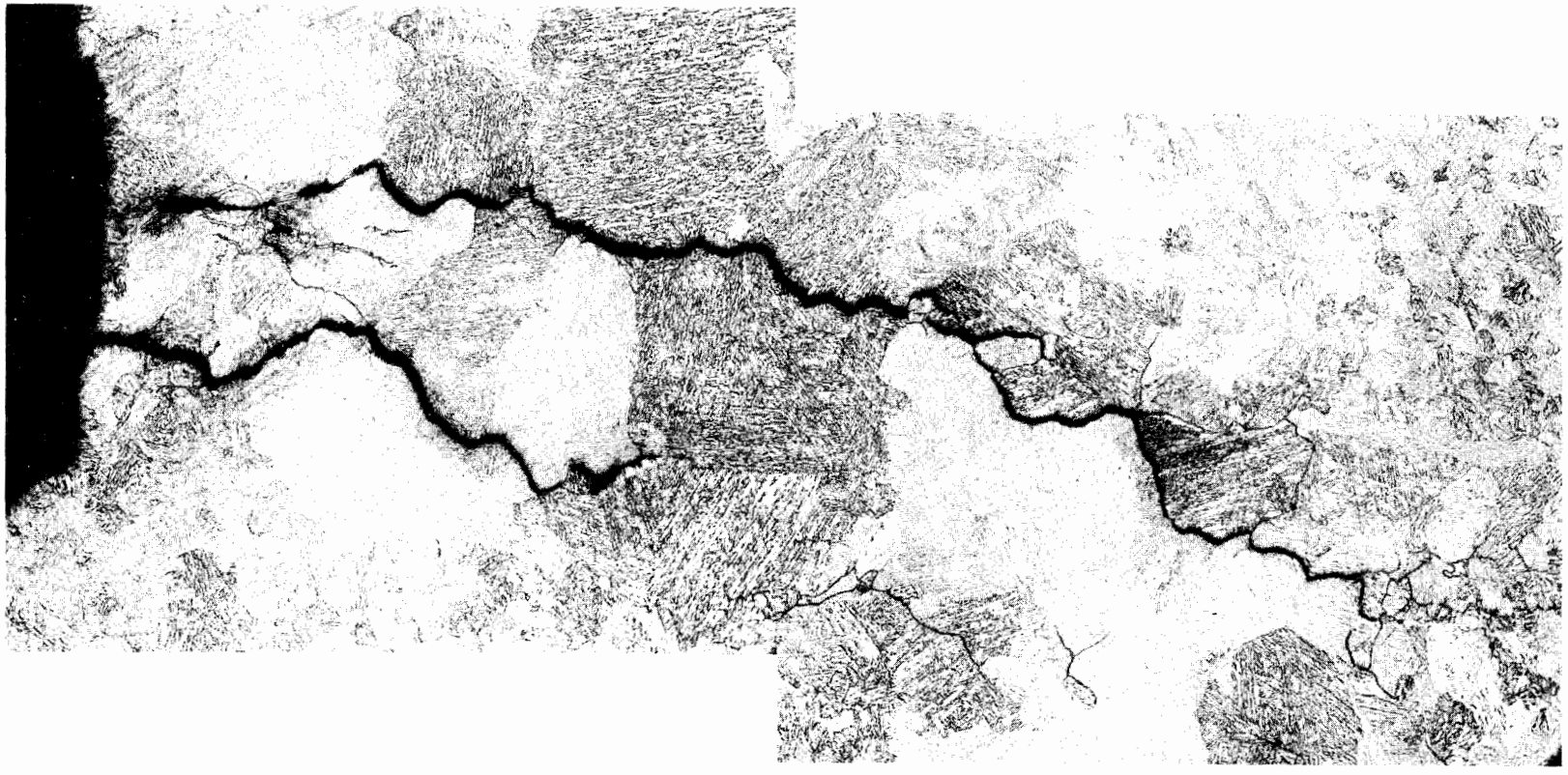

FIGURE D-1. CRACK 176-I-3b, ROW 5R. Section at inlet face. See Figures 4-2 and 4-4(b). Etchant: Nital. 150X

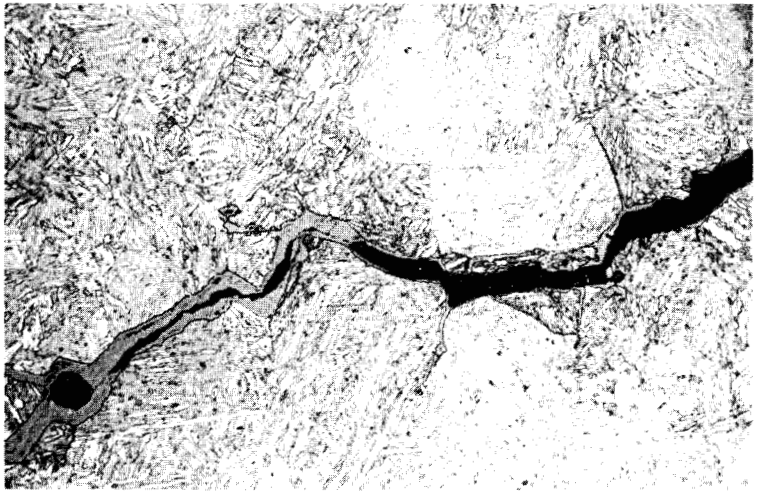

Central portion

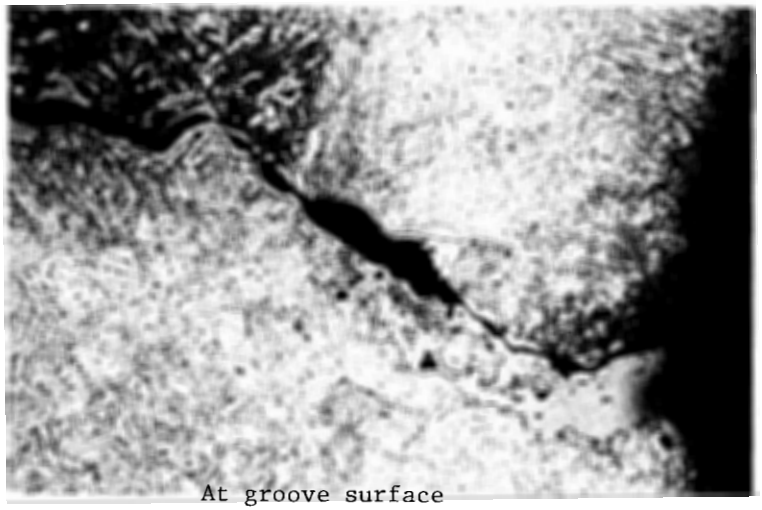

At groove surface

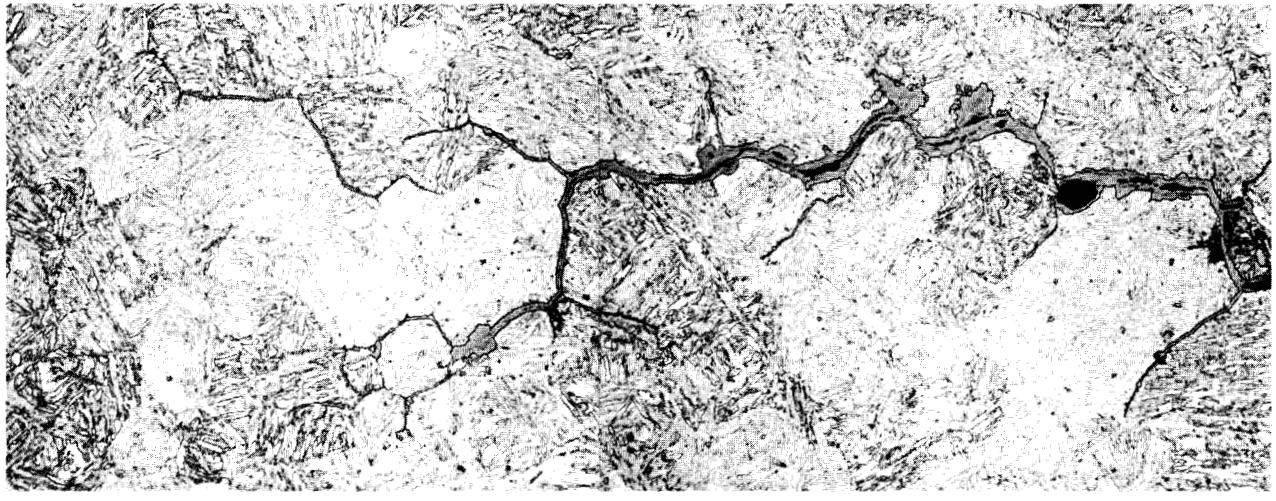

Crack tip

FIGURE D-2. SEGMENTS OF CRACK 210-I-2d, ROW 6R. Section at outlet face. See Figures 4-3 and 4-5. Etchant: Nital. 300X

(These photographs reduced to 90% of their original size)

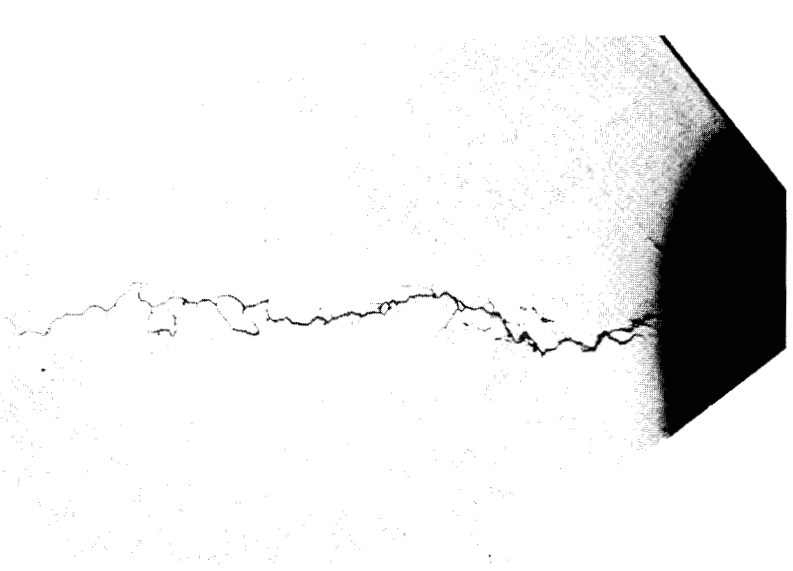

50X

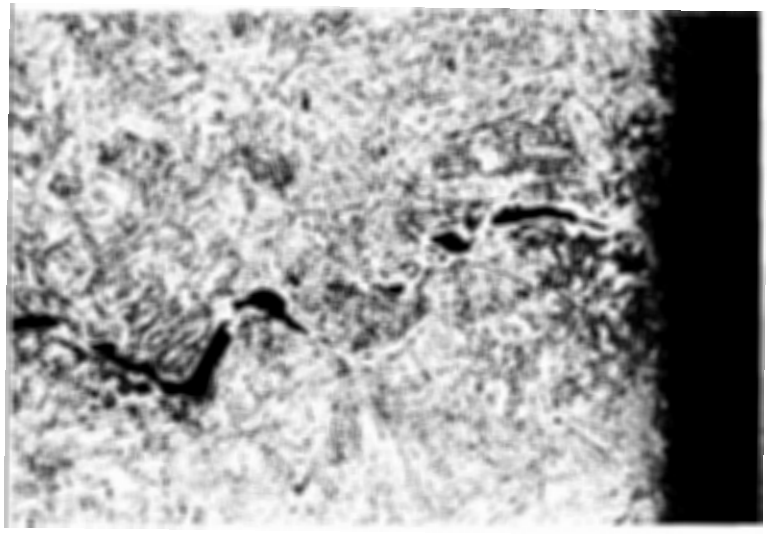

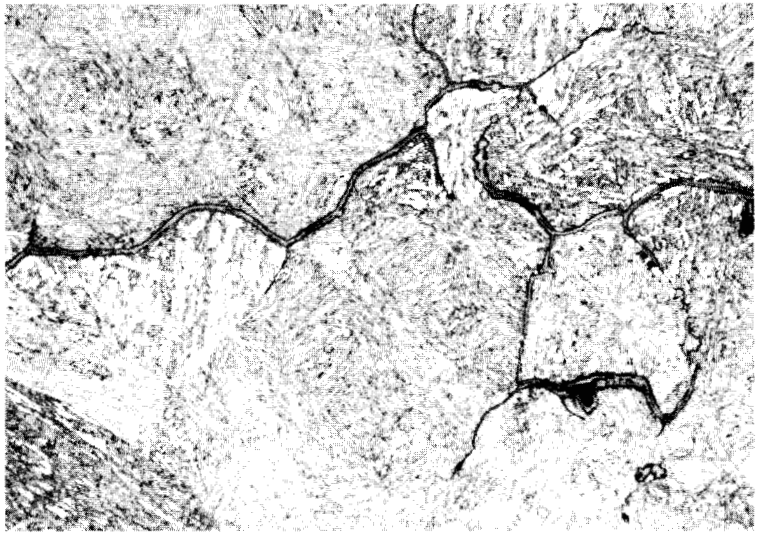

FIGURE D-3. CRACK 210-I-3d, ROW 6R. Section at outlet face. See Figure 4-3. Etchant: Nital.

(These photographs reduced to 90% of their original size)

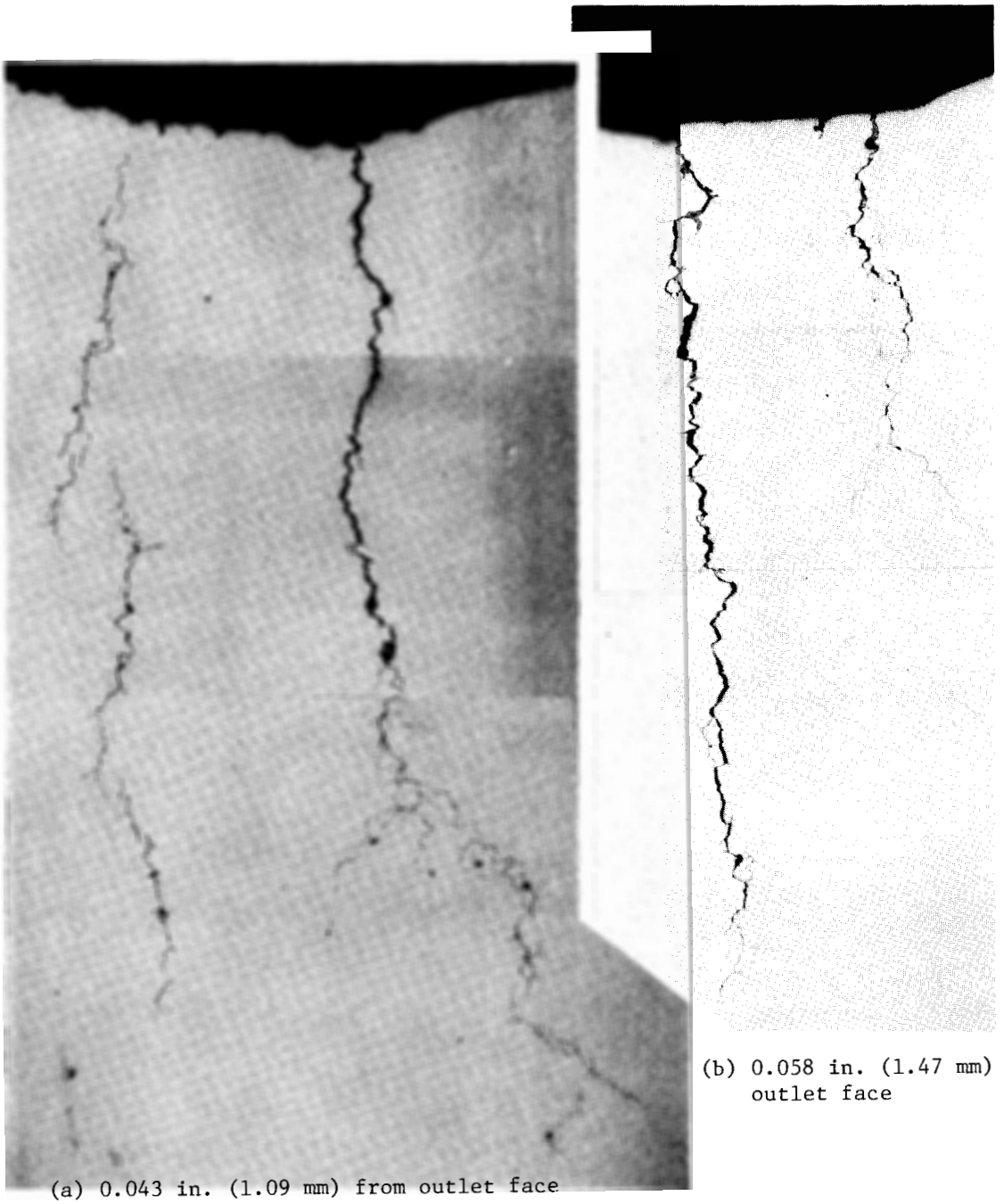

(a) 0.043 in. (1.09 mm) from outlet face

(b) 0.058 in. (1.47 mm) outlet face

FIGURE D-4. SEQUENTIAL SECTIONS THROUGH CRACK 210-II(d), 6R ROW. See Figure 4-9. Unetched. 50X

(These photographs reduced to 90% of their original size)

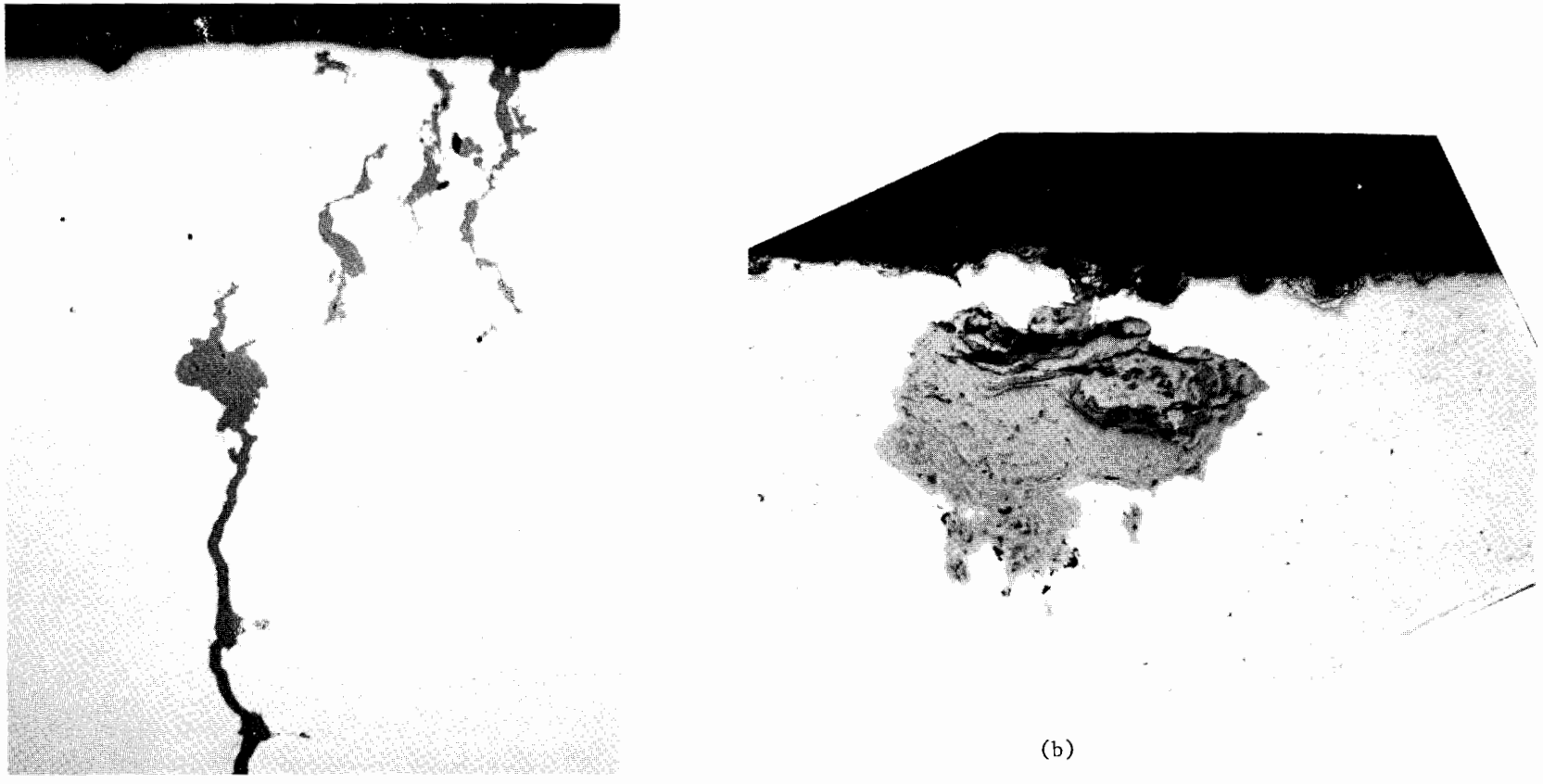

(a) (b)

FIGURE D-5. CRACK 211-II(r) AND ADJACENT PIT. Section at outlet face, See Figure 4-11. Unetched. 300X

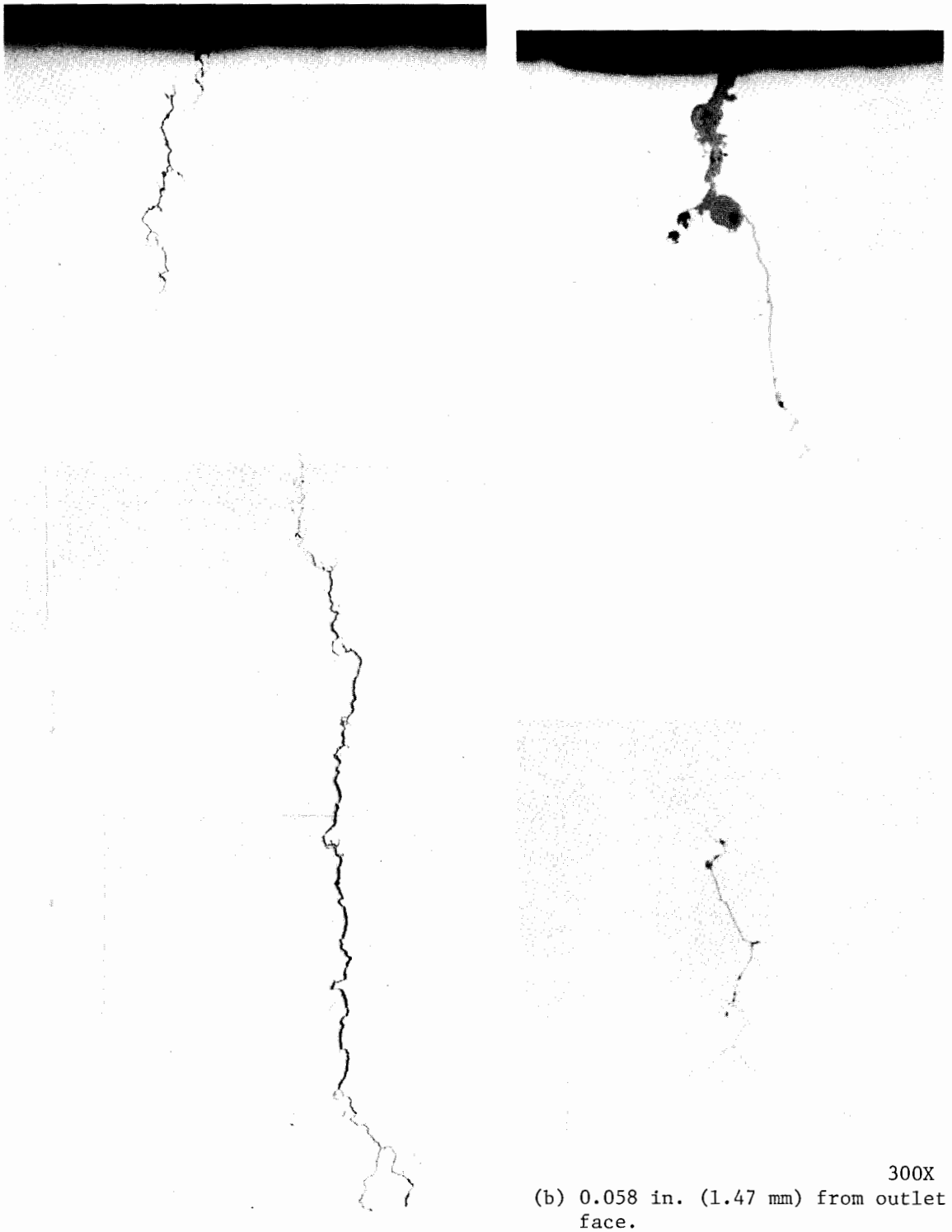

50X

(a) 0.016 in. (0.41 mm) from outlet face.

300X

(b) 0.058 in. (1.47 mm) from outlet face.

FIGURE D-6. SEQUENTIAL SECTIONS THROUGH CRACK 211-II(r), ROW 6R. See Figure 4-11.

(These photographs reduced to 90% of their original size)

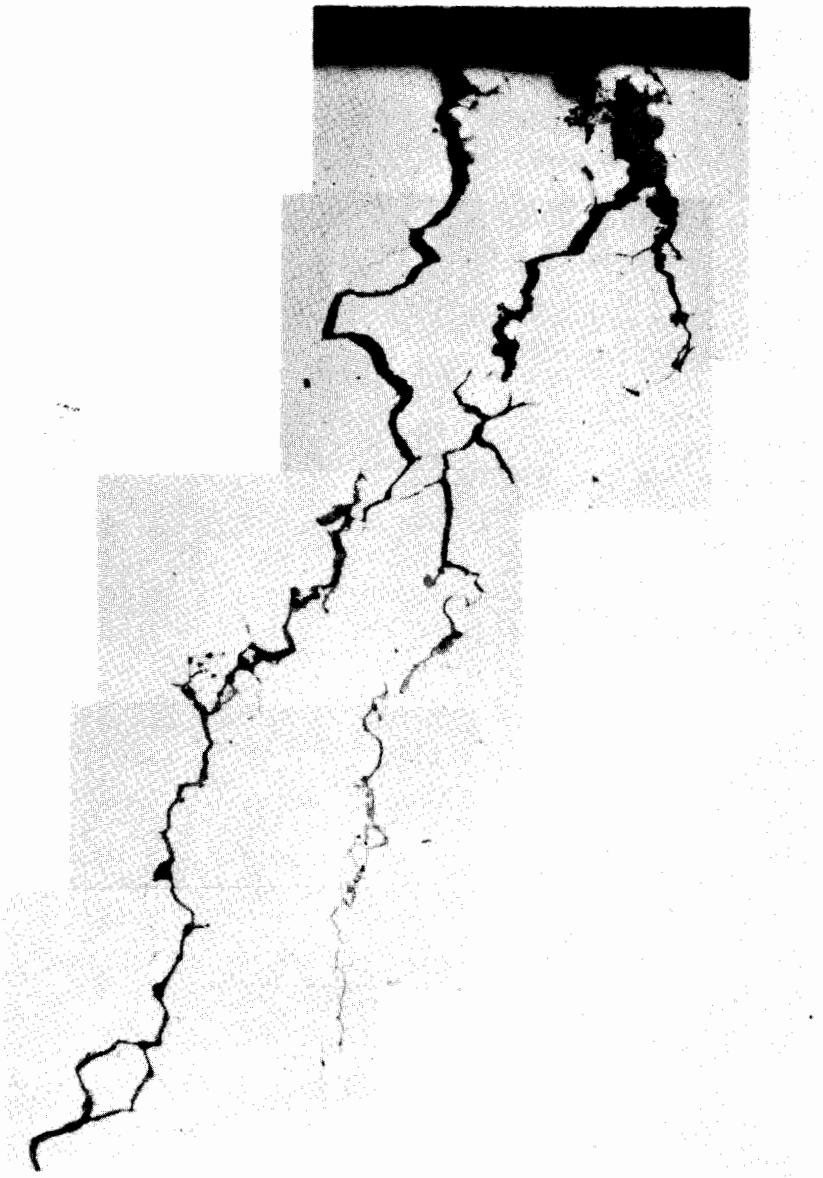

FIGURE D-7. CRACK 210-II(r), ROW 6R. Location 2, Figure 4-3. Section at outlet face. Unetched. 150X

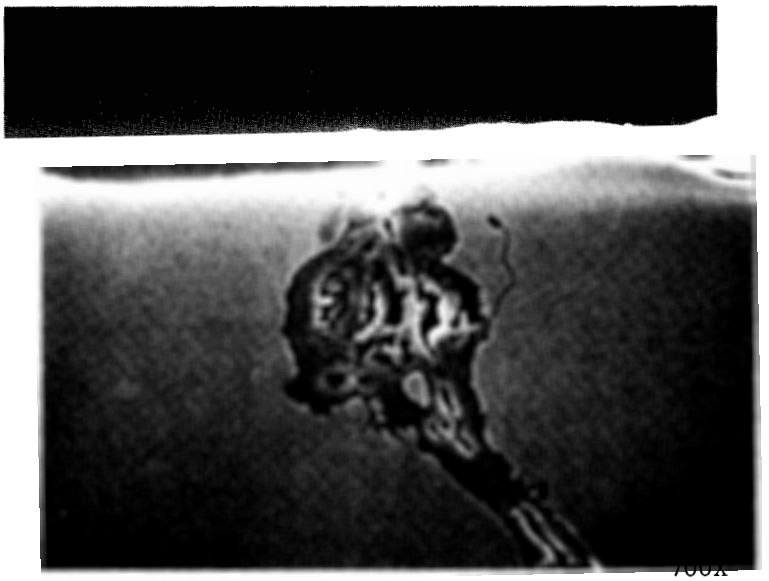

(a) SEM micrograph of deposit in crack at groove surface. Crack 176-I-3b, see Figure D-1.

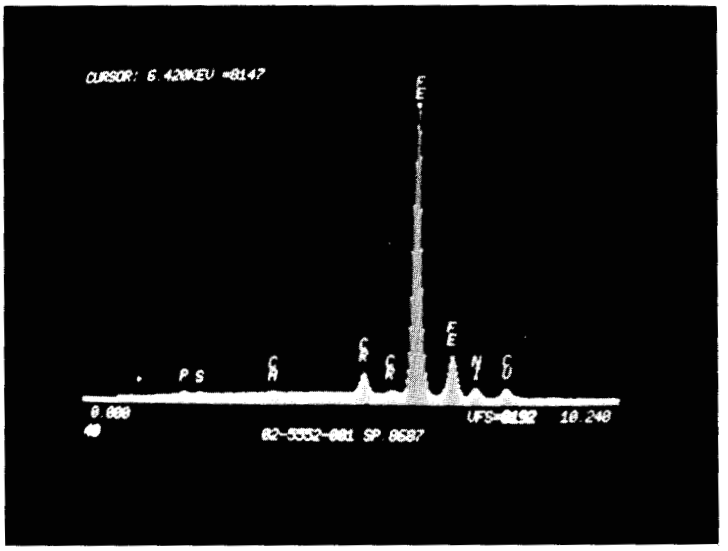

(b) X-ray energy spectra from deposit in (a).

FIGURE D-8. EDS ANALYSIS OF DEPOSIT WITHIN CRACK.

(These photographs reduced to 90% of their original size)

APPENDIX E

SELECTED FRACTOGRAPHS

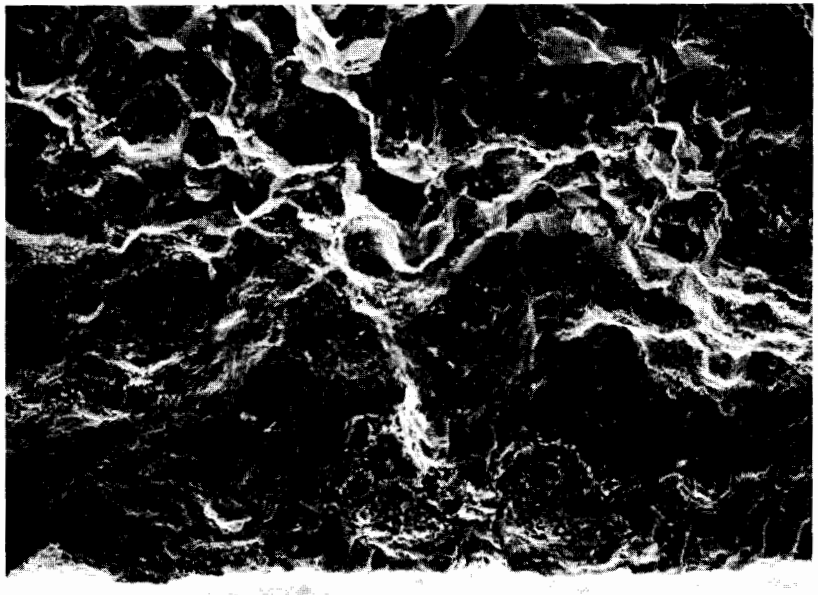

(a) Location 5

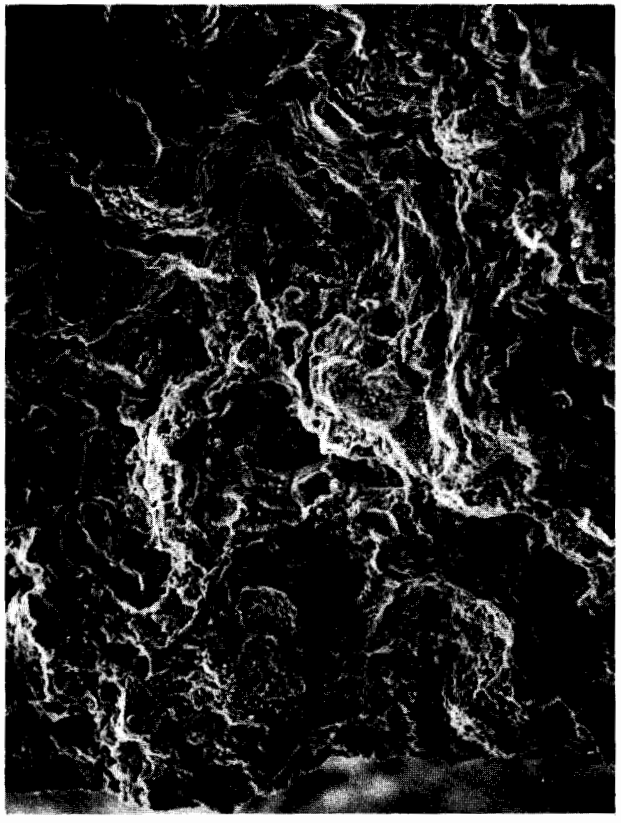

(b) Location 2

FIGURE E-1. SEM FRACTOGRAPHS AT EDGE OF CRACK 213-I-2bd, ROW 6R. Surface as exposed, no cleaning. See Figure 5-3 for locations. 200X

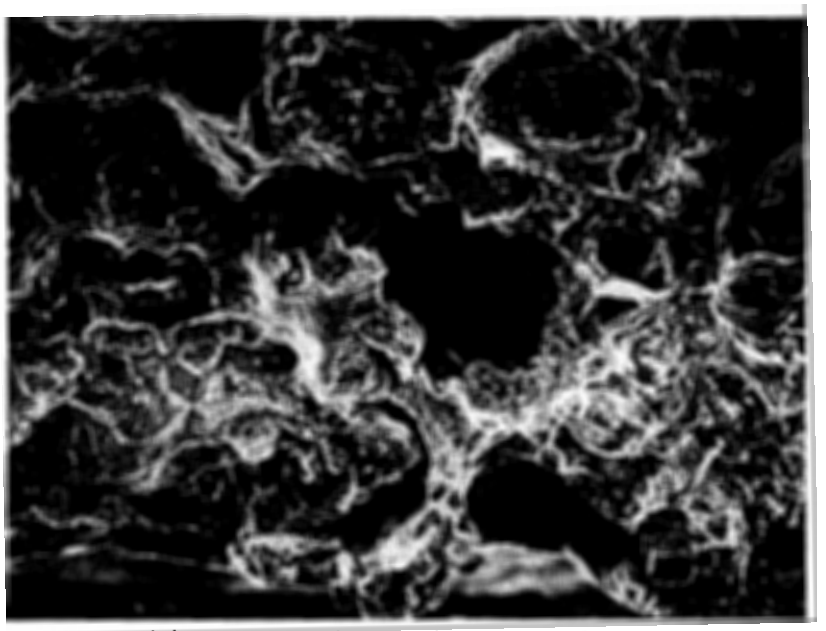

(a) As exposed, no cleaning. Note intergranular facets beneath oxide deposit.

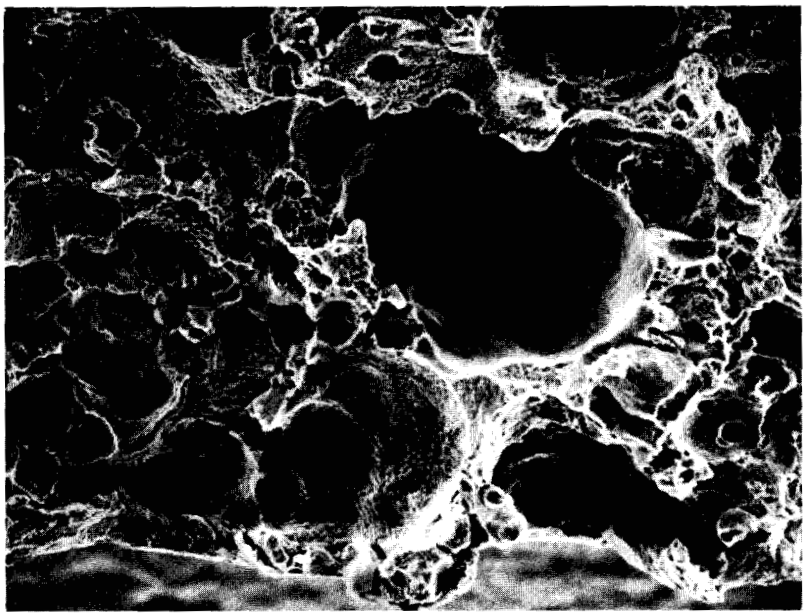

(b) Same as (a) after cathodic cleaning.

FIGURE E-2. SEM FRACTOGRAPHS AT EDGE OF CRACK 213-I-2bd, ROW 6R. Location 4, Figure 5-3. 200X

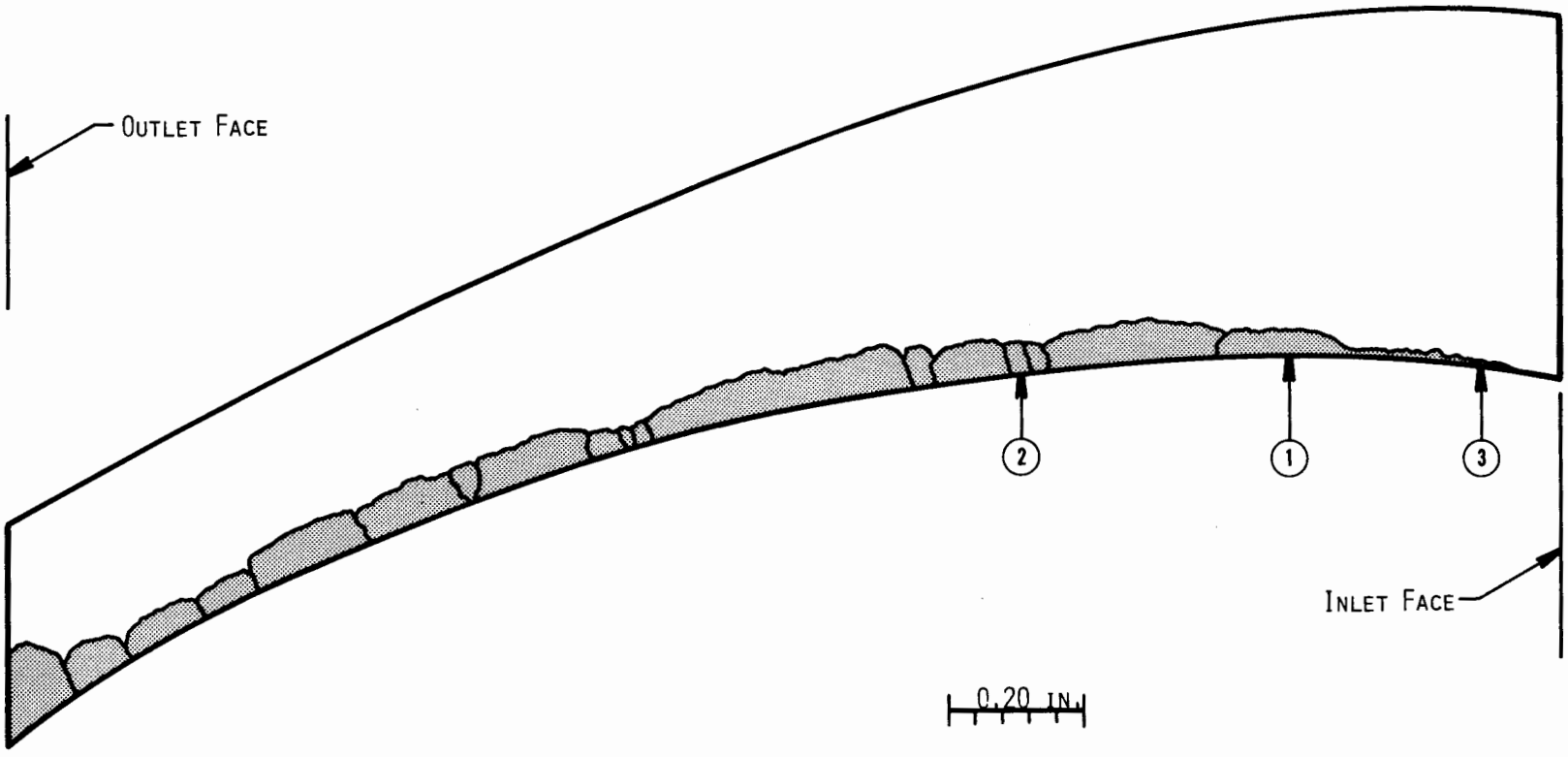

FIGURE E-3. DIAGRAM OF SURFACE OF CRACK 208-I-2b. See Figure 5-7. Outline represents full cross section of steeple at crack location. 4X

(This diagram reduced to 90% of its original size)

FIGURE E-4. TYPICAL TOPOGRAPHY OF CRACK 208-I-2b. Location 1, Figure E-3. SEM fractograph after cathodic cleaning. 200X

(This photograph reduced to 90% of its original size)

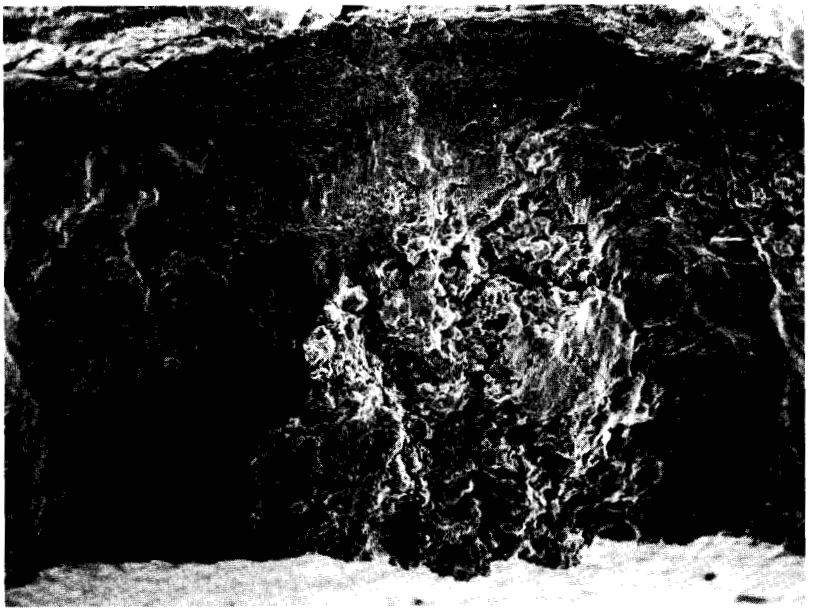

30X

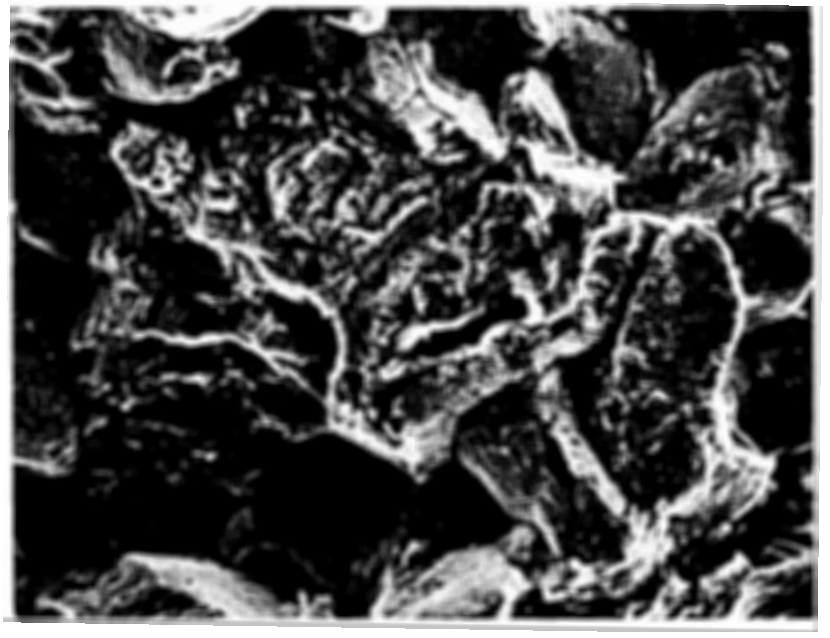

500X

FIGURE E-5. SEM FRACTOGRAPHS FROM CRACK 208-I-2bd. Location 2, Figure E-3. Surface cathodically cleaned.

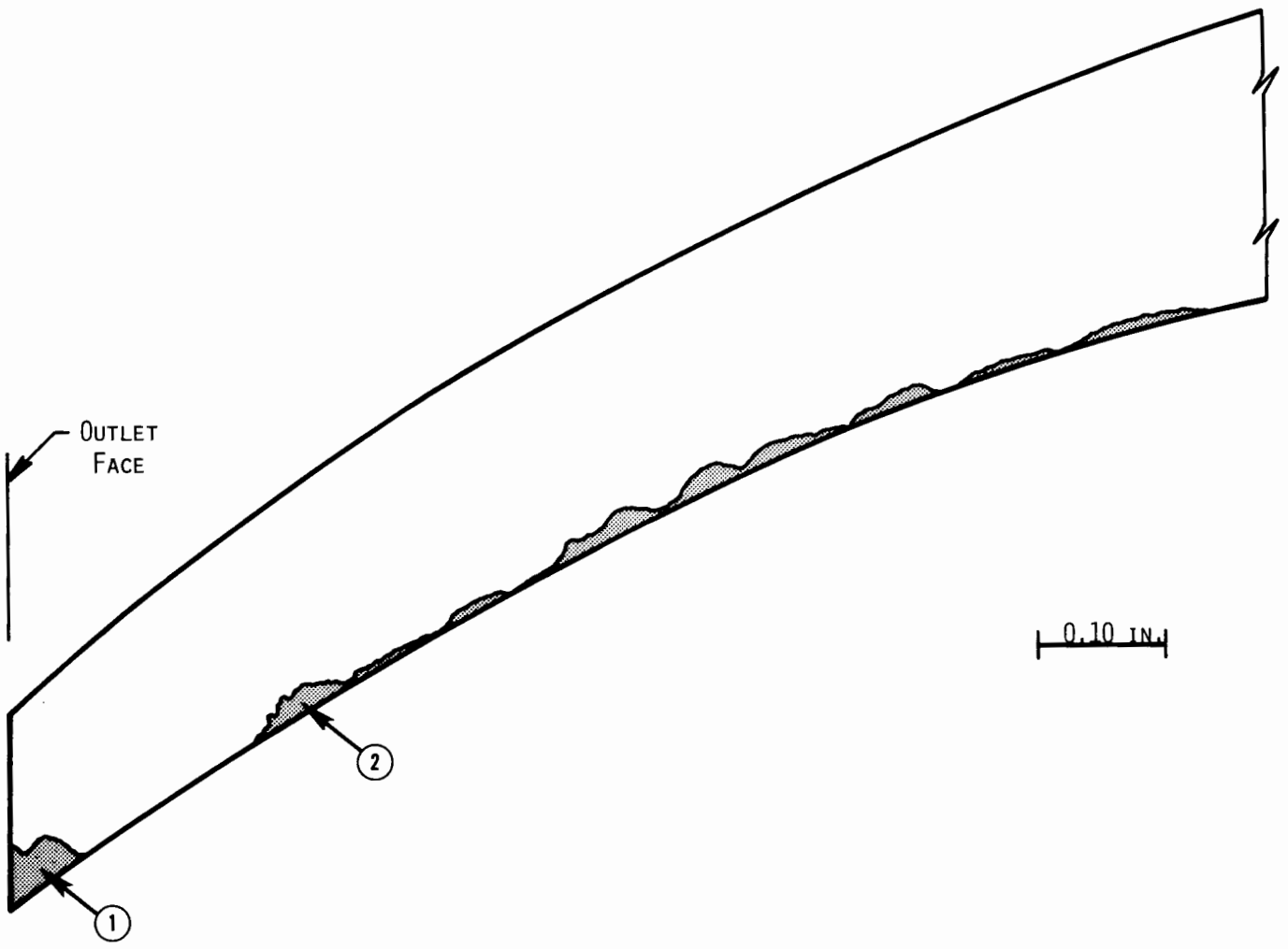

FIGURE E-6. DIAGRAM OF SURFACE OF CRACK 207-I-3d, ROW 6R. Outline represents cross section of steeple at crack location. See Figure 5-11. 8X

(This diagram reduced 90% of its original size)

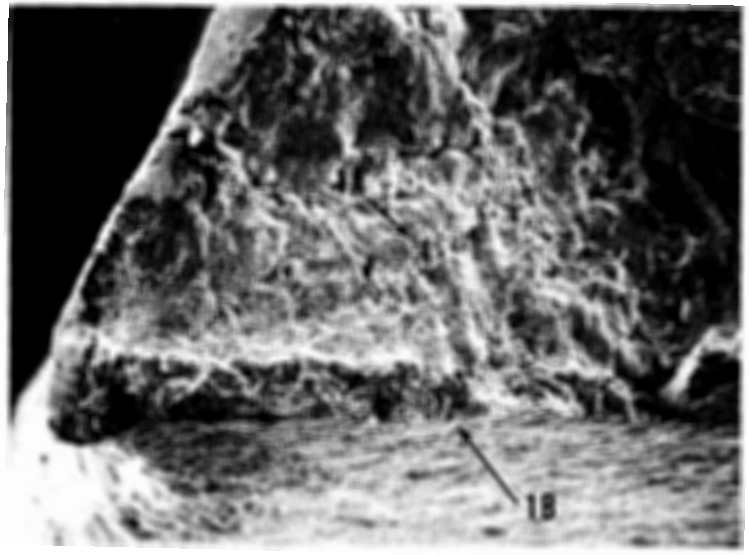

50X

(a) Outlet side corner, Area 1, Figure E-6.

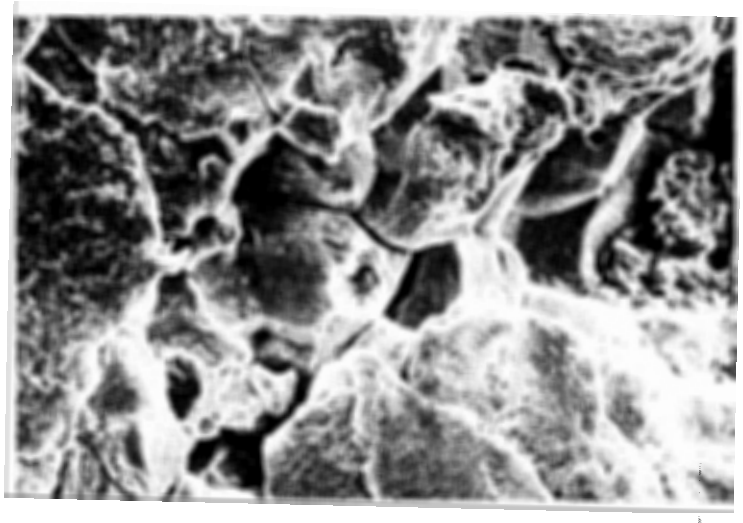

500X

(b) Location 1-A in (a).

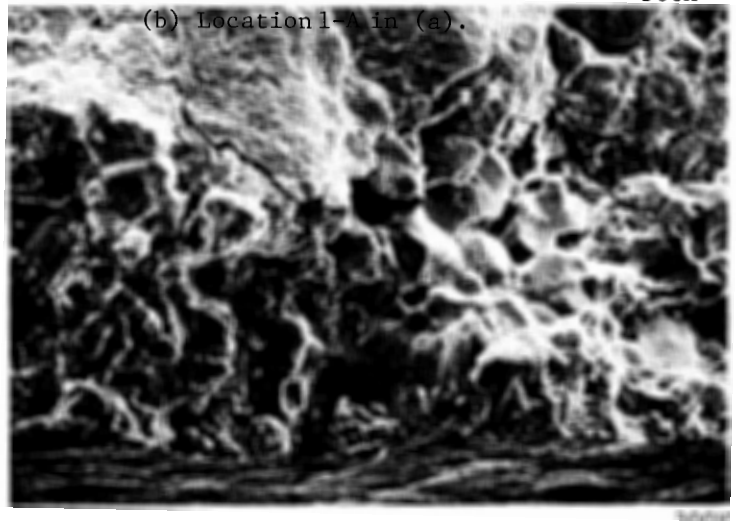

500X

(c) Location 1-B in (a).

FIGURE E-7. SEM FRACTOGRAPHS FROM CRACK 207-I-3(d).

(These photographs reduced to 90% of their original size)

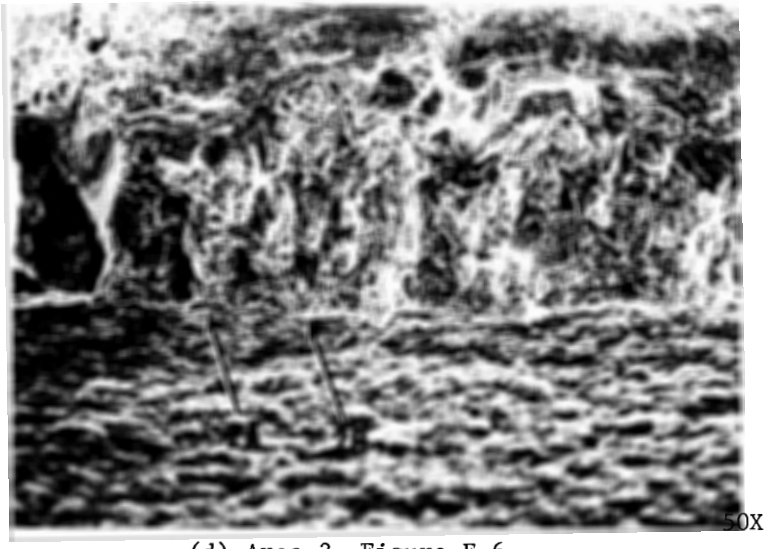

(d) Area 2, Figure E-6.

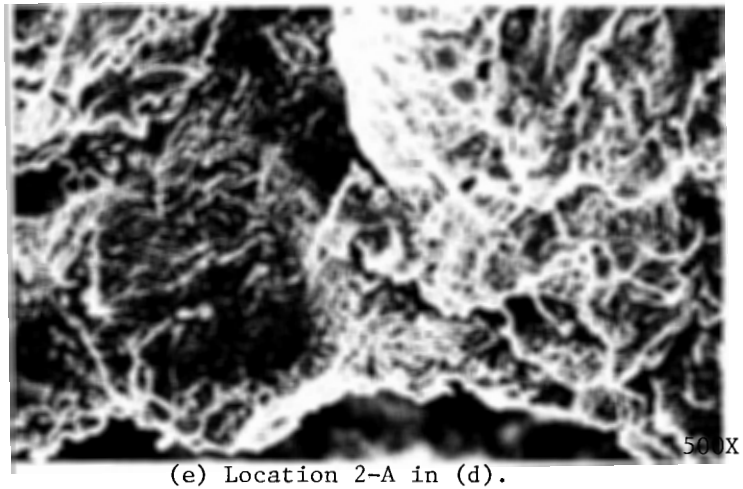

(e) Location 2-A in (d).

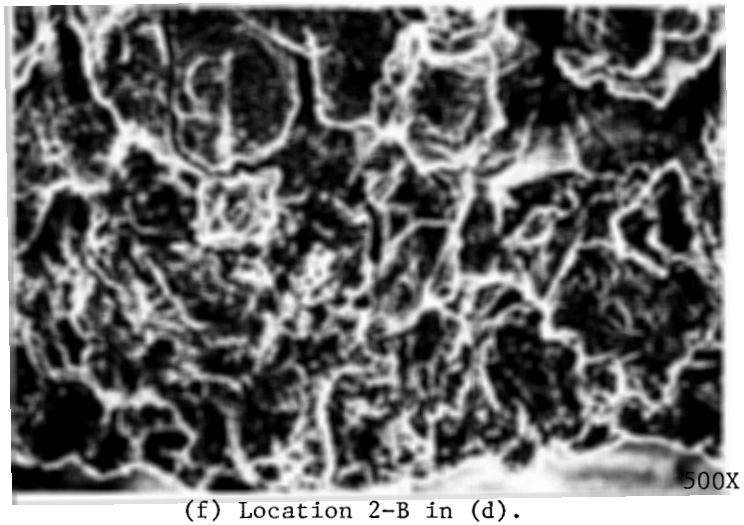

(f) Location 2-B in (d).

FIGURE E-7 (Continued). SEM FRACTOGRAPHS FROM CRACK 207-I-3(d).

(These photographs reduced to 90% of their original size)

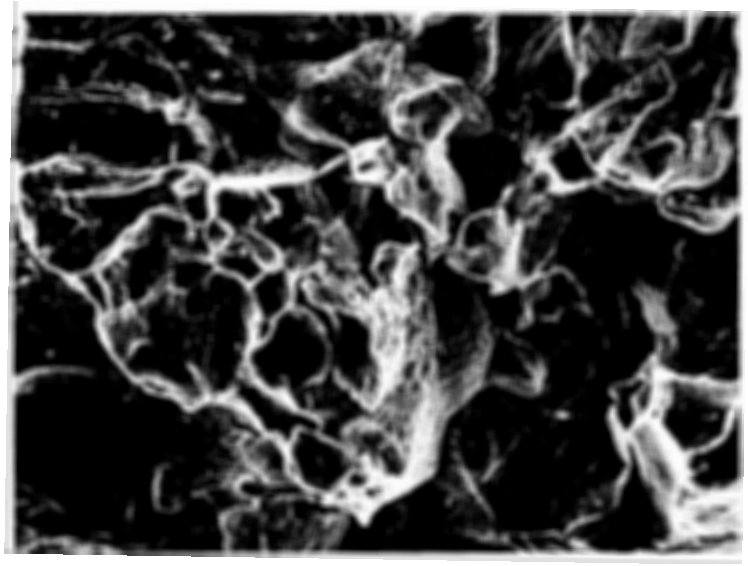

500X

(a) Location 4. At extreme point of crack propagation.

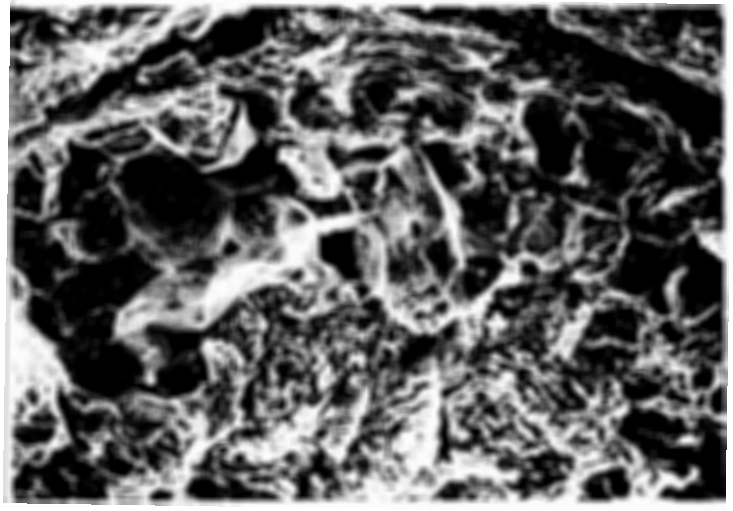

(b) Location 6.

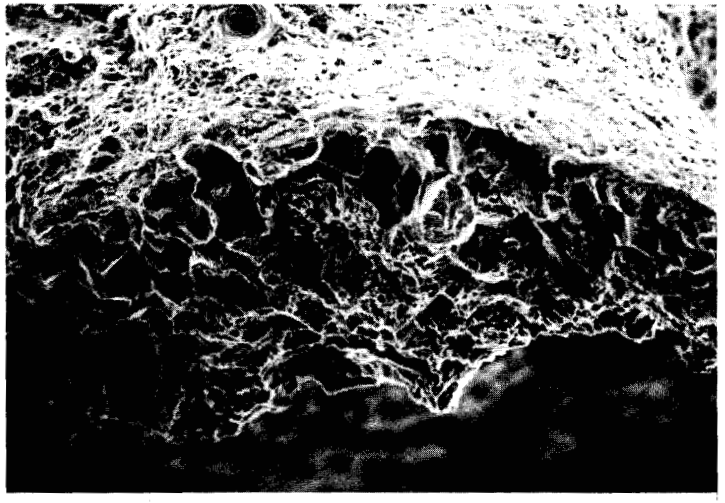

200X

(c) Location 7.

FIGURE E-8. SEM FRACTOGRAPHS FROM CRACK 177-I-2b. See Figure 5-13 for locations.

(These photographs reduced to 90% of their original size)

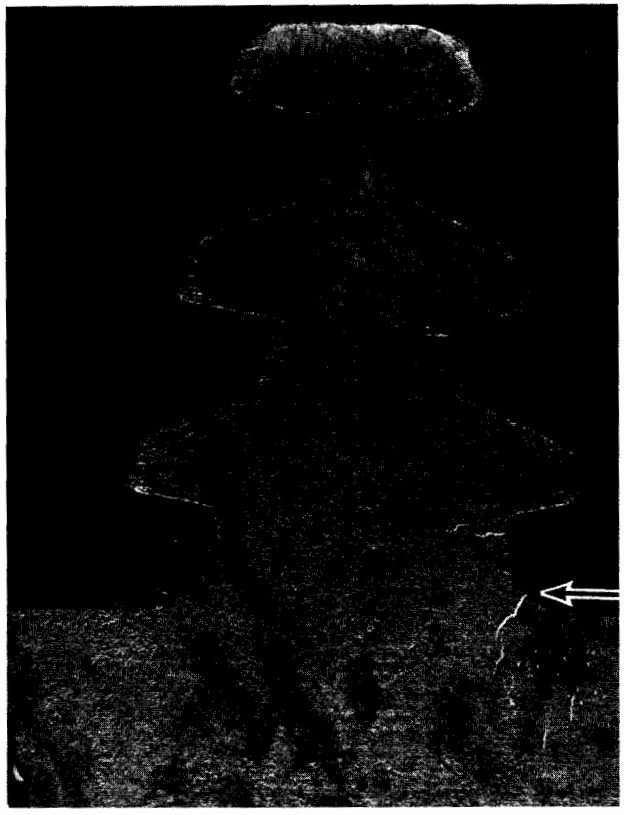

(a) Outlet face. Note separate crack indication below 212-II(d), arrows.

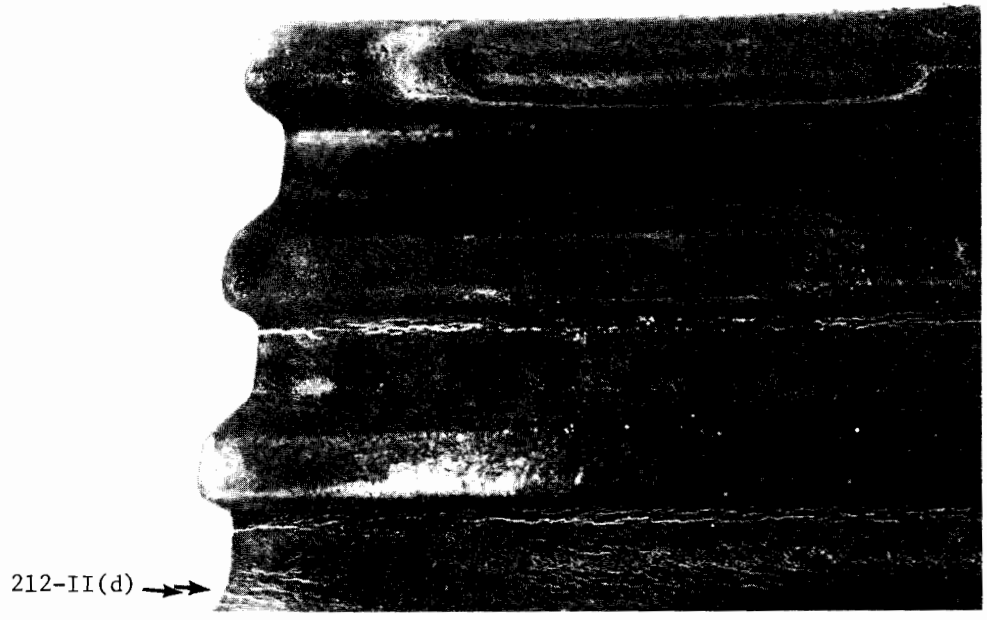

(b) Concave side. Note multiple indications in groove surface adjacent to 212-II(d).

FIGURE E-9. MAGNETIC PARTICLE CRACK INDICATIONS, STEEPLE 212/213, ROW 6R. 2.5X

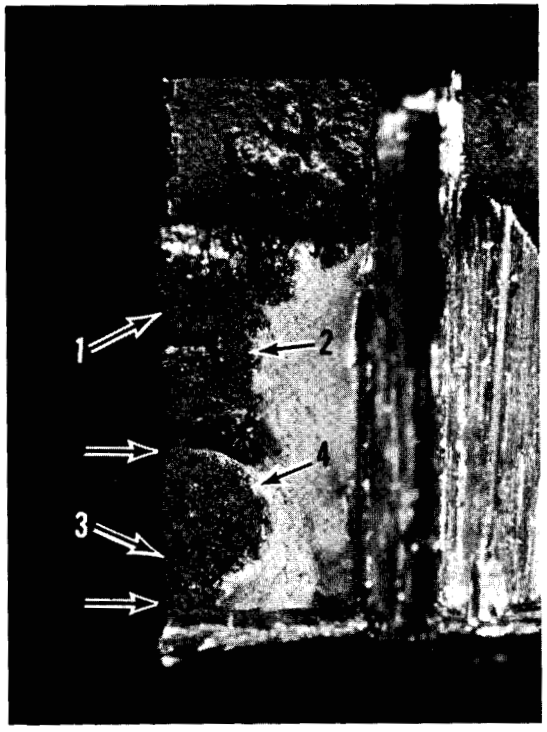

8X

(a) Complete crack surface. Note thumbnail shaped, face initiated crack below 212-II(d) marked by arrows [212-III(d)].

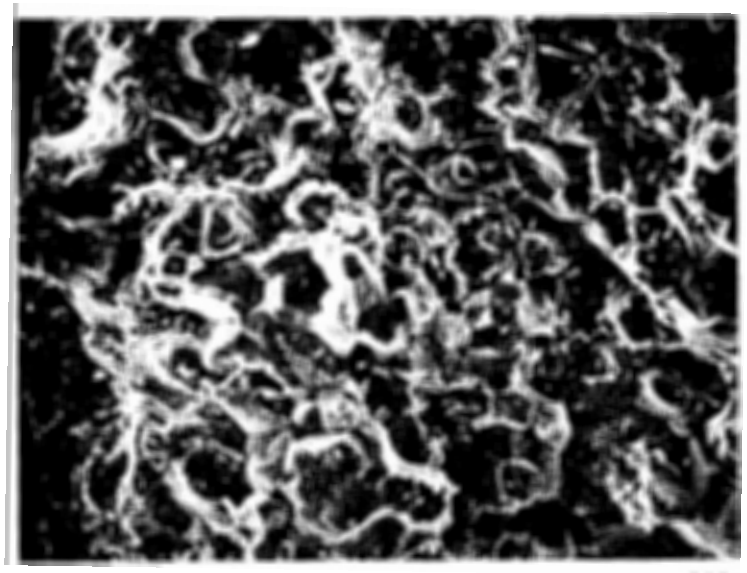

(b) Location 1 in (a). 200X

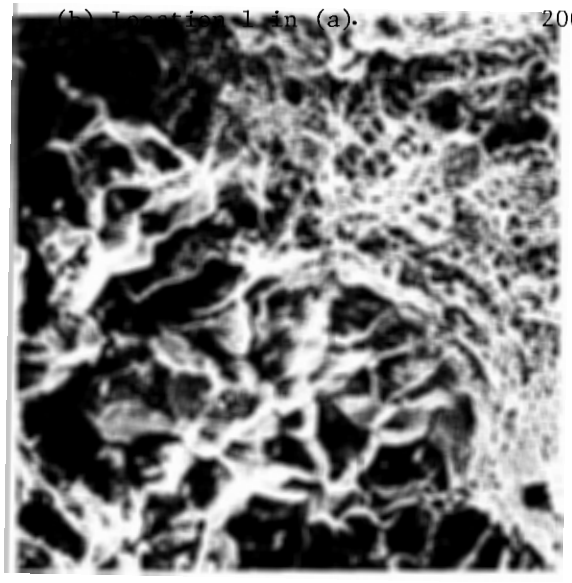

(c) Location 2 in (a). 200X

FIGURE E-10. SURFACE OF CRACK 212-II(d).

(These photographs reduced to 90% of their original size)

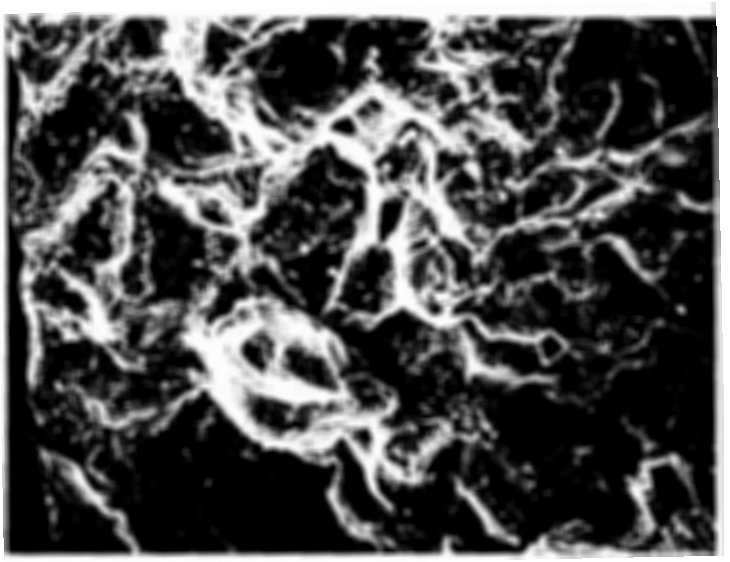

(a) Location 3, Figure E-10(a)

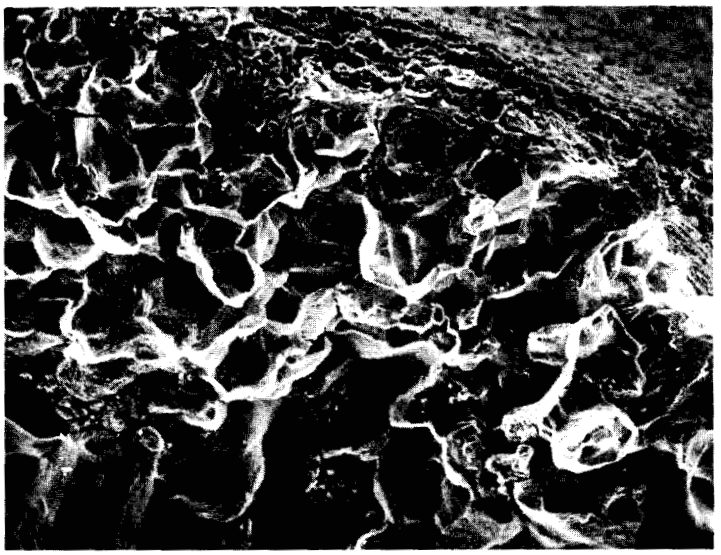

(b) Location 4, Figure E-10(a)

FIGURE E-11. SEM FRACTOGRAPHS FROM FACE INITIATED CRACK AT STEEPLE 212/213. Crack 212-III(d). 200X

(These photographs reduced to 90% of their original size)

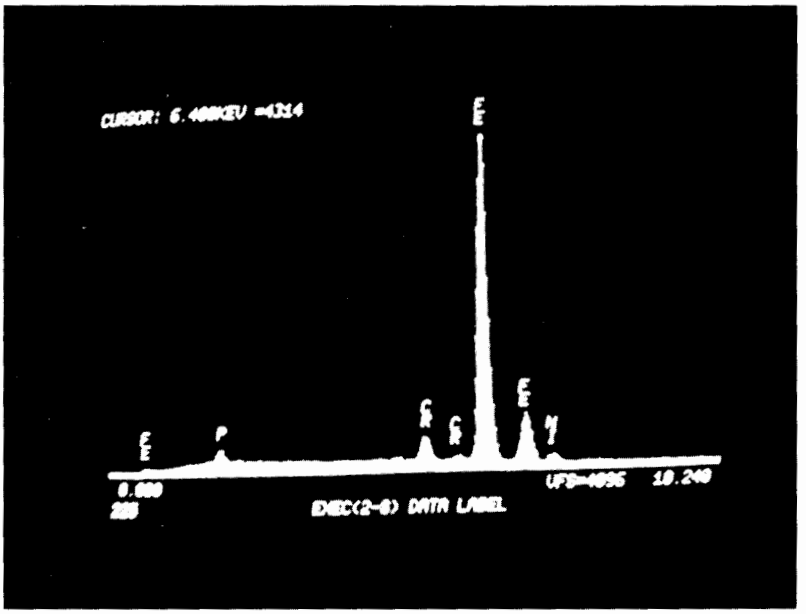

FIGURE E-12. TYPICAL X-RAY ENERGY SPECTRUM FROM CRACK SURFACE.

FINAL REPORT

For

TASK II

ABSTRACT

Mechanical properties tests, metallographic examinations and chemical analyses were performed on material from three LP steam turbine discs which had developed rim cracking in service. Potentiodynamic polarization tests were also performed in a concentrated caustic solution and in deoxygenated water. The objective of the investigation was to characterize the three sample materials and provide data for comparison with disc materials properties data generated in other EPRI programs.

Uniaxial tensile tests were performed on radial, axial and tangential specimens from one of the discs and compared with the tensile properties determined for the second disc in an earlier investigation. Charpy V-notch impact tests were performed on specimens from two of the discs over a temperature range of -101 to 149°C (-150 to 300°F).

The tensile properties of the two discs tested conform to the requirements for ASTM A 471 Cl. 5 NiCrMoV alloy steel. No significant differences in the tensile properties of the two were noted. The two disc samples exhibited very similar impact behavior with an average upper shelf energy of 137 J (101 ft-lbs) and $FATT_{50}$ = -58°C (-72°F).

The chemical compositions of the three disc samples conform to the requirements for A 471 Cl. 5 material in all respects. There was no evidence of abnormally high trace element content or of abnormal grain boundary segregation in any of the three materials.

In the polarization tests, indications of susceptibility to SCC were noted at particular values of imposed potential for all three materials in the caustic solution at 93.3°C. Particular conditions were identified at which further evaluation of the cracking susceptibility of disc materials is warranted.

CONTENTS

ILLUSTRATIONS

TABLES

SUMMARY

Mechanical properties tests, microstructural examinations and chemical analyses were performed on material from three LP steam turbine rotor discs. The three discs were from turbines in three different nuclear steam generating plants and each had developed rim cracking in service. The objective of the investigation was to characterize the three materials, compare the properties of the three available sample materials and provide a basis for future comparison with other disc material properties data generated in other EPRI programs. The particular samples employed for the investigation were as follows.

Plant C-1: Rim segments, Disc No. 3, 5R and 6R blade rows.
Plant D-1: Rim segment, Disc No. 1, 1R, 2R and 3R blade rows.
Plant E-1: Blade attachment steeples, Disc No. 1, 3R blade row.

Uniaxial tensile tests were performed on the C-1 disc material. Specimens with radial, axial and tangential orientations were included in the test series. The average tensile properties determined were as follows.

Ultimate Strength:	955 MPa (139 ksi)
Yield Strength:	866 MPa (126 ksi)
Elongation:	18.4%
Reduction of Area:	61.7%

The tensile properties of the C-1 material conform to the requirements for ASTM A471 Class 5 NiCrMoV alloy steel and are comparable to those determined for the D-1 material in an earlier investigation.

Charpy V-notch impact tests were performed on specimens from the C-1 and D-1 materials. The specimens were oriented so that fracture occurred in a radial direction relative to the original disc configuration. The range of test temperatures was -101 to 149°C (-150 to 300°F). The two materials exhibited very

similar impact behavior. The impact properties for both materials are summarized as follows.

Upper shelf energy: 130-145 J (93-107 ft-lbs)
$FATT_{50}$: -58°C (-72°F)
C_v energy at 21°C (70°F) = 119-141 J (88-104 ft-lbs)
C_v energy at -101°C (-150°F) = 31-44 J (23-33 ft-lbs)

The measured impact properties of both samples exceed the A 471 Cl. 5 requirements.

The fracture surfaces of the impact specimens tested at the lower temperatures were characterized by mixed cleavage and microvoid coalescence (MVC). The proportion of MVC increased with increasing test temperature and specimens tested at 21°C (70°F) and higher fractured completely by MVC. No significant degree of intergranular fracture was observed in any of the impact specimens.

The chemical compositions of all three materials conform to the requirements of ASTM A 471 Cl. 5 in all respects. Analyses were also performed for arsenic, antimony and tin contents with the following results:

As: 0.003-0.006 wt.%
Sb: 0.002 wt.%
Sn: 0.012-0.021 wt.%

These values are within the normal range of trace element contents for NiCrMoV alloy steels. As, Sb and Sn are known to segregate at prior austenite grain boundaries but there is no data available on their influence on intergranular stress corrosion cracking. There is no basis for evaluation of the trace element composition data at present.

The mechanical properties and compositional factors determined for the three sample materials are summarized in the following table:

SUMMARY OF DISC PROPERTIES

Disc Material	Tensile Properties		Impact Properties			Trace Element Composition - wt. %				
	UTS MPa(ksi)	YS MPa(ksi)	C_V Energy at 21°C J (ft-lbs)	Upper Shelf C_V Energy J (ft-lbs)	$FATT_{50}$ °C (°F)	S	P	As	Sb	Sn
Plant C-1	955 (139)	866 (126)	137 (101)	145 (107)	-58 (-72)	0.008	0.007	0.0047-0.0062	0.0015-0.0018	0.0115
Plant D-1	924 (134)	826 (120)	123 (91)	130 (95)	-59 (-74)	0.009	0.006	0.0034-0.0064	0.0016-0.0020	0.0148-0.0211
Plant E-1	--	--	--	--	--	0.010	0.010	0.0047-0.0060	0.0022-0.0025	0.0157-0.0180

Potentiodynamic polarization tests were performed to investigate the electrochemical behavior of the three disc materials in a concentrated caustic solution and in deoxygenated water. Tests were performed at 93.3°C (200°F) and at 37.8°C (100°F).

Indications of susceptibility to caustic SCC were noted at particular values of imposed potential for all three materials. On the basis of the polarization data the C-1 material appears to be the least susceptible of the three materials tested. In the case of the D-1 and E-1 materials, the characteristics of the polarization data suggest the possibility of SCC susceptibility at potentials near the free corrosion potential. Anodic activity was observed at the higher potentials for the C-1 and D-1 materials exposed to the caustic solution at 93.3°C (200°F). This factor suggests that these materials may be particularly susceptible to SCC in the upper cracking range. No indications of SCC susceptibility were observed in any of the polarization tests conducted in deionized water.

The results of the polarization tests identified areas in which further evaluation of the caustic SCC susceptibility of the disc materials is warranted. Controlled potential, slow strain rate tests should be conducted to provide direct SCC data for the conditions where susceptibility is indicated by the polarization tests. In particular, tests at high potentials in caustic solutions, where anodic activity was observed in the upper cracking region, and tests at controlled potentials near the free corrosion potential should be performed. The upper cracking zone is of particular interest since other data indicate that corrosion potentials for alloy steels in caustic solutions may become more positive with increasing exposure time.

Section 1

INTRODUCTION

In-service cracking in the blade attachment region of LP turbine rotor discs has been encountered at several nuclear steam electric generating stations over the past several years. One recent case (Plant C-1) involved rim cracking in the 5R and 6R blade rows of the No. 3 discs at both ends of two tandem LP turbines. A metallurgical evaluation of that cracking incident was performed as Task I of EPRI Project 1398-1. That investigation identified the mechanism of cracking as intergranular stress-corrosion cracking (IGSCC). The results of the metallurgical evaluation are contained in the Task I Key Phase Report dated August 17, 1979.

Task II of the project was initiated to establish the mechanical properties and compositional factors for the Plant C-1 disc material and to provide a comparison of the properties of disc materials from three plants in which rim cracking incidents occurred (Plants C-1, D-1 and E-1). The sample materials available for tests and analyses were as follows.

Plant C-1: Rim segments, Disc No. 3, 5R and 6R rows.
Plant D-1: Rim segment, Disc No. 1, 1R, 2R and 3R rows.
Plant E-1: Blade attachment steeples, Disc No. 1, 3R row.

Uniaxial tensile tests were performed on the Plant C-1 disc material and Charpy impact tests were performed on material from the C-1 and D-1 disc samples. Samples of all three materials were analyzed to determine the chemical compositions of both specified elements and trace elements. Potentiodynamic polarization measurements were also made to establish the electrochemical behavior of the disc materials in caustic solutions and pure water.

Section 2

MECHANICAL PROPERTIES

TENSILE PROPERTIES

Uniaxial tensile tests were performed on specimens from the No. 3 disc of the LP turbine rotor from Plant C-1. The test specimens were taken from the three rim segments provided for a metallurgical evaluation of the cracking (see Key Phase Report, Task I, EPRI 1398-1). Tests were performed on specimens representative of the axial, tangential and radial orientations. The particular test specimens employed were as follows.

3 - 12.7 mm (0.50 in.) dia. x 130 mm (5.0 in.); axial orientation
3 - 12.7 mm (0.50 in.) dia. x 130 mm (5.0 in.); tangential orientation
6 - 9.5 mm (0.375 in.) dia. x 180 mm (7.0 in.); radial orientation
12 - 3.2 mm (0.125 in.) dia. x 70 mm (1.75 in.); radial orientation

The 12.7 mm diameter axial and tangential specimens were taken from positions in the widest portion of the rim, immediately below the blade attachment steeples. The 9.5 mm diameter radial specimens were cut from the segments in a fashion to provide the maximum possible test section length. The purpose of these specimens was to provide for tests which would reflect the minimum strength value through radial dimension of the rim segments. Two 9.5 mm diameter specimens were taken from each of the three available segments, representative of 135°, 270° and 335° positions on the original disc.

Sub-size radial specimens, 3.2 mm in diameter, were tested to provide a measure of possible variations in properties through the rim in a radial direction. The locations of these specimens were arranged so that the center points of individual specimens corresponded to six equally spaced positions through the thickness of the rim segments. One group of six sub-size specimens was taken from each of two rim segments representing circumferential locations approximately 135° apart.

Details of the specimen geometry and specimen locations are given in Appendix A. All tensile tests were performed at room temperature in a servo-controlled, hydraulic actuated testing machine. The test procedures were in conformance to ASTM E8.

Tensile Test Results

The results of the tensile tests on the 12.7 mm (0.50 in.) and 9.5 mm (0.375 in.) diameter specimens are presented in Table 2-1. The properties determined from this group of specimens are generally uniform among the 12 tests and conform to the requirements of ASTM A471 C1. 5.

The average values of ultimate strength and yield strength determined for the 12.7 mm dia. specimens are as follows.

	Ultimate Strength	Yield Strength
Axial	967 MPa (140 ksi)	886 MPa (128 ksi)
Tangential	952 MPa (138 ksi)	853 MPa (124 ksi)

The axial specimens, as a group, exhibited slightly higher ultimate and yield strengths than the tangential specimens. The elongation and reduction of area values were in the range of 16.8-18.6% and 55.4-65.2%, respectively. These data show a slightly lower ductility for the axial specimens consistent with the measured strength.

The average ultimate strength and yield strength in the radial direction, as measured in tests of the 9.5 mm diameter specimens, were 951 MPa (138 ksi) and 863 MPa (125 ksi), respectively. These values are comparable to the strengths measured in the tangential specimens. The ductility for the radial specimens is either comparable to or slightly higher than that of the tangential specimens.

The tensile properties data measured for the 3.2 mm (0.125 in.) radial specimens are presented in Table 2-2. The ultimate strength measured for these specimens was in the range of 938-972 MPa (136-141 ksi) and the yield strength values were 834-889 MPa (121-129 ksi). The data do not show any significant variation in strength in a radial direction through the thickness of the rim segments. The strength values are comparable to those determined for the 9.5 mm diameter radial specimens, while the elongation and reduction in area values are generally

Table 2-1

TENSILE TEST RESULTS
12.7 mm and 9.5 mm Diameter Specimens

Specimen Number	Diameter mm	Diameter (in.)	Orientation	Ultimate Strength MPa	Ultimate Strength (ksi)	Yield Strength MPa	Yield Strength (ksi)	Elongation[1] %	Reduction in Area %
AX-1	12.7	(.50)		973	(141.1)	886	(128.5)	17.3	58.0
AX-2	12.7	(.50)	Axial	964	(139.8)	888	(128.8)	16.8	55.4
AX-3	12.7	(.50)		965	(140.0)	883	(128.0)	18.0	57.6
				Avg. 967 ± 5		Avg. 886 ± 3		Avg. 17.4 ± .6	Avg. 57.0 ± 1.4
TA-1	12.7	(.50)		952	(138.0)	855	(124.0)	18.0	62.2
TA-2	12.7	(.50)	Tangential	958	(139.0)	855	(124.0)	18.5	65.2
TA-3	12.7	(.50)		945	(137.0)	848	(123.0)	18.6	65.3
				Avg. 952 ± 7		Avg. 853 ± 4		Avg. 18.4 ± .3	Avg. 64.2 ± 1.8
A-1	9.5	(.375)		952	(138.0)	862	(125.0)	19.0	60.9
A-2	9.5	(.375)		938	(136.0)	848	(123.0)	20.2	67.3
B-1	9.5	(.375)	Radial	952	(138.0)	862	(125.0)	19.6	66.1
B-2	9.5	(.375)		952	(138.0)	862	(125.0)	19.3	60.9
C-1	9.5	(.375)		958	(139.0)	876	(127.0)	19.4	65.1
C-2	9.5	(.375)		952	(138.0)	869	(126.0)	19.2	64.5
				Avg. 951 ± 7		Avg. 863 ± 9		Avg. 19.5 ± .4	Avg. 64.1 ± 2.7
ASTM A471 C1.5				900 min	(130 min)	824-964	(120-140)	16.0 min	43.0 min

(1) % in 50 mm for 12.7 mm dia.
% in 38 mm for 9.5 mm dia.

Table 2-2

TENSILE TEST RESULTS
3.2 mm Diameter Specimens
Radial Orientation

Specimen Number	Ultimate Strength MPa	(ksi)	Yield Strength MPa	(ksi)	Elongation in 12.7 mm.%	Reduction in Area %
A-12	958	(139)	848	(123)	22.1	74.0
A-18	938	(136)	834	(121)	22.6	71.9
A-25	958	(139)	862	(125)	21.5	71.5
A-37	945	(137)	855	(124)	24.5	71.8
A-42	945	(137)	841	(122)	--	71.3
A-47	952	(138)	862	(125)	22.6	68.9
B-12	986	(143)	889	(129)	22.2	69.4
B-18	965	(140)	862	(125)	17.1	72.2
B-25	972	(141)	876	(127)	18.5	73.6
B-37	972	(141)	876	(127)	--	71.3
B-42	972	(141)	876	(127)	21.6	72.7
B-47	958	(139)	862	(125)	21.5	75.2
Avg.	960 ± 14		Avg. 862 ± 16		Avg. 39.4 ± 5.7(2)	Avg. 72.0 ± 1.8
ASTM A471 C1.5	900 min	(130 min)	824-964	(120-140)	16.0 min	43.0 min

higher. The test results for the 3.2 mm diameter specimens show a small but consistent difference in strength between the specimens from the two different rim segments (A series vs. B series). This factor indicates a slight variation in properties with circumferential position in the disc and suggests that the difference in properties noted between the axial and tangential specimens may be due to specimen location.

In view of the relatively small differences in the results of the tensile tests on the several groups of specimens, the disc material may be characterized by the overall average of the 12.5 mm and 9.5 mm test specimens. These average values are:

Ultimate Strength:	955 MPa (139 ksi)
Yield Strength:	866 MPa (126 ksi)
Elongation:	18.4%
Reduction in Area:	61.7%

The tensile properties determined for the No. 1 disc of another LP turbine rotor which developed cracking in service (Plant D-1) are presented in Table 2-3. In general, the D-1 disc material exhibited slightly lower ultimate strength and yield strength values and a slightly higher ductility. The difference in average strengths of the two discs is of the order of 34 MPa (5.0 ksi).

IMPACT PROPERTIES

Charpy V-notch impact tests were performed on material from two discs; one each from Plants C-1 and D-1. In each case the specimens were taken from the outer three inches of the rim segments immediately below the blade attachment steeples. All impact test specimens were oriented in a tangential direction and the notch was located so that fracture occurred in a radial direction. Tests were performed over a temperature range of -101 to 149°C (-150 to 300°F). The specimen dimensions and test procedures were in accordance with ASTM E23.

Charpy-V Impact Test Results

The impact data obtained for each of the two materials are presented as absorbed energy vs. temperature in Figures 2-1 and 2-2. The test data are tabulated in Appendix B.

Table 2-3

TENSILE PROPERTIES DISC NO. 1
Gov. End, LP-1, Plant D-1

Specimen Diameter mm	(in.)	Orientation	Ultimate Strength MPa	(ksi)	Yield Strength MPa	(ksi)	Elongation[1] %	Reduction in Area %
			927	(134.4)	825	(119.6)	20.4	57.9
12.7	(0.50)	Radial	916	(132.9)	823	(119.3)	20.3	66.8
			933	(135.3)	830	(120.3)	20.5	68.2
		Avg.	925	Avg.	826		Avg. 20.4	Avg. 64.3
			916	(132.8)	819	(118.8)	21.6	69.2
12.7	(0.50)	Tangential	926	(134.3)	826	(119.8)	21.3	67.4
			926	(134.3)	831	(120.5)	20.6	67.2
		Avg.	923	Avg.	825		Avg. 21.2	Avg. 67.9
			956	(138.6)	867	(125.7)	18.0	63.2
3.2	(0.125)	Radial	932	(135.1)	856	(124.2)	17.4	63.2
			961	(139.4)	872	(126.5)	19.4	60.9
		Avg.	950	Avg.	865		Avg. 18.3	Avg. 62.4
ASTM A471 C1.5			900 min	(130 min)	824-964	(120-140)		

(1)% in 50 mm for 12.7 mm dia.
% in 12.7 mm for 3.2 mm dia.

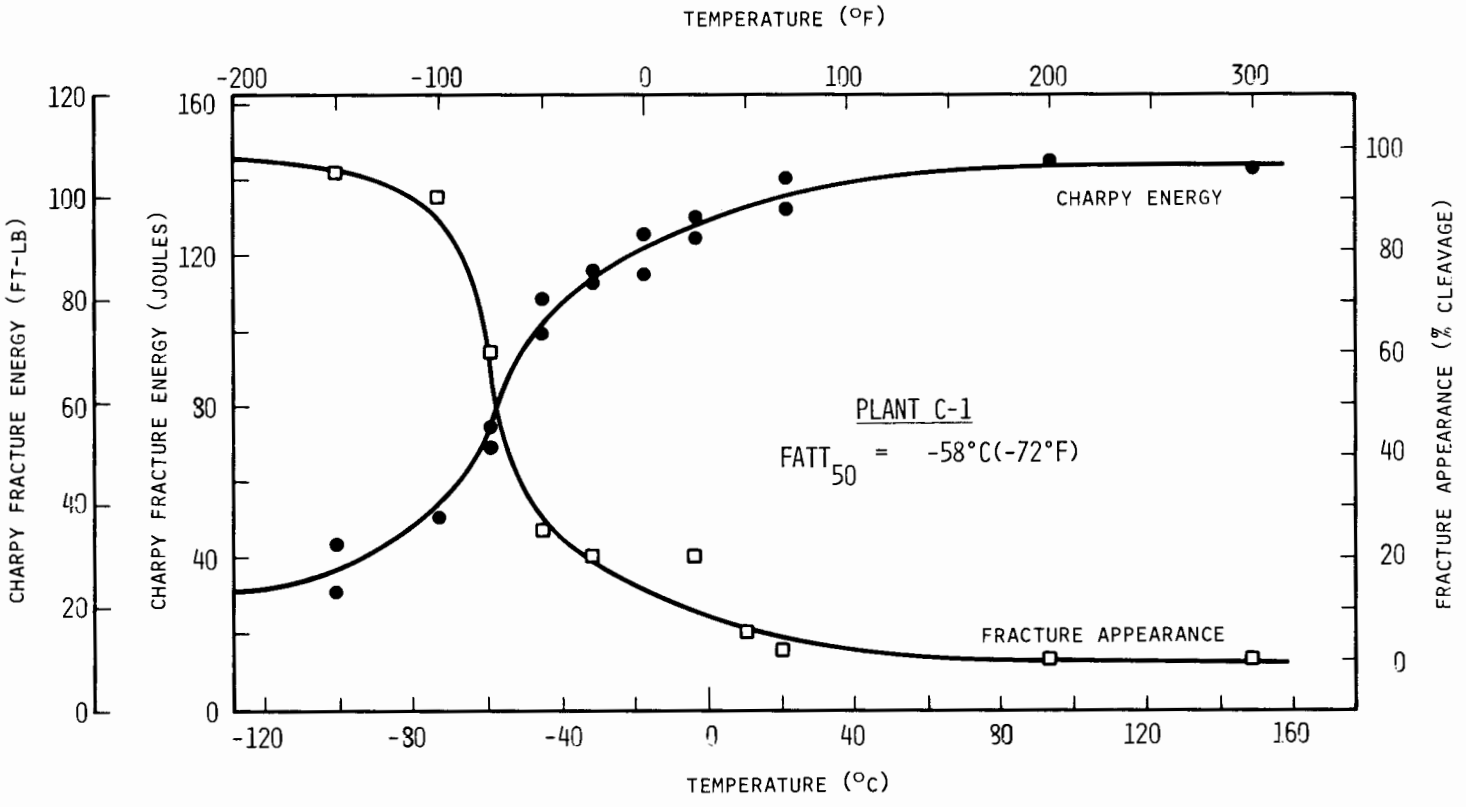

FIGURE 2-1. CHARPY-V IMPACT PROPERTIES. Disc No. 3, Gen. End, LP-2, Plant C-1.

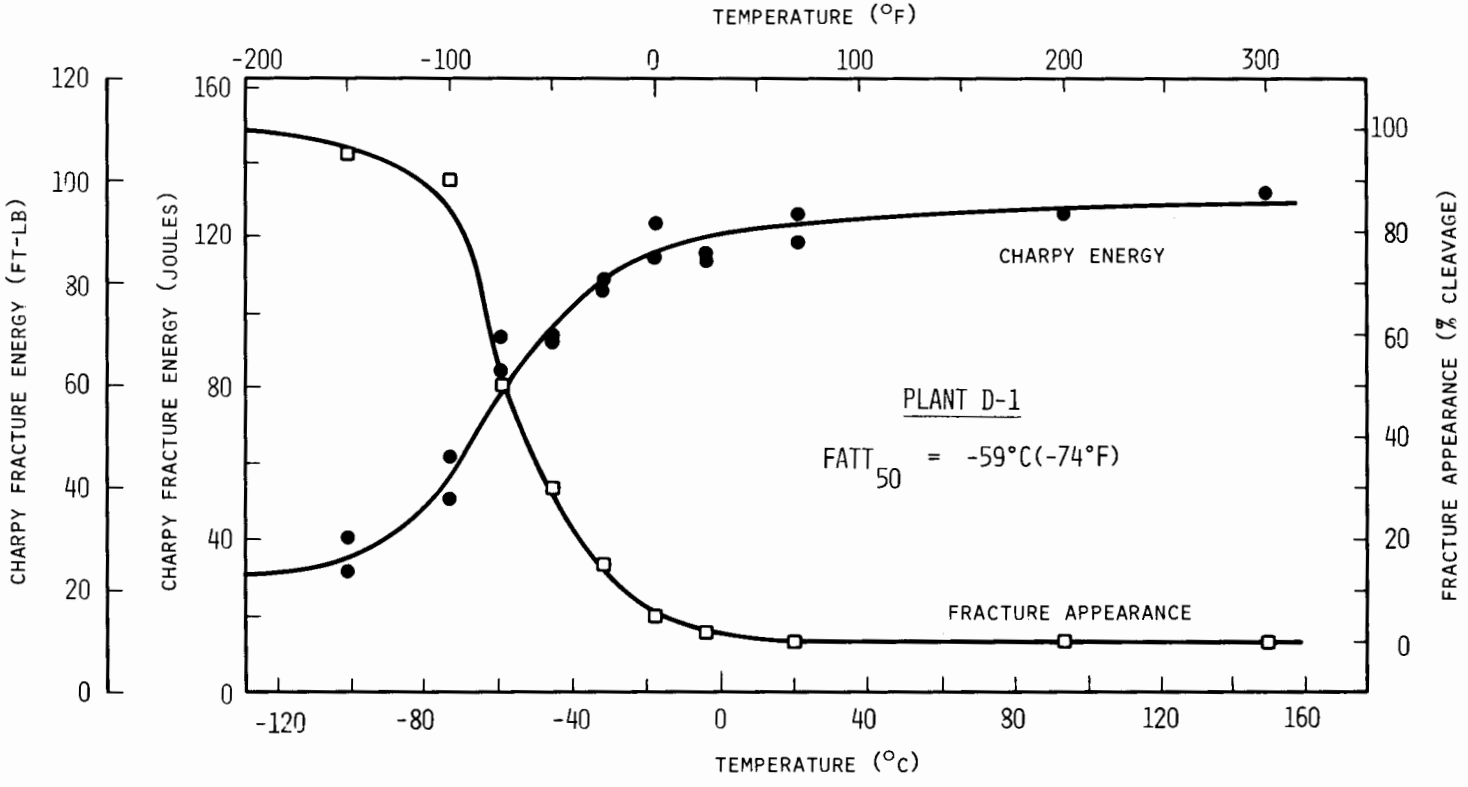

FIGURE 2-2. CHARPY-V IMPACT PROPERTIES. Disc No. 1, Gov. End, LP-1, Plant D-1.

The data for the two discs are generally similar. Both materials exhibit a relatively high upper shelf energy and a clearly defined ductile-brittle transition with decreasing temperature is evident. The upper shelf energies were determined to be 145 J (107 ft-lbs) for the C-1 material and 130 J (90 ft-lbs) for the D-1 material. The absorbed energy values at the lowest test temperature were in the range of 31-44 J (23-33 ft-lbs) for both materials. Extrapolation of the data to lower temperatures indicates a lower shelf energy of approximately 30 J (22 ft-lbs).

The combined absorbed energy data from all tests on both materials are presented in Figure 2-3. Considering all data as a group, the spread in absorbed energy values at the low temperature end of the curve is 13 J (10 ft-lbs). A maximum spread of 22 J (16 ft-lbs) was noted at 21°C (70°F). The spread in absorbed energy values for the entire group of tests is comparable to the normal scatter for Charpy-V impact tests. The test results indicate that there is no significant difference in the impact behavior of the two materials.

The fracture surfaces of specimens representing all test temperatures are shown in Figure 2-4. Some degree of ductility is apparent at the lowest temperature as evidenced by a relatively rough surface and small but well developed shear lips. The progressive increase in ductility with increasing temperature is clearly evident. Those specimens tested at room temperature and above exhibit a fully ductile appearance. The 50% fracture appearance transition temperatures were established as

C-1 material: $FATT_{50}$ = -58°C (-72°F)
D-1 material: $FATT_{50}$ = -59°C (-74°F)

The impact properties specified for A471 C1. 5 material are as follows.

C_V energy at room temperature: 54 J (40 ft-lbs) min.
Transition temperature, $FATT_{50}$: -12°C (10°F) max.

The measured properties for both disc materials exceed the A471 C1. 5 requirements.

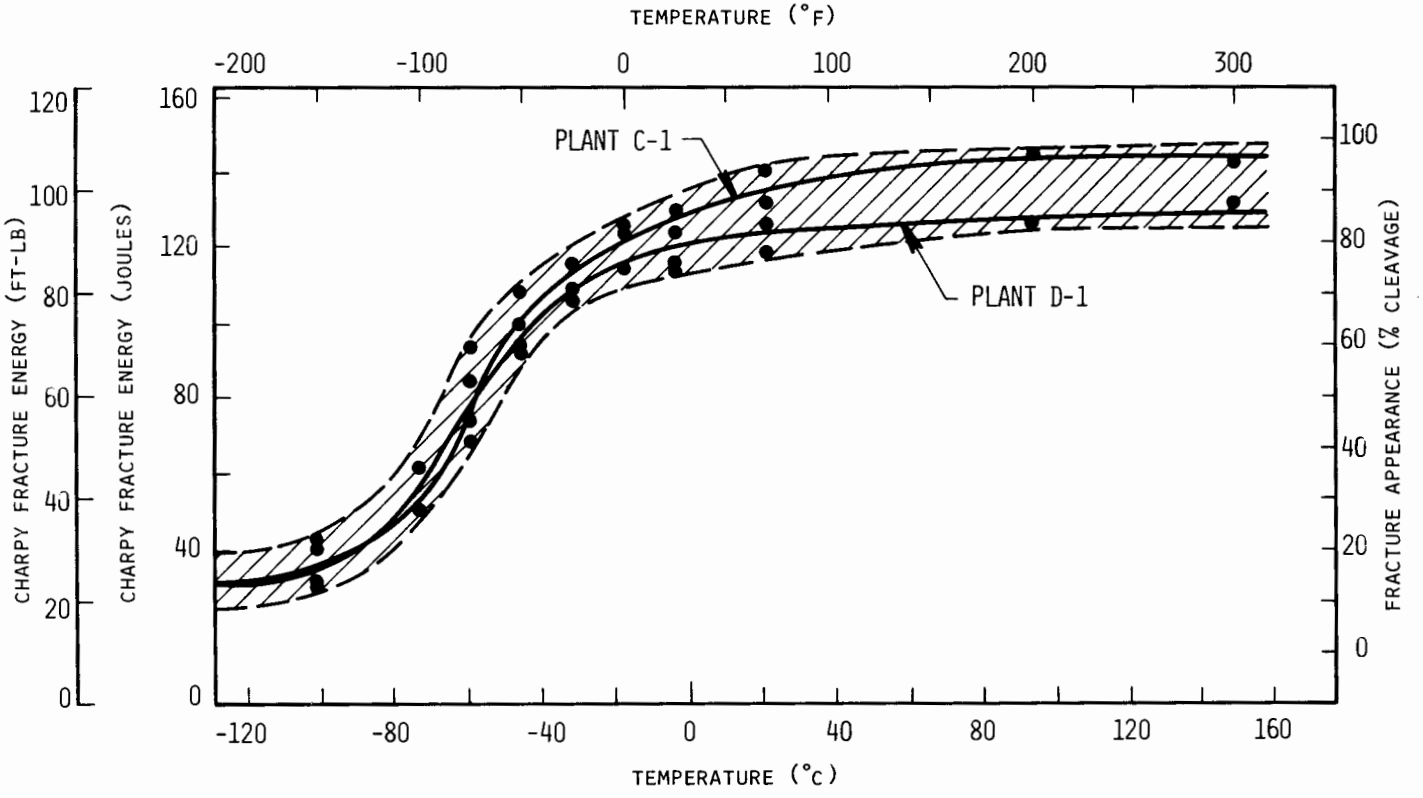

FIGURE 2-3. COMBINED CHARPY-V IMPACT DATA FOR DISCS FROM TWO PLANTS.

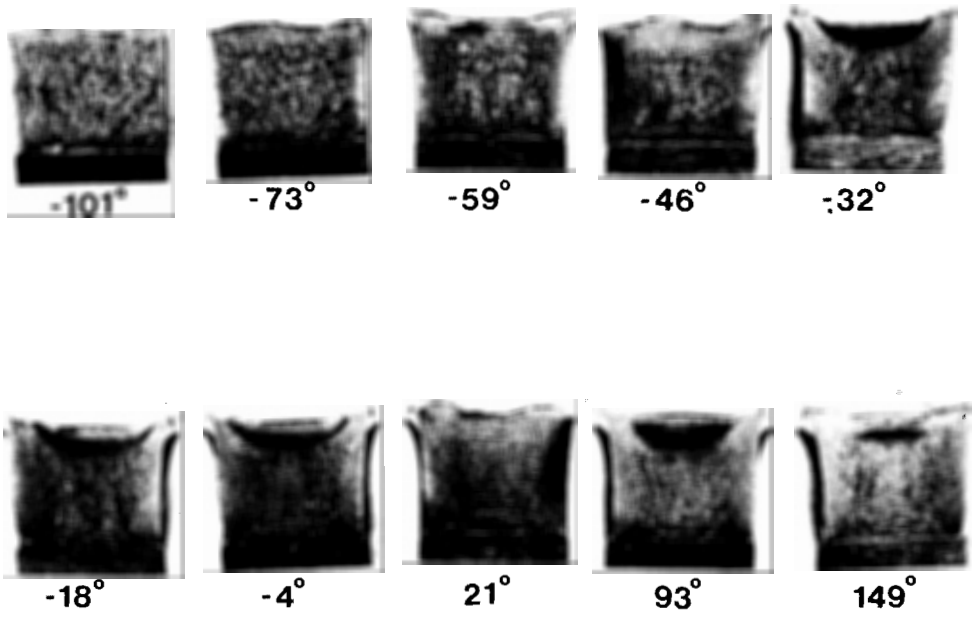

Plant C-1

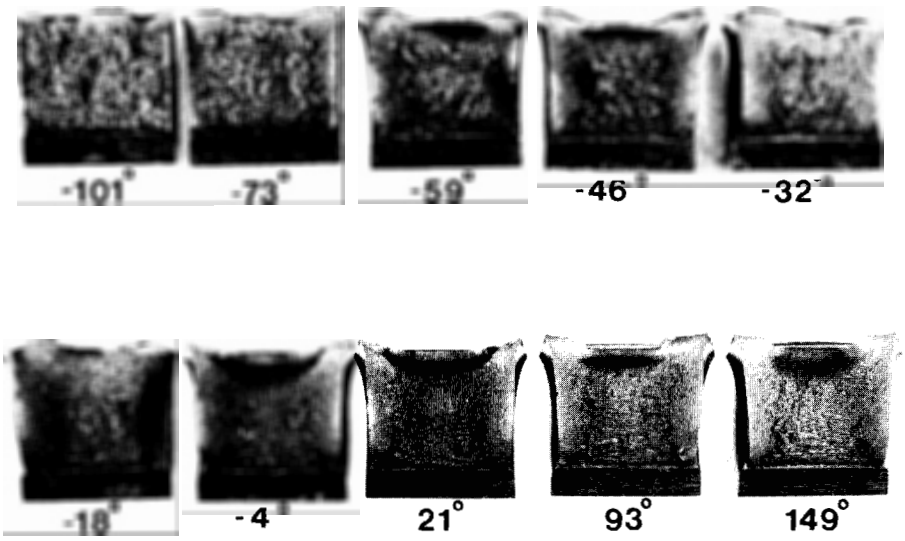

Plant D-1

FIGURE 2-4. CHARPY V-NOTCH IMPACT SPECIMENS. Temperatures shown in °C. ≈2X (These photographs reduced to 90% of their original size)

Fractographic Examinations

Selected Charpy impact specimens were examined in the scanning electron microscope (SEM) to identify the micro-mechanistic aspects of the test fractures over the full range of test temperatures. The specimens were chosen to be representative of the lowest test temperature, the ductile-brittle transition zone and the upper shelf. Specimens from each of the two disc materials were included to provide a comparison of fractographic features at a single test temperature. The particular specimens selected for examination were as follows.

Test Temp °C (°F)	Plant C-1	Plant D-1
-101 (-150)	RO-41; 31.2 J (23.0 ft-lbs)	RS-24; 32.5 J (24.0 ft-lbs)
- 73 (-100)	RO-13; 51.5 J (38.0 ft-lbs)	--
- 59 (-75)	RO-34; 69.8 J (51.5 ft-lbs)	RS-25; 94.2 J (69.5 ft-lbs)
- 46 (-50)	RO-35; 99.7 J (73.5 ft-lbs)	--
- 32 (-25)	RO-14; 116.5 J (86.0 ft-lbs)	--
- 4 (25)	RO-21; 130.9 J (96.5 ft-lbs)	RS-21; 114.6 J (84.5 ft-lbs)
21 (70)	RO-45; 141.0 J (104.0 ft-lbs)	RS-11; 119.3 J (88.0 ft-lbs)
93 (200)	RO-22; 145.8 J (107.5 ft-lbs)	RS-22; 126.8 J (93.5 ft-lbs)

In general, the specimens tested at the lower temperatures were characterized by mixed cleavage and microvoid coalescence (dimpled rupture). All specimens from the transition zone (including the -101°C tests) exhibited a narrow zone of dimpled rupture at the edge along the notch. An increasing degree of dimpled rupture was evident with increasing temperature to the point of 100% microvoid coalescence at room temperature and above. No significant degree of intergranular fracture was observed in any of the specimens.

The fractographic features of specimens tested at -101°C (-150°F) are illustrated in Figures 2-5 and 2-6. These specimens were characterized by flat fracture with a relatively rough texture over 95% of the cross-sectional area and small but well developed shear lips, see Figure 2-5(a). A zone of dimpled rupture is apparent at the bottom of the notch, see Figure 2-5(b). This feature is typical of all specimens tested at temperatures within the transition zone.

The typical fine-scale features of the flat fracture zones are shown in Figures 2-5(c) and 2-6(c) and (d). The fracture surface is characterized by a

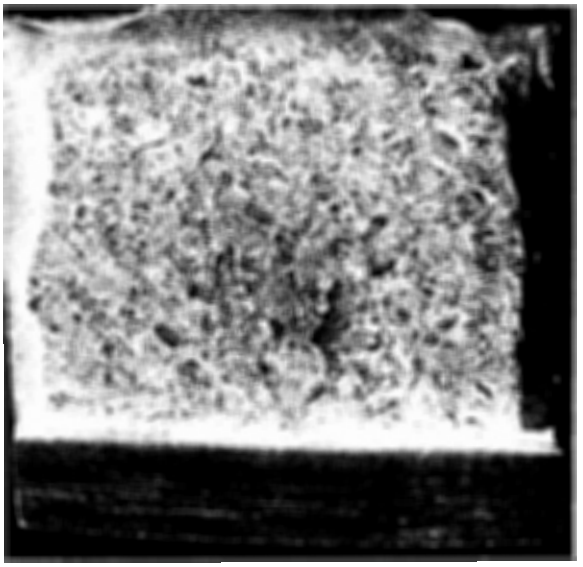

(a) ≃ 7X

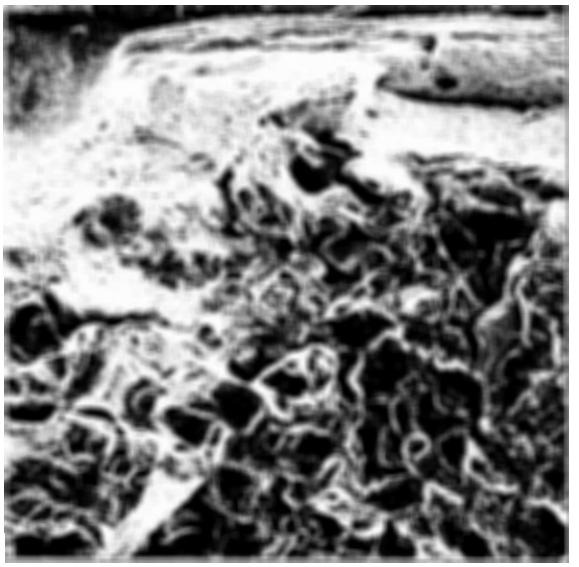

(b) At notch. 84X

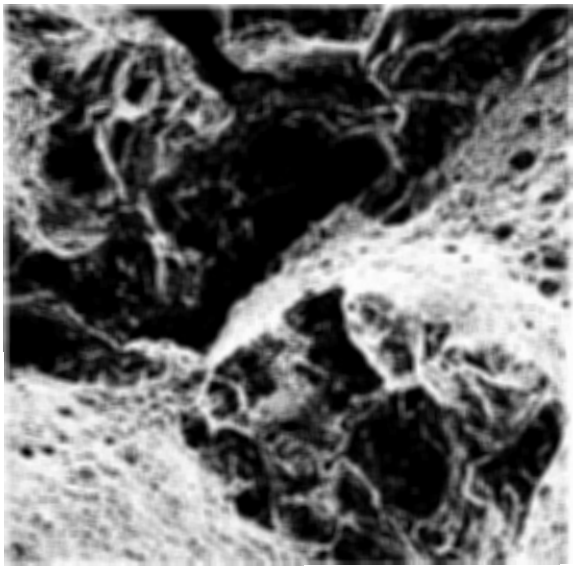

335X

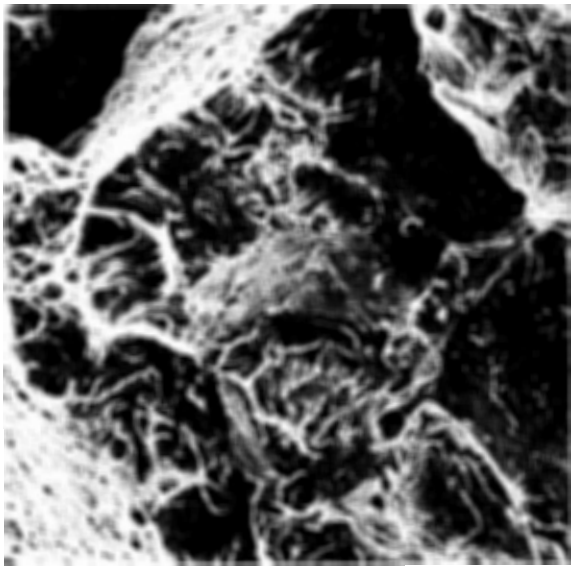

840X

(c) Location near notch

FIGURE 2-5. CHARPY IMPACT SPECIMEN TESTED AT -101°C(-150°F). Specimen RO-41, Plant C-1.

(These photographs reduced to 90% of their original size)

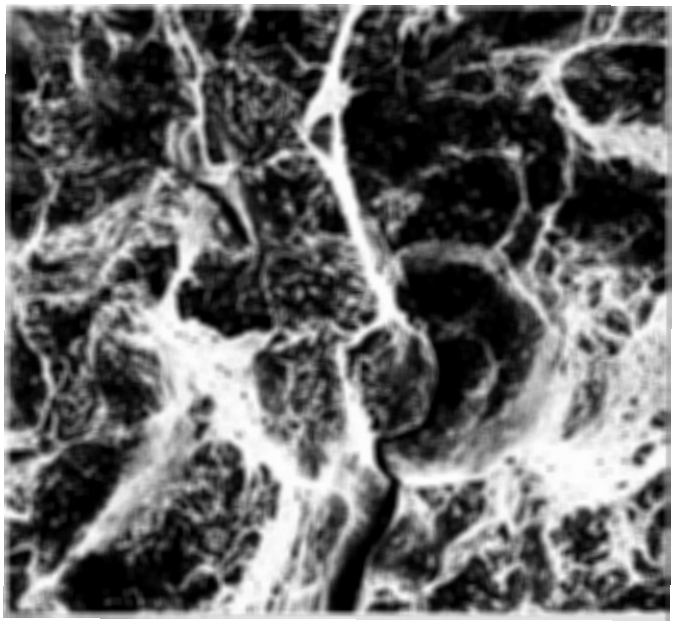

(a) Central Zone, RO-41. 335X

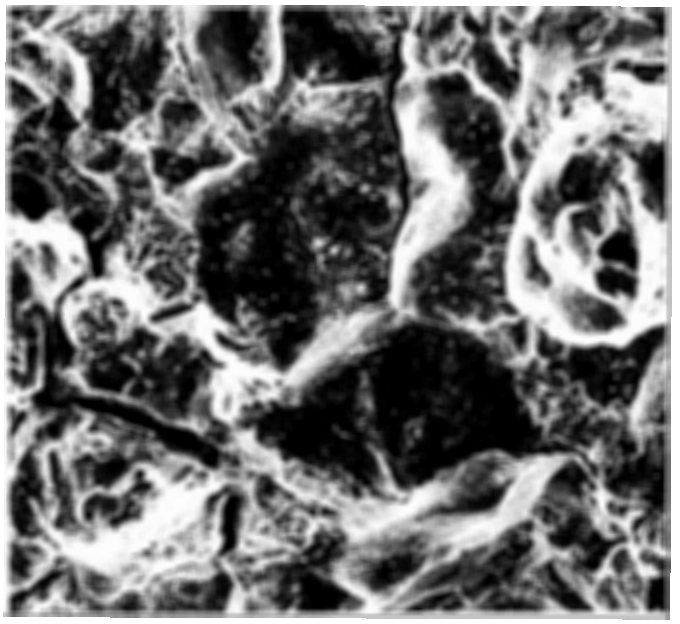

(b) Central Zone, RO-41. 335X

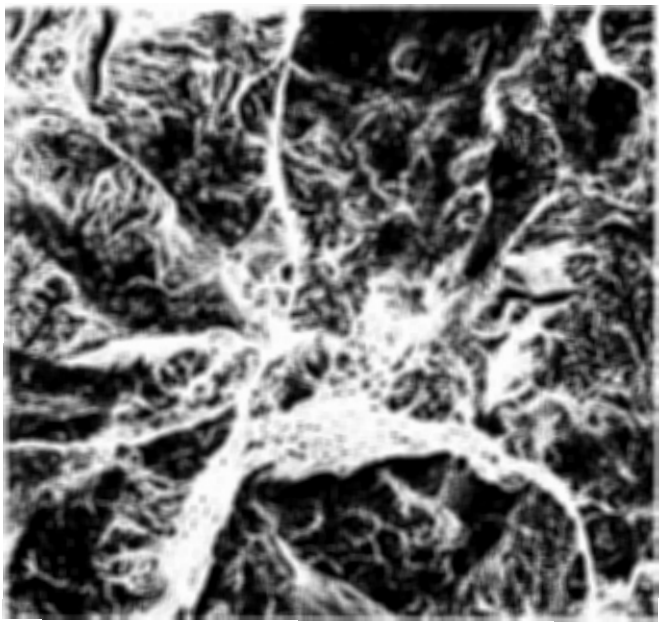

(c) Central Zone, RS-24. 335X

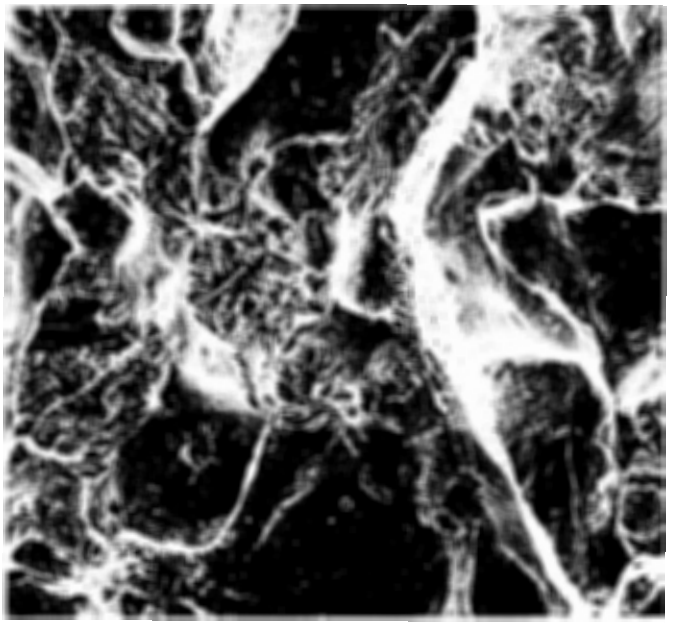

(d) Central Zone, RS-24. 335X

FIGURE 2-6. CHARPY IMPACT SPECIMEN TESTED AT -101°C(-150°F).
(a) and (b) Plant C-1; (c) and (d) Plant D-1.

predominance of cleavage with zones of small dimples at steps connecting cleavage zones. It should be noted that the features are different from those of classic, deformation free cleavage, indicating that some degree of plastic deformation was involved in the formation of the cleavage facets. Short, disconnected secondary cracks were also evident, especially at locations near the notch, see Figures 2-6(a) and (b). The shape of some of the secondary cracks suggest that they may be intergranular, but there was no evidence of linking up of any such cracks so that they do not represent a significant portion of the total fracture surface.

A number of isolated zones with smooth features were noted, see Figures 2-5(a), (b) and (c). Some of these smooth features are probably isolated large dimples [Figure 2-5(a)] while others are isolated intergranular facets. The only intergranular fracture observed was confined to 2-3 adjacent grains at widely dispersed locations.

SEM fractographs from specimens corresponding to the 50% fracture appearance transition temperature are shown in Figures 2-7 and 2-8. All areas within the flat fracture zones exhibited a mixture of cleavage and microvoid coalescence. The increased ductility, as compared to the -101°C specimens, is evidenced by more extensive patches of small dimples [Figures 2-7(a) and 2-8(b) and (c)] and more numerous large dimples [Figures 2-7(b) and (d)]. No significant degree of intergranular fracture was observed.

The typical fractographic features of specimens from the upper shelf region are illustrated in Figure 2-9. On a macroscopic scale, all specimens tested at room temperature or above were characterized by large shear lips and a predominantly ductile appearance. The microscopic features consisted of uniform, small equiaxed dimples.

SEM fractographs from other specimens from the ductile-brittle transition zone, demonstrating the increasing degree of microvoid coalescence with increasing test temperature and certain details of the fracture surfaces, are presented in Appendix B, Figures B-1 through B-4.

(a) ≃ 7X

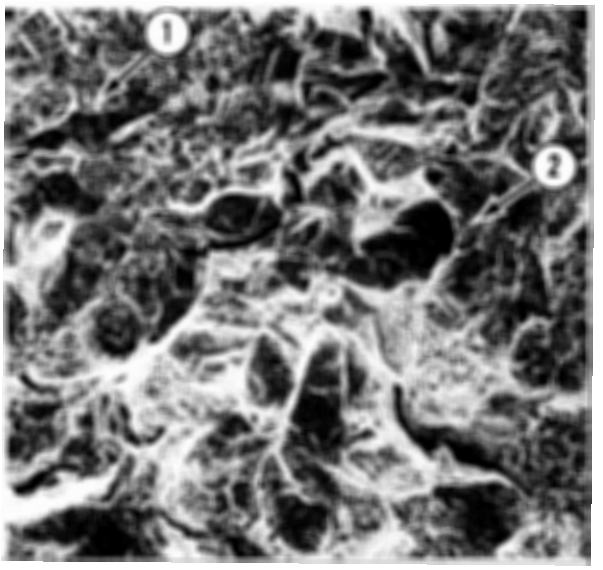

(b) Central Zone. 84X

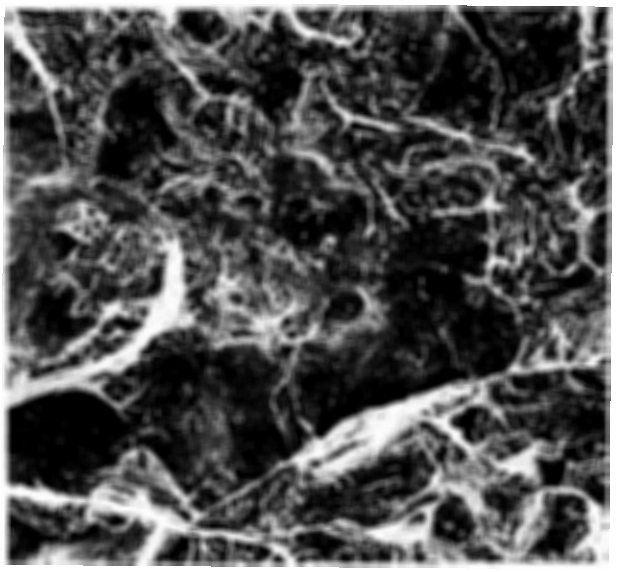

(c) Location 1 in (b). 335X

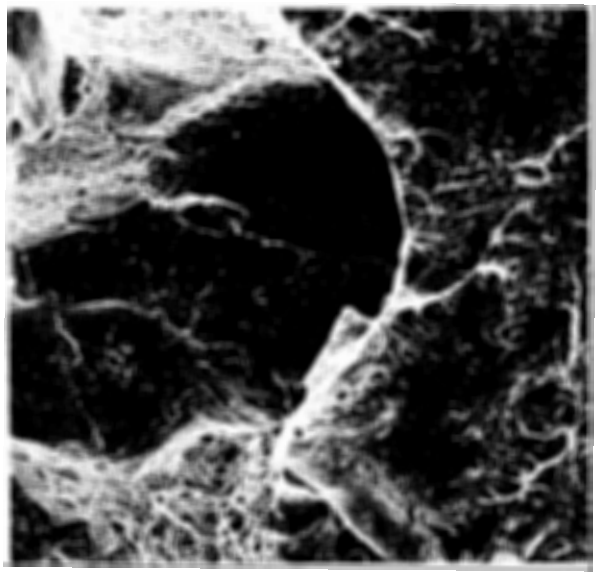

(d) Location 2 in (b). 335X

FIGURE 2-7. CHARPY IMPACT SPECIMEN TESTED AT -59°C(-75°F).
Specimen RO-34, Plant C-1.

(These photographs reduced to 90% of their original size)

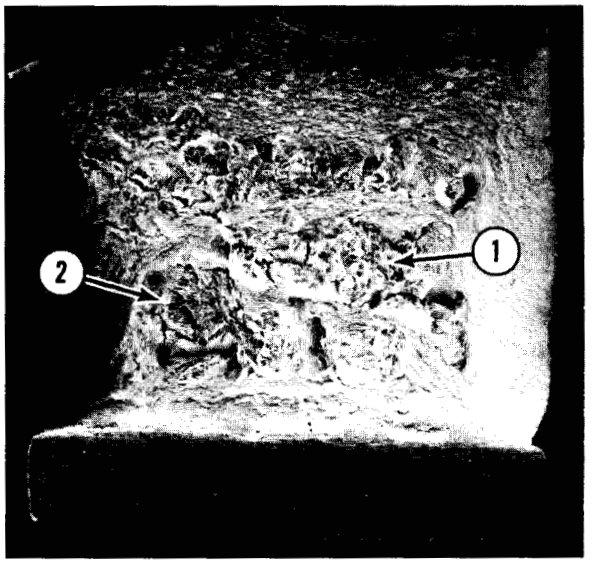

(a) ≈ 7X

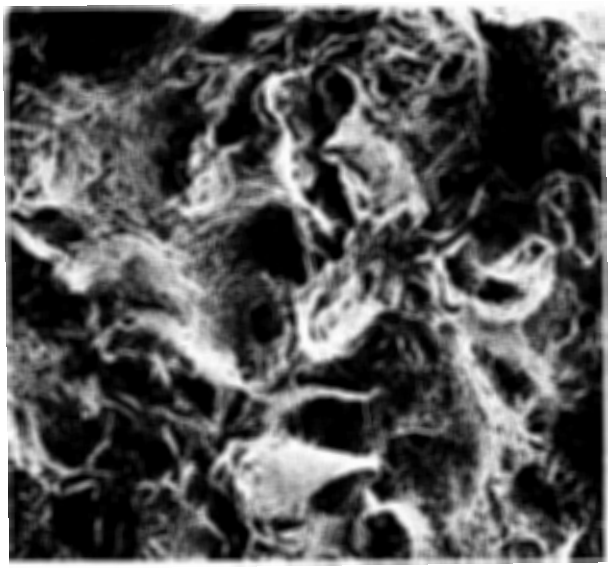

(b) Location 1 in (a). 84X

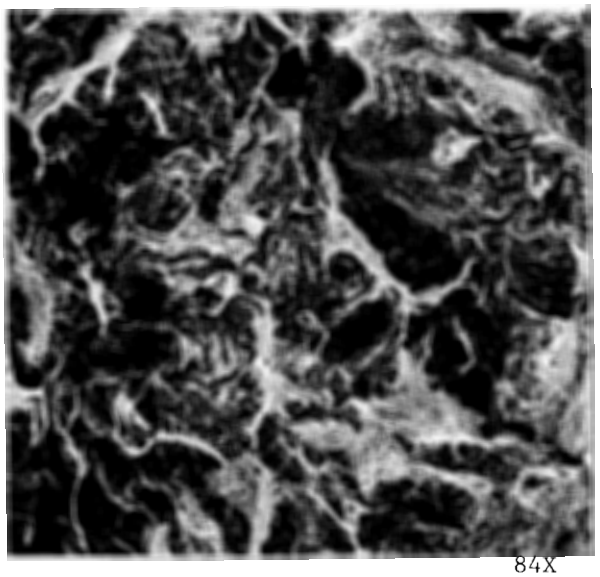

84X

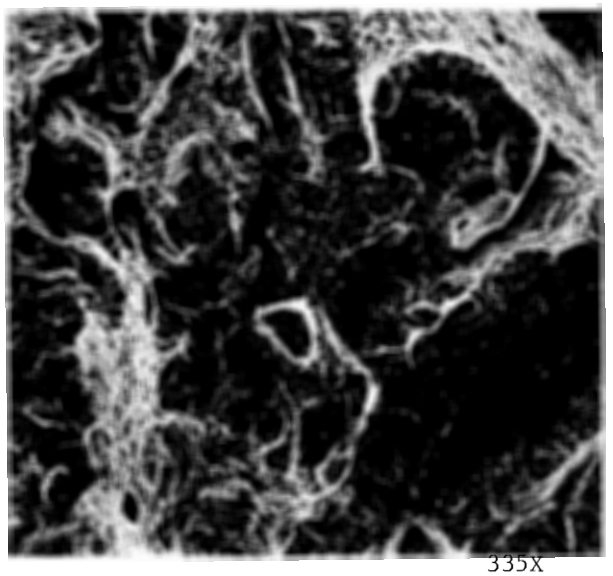

335X

(c) Location 2 in (a)

FIGURE 2-8. CHARPY IMPACT SPECIMEN TESTED AT -59°C(-75°F). Specimen RS-25, Plant D-1.

(These photographs reduced to 90% of their original size)

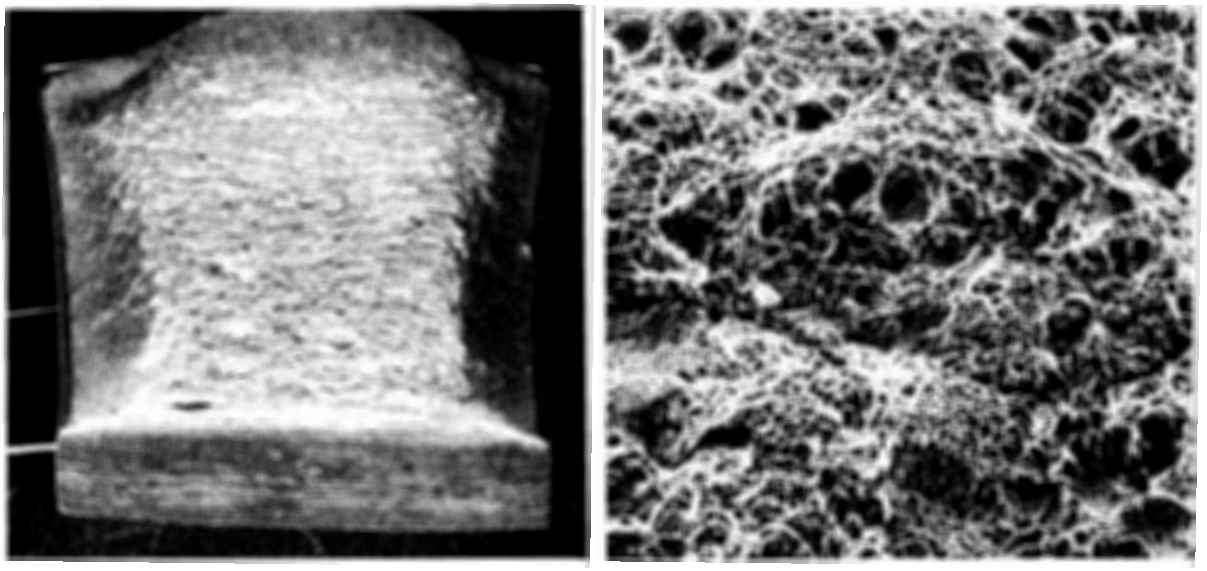

≃ 7X 335X

(a) Specimen RS-11. 21°C(70°F).

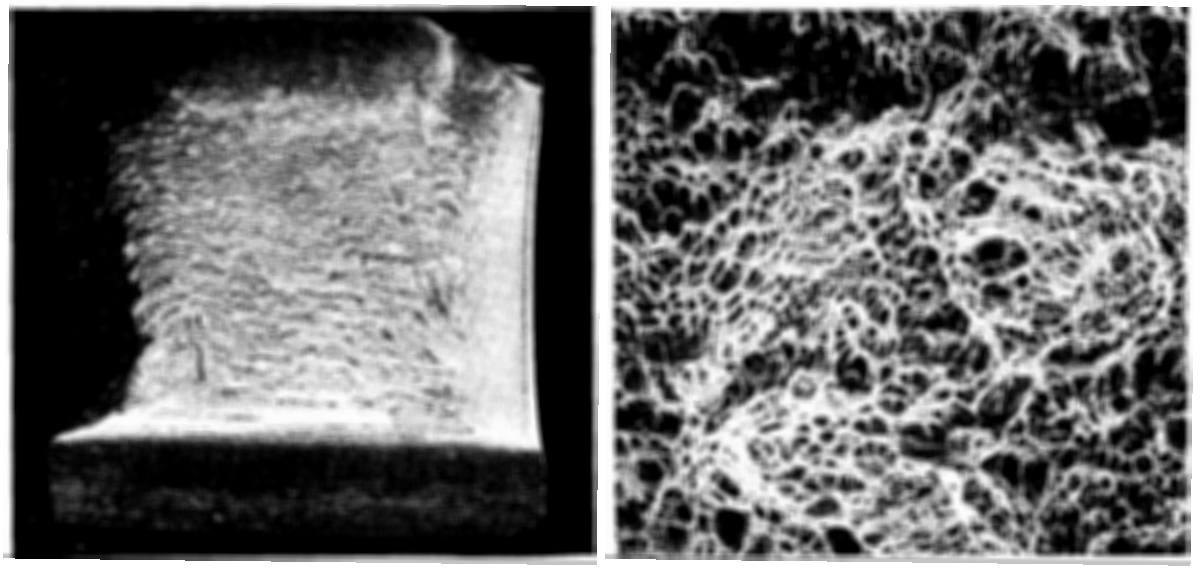

≃ 7X 335X

(b) Specimen RS-22. 93°C(200°F).

FIGURE 2-9. CHARPY IMPACT SPECIMENS REPRESENTATIVE OF UPPER SHELF REGION.

(These photographs reduced to 90% of their original size)

Section 3

COMPOSITION AND MICROSTRUCTURE

Specimens from each of the three available disc materials were analyzed to determine the composition of the elements specified by ASTM A 471. The results of these analyses are presented in Table 3-1. The compositions of the three samples are essentially identical and all three materials conform to the compositional requirements of A 471 Cl. 5 in every respect.

The three disc materials were also analyzed by atomic absorption techniques to determine the arsenic, antimony and tin contents. These elements are known to segregate at prior austenitic grain boundaries and can promote temper embrittlement in the NiCrMoV alloy steels. It is conceivable that the grain boundary concentration of these elements could influence susceptibility to IGSCC.

The results of the trace element analyses are presented in Table 3-2. The analyses indicate a fairly uniform concentration of each of the three elements over the three disc samples. The As and Sb contents were determined to be in the order of 0.005 wt.% and 0.002 wt.%, respectively, while the Sn content is in the range of 0.012 to 0.021 wt.%. These values are all within the range of trace element composition generally considered as normal for NiCrMoV alloy steels. No critical composition of these elements, with regard to temper embrittlement of the NiCrMoV alloy steels, has been firmly established and there is no data available on the influence of these elements on IGSCC susceptibility. As a result, there is no basis for evaluation of the trace element composition data at present. The results are reported as one additional parameter for characterizing the materials.

Table 3-1

COMPOSITION OF DISC MATERIAL

Material Identification	Composition - Wt. %									
	C	Mn	Si	Cr	Ni	Mo	V	Cu	P	S
Plant C-1	0.27	0.25	0.03	1.72	3.43	0.37	0.14	0.11	0.007	0.008
Plant D-1	0.25	0.26	0.03	1.70	3.45	0.37	0.14	0.15	0.006	0.009
Plant E-1	0.25	0.23	0.02	1.63	3.58	0.36	0.13	0.12	0.010	0.010
ASTM A471 Class 5	0.35 max	0.70 max	0.10* max	0.75-2.00	2.00-4.00	0.20-0.70	0.05 min	--	0.015 max	0.015 max

*When vacuum deoxidation is specified.
Otherwise Si content is 0.15-0.35

Table 3-2

TRACE ELEMENT ANALYSES

Material Identification	Composition - µg/gm (wt.%)		
	As	Sb	Sn
Plant C-1	47-62 (0.0047-0.0062)	15-18 (0.0015-0.0018)	115 (0.0115)
Plant D-1	34-64 (0.0034-0.0064)	16-20 (0.0016-0.0020)	148-211 (0.0148-0.0211)
Plant E-1	47-60 (0.0047-0.0060)	22-25 (0.0022-0.0025)	157-180 (0.0157-0.0180)

Note: The tabulated ranges of composition are the results of independent analyses at two laboratories.

Metallographic specimens of each of the three disc materials were examined to determine the relative grain boundary etching sensitivity. The specimens were prepared in a single mount and immersion etched for 90 minutes in a saturated aqueous solution of picric acid plus 1% sodium tridecylbenzene sulfonate. The microstructural features developed by this etching procedure are shown in Figure 3-1. In each case, the grain boundaries are clearly delineated but the boundaries are only lightly etched. No differences in grain boundary structure or grain boundary etching response was noted among the three specimens.

The etching sensitivity of a material to this particular reagent is a function of grain boundary phosphorus content(1). In general, the degree of etching of the boundaries increases with increasing phosphorus content. The observed etching response provides evidence of phosphorus segregation at grain boundaries in all three samples. However, this etching effect is not necessarily indicative of abnormally high phosphorus content or of an abnormal degree of grain boundary segregation.

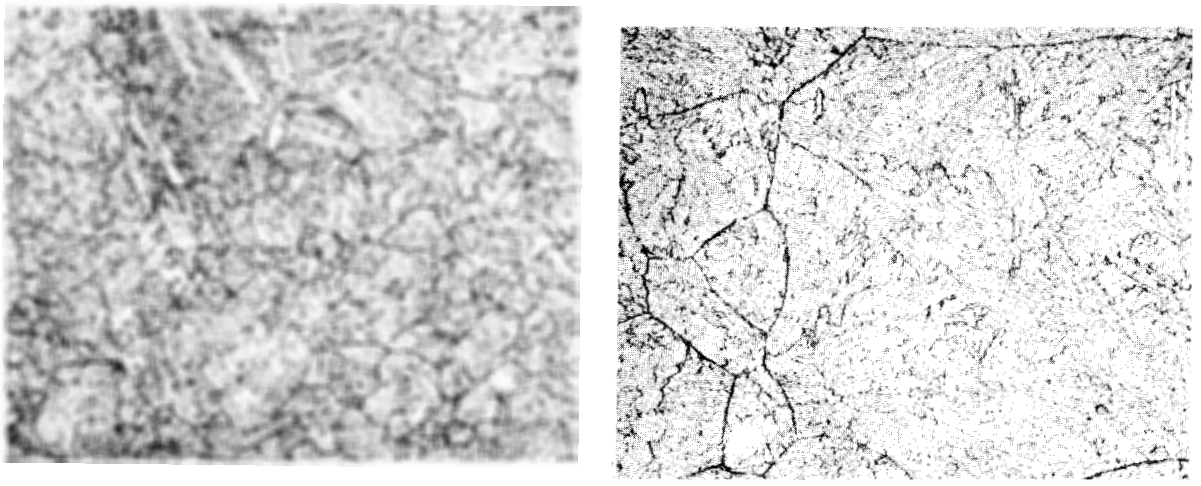

144X 720X

(a) Plant C-1

FIGURE 3-1. MICROSTRUCTURE OF DISC MATERIAL.

(These photographs reduced to 75% of their original size)

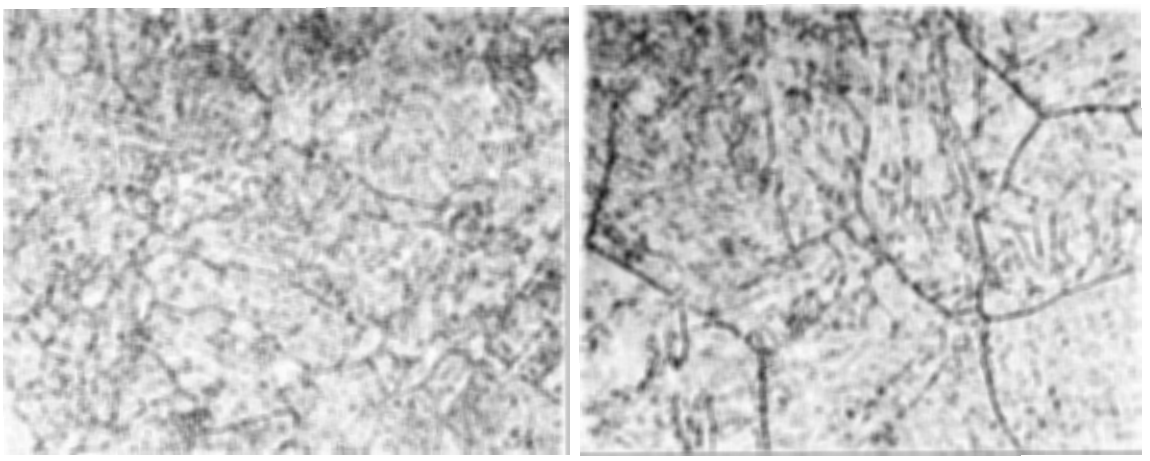

144X 720X

(b) Plant D-1

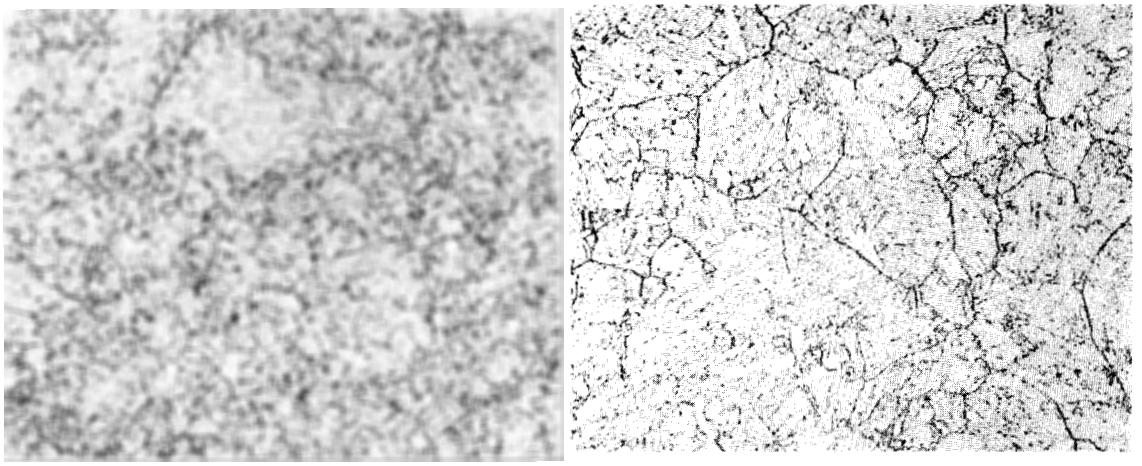

144X 720X

(c) Plant E-1

FIGURE 3-1 (CONTINUED). MICROSTRUCTURE OF DISC MATERIAL.

(These photographs reduced to 73% of their original size)

Section 4

POTENTIODYNAMIC POLARIZATION MEASUREMENTS

Potentiodynamic polarization tests were performed to investigate the electrochemical behavior of the disc materials in a concentrated caustic solution and in essentially pure water. This test involves the imposition of a variable potential on a specimen exposed to the test environment and measurement of the current density as a function of applied potential.

A schematic diagram of a polarization curve for an iron-base alloy exposed in a strongly alkaline solution is shown in Figure 4-1. The solid curve is the typical potential vs log current density trace recorded from a polarization test. This curve is the sum of the anodic current (dissolution of iron, e.g., $Fe \rightarrow HFeO_2^-$) and the cathodic current (reduction of hydrogen, $H^+ \rightarrow H^\circ$). The free corrosion potential lies at the value at which the anodic and cathodic currents are equal. Since the recorded current density is the sum of these two currents, the point at which current density decreases to zero corresponds to the free corrosion potential (point E_c in Figure 4-1). The value of current i_c, corresponding to the intersection of the anodic and cathodic reaction curves, is the free corrosion current and is a measure of the corrosion rate of the specimen material under freely corroding conditions where iron is oxidized to soluble $HFeO_2^-$. As the corrosion potential is increased above E_c values are reached where Fe_3O_4 and Fe_2O_3 can be formed (regions B-C and C-D in Figure 4-1). These oxides form partially and fully protective layers, respectively, and reduce the corrosion rate. The region in which the protective Fe_2O_3 layer is formed is termed the passive region (region C-D in Figure 4-1). At potentials above D the stable films begin to dissolve and soluble species, e.g. FeO_2^{--}, form with a corresponding increase in corrosion rate.

It is generally recognized that mild steels and low alloy steels are susceptible to caustic SCC only within a limited potential range. Studies of the polarization behavior of mild steels and low alloy steels have established that the regions of high anodic activity overlap the potential ranges in which SCC occurs.(2,3) These regions include the ranges of potential where conditions are

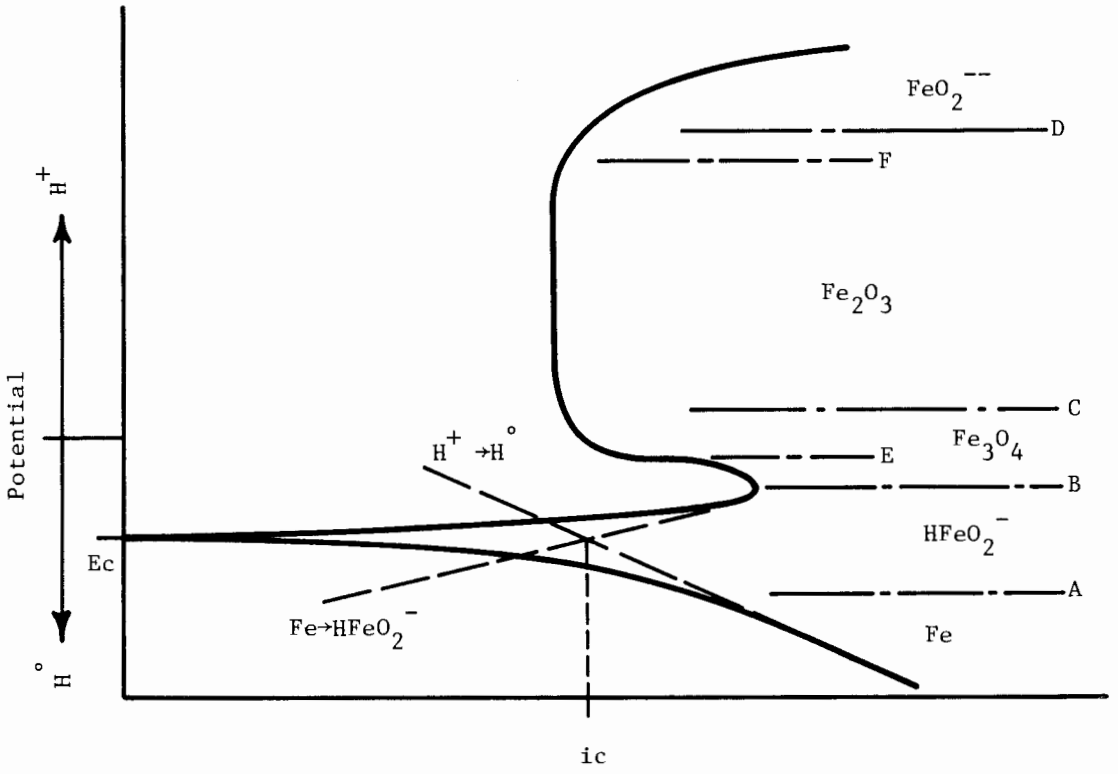

FIGURE 4-1. SCHEMATIC POLARIZATION CURVE.

borderline between the formation of a stable protective film and active dissolution of the base metal. In terms of the polarization curve there are two such critical potential regions in which caustic SCC is likely to occur. These are designated as regions E-C (lower cracking region) and F-D (upper cracking region) in Figure 4-1. Under some conditions, the lower cracking range may extend below the anodic peak, i.e., into the active corrosion region, A-B.

It has also been observed that polarization curves determined at fast and slow potential scan rates may show substantial differences in current density in certain ranges of applied potential. Such differences represent the ratio of the corrosion rates experienced when protective films are ruptured and bare metal is exposed. The potential ranges corresponding to large differences in current density in potentiodynamic polarization tests frequently correlate with the critical potential ranges for SCC. Parkins (3) has suggested that differences in current of an order of magnitude or greater are an indication of susceptibility to SCC. Considering the factors discussed above, potentiodynamic polarization tests provide one means of evaluating the susceptibility of low alloy steels to SCC in particular environments. Polarization curves have been used to predict the incidence of SCC in systems which were not suspected to be conducive to SCC.(4)

Polarization tests were performed on each of the three disc materials in a deoxygenated 28% aqueous NaOH solution and in deionized and deoxygenated water* at 93.3°C (200°F) and 37.8°C (100°F). The fast and slow potential scans were made at 0.02 volts/sec and 0.001 volts/sec, respectively, utilizing an Aardvark Model V-2LR potentiostat.

The potentiodynamic polarization curves obtained for the three disc materials in the caustic solution were generally similar and exhibited features characteristic of an iron-base alloy in a high-pH solution. The curves obtained at 93.3°C (200°F) are shown in Figures 4-2, 4-3 and 4-4. The indicated corrosion potentials at 93.3°C (200°F) were in the range of -1.10 to -1.22 volts. Regions of anodic activity were observed for both the fast scan and slow scan at potentials in the range of -0.9 to -1.0 volts. Definite passive zones,

*0.01 M Na_2SO_4 added to provide the conductivity necessary for polarization tests.

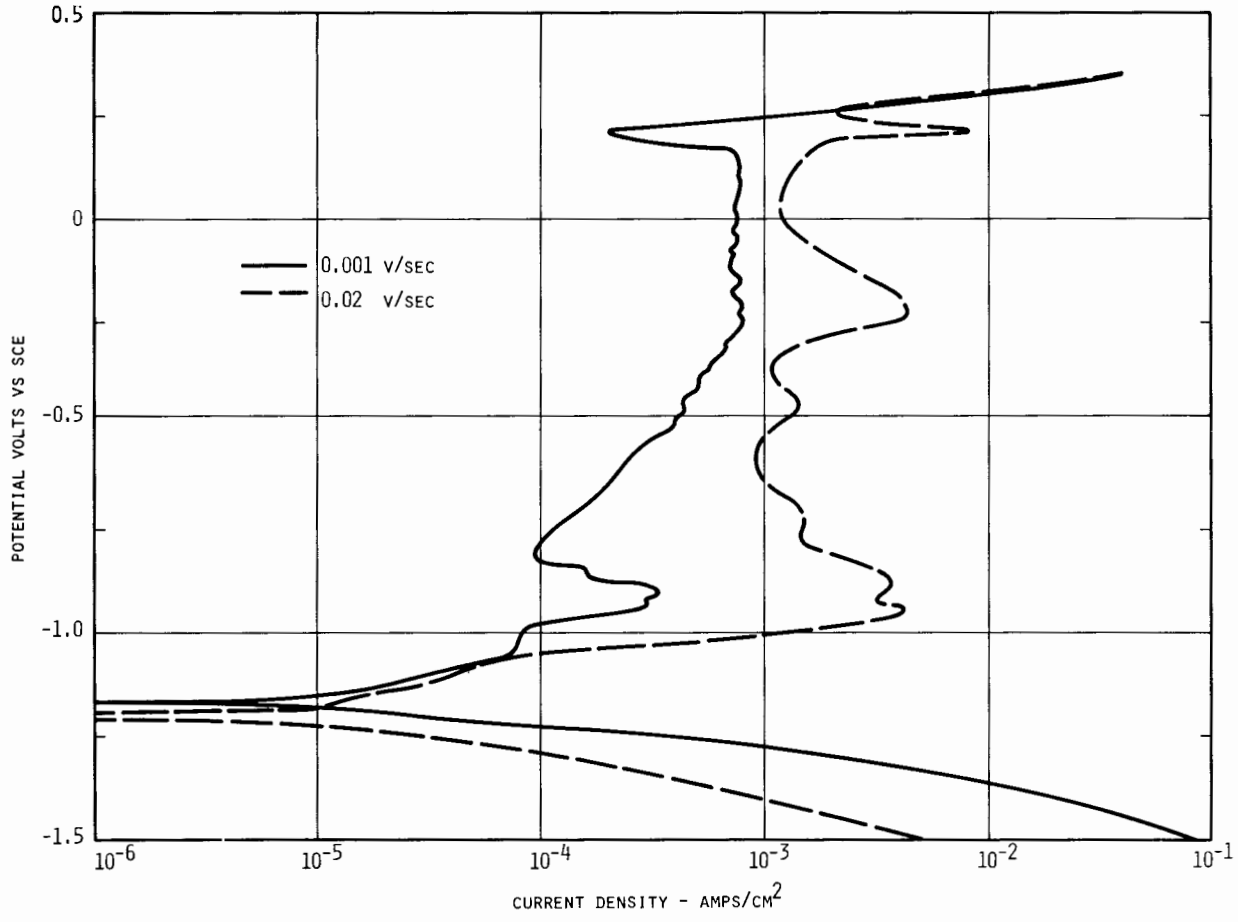

FIGURE 4-2. POLARIZATION CURVE. C-1 Disc material. 28% NaOH, 93.3°C (200°F).

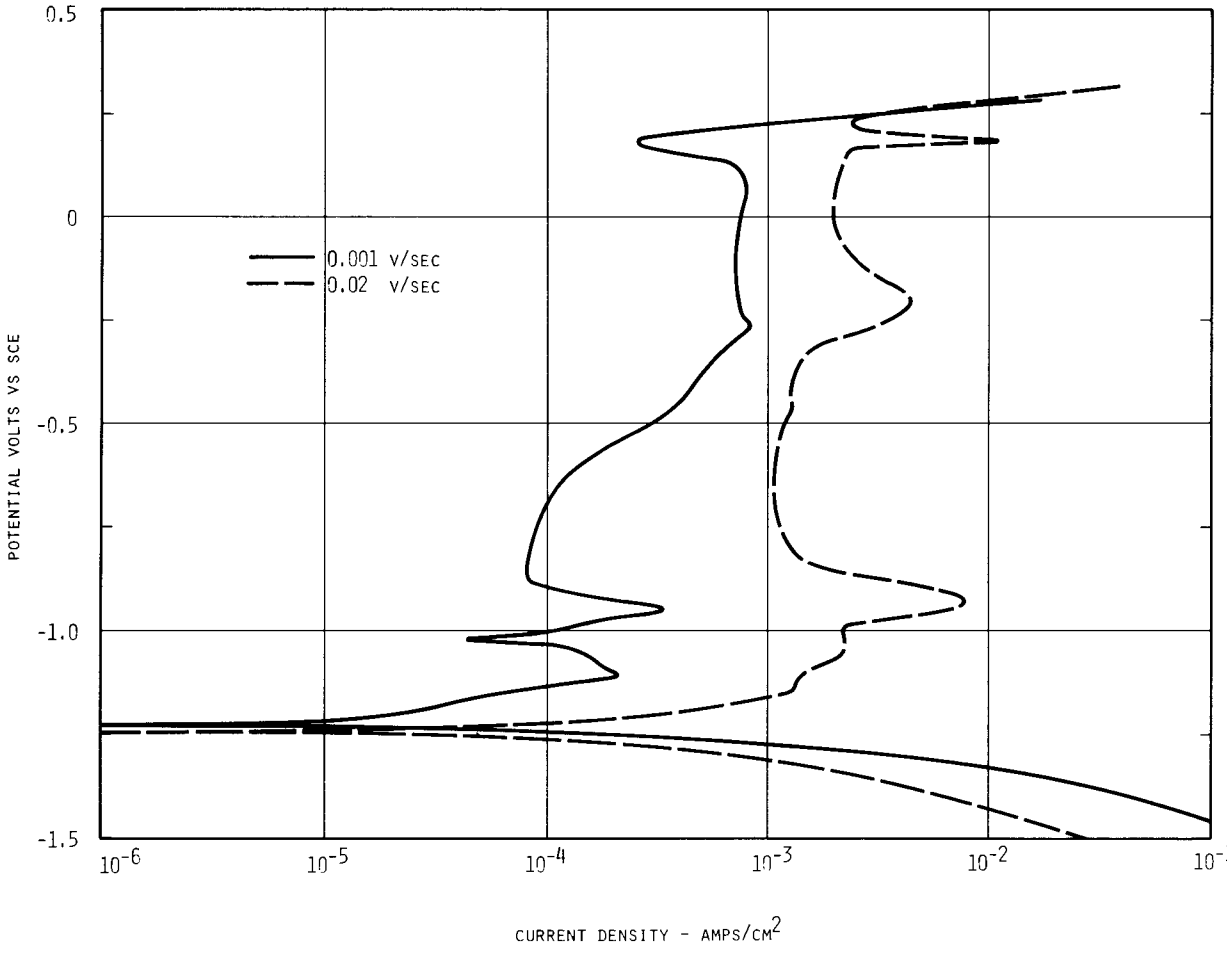

FIGURE 4-3. POLARIZATION CURVE. D-1 Disc material. 28% NaOH, 93.3°C (200°F).

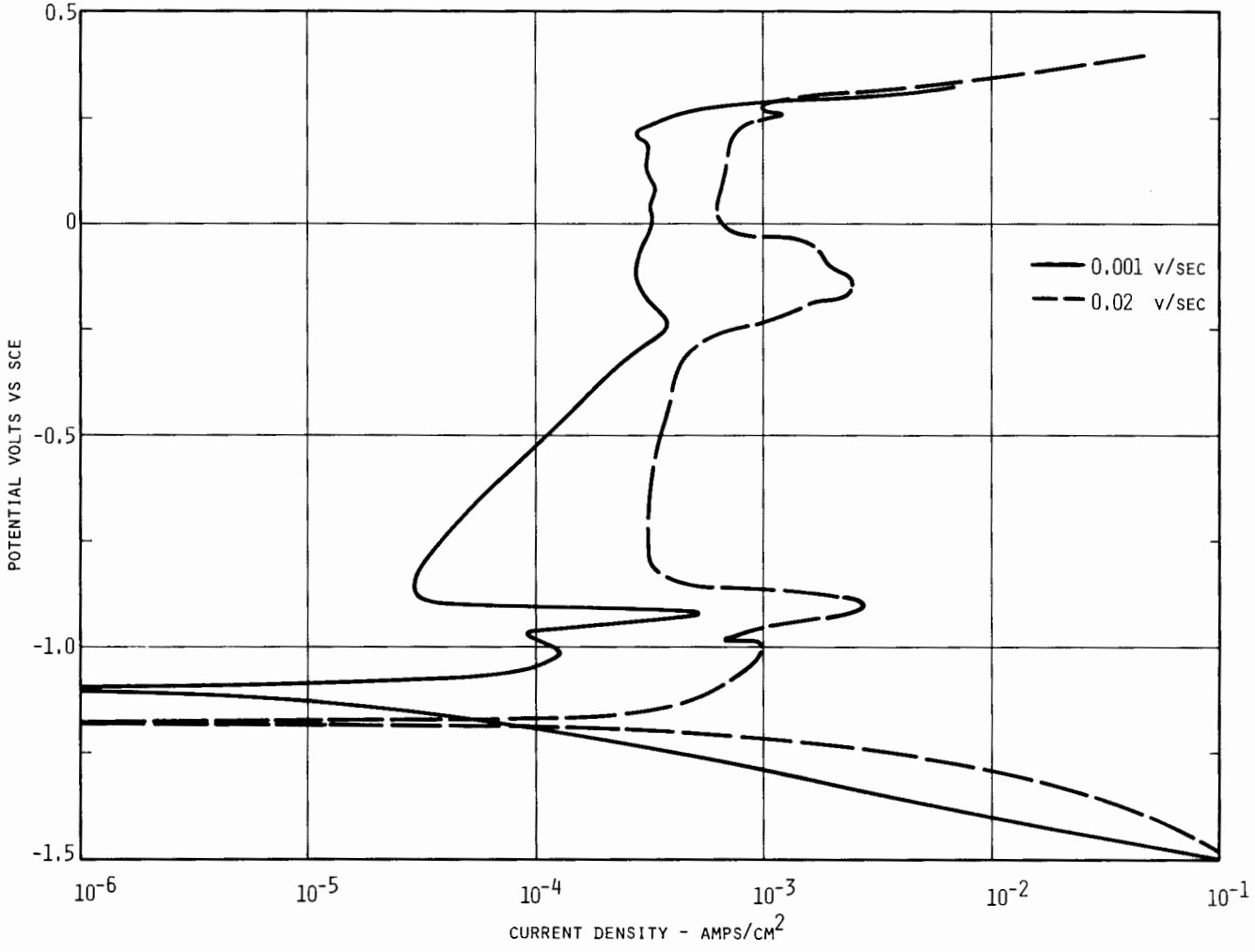

FIGURE 4-4. POLARIZATION CURVE. E-1 Disc material. 28% NaOH, 93.3°C (200°F).

extending over a potential range of -0.90 to 0.20 volts, were observed for all three materials.

At potentials near the lower anodic peak (-0.8 to -1.1 volts) the current densities for the slow and fast scans differ by an order of magnitude or more in all three cases. By Parkins' criterion, this factor is an indication of susceptibility to SCC and together with the distinct lower anodic peak identifies a lower cracking region. In the case of the C-1 disc material the indicated lower cracking region occurs in the potential range of -0.82 to -0.98 volts. In this region the maximum value of the ratio of current densities (fast-scan/slow-scan is 22, see Figure 4-2. In the corresponding regions of the polarization curves for the D-1 and E-1 materials, the current density ratios were 50 and 77 respectively, see Figures 4-3 and 4-4. These results suggest a lower degree of susceptibility for the C-1 material. For the fast potential scans the D-1 material exhibited the highest value of maximum current density ($8x10^{-3}$ vs $2.8x10^{-3}$ and $4.1x10^{-3}$ amps/cm^2) indicating a higher corrosion rate for bare metal.

Some differences in the polarization behavior of the three materials were also noted at potentials below the maximum anodic current density and just above the free corrosion potential. In the case of the C-1 material the lower portions of the fast scan and slow scan curves are nearly superimposed so that at any given potential the difference in current for the two scans is small. In contrast, the low-potential portions of the curves for the D-1 and E-1 material are displaced so that large differences in current exist at a given potential in the range of -1.0 to -1.2 volts. By Parkins' criterion, this suggests the possibility of SCC susceptibility for the D-1 and E-1 materials at potentials just below the free corrosion potential, if a surface oxide can be formed in this potential range. Formation of a protective oxide is unlikely in this range of potentials, since Fe_3O_4 normally does not occur at potentials below the lower major anodic peak. However, definite differences in the anodic dissolution kinetics of the fast and slow curves exist in this range. One possible explanation may be adsorption of hydroxide ions onto the surface. In view of the differences in anodic kinetics (abbeit, the cause is unclear), further investigation of SCC susceptibility in this range is warranted.

The features of the lower cracking regions of the polarization curves suggest a difference in degree of SCC susceptibility among the three materials and suggest a ranking in the order of increasing susceptibility as follows:

1) C-1 disc material; lowest value of maximum current density ratio.
2) E-1 disc material; higher value of maximum current density ratio.
3) D-1 disc material; higher value of maximum current density ratio and highest absolute value of current density (i.e., highest bare-metal corrosion rate).

The upper portions of the three polarization curves are similar in that a sharp increase in current density occurs at potentials above 0.2 volts for the slow scan curve in all cases. This increase in current density corresponds to the point of dissolution of the protective films, point D in Figure 4-1. In general, the region immediately below this change in current is a zone of possible SCC susceptibility. In the case of the C-1 and D-1 materials, a marked increase in current for the fast scan and a marked decrease in current for the slow scan occurred at a potential of approximately 0.2 volts, see Figures 4-2 and 4-3. This factor results in a significant difference between the fast scan and slow scan currents (current density ration of 40) and suggests that these materials may be particularly susceptible to the SCC in the upper cracking region. The E-1 disc material did not exhibit a large anodic peak at the high potential end of the polarization curve, see Figure 4-4.

The results of the 37.8°C (100°F) test on the C-1 material in the caustic solution are presented in Figure 4-5. The indicated free corrosion potential is -1.13 volts and the shape of the polarization curve is generally similar to that of the 93.3°C test. Within the passive zone the absolute current values were reduced by an order of magnitude from those measured at the higher temperature. The difference in the current between the slow and fast scans were comparable to or less than those of the 93.3°C test over the entire potential range. These factors are indicative of a lower degree of SCC susceptibility at the lower temperature. In view of these results, no further tests were conducted at 37.8°C.

The polarization curves obtained for the three disc samples in deoxygenated water are shown in Figures 4-6, 4-7 and 4-8. The free corrosion potentials indicated in these tests were in the range of -0.75 to -0.85 volts. No anodic peak was observed for any of the materials and the current differences between the fast scan and slow scan curves were relatively small. No distinct passive zone was evident in any case. The C-1 material exhibited a zone of restricted

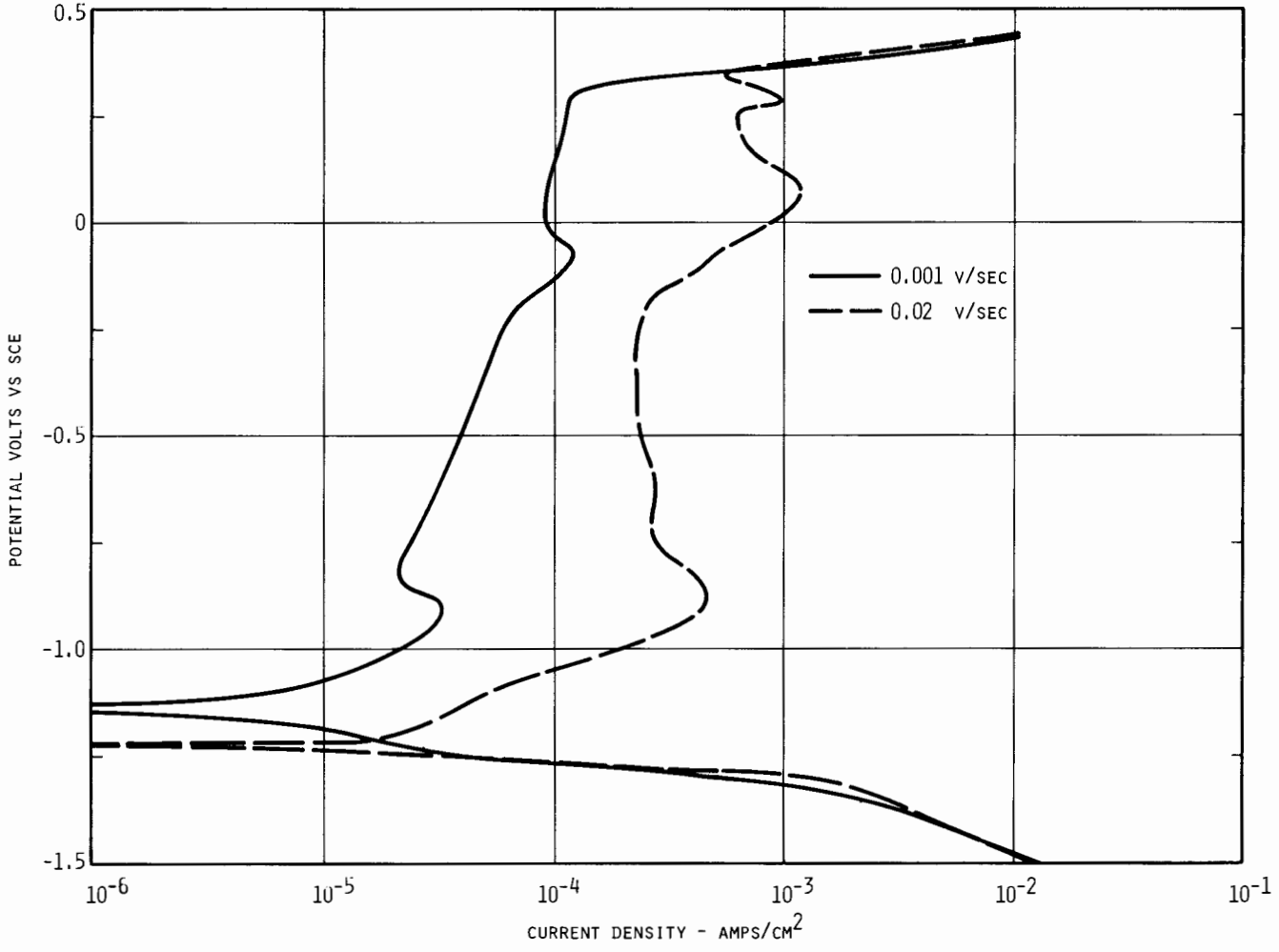

FIGURE 4-5. POLARIZATION CURVE. C-1 Disc material. 28% NaOH, 37.8°C (100°F).

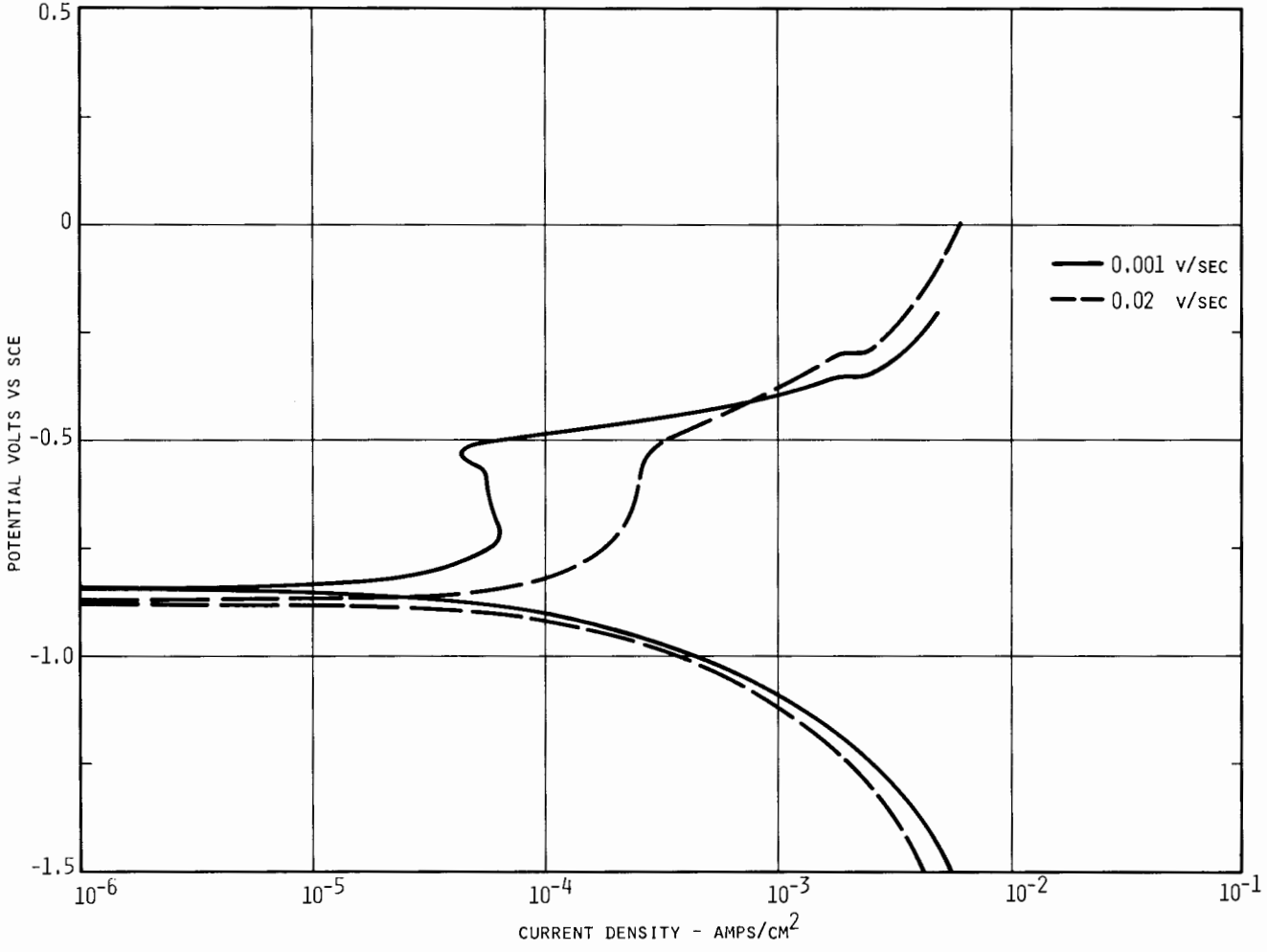

FIGURE 4-6. POLARIZATION CURVE. C-1 Disc material. H_2O + 0.01M Na_2SO_4, deoxygenated. 93.3°C (200°F).

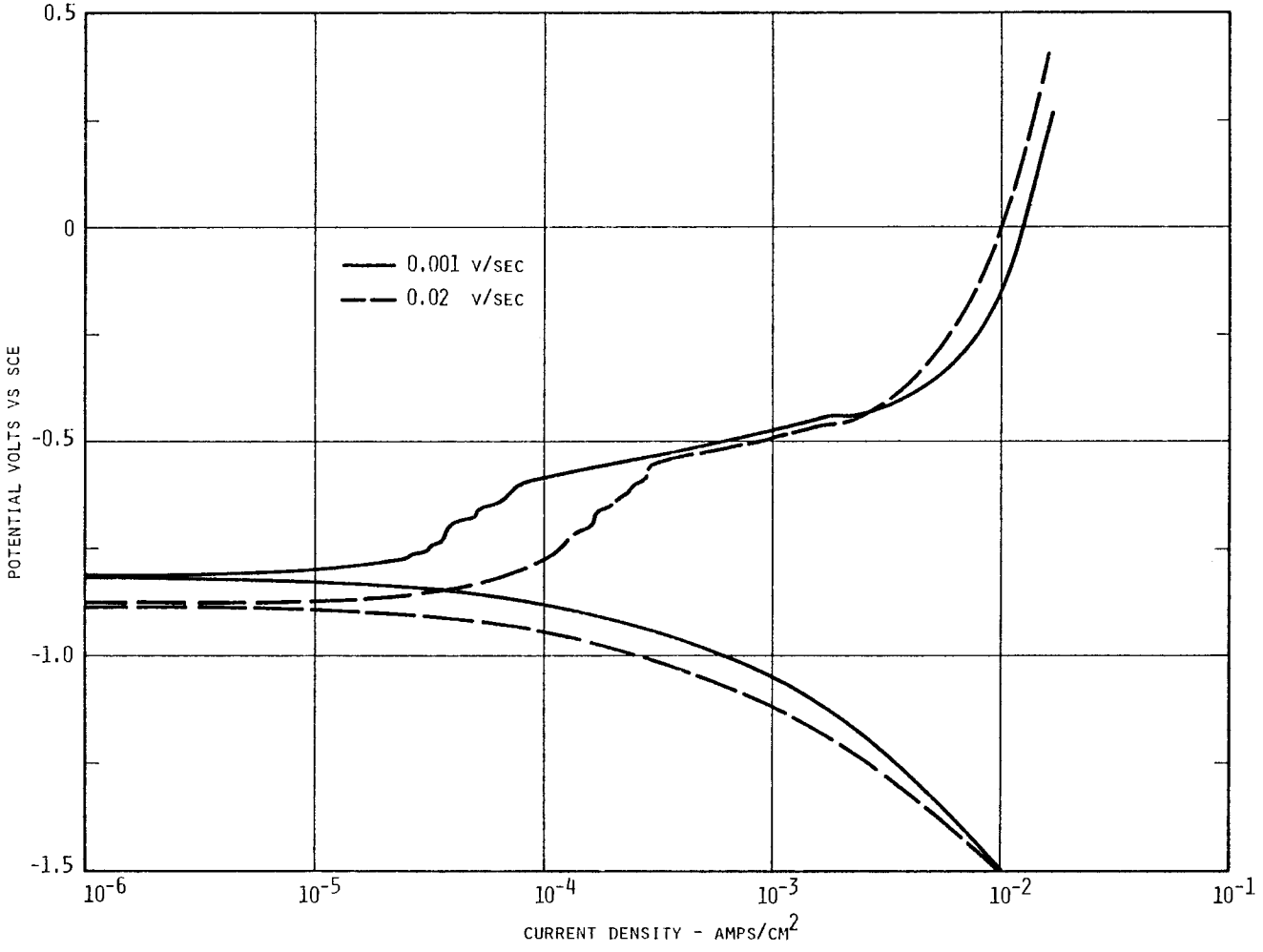

FIGURE 4-7. POLARIZATION CURVE. D-1 Disc material. H_2O + 0.01M Na_2SO_4, deoxygenated. 93.3°C (200°F).

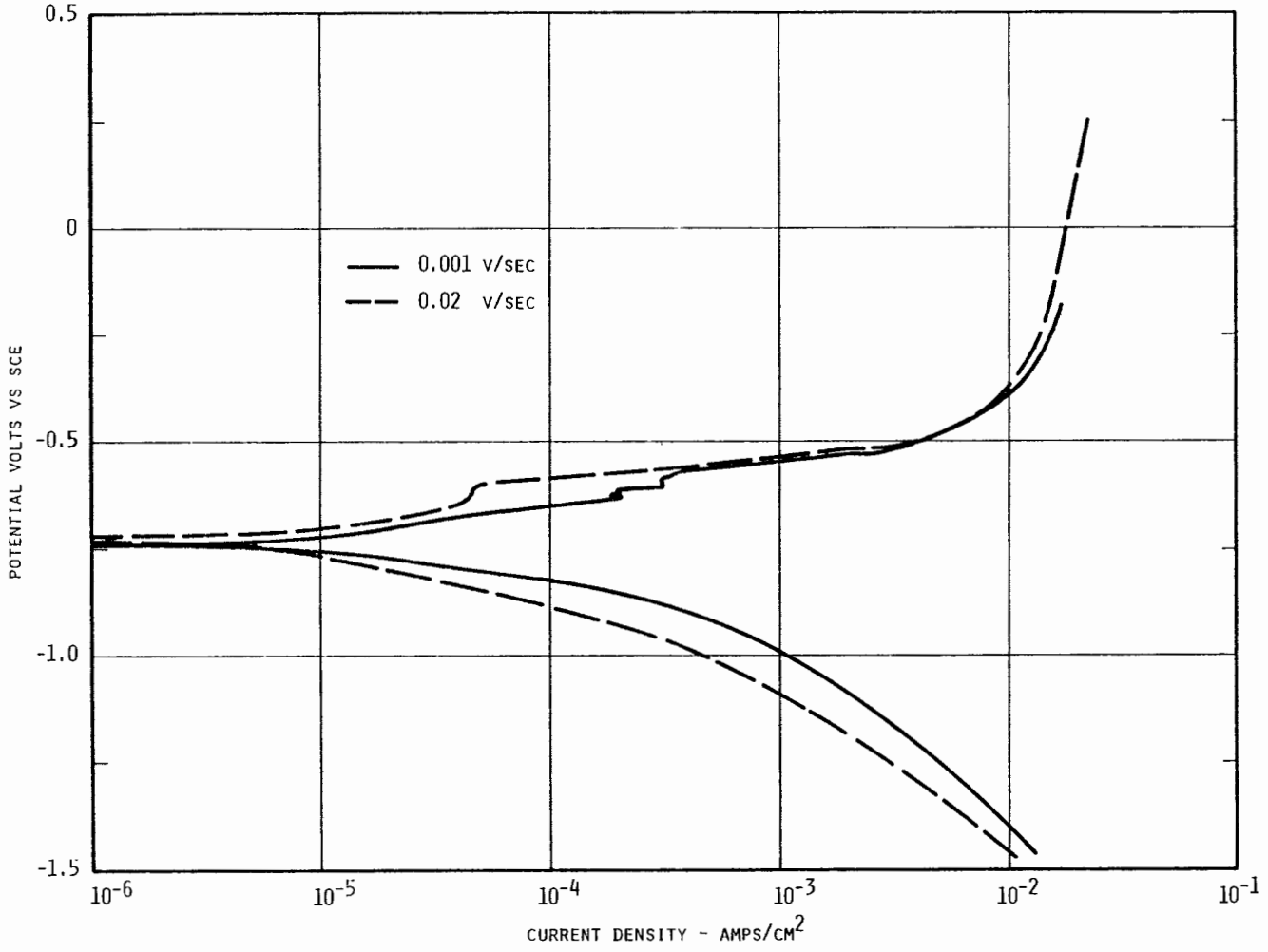

FIGURE 4-8. POLARIZATION CURVE. E-1 Disc material. H_2O + 0.01M Na_2SO_4, deoxygenated. 93.3°C (200°F).

dissolution over a potential range of -0.75 to -0.5 volts but active corrosion (at a very low corrosion rate) was indicated at all potentials above the free corrosion potential for the D-1 and E-1 materials. The results of the polarization tests in deionized water did not provide any evidence of SCC susceptibility for any of the three disc materials.

In summary, indications of susceptibility to caustic SCC at particular values of imposed potential were obtained for all three materials at 93.3°C. On the basis of the polarization data the C-1 material appears to be the least susceptible of the three materials tested. In the case of the D-1 and E-1 materials the electrochemical behavior suggests possible susceptibility at potentials at or near the free corrosion potential. Also, anodic activity was observed for the C-1 and D-1 material at high potentials indicating the possibility of susceptibility to SCC in the upper cracking region. No indications of SCC susceptibility were observed in any of the polarization tests conducted in deionized water.

Polarization data cannot be considered as an absolute means of predicting the SCC behavior of a particular system. The information obtained can only serve as a guide to direct SCC testing or to supplement SCC test data. In the present case, the results indicate specific areas in which further evaluation of the SCC susceptibility of the disc materials is warranted. Controlled potential, slow strain rate tests should be conducted to provide direct SCC data for the conditions where susceptibility is indicated by the polarization tests. In particular, tests at high potentials in caustic solutions, corresponding to the anodic activity observed in the upper cracking region, and tests at controlled potentials near the free corrosion potential should be performed. The upper zone is of particular interest because British data (4) indicate that the corrosion potentials of 3 CrMo steels exposed to caustic solutions become more positive with increasing exposure time. Potential increases of 0.50 to 0.85 V have been observed, depending upon the caustic concentration. No such data are available for 3-1/2 NiCrMoV steels; if they behave similarly, then the steady state potential may well be in or near the possible upper cracking zone.

REFERENCES

1. A. H. Ueisik, C. J. McMahon and H. C. Feng, "The Influence of Intercritical Heat Treatment on the Temper Embrittlement Susceptibility of P-Doped Ni-Cr Steel," Met. Trans., Vol. 9A, March 1978, p. 321.

2. K. Bohnenkamp and E. Riecke, "Intergranular Stress Corrosion Cracking of Mild Steels in Concentrated Sodium Hydroxide Solutions," Proceedings of the Third International Congress on Metallic Corrosion, Vol. 2, pg. 333 (1966).

3. M. J. Humphries and R. N. Parkins, "Stress Corrosion Cracking of Mild Steel in Sodium Hydroxide Solutions Containing Various Additional Substances," Corrosion Science, Vol. 7, pg. 747 (1967).

4. J. F. Newman, "The Polarization Behavior of 3% CrMo Steel in Sodium Hydroxide Solution and Its Relationship to Stress Corrosion Cracking," CERL Laboratory Note No. RD/L/N 178-74, Central Electricity Research Laboratories, Surrey (1974).

Appendix A

TENSILE SPECIMENS AND STRESS-STRAIN DIAGRAMS

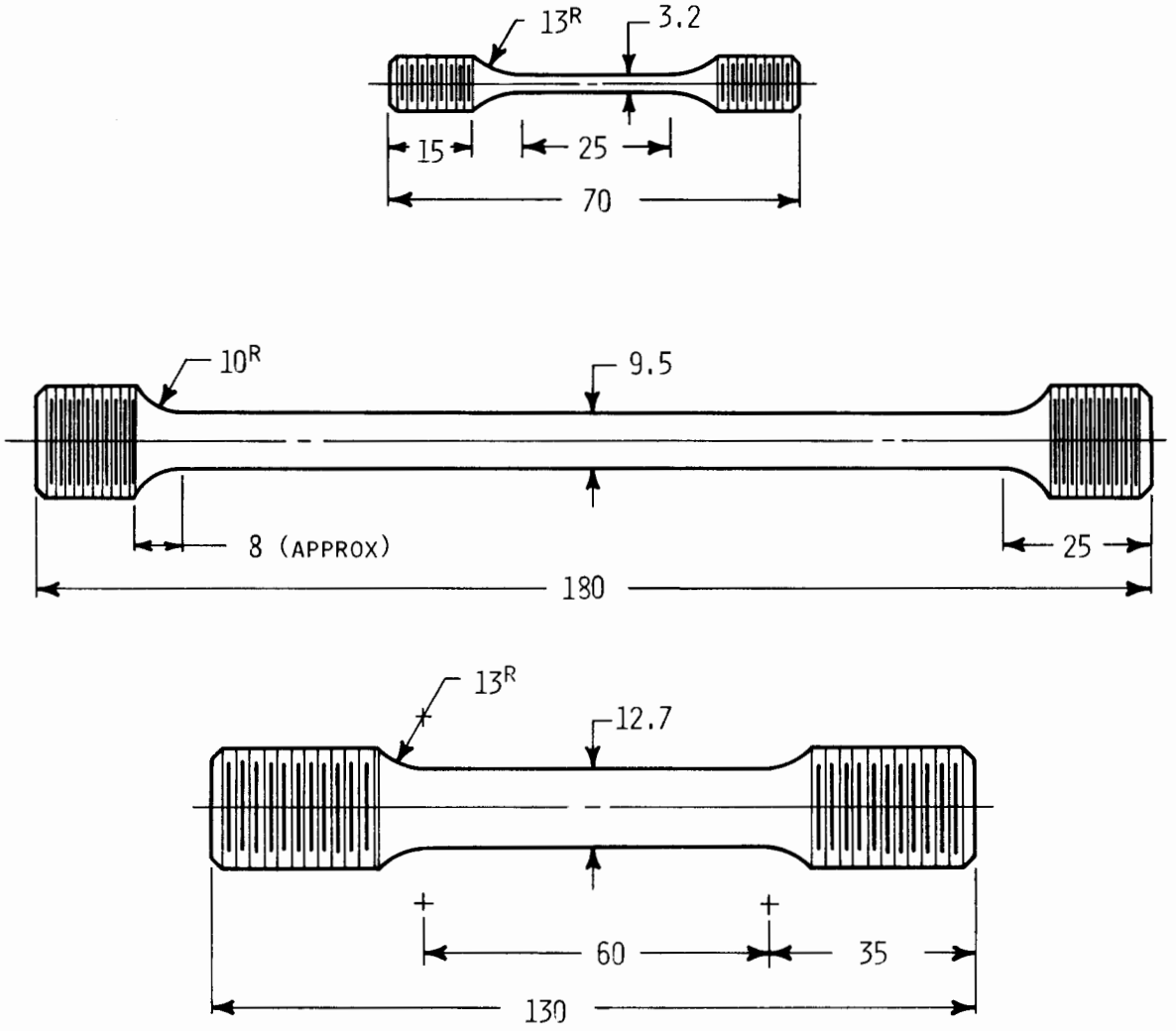

FIGURE A-1. TENSILE TEST SPECIMENS.
All dimensions in mm.

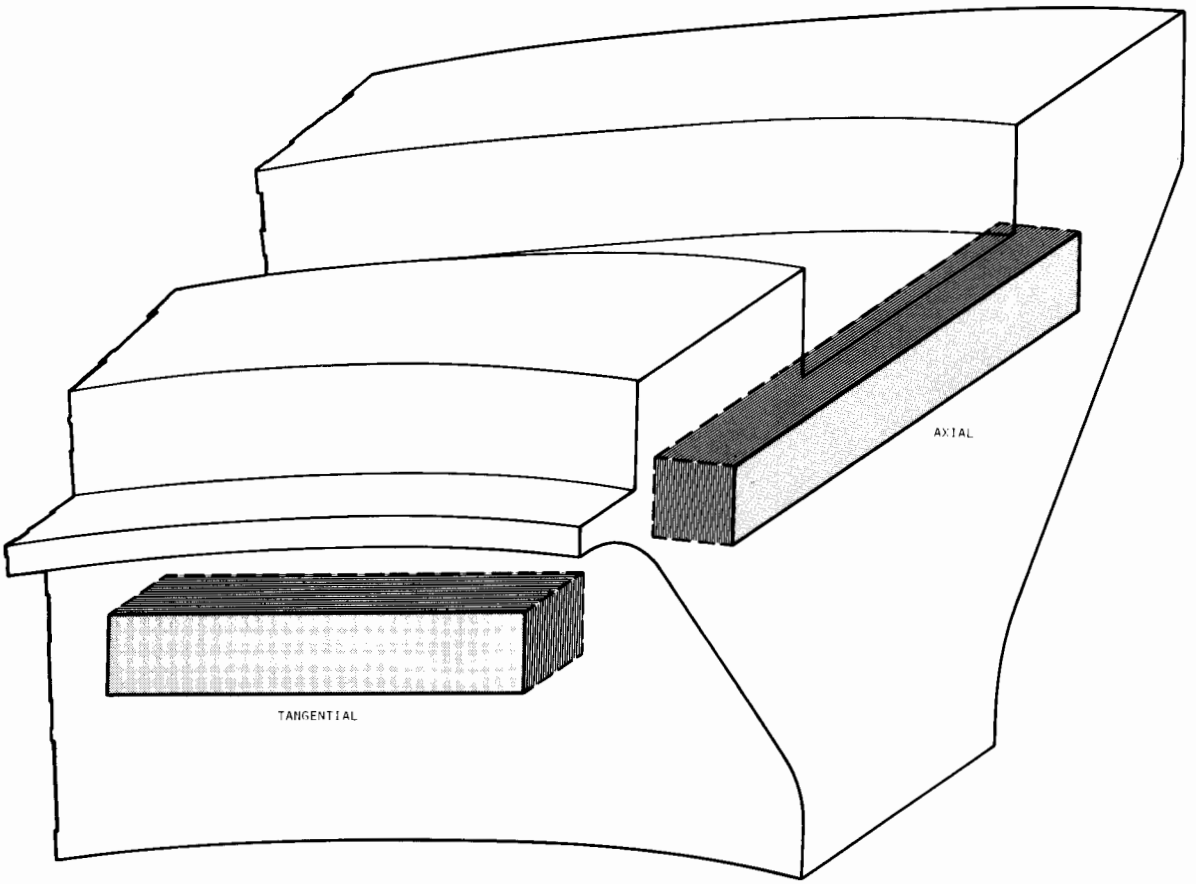

FIGURE A-2. TENSILE SPECIMEN LOCATIONS.
12.7 mm dia. specimens.

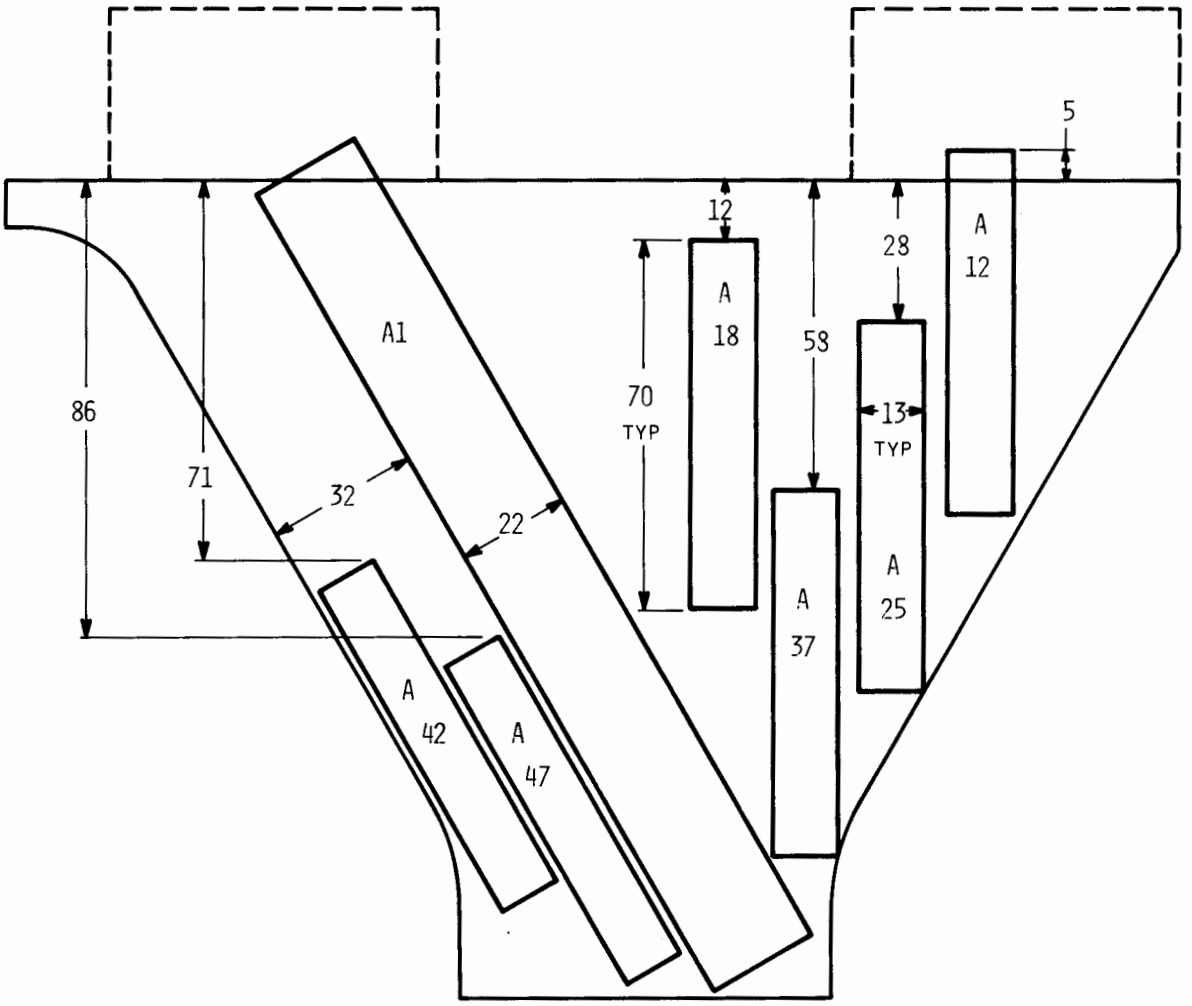

FIGURE A-3. TENSILE SPECIMEN LOCATIONS. 9.5 mm and 3.2 mm dia. specimens. All dimensions in mm.

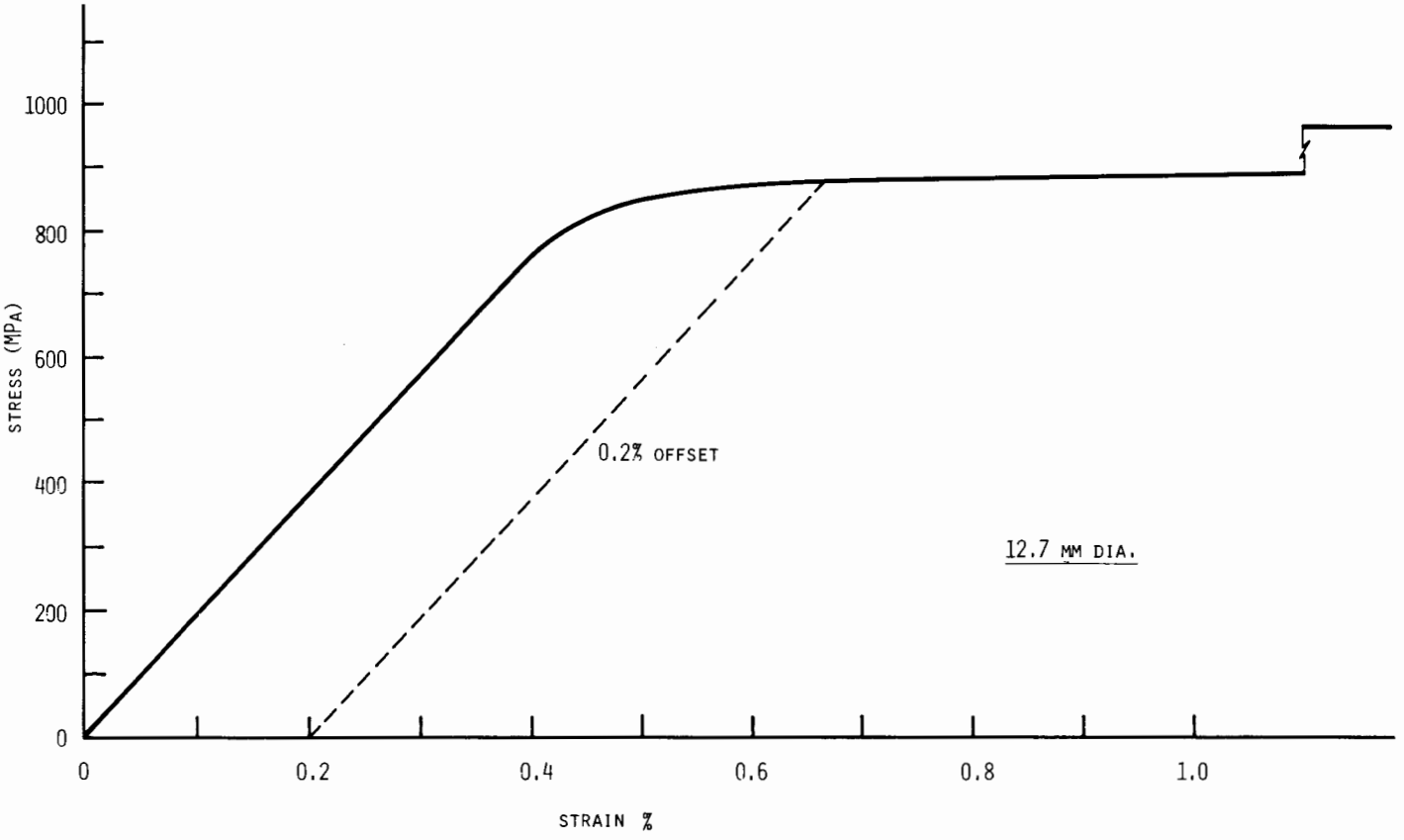

FIGURE A-4. TYPICAL STRESS-STRAIN DIAGRAM.
12.7 mm dia. specimens.

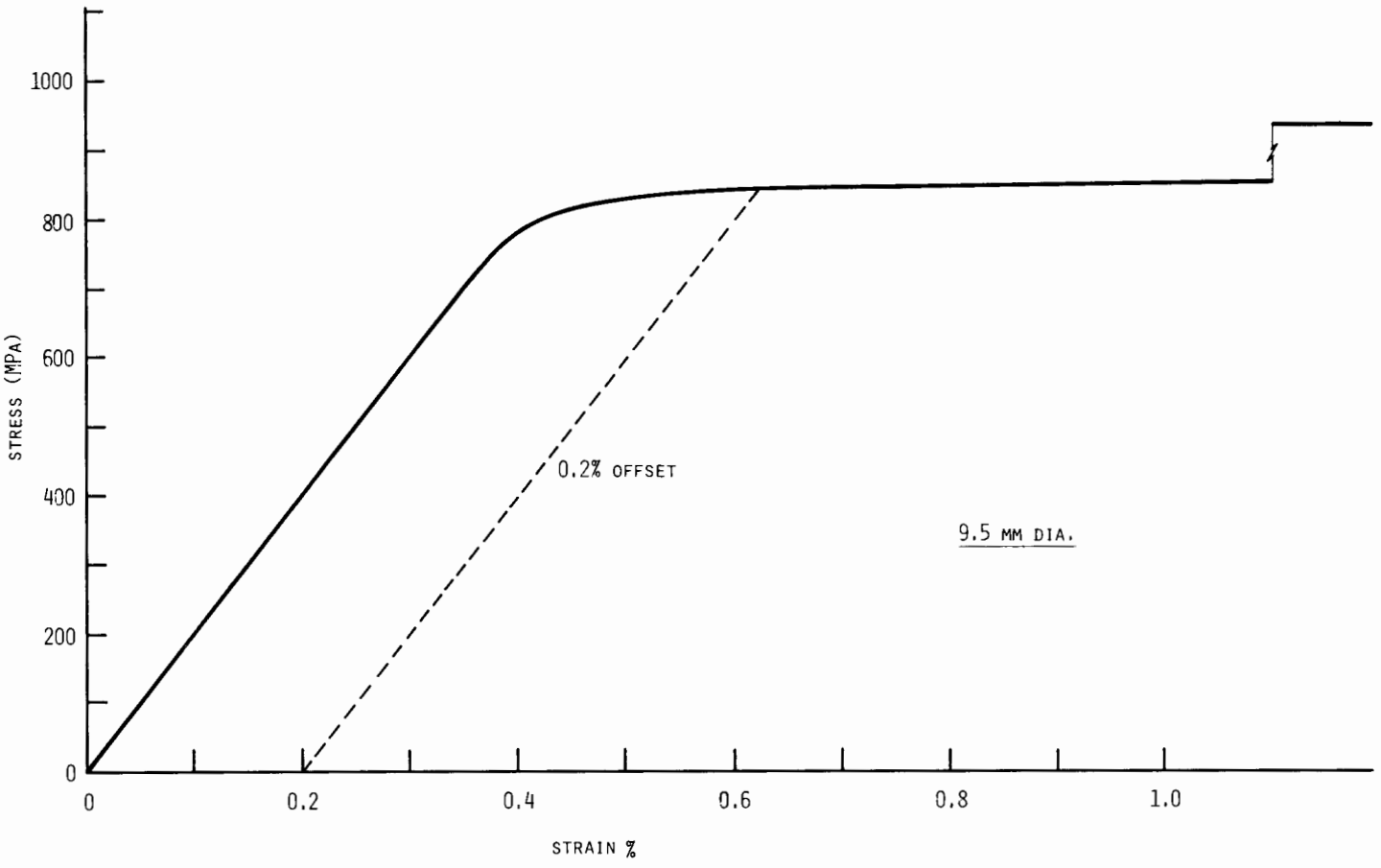

FIGURE A-5. TYPICAL STRESS STRAIN DIAGRAM.
9.5 mm dia. specimens.

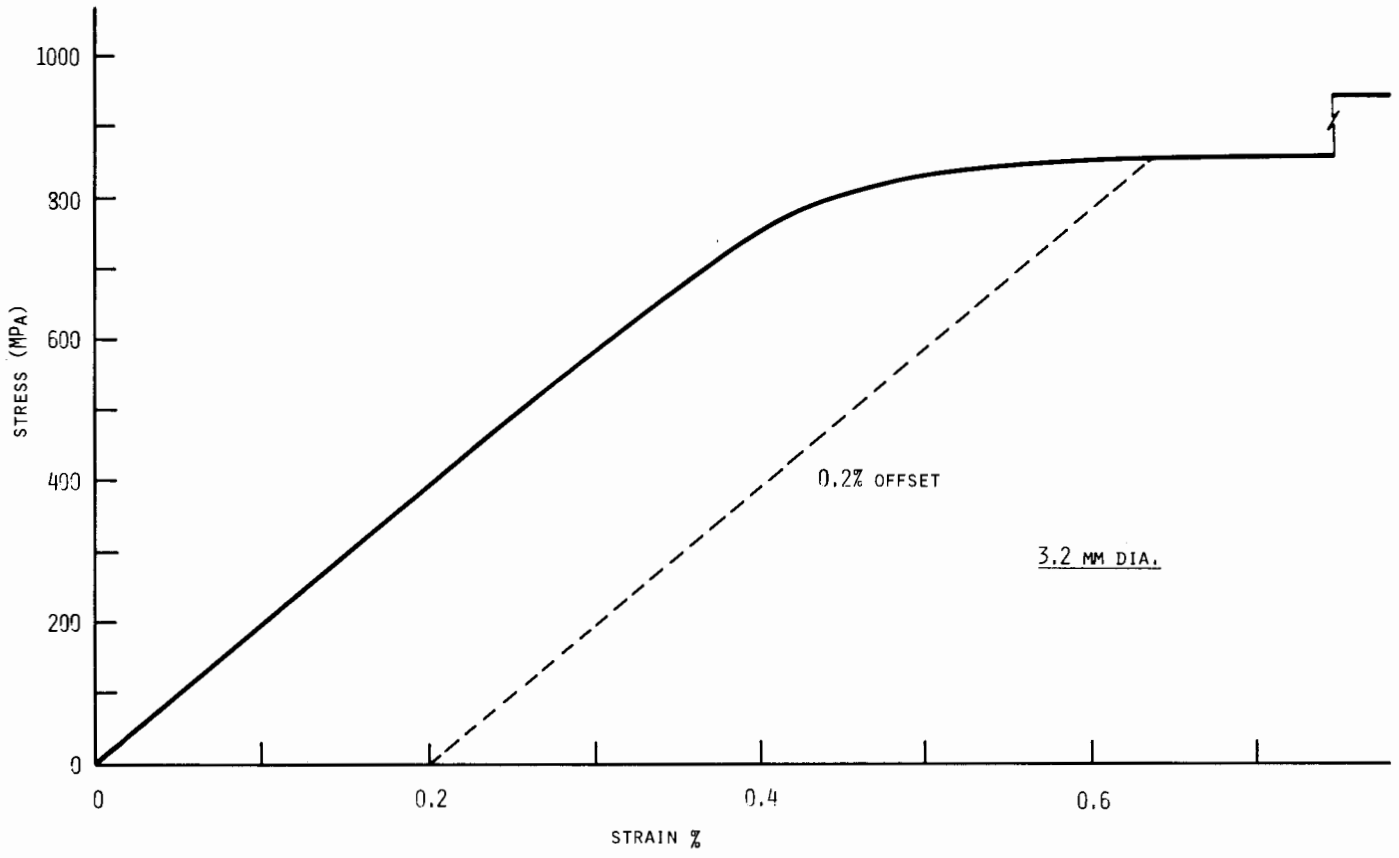

FIGURE A-6. TYPICAL STRESS STRAIN DIAGRAM.
3.2 mm dia. specimens.

Appendix B

IMPACT TEST DATA

Table B-1

CHARPY -V IMPACT RESULTS
Plant C-1, Disk No. 3, LP-2, Generator End

Specimen Number	Temperature °C	Temperature (°F)	Charpy Energy Joules	Charpy Energy (Ft-Lb)	Lateral Expansion mm	Lateral Expansion (in.)	Fracture Appearance % Cleavage
RO-24	-101	(-150)	44.1	(32.5)	.46	(.018)	95
RO-41	-101	(-150)	31.2	(23.0)	.36	(.014)	95
RO-13	-73	(-100)	51.5	(38.0)	.61	(.024)	90
RO-43	-73	(-100)	51.5	(38.0)	.64	(.025)	90
RO-25	-59	(-75)	75.3	(55.5)	.91	(.036)	60
RO-34	-59	(-75)	69.8	(51.5)	.89	(.035)	60
RO-15	-46	(-50)	109.2	(80.5)	1.12	(.044)	25
RO-35	-46	(-50)	99.7	(73.5)	1.12	(.044)	25
RO-14	-32	(-25)	116.5	(86.0)	1.17	(.046)	20
RO-23	-32	(-25)	113.2	(83.5)	1.37	(.054)	20
RO-12	-18	(0)	126.1	(93.0)	1.55	(.061)	20
RO-44	-18	(0)	115.9	(85.5)	1.37	(.054)	20
RO-21	-4	(25)	130.9	(96.5)	1.60	(.063)	5
RO-33	-4	(25)	125.4	(92.5)	1.52	(.060)	5
RO-11	21	(70)	132.9	(98.0)	1.63	(.064)	2
RO-45	21	(70)	141.0	(104.0)	1.47	(.058)	2
RO-22	93	(200)	145.8	(107.5)	1.68	(.066)	0
RO-31	149	(300)	143.7	(106.0)	1.78	(.070)	0

Table B-2

CHARPY-V IMPACT RESULTS
Plant D-1, Disk No. 1, LP-2, Governor End

Specimen Number	Temperature °C	Temperature (°F)	Charpy Energy Joules	Charpy Energy (Ft-Lb)	Lateral Expansion mm	Lateral Expansion (in.)	Fracture Appearance % Cleavage
RS-24	-101	(-150)	32.5	(24.0)	.38	(.015)	95
RS-41	-101	(-150)	41.4	(30.5)	.48	(.019)	95
RS-13	-73	(-100)	62.4	(46.0)	.76	(.030)	90
RS-43	-73	(-100)	51.5	(38.0)	.64	(.025)	90
RS-25	-59	(-75)	94.2	(69.5)	1.04	(.041)	50
RS-34	-59	(-75)	85.4	(63.0)	1.04	(.041)	50
RS-15	-46	(-50)	92.9	(68.5)	1.12	(.044)	30
RS-35	-46	(-50)	94.9	(70.0)	1.02	(.040)	30
RS-14	-32	(-25)	106.4	(78.5)	1.17	(.046)	15
RS-23	-32	(-25)	109.2	(80.5)	1.37	(.054)	15
RS-12	-18	(0)	115.3	(85.0)	1.42	(.056)	5
RS-44	-18	(0)	124.1	(91.5)	1.32	(.052)	5
RS-21	-4	(25)	114.6	(84.5)	1.45	(.057)	2
RS-33	-4	(25)	116.6	(86.0)	1.45	(.057)	2
RS-11	21	(70)	119.3	(88.0)	1.50	(.059)	0
RS-45	21	(70)	126.8	(93.5)	1.27	(.050)	0
RS-22	93	(200)	126.8	(93.5)	1.63	(.064)	0
RS-31	149	(300)	132.2	(97.5)	1.65	(.065)	0

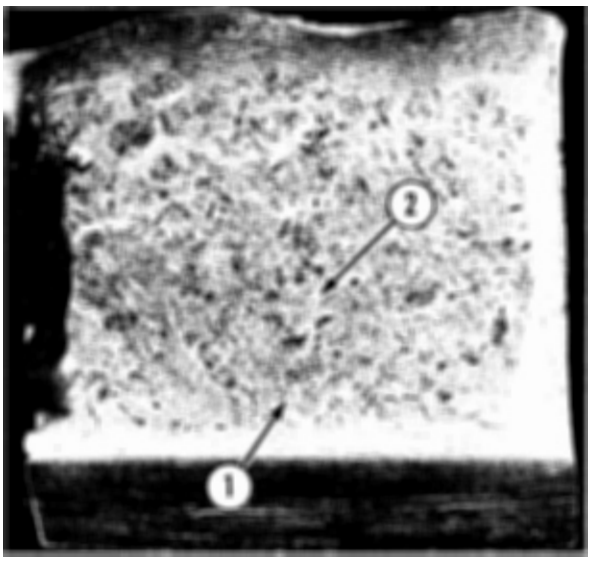

(a) ≃ 7X

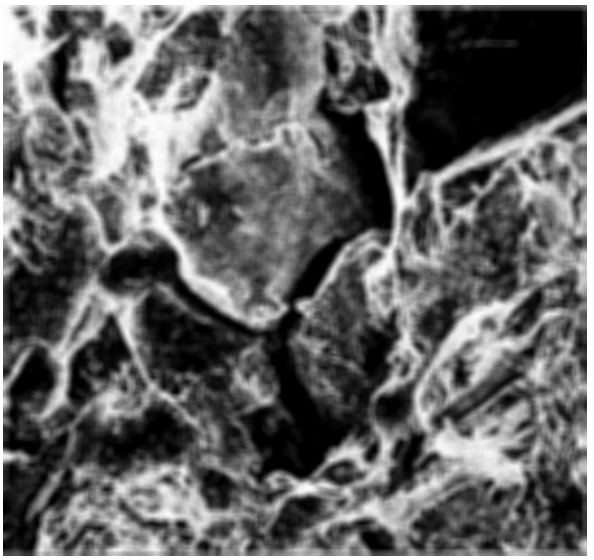

(b) Location 1 in (a). 335X

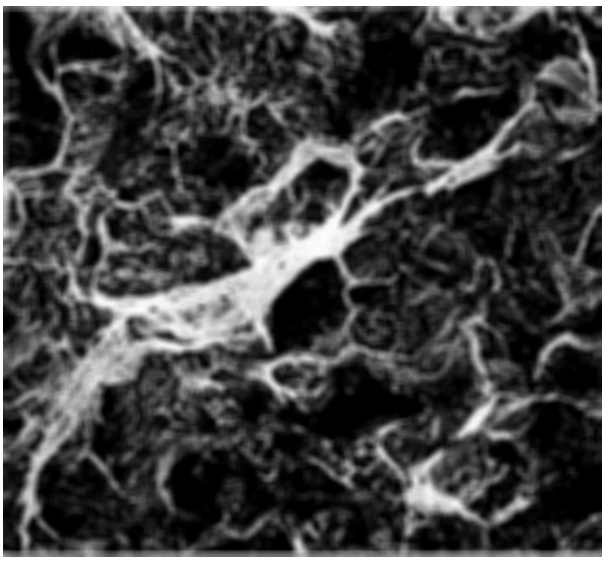

(c) Location 2 in (a). 335X

FIGURE B-1. CHARPY IMPACT SPECIMEN TESTED AT -73°C(-100°F). Specimen RO-13, Plant C-1.

(These photographs reduced to 90% of their original size)

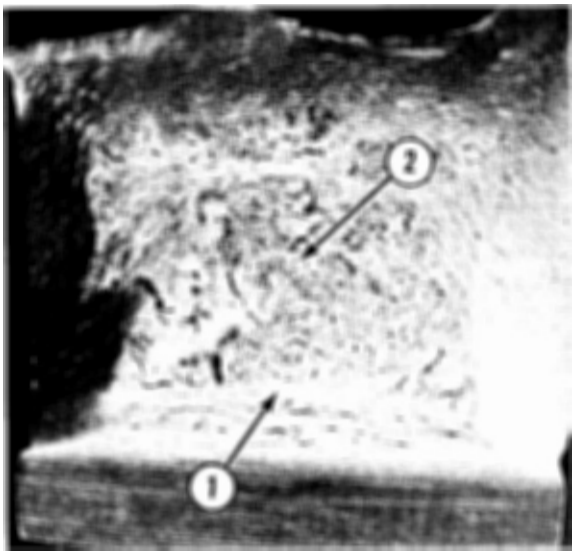

(a) ≈ 7X

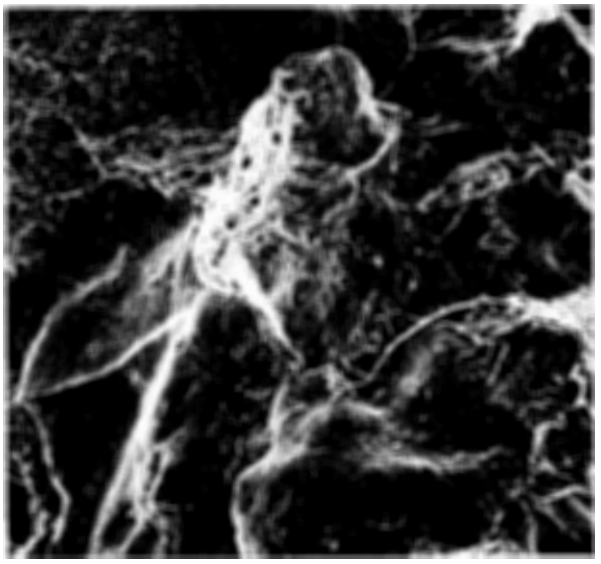

(b) Location 1 in (a). 335X

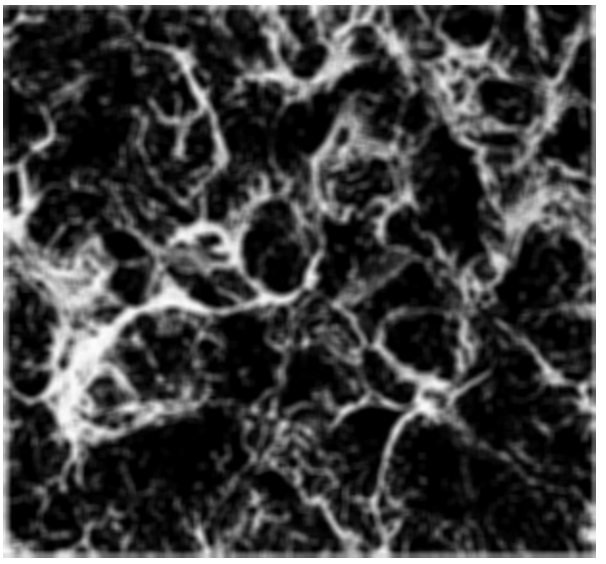

(c) Location 2 in (a). 335X

FIGURE B-2. CHARPY IMPACT SPECIMEN TESTED AT -46°C(-50°F). Specimen RO-35, Plant C-1.

(These photographs reduced to 90% of their original size)

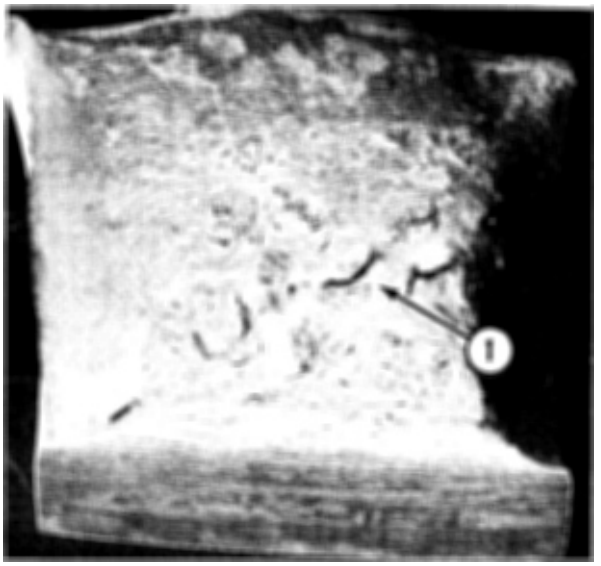

(a) ≈ 7X

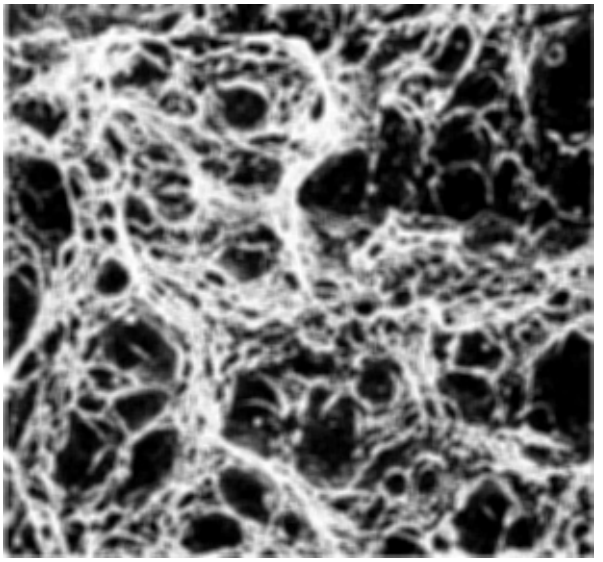

(b) Typical Topography. 840X

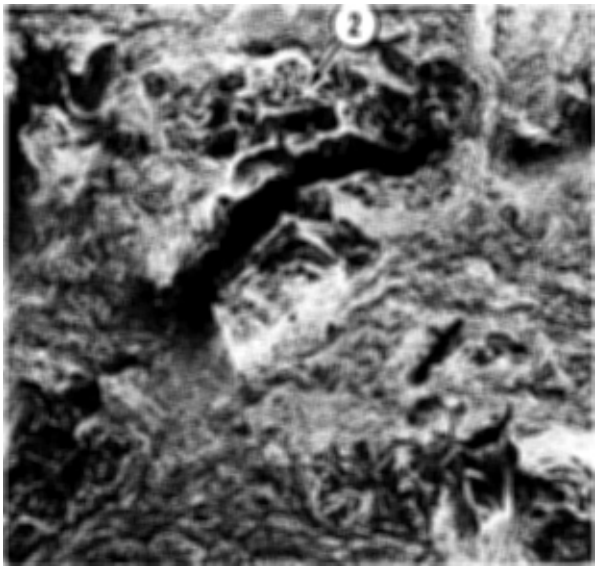

(c) Location 1 in (a). 35X

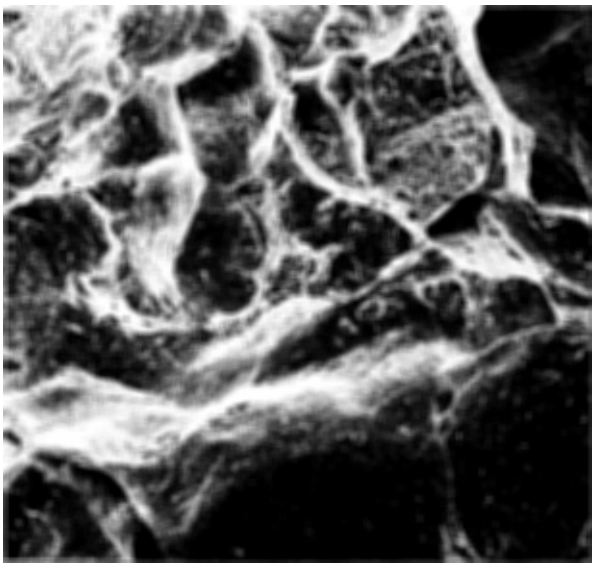

(d) Location 2 in (c). 335X

FIGURE B-3. CHARPY IMPACT SPECIMEN TESTED AT -32°C(-25°F).
Specimen RO-14, Plant C-1.

(These photographs reduced to 90% of their original size)

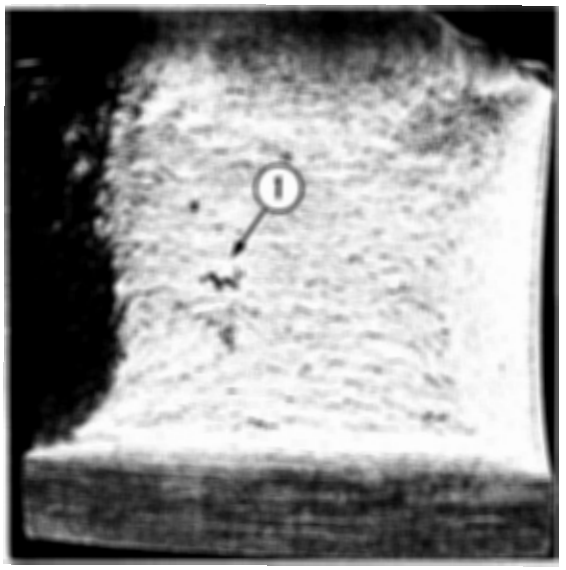

(a) ≃ 7X

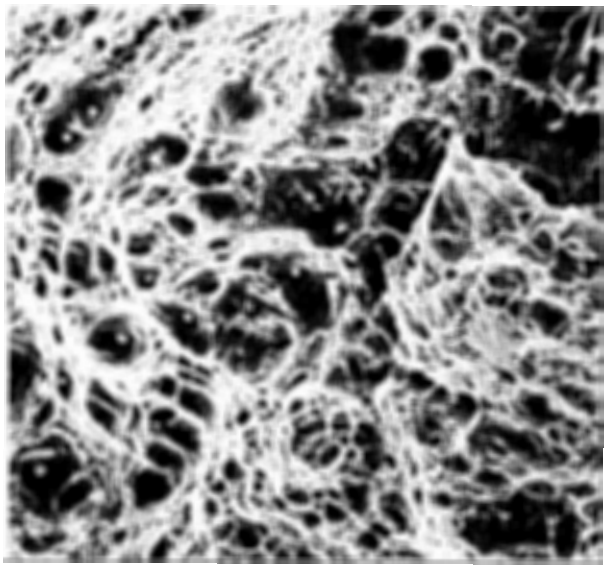

(b) Typical Topography. 840X

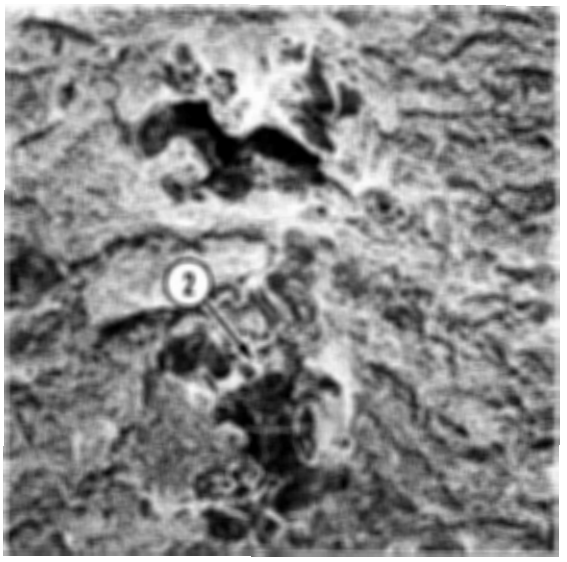

(c) Location 1 in (a). 35X

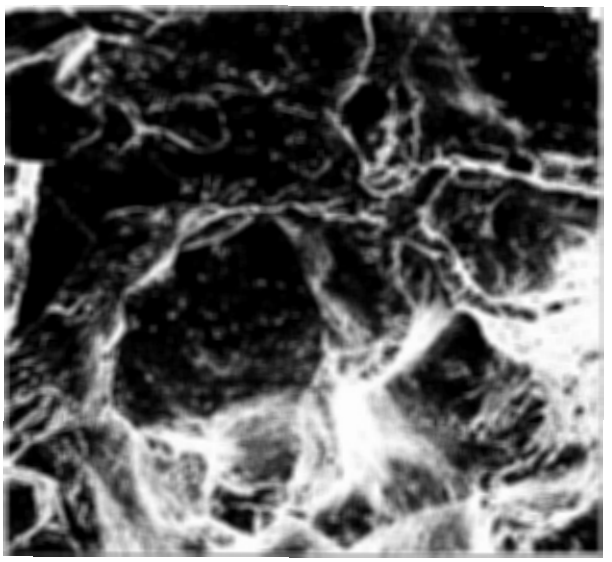

(d) Location 2 in (c). 335X

FIGURE B-4. CHARPY IMPACT SPECIMEN TESTED AT -4°C(25°F).
Specimen RO-21, Plant C-1.

(These photographs reduced to 90% of their original size)